UNIVERSITAT JAUME I

inam Institute of Advanced Materials UJI Castelló

Development and Characterization of Electro- and Photo-Electrochemical Systems for High-Added-Value Products

Ramón Arcas Martínez

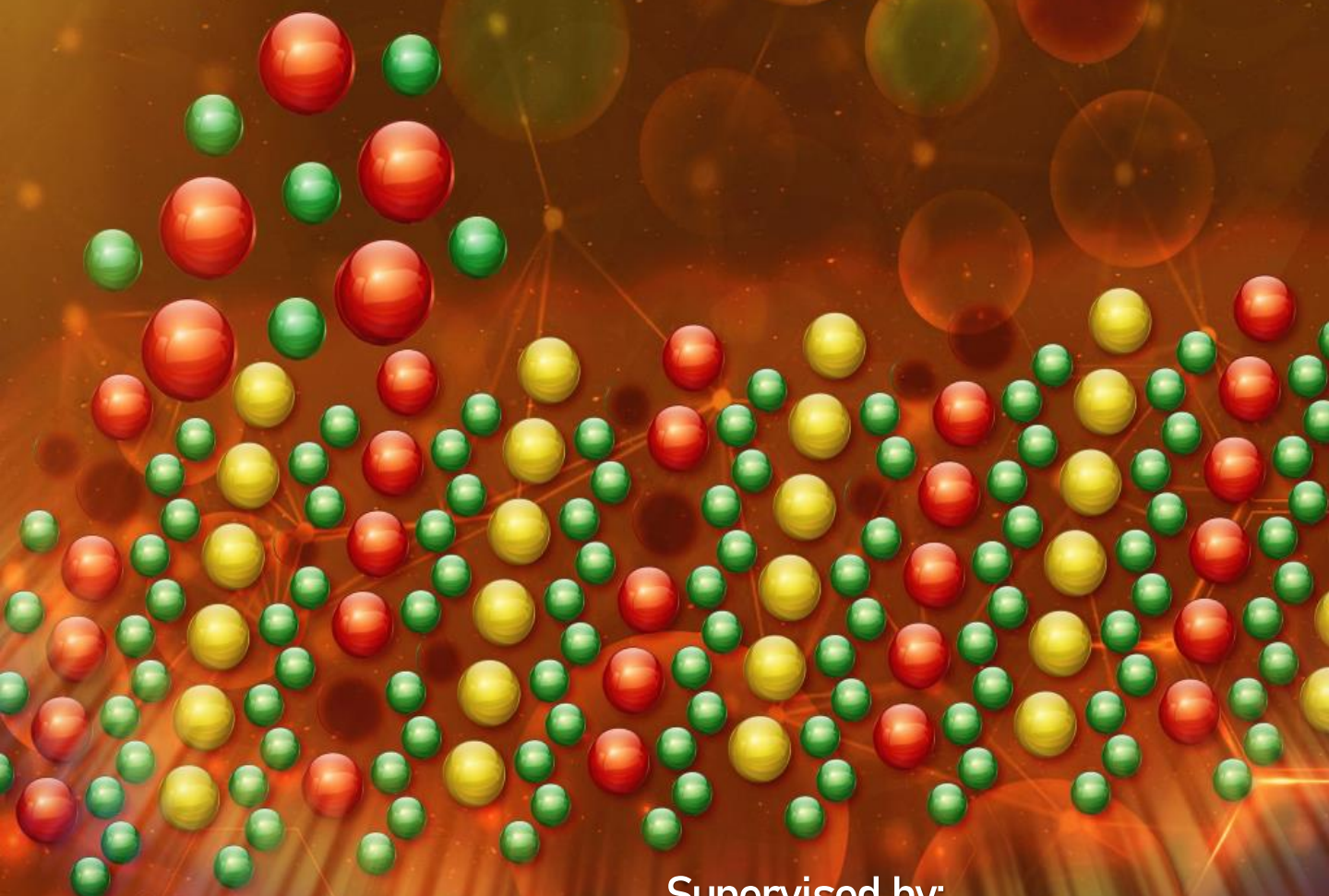

Supervised by:
Prof. Francisco Fabregat Santiago
Dr. Elena Mas Marzá

UNIVERSITAT JAUME·I

Programa de Doctorado en Ciencias

Escuela de Doctorado de la Universitat Jaume I

Development and Characterization of Electro- and Photo-Electrochemical Systems for High-Added-Value Products

Memoria presentada por **Ramón Arcas Martínez**
para optar al grado de doctor por la Universitat Jaume I

FRANCISCO |FABREGAT| SANTIAGO
Firmado digitalmente por FRANCISCO|FABREGAT|SANTIAGO
Nombre de reconocimiento (DN): cn=FRANCISCO|FABREGAT|SANTIAGO, serialNumber=18972796G, givenName=FRANCISCO, sn=FABREGAT SANTIAGO, ou=CIUDADANOS, o=ACCV, c=ES
Fecha: 2023.02.03 16:03:49 +01'00'

Director
Prof. Francisco Fabregat-Santiago

Doctorando

RAMON ARCAS MARTINEZ - NIF:21692857Q
Digitally signed byRAMON ARCAS MARTINEZ - NIF:21692857Q
ND:CN=RAMON ARCAS MARTINEZ - NIF:21692857Q, SERIALNUMBER=21692857Q, G=RAMON, SN=ARCAS MARTINEZ, OU=CIUDADANOS, O=ACCV, C=ES
Reason:I am the author of this document
Ubicació:
Data:2023-02-02 23:41:35
Lector Foxit Versió: 9.0.1

Ramón Arcas Martínez

ELENA| MAS| MARZA
Firmado digitalmente por ELENA|MAS|MARZA
Nombre de reconocimiento (DN): cn=ELENA|MAS|MARZA, serialNumber=20460029B, givenName=ELENA, sn=MAS MARZA, ou=CIUDADANOS, o=ACCV, c=ES
Fecha: 2023.02.03 15:36:22 +01'00'

Co-Director
Dr. Elena Mas Marzá

Castelló de la Plana, February 2023

Funding

The following sources were responsible for founding the research carried out in this thesis:

1. Project: NASCENT: Nuevos conceptos de células solares de bajo coste y alta eficiencia en configuración tándem 2015-2017. Ministerio de Economía y Competitividad (MINECO). MAT2013-47192-C3-1-R
2. Project: ValPEC: Síntesis de productos de alto valor añadido mediante sistemas fotoelectrocatalíticos avanzados. 2018-2020 Ministerio de Economía y Competitividad (MINECO). ENE2017-85087-C3-1-R.
3. Project: NO-LIMIT: Boosting photovoltaic performance by the synergistic interaction of halide perovskites and semiconductor quantum dots. European Research Council (ERC) Consolidator grant. 724424
4. Fundació Balaguer-Gonel Hermanos, per a estades d'investigació d'estudiantat de l'Escola de Doctorat de la Universitat Jaume I que realitza tesis doctorals que opten a la menció de doctor o doctora internacional

Declaration

I hereby declare that this thesis contains no material that has been used to obtain any other degree or certification. The co-authors of the publications arising from this work have waived their right to present them as part of another PhD thesis.

The research work for this thesis was carried out at the Institute of Advanced Materials (INAM), Department of Physics, Universitat Jaume I in Castellon de la Plana, Spain, under the direction of Prof. Dr Francisco Fabregat-Santiago who served as both supervisor -tutor and co-direction of Dr Elena Mas Marzá.

Acknowledgements

No puedo acabar esta etapa sin dejar de agradecer a todos aquellos que han hecho posibles estos años. En esta ocasión resulta especialmente relevante ya que sin vosotros esta tesis no hubiera salido adelante.

En primer lugar, me gustaría dar las gracias a mis directores de tesis, el profesor Francisco Fabregat y la Dra. Elena Mas, por ofrecerme la oportunidad de participar en este proyecto. Su experiencia y conocimiento del tema han sido cruciales en mi proceso de aprendizaje y en el progreso de mis habilidades investigadoras, pero sobre todo vuestra guía, insistencia y apoyo, han resultado imprescindibles para conseguir todos los objetivos propuestos. Me siento muy orgulloso y afortunado por haber iniciado esta nueva línea de investigación en el INAM junto a vosotros.

Los resultados presentados en esta tesis son producto de importantes colaboraciones con otros grupos o centros de investigación. Me gustaría destacar en este punto la aportación del Prof. Sixto Giménez y todo su grupo de trabajo, cuyos conocimientos teóricos y experiencia en sistemas fotoelectrocatalíticos me han ayudado a entender y mejorar los "desastres" que normalmente ocurrían durante las primeras experiencias en el laboratorio. También al Prof. Jordi Arbiol y la Dra. María Chiara Spadaro por ayudarme encontrar soluciones y entender mejor los resultados vistos desde un punto de vista atómico. Finally, I would also like to thank Prof. Seigo Ito and Yuuki Koshino for showing me that electrocatalysis can be done with anything, even a pencil graphite rod such as those used continuously at school.

Gostaria também de agradecer à Prof. Beatriz Royo e ao Prof. Paulo Nuno Martinho por me permitirem fazer a minha estadia de investigação nos laboratórios do ITQB e da Universidade Nova de Lisboa. Gostaria também de agradecer à Dra. Sara Realista por toda a sua ajuda e apoio, o que tornou a minha vida muito mais fácil durante estes três meses. É uma pena que não tenha tido mais tempo e melhores condições para publicar todo o trabalho que fizemos. Muito obrigado.

Al personal técnico de los Servicios Centrales de Instrumentación Científica de la UJI por el apoyo para la realización de los análisis estructurales y morfológicos, en especial a José Javier Gómez, Esther Irles, Cristian Vicent, José Miguel Pedra y Gabriel Peris.

A todo el personal de administración del INAM, especialmente a Loles y Sandra por ayudarnos en la gestión de cualquier asunto económico o burocrático, pero sobre todo por hacer la vida más fácil y más divertida para todos los que estamos allí.

A todos y cada uno de los miembros de los grupos de investigación de GAME y GAS con los que he podido compartir mi día a día (si los nombrase a todos siempre me dejaría alguno seguro). También, a todos aquellos que han realizado su estancia en el INAM, en especial a Loengrid y Yuuki que han demostrado que tres meses son suficientes para dejar su huella. Espero que algún día nos volvamos a ver.

A todo el INAM FC por esas derrotas que solo duraban hasta las cervezas de después del partido.

A mi compadre cabrón, Cam, porque a pesar de llegar demasiado tarde, no has dudado en implicarte, colaborar y ayudarme a conseguir todos los retos que aún tenía por delante.

A Nuria, Marta, Drialys y Roser por acogerme en "centralita" y hacer de cada día una nueva forma de entender la vida. Gracias por vuestro apoyo y por darme la confianza para poder hablar de cualquier cosa en cualquier momento. Todos los momentos vividos se quedan para nosotros y espero que haya muchos nuevos por vivir.

A Clara, Agus, Marise y Fabi porque lo vuestro es imposible de explicar con palabras. Solo deciros que una parte de este logro es vuestra y que espero estar ahí para cualquier cosa que necesitéis en un futuro. Gracias por tantos momentos únicos.

A Nuria y Jose por acogerme todos estos días en vuestra casa y hacer que esta etapa tan complicada para mi haya sido un poco más fácil. Iria y Emma vuestros "no te vayas, tío" o "vuelve todos los días" son realmente especiales. Imagino que algún día eso acabará, pero espero que siempre contéis con vuestro tío o "titi" para lo que vosotras necesitéis.

A Yaiza porque has tenido que aguantarme y sufrirme como nadie más en esta etapa, porque a partir de ahora todo va a ser diferente. Me gustaría que futuros logros que podamos conseguir, los superemos juntos de nuevo.

Por último, los más importantes, los que han sido, son y serán un pilar fundamental, mis padres, Ramón y Agustina. Sin ellos, y sin su esfuerzo, nunca habría sido posible hacer realidad este reto. Por inculcarme desde pequeño, valores como la responsabilidad, el esfuerzo, la perseverancia y la lucha por lo que quiero y creo, GRACIAS.

Publications Included in this Thesis

1. **R. Arcas**, Y. Koshino, E. Mas-Marzá, R. Tsuji, H. Masutani, E. Miura-Fujiwara, Y. Haruyama, S. Nakashima, S. Ito and F. Fabregat-Santiago, Pencil Graphite Rods Decorated with Nickel and Nickel Iron as Low-Cost Oxygen Evolution Reaction Electrodes. *Sustainable Energy Fuels*, **2021**, 5, 3929 DOI: 10.1039/D1SE00351H. Impact factor: 6.813

2. **R. Arcas**, E. Peris, E. Mas-Marzá and F. Fabregat-Santiago, Revealing the contribution of singlet oxygen in the photoelectrochemical oxidation of benzyl alcohol. *Sustainable Energy Fuels*, **2021**, 5, 956 DOI: 10.1039/D0SE01322F. Impact factor: 6.813

3. **R. Arcas**, Cardenas-Morcoso, D., Spadaro, M.C., García-Tecedor, M., Mesa, C.A., Arbiol, J., Fabregat-Santiago, F., Giménez, S. and Mas-Marzá, E. Direct Observation of the Chemical Transformations in $BiVO_4$ Photoanodes upon Prolonged Light-Aging Treatments. *Sol. RRL*, **2022** 6: 2200132. DOI: 10.1002/solr.202200132. Impact factor: 8.13

This thesis has been accepted by the co-authors of the publications listed above that have waived the right to present them as part of another PhD thesis.

Publications not Included in this Thesis

1. Agustin O. Alvarez, **Ramón Arcas**, Clara A. Aranda, Loengrid Bethencourt, Elena Mas-Marzá, Michael Saliba, and Francisco Fabregat-Santiago. Negative Capacitance and Inverted Hysteresis: Matching Features in Perovskite Solar Cells, *The Journal of Physical Chemistry Letters* **2020**, *11*, 8417. DOI: 10.1021/acs.jpclett.0c02331. Impact Factor: 6.475.

2. Carvajal, D., **Ramón Arcas**, Mesa, C. A., Giménez, S., Fabregat-Santiago, F., Mas-Marzá, E., Role of Pd in the Electrochemical Hydrogenation of Nitrobenzene Using CuPd Electrodes. *Adv. Sustainable Syst.* **2022**, 6, 2100367. DOI: https://doi.org/10.1002/adsu.202100367. Impact factor 2021: 6.737

List of abbreviations and acronyms

GHG	Greenhouse gases
IPCC	Intergovernmental Panel on Climate Change
SDG	Sustainable Development Goals
EC	Electrochemical cell
OER	Oxygen evolution reaction
HER	Hydrogen evolution reaction
LDH	Layered double hydroxides
PV-EC	Photovoltaic-electrochemical cell
PEC	Photoelectrochemical cell
PV-PEC	Photovoltaic-photoelectrochemical cell
HMF	5-Hydroxymethylfurfural
TCO	Transparent conducting oxides
FTO	F-doped SnO_2
ATO	Sb-doped SnO_2
ITO	Sn-doped In_2O_3
AZO	Al-doped ZnO
PGR	Pencil Graphite Rod
$Ni(OH)_2$	Nickel hydroxide
NiOOH	Nickel oxyhydroxide
AM 1.5G	Air Mass 1.5 Global
OV_s	Oxygen vacancies
η	Solar light conversion efficiency
η_{abs}	Solar light absorption efficiency
η_{sep}	Charge separation efficiency
η_{trans}	Surface charge transfer efficiency
IPCE	Photon to current conversion efficiencies

Abstract

Nowadays, the limited use of fossil fuels such as oil, coal and natural gas is the major challenge to be faced by humanity. Under this scenario, electro- and photo-electrochemical cells are one of the most promising and economically feasible future technologies for producing alternative energy sources, such as green hydrogen. Their use, combined with renewable energy sources, such as solar or wind, generates H_2 in a clean and emission-free way.

The main challenge in the development of electrochemical and photoelectrochemical systems is the kinetics of the anodic oxygen evolution half-reaction (OER), which is intrinsically slow. For this reason, in this thesis all efforts have been devoted to elaborate strategies that allow a better exploitation of the oxidative process in (photo)-electrochemical cells. Among these strategies, on the one hand, porous electrodes based on pencil graphite rods and doped with NiFe have provided a large surface area and have been used for the electrochemical oxidation of water to oxygen. On the other hand, new oxidation systems have been employed, such as the photoelectrochemical oxidation of primary alcohols, which have allowed the selective synthesis of organic chemical products with high added value.

Finally, a set of characterization techniques including structural and morphological techniques, as well as analytical and electrochemical methods, have allowed us to differentiate and understand the processes that take place in the (photo)-electrochemical cells studied. Among the different techniques used, impedance spectroscopy has proved to be fundamental for the determination of surface states related to these processes.

Resumen

En la actualidad, las restricciones en el uso de combustibles fósiles como el petróleo, el carbón y el gas natural es el mayor reto al que se enfrenta la humanidad. En este escenario, los sistemas electroquímicos y fotoelectroquímicos son una de las tecnologías futuras económicamente viables y más prometedoras para obtener fuentes de energía alternativas, como el hidrógeno verde. Gracias al uso de estos sistemas en combinación con fuentes de energía renovable, como la solar o la eólica, se puede generar H_2 de una manera limpia y con cero emisiones.

La principal dificultad del desarrollo de los sistemas electroquímicos y fotoelectroquímicos es la cinética de la semirreacción anódica de evolución del oxígeno (OER) que es intrínsecamente lenta. Por este motivo, en esta tesis doctoral todos los esfuerzos han sido dedicados a elaborar estrategias que permitan un mejor aprovechamiento del proceso oxidativo en la celda (foto)-electroquímica. Entre estas estrategias, se han utilizado electrodos porosos basados en minas de grafito y decorados con NiFe que han proporcionado una gran área superficial, con los cuales se ha realizado de forma satisfactoria la oxidación electroquímica de agua a oxígeno. Por otro lado, se han empleado nuevos sistemas de oxidación, como la oxidación fotoelectroquímica de alcoholes primarios, que ha permitido la síntesis selectiva de productos químicos orgánicos con alto valor añadido.

Finalmente, se han utilizado un conjunto técnicas de caracterización entre los que se incluyen técnicas estructurales y morfológicas, así como métodos analíticos y electroquímicos que ha permitido diferenciar y conocer los procesos que tienen lugar en las celdas (foto)-electroquímicas estudiadas. Entre las diferentes técnicas utilizas, la espectroscopia de impedancia ha demostrado ser fundamental para la determinación de estados superficiales relativos a estos procesos.

Table of Content

1. Introduction

1.1. Energy and development

The availability of cheap energy represents an essential driving force for both the economic growth and welfare improvement of human beings. However, the huge and growing energy demand in the last decades (**Figure 1a**), as a consequence of world's overpopulation and current technological developments, has become a serious problem for our Planet.

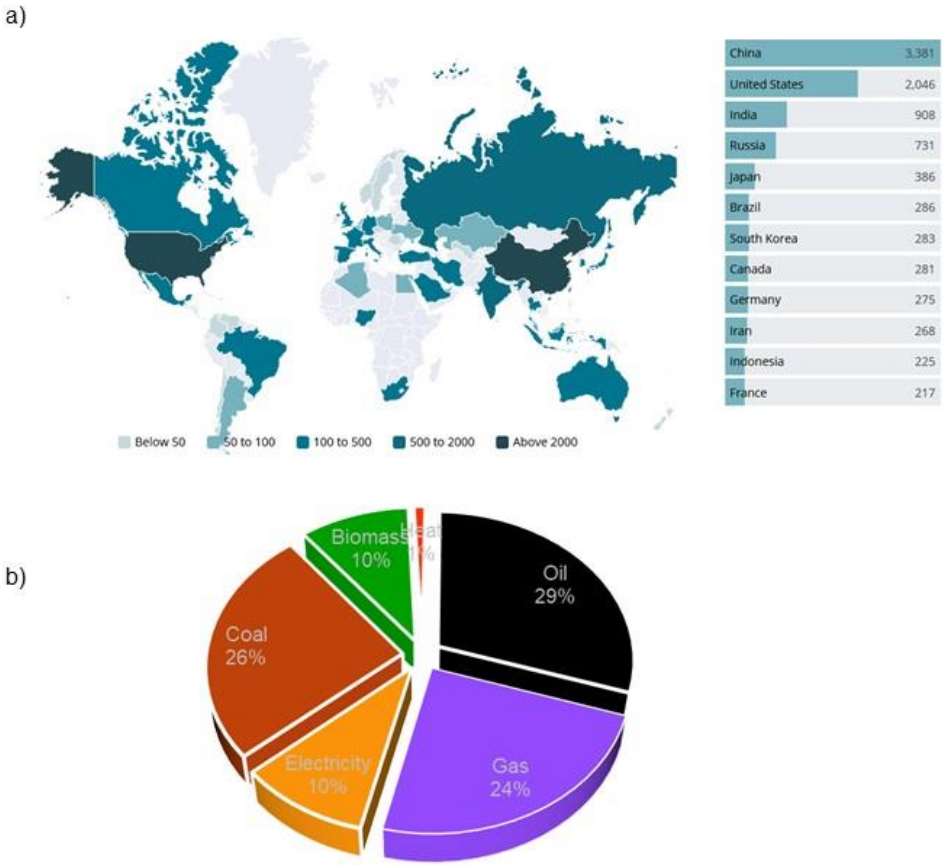

Figure 1. (a) Total energy consumption by country (Mtoe) Includes coal, gas, oil, electricity, and biomasss. (b) breakdown by energy. Source: Enerdata.

Nowadays, the way of satisfying our energy requirements is mainly based on the use of non-renewable energy sources, such as fossil fuels, oil, coal and gas, which represent >80% of energy consumption, see **Figure 1b**, whose combustion is directly related to the emission of greenhouse gases (GHG). Recently, the Intergovernmental Panel on Climate Change (IPCC) reported the detrimental effect of GHG from an economic and environmental point of view, highlighting the need to change the current energy production model to avoid further serious climate change consequences.[1] Furthermore, the United Nations included *affordable and clean energy* as one of the 17 Sustainable Development Goals (SDG7).[2]

Talking about energy in a sustainable context implies to find a way to produce and use clean energy, involving as well social and environmental backgrounds. In this scenario, "**net zero emissions"** objective has emerged as a future energy plan to achieve net zero GHG emissions in 2050. This means reducing greenhouse gasses as close to zero as possible by reabsorbing the remaining emissions from the atmosphere, for example, through the oceans and forests. The change towards a more sustainable energy system, with cero GHG emissions, implies the replacement of the traditional centralized energy system (based on large power plants) by a decentralized and flexible system that allows the adequate integration of energy supply through renewable technologies.

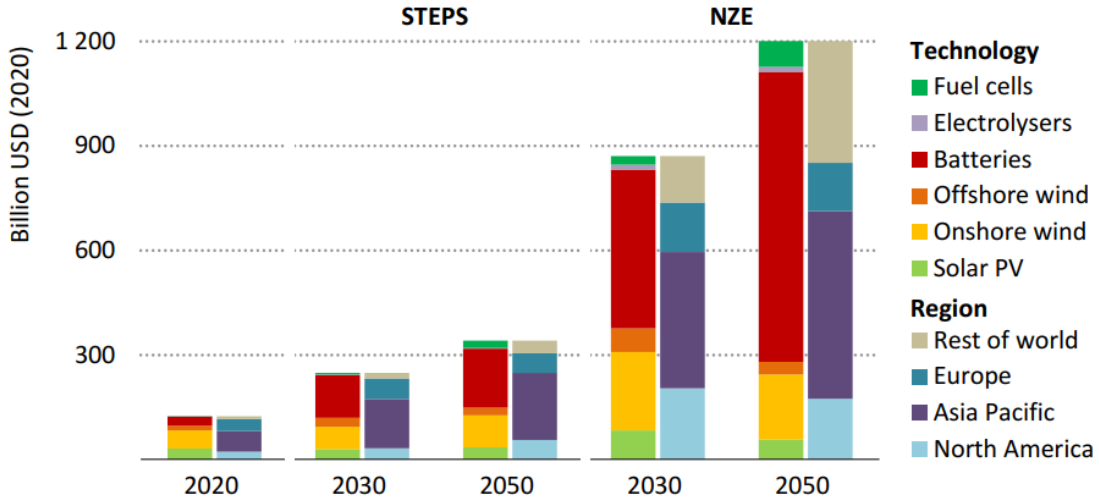

Figure 2. Estimated market size for selected clean energy technologies by technology and region in the following years until reaching the net zero emissions. Source: International Energy Agency.

Among the different energy technologies based on renewable sources, solar and wind have attracted great attention during the last decades for the production of *green electricity*, **Figure 2**. Their intermittent character principally characterizes these technologies. For this reason, their full implementation requires the development of efficient storage systems for those moments when there is a production deficit. In other words, an increase in the use of renewable energies requires an increasing necessity to store such intermittent and unpredictable green electricity source. Therefore, the development of large capacity and low-cost energy storage systems is key to provide the flexibility needed by the future energy systems aimed to achieve the climate neutrality goal.

The main motivation of the doctoral thesis presented here is contributing to the development of such energy storage systems by providing new strategies to the solar-fuel conversion technologies. The systems presented here has a large potential for reducing costs and improving the efficiency of the different processes involved in these electrochemical processes.

1.2. Sustainable fuels: the hydrogen opportunity

Hydrogen (H_2) is the simplest molecule able to store large amounts of energy. The main reasons for using H_2 to store energy include: its light weight , its abundancy -is the most abundant gas in the Universe-, its energy yield per H_2 molecule (122 $kJ \cdot g^{-1}$, almost 3 times higher than the energy content per weight of any other hydrocarbon fuel and 5 times higher than methanol and ethanol),[3] and finally, when hydrogen is used as a fuel, it generates only water as by-product with zero emissions of CO_2 or other pollutants.

In contrast, H_2 has a number of disadvantages that have limited its use. H_2 is a compound that is difficult to store, so the volume consumed to obtain the same energy takes up three times more volume of hydrogen than of natural gas. In addition, H_2 is a dangerous and hazardous substance because it is flammable, volatile and, due to its lightness, very easily dispersible.

As benefits overcome by far the drawbacks, in the last years H_2 has become a very popular energy vector and the base of many discussions and proposals about an H_2-based economy.[4] Consequently, the use of hydrogen has begun to be promoted worldwide. A large amount of investments are currently being directed to implement the use of hydrogen as fuel in smart cities and industries with large energy needs.

The processing routes to harvest hydrogen have different cost and material requirements depending on the technology and the energy source selected. In this sense, the potential of hydrogen to reduce the GHG emissions is strongly dependent on how it is produced. For this reason, hydrogen has been classified in a simple way according to a colour scale based on the raw materials used and the CO_2 emissions generated during its production.[5] A simple classification of the different colors of hydrogen contain:

i*) Black or brown hydrogen*: hydrogen is obtained using carbon, water and electricity from non-renewable sources including nuclear power plants. This process generates large quantities of CO_2 among other by-products.

ii) *Grey Hydrogen*: hydrogen is obtained from natural gas or light hydrocarbons using reforming processes. Practically, 99% of hydrogen produced nowadays is of this type. It produces 23 kg of CO_2 per kg of H_2

iii) *Blue Hydrogen*: hydrogen is produced as described in the grey hydrogen but after the reforming process there are extra steps for carbon capture, utilization and storage (CCUS). This allows to reduce the CO_2 emissions of the overall process in more than 95%.

iv) *Green hydrogen* (or renewable hydrogen): Hydrogen is generated using renewable electricity using water as hydrogen-source by electrolysis i.e. water splitting. It is also considered green hydrogen the one obtained from biogas reforming or the one obtained from biochemical conversion of biomass under certain sustainability criteria.

Based on these considerations, the conversion of renewable energy into hydrogen seems to be the perfect strategy to provide, convert and store the energy in a sustainable and environmentally friendly manner. On this way, the hydrogen generated by electrolysis could eliminate the intermittent character of renewable sources and contribute to the decarbonisation of our society removing the carbon combustion from the energy production equation. Moreover, the hydrogen provided by sun energy could reach to a larger number of population, thus avoiding the current energy deficiencies in some areas of the world.

1.2.1. Electrochemical systems

Electrochemical systems allow, by applying an overpotential, combining oxidation and reduction processes that take place at the anode and cathode, respectively. In general, in electrochemical systems a wide variety of reactive intermediates can be formed at the surface of the electrode (anode or cathode) by electron transfer mechanism, without the need of using toxic reagents. Consequently, these systems are considered a very powerful tool to carry out chemical transformations.

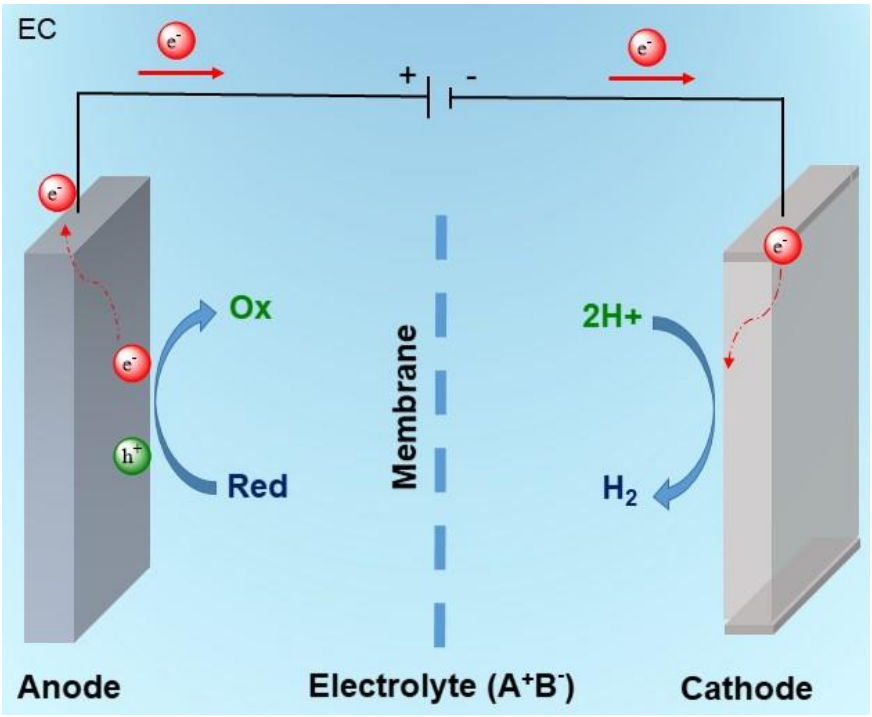

Figure 3. Schematic diagram of an electrochemical cell.

To provide electrochemical transformations, it is mandatory to have an electrochemical system that meets the specific conditions of the process. Within the electrochemical configurations used to perform chemical reactions, different strategies have been adopted over the years. The most successful configuration is an electrochemical cell (**Figure 3**) consisting of a cell with two metal electrodes (cathode and anode) separated by a membrane which is able to exchange protons between the electrodes. These systems are able to work at low pressure conditions and the two

electrodes need an external source of energy to make the process possible, generating an electron flux from the anode to the cathode)

The electrocatalytic water splitting is a reaction where water is dissociated into oxygen and hydrogen by the action of an energy input.[6] This reaction occurs in two stages according to the reactions involved in each compartment. In this sense, when a cell voltage higher than the thermodynamic potential (>1.23 V vs. RHE) is applied, in the anode compartment, the oxygen evolution reaction (OER) occurs, forming O_2 and releasing $4e^-$ in the process. The corresponding reactions for OER, depending on the pH of the electrolyte media (basic or acid) are:[7]

$$4OH^- \rightarrow O_2 + 2H_2O + 4e^- \text{ (basic media)} \quad (1)$$

$$2H_2O \rightarrow O_2 + 4H^+ + 4e^- \text{ (acid media)} \quad (2)$$

Fundamentally, the OER involves the formation of a sequence of different intermediates at the surface of the anode (MOH, MO and MOOH, see following reactions). In each step, an electron is transferred from the M-O bound though the conductive channel and consequently the metal surface of the electrode is oxidized from M^o to M^{4+}.[8] Therefore, the bonding interactions between the anode and the intermediates are essential from the electrocatalytic point of view.[9,10]

$$M + OH^- \rightarrow MOH + e^- \quad (3)$$

$$MOH + OH^- \rightarrow MO + H_2O + e^- \quad (4)$$

$$MO + OH^- \rightarrow MOOH + e^- \quad (5)$$

$$MOOH + OH^- \rightarrow M + O_2 + H_2O + e^- \quad (6)$$

On the other hand, in the cathode compartment the electrons produced at the anode are used for the hydrogen evolution reaction (HER) which generates the final H_2. The following reactions take place in this compartment (depending on the basic or acidic medium).

$$4H_2O + 4e^- \rightarrow 2H_2 + 4OH^- \text{ (basic media)} \quad (7)$$

$$4H^+ + 4e^- \rightarrow 2H_2 \text{(acid media)} \quad (8)$$

In general, the slow kinetics of OER are the bottleneck in the electrocatalytic water splitting thus limiting the productivity of the overall electrochemical cell.[11] Precious metals, for its low overpotentials, have long been considered the perfect candidates to be used in the production of OER and HER, being Ir_2O or RuO_2 for OER and Pt for HER the most efficient and stable combination in acidic conditions.[12–15] However, the availability and high cost of these materials, particularly iridium, together with limitations in long term stability makes their widespread commercial use uneconomical and impractical, despite their excellent electrocatalytic performance.[16]

Considering the above limitations, first row transition metals oxides offer a compromise solution. Despite their lower electrocatalytic activity for OER in comparation with precious metals, their relatively low-cost and long-term corrosion resistance in basic media make them desirable materials for their use as OER anodes.[17] In this context, nickel and iron have received special attention and the new generation of electrocatalysts based on Ni and Fe (especially layered double hydroxides, LDH) show excellent stabilities and low overpotentials to oxidize water, which are comparable to those achieved with precious metal catalysts.[18] In fact, top publications with this material have reported overpotentials for 10 $mA \cdot cm^{-2}$ of 180 mV employing NiFe nanowires as electrode support and 214 mV using a graphene based substrate.

The presence of Fe, either in the electrode, shaping the NiFe LDH,[19,20] or as impurities in the electrolyte[21], has resulted in an improvement of the electrochemical performance for water splitting on Ni based electrocatalysts. However, the influence of this metal on the oxidation mechanism is still under debate. On the one hand, it has been calculated by theoretical calculations that the presence of Fe affects the oxidation state of Ni, thus modifying the M-OH bond distance.[22,23] On the other hand, mechanistic studies with atomic markers, have revealed different oxidation mechanisms depending on the presence or absence of Fe, with the lattice oxygen participating in OER in the case of Fe absence.[24] Understanding the specific kinetics and mechanisms of operation of NiFe-based electrocatalysts is still lacking. Therefore, new characterization techniques need to be further developed and exploited for this purpose.

1.2.2. Photoelectrochemical systems

In the recent years, electrochemical systems powered by renewable energies have emerged as sustainable synthetic processes. In the case where the energy input is supplied by the sun, the system is called photoelectrochemical.

When designing photoelectrochemical systems there are three main configurations. On the one hand, a photovoltaic device can be coupled in series with the electrocatalyst, totally separating the energy generation from the catalytic part (PV-EC configuration).[25] With this approach, the photovoltaic part needs to accomplish the energy requirements of the catalytic process. The drawbacks of two different devices connected is the need of cables, current stabilizing systems and diodes between the two parts, in order to prevent the current from flowing in the opposite direction and damaging the photovoltaic device. All these extra elements lead to energy losses and increased production costs.

A simpler configuration consists of using a semiconductor to carry out the electronic processes by activating it directly with sunlight (PEC configuration).[26] In this approach, only one semiconductor could provide the energy needed in the process; however, in some cases extra energy is required. In this case, both electrodes could be active to sun energy and a photovoltaic

device could be coupled to the photoelectrochemical cell to provide the extra power needed (**Figure 4**. PV-PEC configuration).[27]

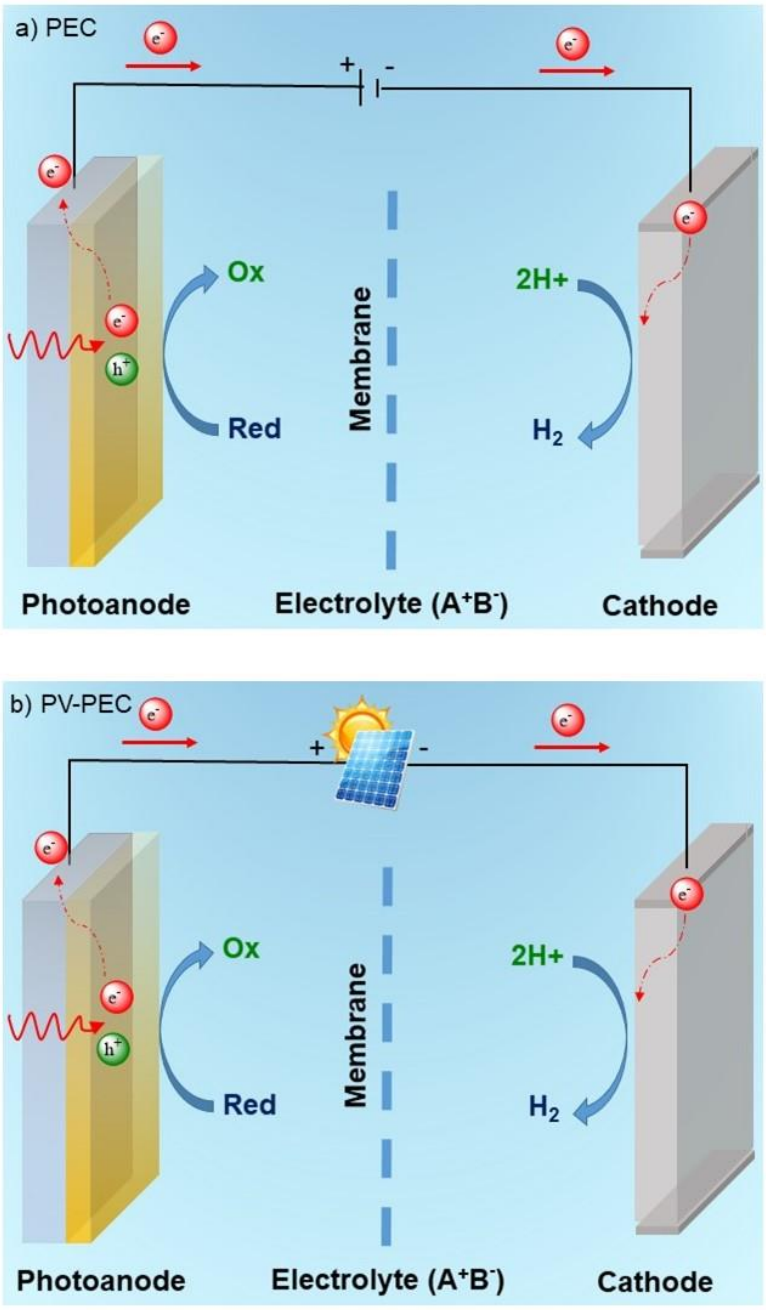

Figure 4. Schematic diagram of (a) PEC and (b) PV-PEC system.

Selection of the type of configuration (PV-EC, PEC or PV-PEC) will depend on the type of reaction to be studied, considering factors such as stability, materials compatibility, selectivity, applied potential, etc. The main short- and medium-term objectives of electro and photoelectrochemical systems are to discover new systems to, reduce costs and increase the lifetime of those systems, as well as to promote the reuse and recycling of the devices once their useful life has expired.

In any case, the production of the corresponding products originating from this type of cell becomes totally green as the energy required is entirely from the sun.

In the case of photo-assisted electrochemical water splitting (PEC configuration), the materials used as semiconductors must be able to accomplish several requirements for optimum performance as a photoelectrode and consequently to favour the electrical into chemical transformation.

i. *Strong visible light absorption:* Transform the solar energy into electricity and use it to drive the chemical reaction is only feasible if the band gap (E_g) of the semiconductor is larger enough to overcome the overpotentials required for OER.[28,29] As water splitting is not a spontaneous process but requires an energy supply of 1.23 eV, plus the overpotentials due to thermodynamic and kinetic losses, a minimum of 1.9 eV is required. In addition, the maximum value of E_g is determined by the solar spectrum. Since below 400 nm, the intensity of sunlight drops sharply, and absorption below this wavelength would use only a very small portion of the solar spectrum. Therefore, the optimum value of the semiconductor should be between 1.9-3.1 eV (corresponding to 650-400 nm of the visible region).

ii. *Effective charge separation and transport mobility.* The photogenerated charges have to reach the semiconductor/electrolyte interface in order to perform the photoelectrochemical reaction.[30] Consequently, the material employed needs high conductivity and high charge mobility to mitigate the losses due to electron-hole recombination.

iii. *High charge injection.* For effective charge transfer, the band edge positions of the semiconductor and the redox potential of the electrolyte must be in perfect alignment.[31,32] Thus, the valence band must be located below chemical potential of anodic reaction, to allow hole injection. Contrary, the conduction band edge must be above the cathodic reaction, favouring the electron injection.

iv. *High chemical stability*. For practical applications, the material semiconductor must be stable in aqueous media for long time, both in the dark and under illumination conditions.[33] Many factors can influence semiconductor stability, such as the composition of electrolyte and pH, the effect of light, the synthesis and deposition route, the presence of dopants, and the oxygen stoichiometry of the electrode.

v. *Low cost processing and Earth-abundant components.* The semiconductor materials for PEC devices must be achieved through low cost and environmentally friend synthetic routes, from Earth-abundant and non-toxic materials.

1.3. Oxygen valorisation

Electrocatalysis and photoelectrocatalysis have mainly been focused on replicating and optimizing the reactions involved in photosynthesis.[34,35] Thus, the main reactions that have been investigated comprise the production of hydrogen and oxygen from water hydrolysis[36] and the synthesis of other solar fuels (CH_4, CH_3OH...) from CO_2. The one is very interesting in terms of reducing the accumulation of CO_2 in the atmosphere.[37,38]

In either water hydrolysis or CO_2 reduction, the oxidation step only serve to supply electrons and protons to feed the cathodic reactions, as the produced O_2 in the anode is of little or no value considering its abundance in the atmosphere. To avoid this, attractive alternatives to OER are based on oxygen valorisation processes in which oxygen is revalorised to obtain products different from O_2.[39] Among the advantages of these electrochemical oxidation reactions, we found that these processes allows increasing chemical complexity and, in some cases, to introduce new heteroatoms and other functional groups to the organic structure, without requiring the use of toxic reagents.[40] In addition, these oxidation reactions releases H^+, which can be used to generate H_2 at the cathode. In this way, these electrochemical system becomes more economically efficient since both oxidation and reduction reactions produce compounds with increased value respect to the O_2 generated in water splitting.[41,42]

Several examples of organic oxidation reactions that potentially offer high-value alternatives to OER have been described in the bibliography. For example, the selective oxidation of alcohols or the conversion of biomass and waste are generating growing interest.[43] Bifunctional Ni-based anodes and more recently NiOOH electrodes have shown to be very efficient electrocatalysts for these oxidations.[42,44] However, in order to carry out these processes, high overpotentials are required, which in many occasions give rise to very reactive radicals that generate the decomposition of the product and/or side reactions of neighbouring functional groups.

The employment of redox mediators such as TEMPO (2,2,6,6-tetramethylpiperidine N-oxyl) or PINO (phthalimide N-oxyl) aims to transfer the electron through these organic intermediates, reducing the overpotential required for these processes.[45] Through this strategy, several chemoselective organic transformations have afforded the functionalization of nitrogen-adjacent C-H bonds in piperidine derivatives and other saturated heterocycles,[46] the oxygenation and iodination of benzylic C-H bonds,[47] and the intramolecular amination of benzylic and aliphatic C-H bonds.[48]

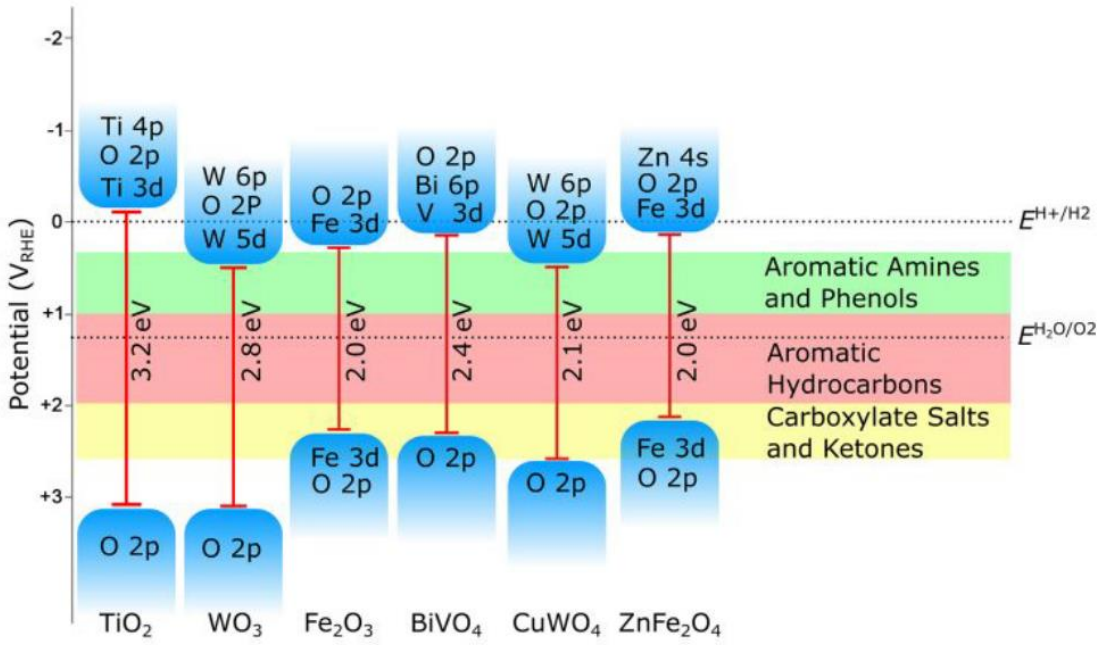

Figure 5. Band structures of metal oxide semiconductors for high added value transformations. Colored areas represent the typical potentials of alternative oxidation reactions. Reprinted with permission[39] Copyright © 2019, American Chemical Society.

In a more renewable scenario, some examples have described the generation of high added value organic species directly transformed in a PEC, employing metal oxide semiconductors as photoanodes.[39,49,50] These 'classical oxide semiconductors', known as n-type metal oxides, possess a highly oxidizing valence band as well as relatively small band gaps (2.5-2.7 eV) that allow the materials to absorb a portion of visible light (**Figure 5**). Moreover, as can be seen in the figure, the typical band gap of these materials is larger enough to overcome the range of potential of different alternative oxidation reactions represented by the colored areas. Thus makes, metal oxide materials, particularly intriguing candidates for applying towards the oxidation of alternative substrates. In fact, in recent bibliography, $BiVO_4$ and WO_3 photoanodes have been successfully applied for the photoelectrochemical oxidation of 5-hydroxymethylfurfural (HMF),[51,52] benzyl alcohols,[53,54] furans,[55] tetralins,[56] cyclohexane,[57,58] glycerol[59,60] and urea.[61]

1.4. Materials

1.4.1. Conductive substrates

In the case of electrochemical or photoelectrochemical measurements, thin film sample always needs a conductive substrate as back contact. Generally, in PEC systems, optical transparent substrates are preferred because this also allows illumination of the sample from the back side. To ensure a current flow, it is important that the substrate will be in ohmic contact with the photoactive material. Thus, n-type photoanodes require conductive materials whose work function is lower compared to that of the photoanode itself. Commonly, transparent conducting oxides (TCOs) are employed for that purpose.[62] These materials have high carrier concentrations and mobilities, but still show good optical transparency (>80%) because their plasma frequencies are in the near infrared.[63] Some examples of TCOs are F-doped SnO_2 (FTO), Sb-doped SnO_2 (ATO), Sn-doped In_2O_3 (ITO), and Al-doped ZnO (AZO).

Complementarily, in electrochemistry, most of the experimentally prepared electrocatalysts are in powder form or often the electrocatalyst is deposited on a supporting substrate by thin film methodologies. This is very cost-effective economically, since the material employed as a support is often cheaper than the electrocatalyst itself. In this regard, metal foils and especially carbon-based electrodes are usually necessary to load them for electrocatalysis.

Among the carbon-based electrodes, Pencil Graphite Rods (PGR) are nanocomposite materials consisting mainly of graphite and small clay particles recovered by an organic binder and spindle oil to form the agglomerate. This material stands out for its low price and wide availability. For this reason, in recent years, this material has been popularised and it appears in a large number of publications. In fact, in a search through the Web Of Science application more than 1500 papers with the title "pencil graphite" have been published since 2010. The most widely applications of PGR are sensors,[64–66] biosensors,[67,68] super capacitors,[69,70] electrocatalysis,[71–74] etc. The use of PGR as supporting electrode for the electrocatalytic water oxidation has been recently studied.[73,74]

Electrochemistry occurs at the interfacial region between electrode and solution. Therefore, maximizing the effective PGR surface is a key aspect that determines the response of the electrodes. In this regard, two important treatments could favour the electrical properties of PGR. Firstly, controlling of the PGR surface aids to reproducible results between different electrodes and, secondly the removal of the organic binder increases the porosity of the rod.

1.4.2. Ni based electrodes

The use of nickel and its great solid-phase properties to carry out redox transformations by electrochemical measurements has been known for years. In fact, Bode et al. proposed an initial general reaction scheme in which the different structural features of nickel hydroxide $Ni(OH)_2$ and its structural transitions to nickel oxyhydroxide, NiOOH were defined.[75] Afterwards, numerous attempts were made to explain this material as an electrode, including: (1) the structural and physicochemical characteristics of nickel (II) hydroxide, (2) the hydroxides and oxyhydroxides transformations, (3) the nature of the electrolyte and foreign cations, and (4) the kinetic and thermodynamic behaviour.[76]

However, in spite of the efforts made, it was not until years later that Louie et al. discovered the effect of iron in this material, for their employment in water splitting by electrolysis.[77] The formation of the Ni-Fe layered double hydroxide with 40% Fe content exhibited OER current densities two orders of magnitude higher than the fresh material and three orders of magnitude higher the pure Fe layer. The result is a material capable of competing in terms of activity with the noble metals typically used for this purpose.

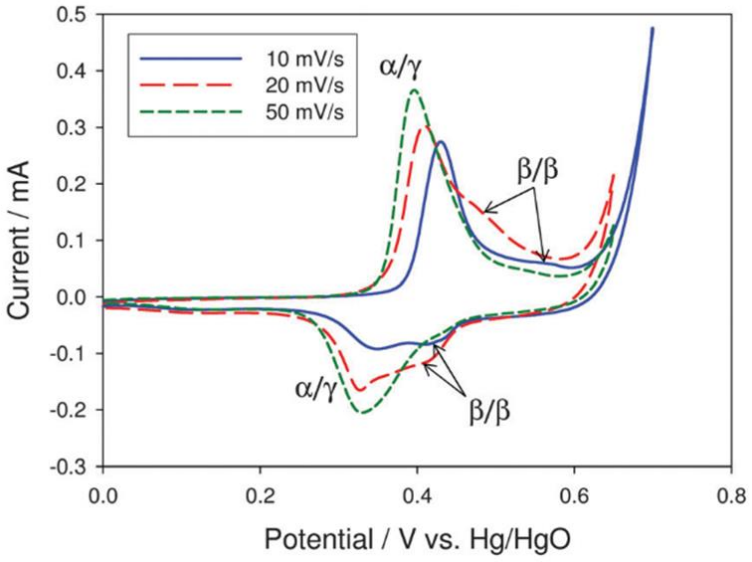

Figure 6. Cyclic voltammograms of reversible current peak observed in Ni based electrocatalysts. Reprinted with permission[78] Copyright 2014, Royal Society of Chemistry.

The special activity of NiFe LDH takes place in basic media. In opposition to noble metals where acid media is also appropriate, alkaline environment is necessary in NiFe LDH to form spontaneously the $Ni(OH)_2$ and to promote the electrochemical transformation into nickel oxyhydroxide (NiOOH) which is responsible of the visible and reversible current peak during cyclic voltammetry (**Figure 6**).

The introduction of Fe into the electrode leads to an increase in the potential at which the $Ni(OH)_2$/NiOOH redox occurs. This change in redox potential implies that the electrochemical oxidation of $Ni(OH)_2$ to NiOOH is altered by the presence of Fe. Furthermore, OER is catalyzed by Ni and the presence of Fe lowers the overpotentials at which the current increase as a consequence of water oxidation is observed (**Figure 7**).[79,80]

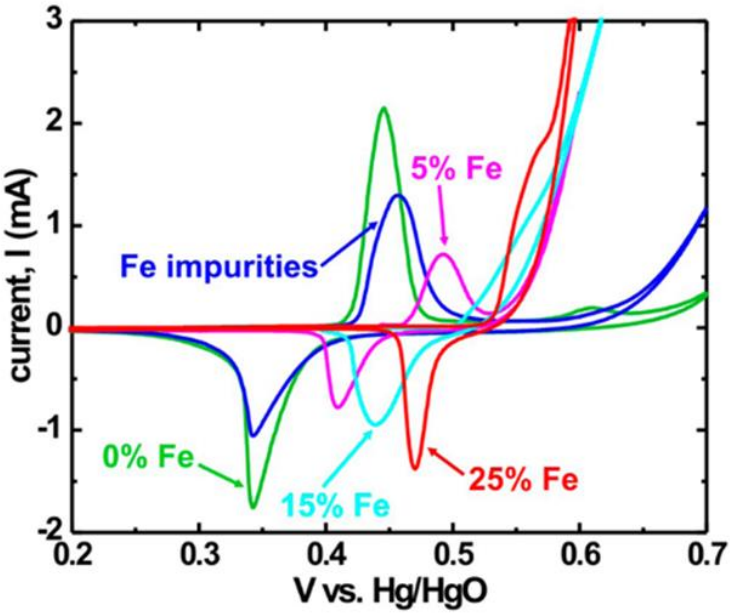

Figure 7. Effect of iron in cyclic voltammetries. Reprinted with permission[79] Copyright 2014, American Chemical Society.

A number of different studies have attempted to understand the effect of iron within the crystal structure of nickel. As an example, Friebel et al. points to the presence of Fe^{3+} in $Ni_{1-x}Fe_xOOH$ occupies octahedral sites with unusually short Fe-O bond distances induced by edge sharing with the surrounding [NiO_6] octahedra.[20] In this way, the energies relative to the OER-interacting intermediates are optimized leading to the low overpotentials observed in the presence of Fe. On the other hand, Zhou et al. show how Fe doping enlarges the stability area of metastable oxyhydroxo species, thus modifying the Pourbaix diagram of Ni electrodes. Therefore, Fe ion adsorption and intercalation tune the oxidation states of ions near the active site and then effectively lower the OER overpotential.[81] Different ways of explaining the same process are possible, which implies that new characterization techniques that enable a better understanding of this subject are desirable.

1.4.2.1. Synthesis and deposition techniques

Several physical and chemical methodologies have been proposed for the preparation of NiFe LDH, such as hydrothermal synthesis,[82,83] pulsed laser deposition,[84] sputtering,[85] chemical vapor deposition,[86] sol-gel methodologies[87] and precipitation techniques.[88]

The most simple and more versatile of the existing synthetic approaches, however, is possibly electrochemical deposition.[89,90] In this method, electrically conductive substrate is anodically or cathodically coated with a metal oxide or hydroxide film from an electrolytic solution containing a suitable metal salt. Various experimental techniques have been used, such as potentiostatic[91,92], galvanostatic,[93–96] potentiodynamic,[97–99] and pulse techniques and, depending on the specific parameters, metal oxides and hydroxides of different nanostructures can be prepared. In this way, electrochemical techniques provide unique control on the physical and chemical properties of the oxide/hydroxide layers.

In particular, the composition of $Ni(OH)_2$ generated galvanostatically or potentiostatically from an aqueous solution containing nickel nitrate is determined by the direct or indirect reduction of the nitrate ion to nitrous acid, hydroxylamine or nitrite ion.[93,100,101] Louer et al. who devoted many studies to nickel hydroxynitrates, promoted the idea that "α hydroxides" commonly nitrate baths might well be regarded as highly hydrated, degenerate forms of Ni(II) hydroxy-nitrates.[102,103] However, in all cases, the hydroxyl ion is generated, resulting in the formation of α-$Ni(OH)_2$ or β-$Ni(OH)_2$ according to the following reaction:

$$Ni_{aq}{}^{2+} + 2OH^- \rightarrow Ni(OH)_2 \quad (9)$$

Alternatively, $Ni(OH)_2$ may also be formed according using potentiodynamic methodologoies. Under these conditions the potential is cycled anodically. Thus, it has been noted that the process may occur as following:[75,99]

$$OH^- \rightarrow OH_{ads} + e^- \quad (10)$$

$$Ni_{aq}{}^{2+} + H_2O + OH_{ads} \rightarrow NiOOH + 2H^+ \quad (11)$$

Therefore, both $Ni(OH)_2$ and NiOOH could be formed during the course of the potential sweep perturbation.

1.4.2.2. Crystalline and structural properties

NiFe LDH occurs in two different pseudo-polymorphs, α-$Ni(OH)_2$ and β-$Ni(OH)_2$ (**Figure 8**). The main difference between the two polymorphs is the layer distance, which is 0.76 nm for α-$Ni(OH)_2$ and 0.46 nm for β- $Ni(OH)_2$, . Both hydroxides can be reversibly oxidized to their corresponding oxyhydroxides, γ-NiOOH and β-NiOOH. In this section, the difference in structural properties will be further described.

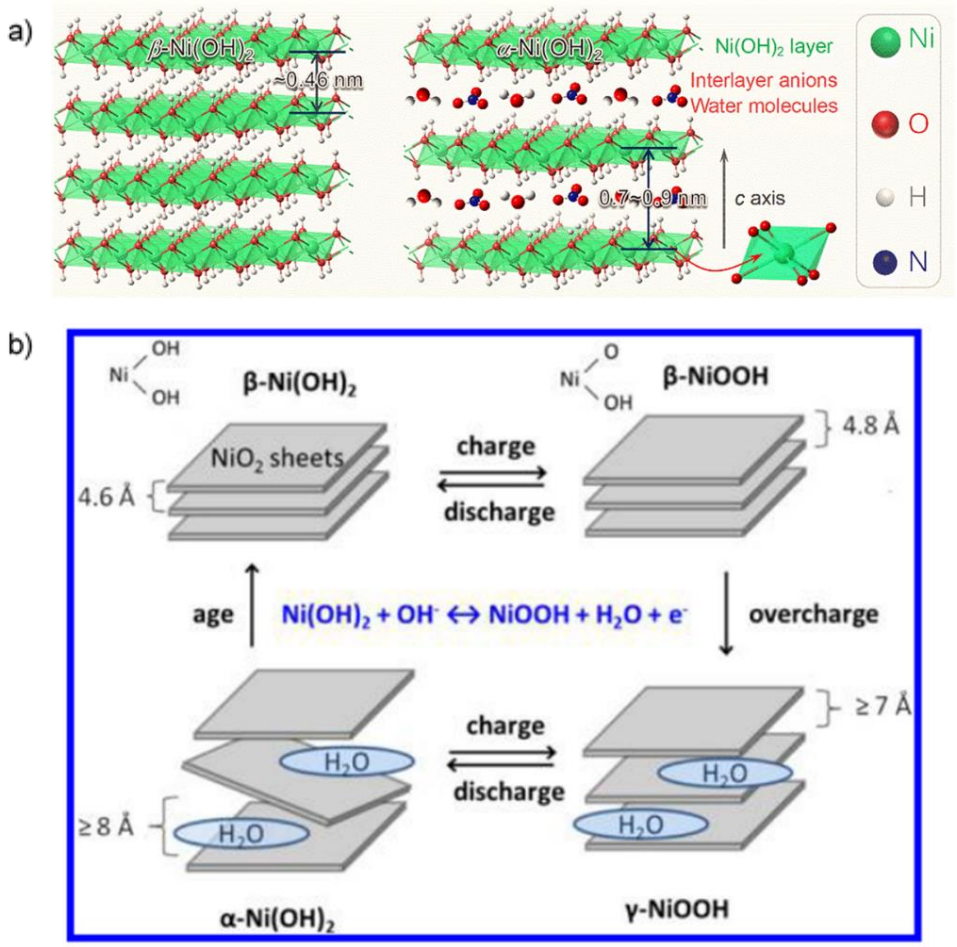

Figure 8. (a) Crystaline structures of α and β $Ni(OH)_2$ phases, (b) redox transformations diagram for Ni based electrodes. Reprinted with permission[21] Copyright 2015, American Chemical Society.

α-$Ni(OH)_2$ contain a variable excess of intersheet water (+ foreign ions) and exhibit low crystallinity. Thus, α-$Ni(OH)_2$ is a disordered Ni (II) hydroxides and does not represent a well defined polymorph of $Ni(OH)_2$.[76]

Contrary, β-$Ni(OH)_2$ crystallizes in the hexagonal system ($P3ml-D^3 3d$) similar to several halogenides (CdI_2 type) and to other hydroxides $M(OH)_2$ (M = Ca, Mg, Fe, Co, Mn, Cd), with the unit cell parameters (a = 3.126 Å and c = 4.605 Å).[76] The structure of β-$Ni(OH)_2$ can be illustrated as a hexagonal structure of hydroxyl ions (AB packing of oxygen) with Ni(II) occupying the octahedral interstices every one of two planes. It may also be visualized as a layered structure, each layer comprising a planar hexagonal arrangement of Ni (II) ions with an octahedral oxygen coordination, three oxygen atoms situated above the nickel plane and three situated below. The layers are piled along the c-axis and there is no hydrogen bonding between the OH groups of two adjacent layers.

The "γ" denomination was first given by Glemser et al. to a compound exhibiting a large intersheet distance and a high oxidation state.[104] Glemser's γ-NiOOH crystallized in the

rhombohedral system, with corresponding hexagonal parameters a = 2.82 Å and c = 20.65 Å. Years later, Bode et al. similarly prepared "γ type" oxyhydroxides by solid state hydrolysis. The repetition of the same procedure on a single crystal of NaNiO, allowed Bode et al. to obtain a single monoclinic crystal with parameters a = 4.90 Å, b = 2.83 Å, c = 7.17 Å, β = 103.1º. depending on the experimental conditions, a whole family of compounds having roughly similar X-ray diffraction patterns, but oxidation states of nickel ranging from 3.3 to 3.75, and different water and alkali cation contents within the sheets, can be obtained.

β-NiOOH was first studied by Glemser and Einerhand,[104] who synthesized it by oxidation of nickel nitrate with $K_2S_2O_8$ in a 1N KOH solution at room temperature. β-NiOOH crystallizes in the hexagonal system (a = 2.82 Å, c = 4.85 Å) and can be regarded as deriving from β-$Ni(OH)_2$, by a direct reaction removing one proton and one electron.

The structure can be described as NiO_2 sheets of edge-sharing NiO_6 octahedra, protons being intercalated between the slabs, and oxygen atoms forming a hexagonal (AB) close-packing (idem β-$Ni(OH)_2$,). It is noticeable that the a parameter, which corresponds to the Ni-Ni distance within the sheets, is significantly lower in NiOOH than in the case of $Ni(OH)_2$: 2.82 Å vs 3.12 Å. On the other hand, the increase in the c parameter (inter-sheet distance), 4.85 Å vs 4.60 Å, results from the enhancement of the repulsion between oxygen layers of adjacent NiO_6 sheets once protons are removed.

1.4.2.3. Strategies to improve the electrocatalytic performance

a) Surface morphology and size control

Several approaches have been considered to design architectures with good electrical connectivity and high surface area. Regarding these strategies, some could include enlarging the metal area by introducing porosity into the metal substrate. For example, Lu et al. and Perez-Alonso et al. showed high OER current densities by depositing Ni(Fe)OOH on a porous Ni foam.[105,106] Other strategies tend to synthesize a material with high porosity morphology that provides high mass loadings of the catalyst and increases the electrolyte-catalyst interface. For instance, Shudo et al. reported a 3D porous Ni/NiO_x bifunctional oxygen electrocatalyst derived from freeze-dried $Ni(OH)_2$ with exceptional activity. This last approach allows the use of equally efficient electrodes at a lower cost as lower contents of metallic materials are employed. Moreover, this approach allows the use of new alternative materials as back contact substrates which opens a new market to carbon-based materials. Some examples, Ma et al. stacked alternating layers of Ni(Fe)OOH on conductive reduced graphene oxide.[107] Gong et al. reported higher electrocatalytic activity by using carbon nanotubes as scaffolds for Ni(Fe)OOH.[80] Marini et al. used selective dissolution of Al to form a porous "Raney" Ni OER catalyst.[108]

b) Activation treatments

Electrochemical aging treatments for NiFe LDH electrodes developed by potential multicycling at a slow scan rate, significantly increases the OER performance of hydrous nickel oxide electrode. As observed by three performance indicators, consecutive CV scans on NiFe LDH electrodes: (1) increase the current density of both the anodic and cathodic peaks, (2) reduce the OER overpotential and (3) improve the kinetics toward the OER due to the formation of an active oxy(hydroxide) surface layer. Electrochemical aging is conducted until stabilization of the anodic and cathodic peaks measured in the CV profiles. In this moment indicates when the system had reached a steady-state condition. During this electrochemical aging process, changes of the surface morphology are driven by the formation of the β-$Ni(OH)_2$/β-NiOOH LDH phases. However the nature dramatic increase in activity of aged $Ni(OH)_2$/NiOOH has been attributed to the absorption of Fe impurities.[79]

1.4.3. $BiVO_4$ based photoelectrodes

In this section, the photoelectrodes based in bismuth vanadate ($BiVO_4$) materials are going to be addressed. We will begin by describing the crystal structures in which this material is presented, together with the accompanying structural properties. Next, we will detail its optoelectronic properties correlating them to its crystal structures, focusing on those corresponding to the monoclinic one. The presence of oxygen vacancies and their implications on these properties are explained in depth, as well as the strategies used to balance their presence for the benefit of the solar energy efficiency.

$BiVO_4$ present optimal qualities for an efficient light absorption due to its favourable indirect band gap energy of 2.4 eV (≈516 nm band edge), which allows for a theoretical maximum photocurrent density of 7.5 mA cm^{-2} under Air Mass 1.5 Global (AM 1.5 G) solar illumination.[109] In fact, $BiVO_4$ has been suggested as one of the best PEC performance photocatalyst for solar light driven water oxidation reactions.[110] The use of monoclinic $BiVO_4$ as an n-type semiconductor for photoelectrochemical water oxidation was firstly reported by Kudo et al, comparing the photocatalytic activity of WO_3 and $BiVO_4$ powder, they reported the interesting properties of this material in photocatalysis.[111] Currently, $BiVO_4$ shows an impressive photocurrent up to 6 $mA \cdot cm^{-2}$ at 1.23 V vs RHE with a photovoltage of 1,0 V for the OER.[112] These outstanding values are achieved through improvement strategies that will be detailed in the final part of this section.

The excellent properties of $BiVO_4$ are confirmed by its ability to react with organic substrates with high thermodynamic energy demand, allowing to minimize the overpotential required for it. The reactions can be successfully completed both in aqueous and organic solutions.

In terms of stability, the synthesis and calcination conditions of the material play a crucial role,[113] controlling the photoinduced corrosion potential of $BiVO_4$, which has been estimated to be more positive than the oxidation potential of water. This suggest that it could be resistant to photoinduced corrosion during high applied bias conditions, but its photoelectrochemical instability has been demonstrated by several reports.[33,114] This instability has been attributed primarily to kinetic factors limiting the structural transformation of the V-deficient degradation product into a stable Bi oxide phase at room temperature.[33] Additionally the accumulation of holes on the $BiVO_4$ surface is estimated to be able to destabilize the $BiVO_4$ lattice by increasing the dissolution rate of V species into the solution.[115] Along its energetic properties, the low price of the components of $BiVO_4$ and its harmlessness nature make it an excellent environmentally sustainable option for further research.

1.4.3.1. Crystalline and structural properties

The crystallization form of $BiVO_4$ is different depending on the environmental conditions in which it is formed. Thus, while in nature $BiVO_4$ crystallizes in the pucherite form, in the laboratory it usually crystallizes in the tetragonal form (dreyerite) or in the monoclinic form (clinobisvanite). At room temperature, the monoclinic phase is the most stable phase and the structure is formed by a four-atom O-coordinated V ion on a tetrahedral site and an eight-atom O-coordinated Bi ion (hence BiO_8) from eight different tetrahedral VO_4 units, as it is represented in **Figure 9**.

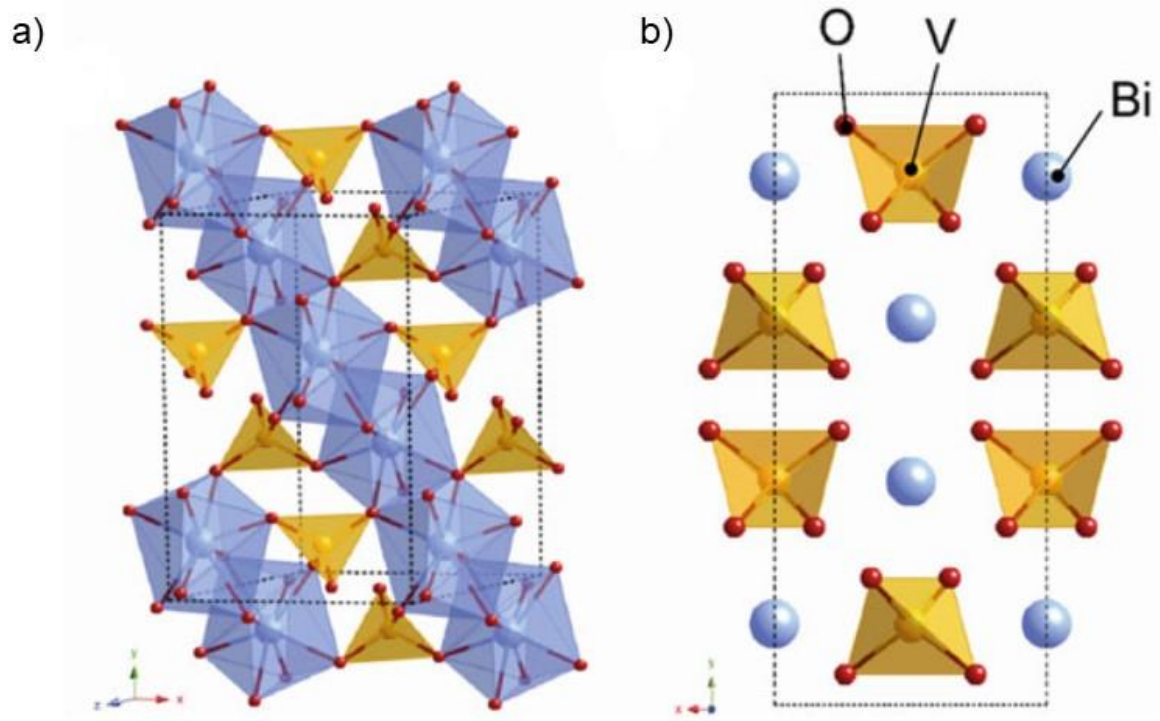

Figure 9. (a) Unit cell structure of monoclinic (clinobivasnite) phase in $BiVO_4$. (b) Side view (c-axis) of the monoclinic structure. Reprinted with permission[116] Copyright 2016 Springer Nature.

The monoclinic phase, having a C2/c group space parameters with a = 7.247 Å, b = 11.697 Å, c = 5.09 Å, and β = 134.226º, shows a high asymmetry of the crystal structure with different Bi-O and V-O distances.[117,118] It was shown that the monoclinic $BiVO_4$ has superior photocatalytic responses in comparison with the tetragonal $BiVO_4$,[119] the reasons for this difference in performance are discussed below.

1.4.3.2. Electronic structure and optoelectronic properties

The different crystalline structures have different electronic structures, which are strongly correlated with the optoelectronic properties of the material. In the case of photoelectrochemical systems, the optoelectronic properties control the photocatalytic activity. As mentioned above, for the $BiVO_4$, the photocatalytic activity of the monoclinic structure is superior to the tetragonal structure, which can be attributed mainly to two reasons:

- Narrowed bandgaps:
  - The bandgap of the tetragonal structure is 2.9 eV, resulting in a poor photo-response in the visible light regime.[120]
  - Although the bandgap of the monoclinic structure has been shown to be smaller, 2.4 eV as shown in **Figure 10**, the nature of the optical transitions has been controversial in the literature. However, recent work, combining computational methods with numerous experimental techniques, has concluded that this bandgap is indirect. Nevertheless, it was proven that the direct transition is ~0.2 eV smaller than that of the tetragonal structure[121,122]. As a consequence, the monoclinic structure can absorb a larger portion of the light spectrum.
- Lighter effective masses of the carriers.[120,123]
  - This is desired because this result in a higher probability of the charges reaching the interfaces, and therefore increases the photocatalytic activity.

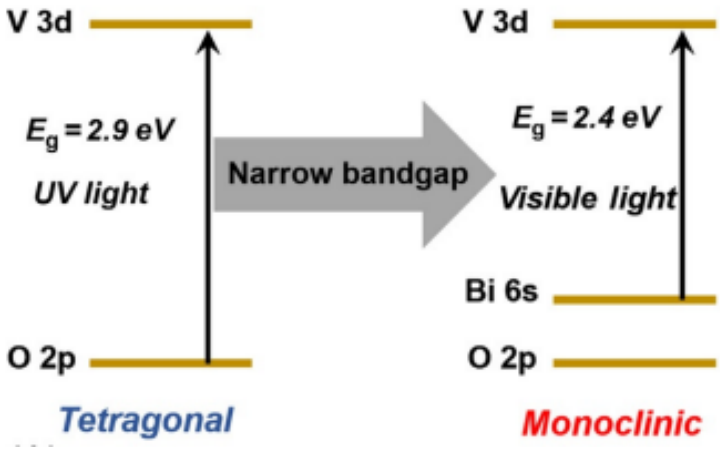

Figure 10. Schematic band structure of tetragonal and monoclinic $BiVO_4$. Reprinted with permission[116] Copyright 2016 Springer Nature.

1.4.3.3. Intrinsic point defects in $BiVO_4$

Structural point defects are those structural imperfections in the lattice of a solid limited to one site and its immediate neighbour. These defects comprise any change in the atomic composition of the lattice structure and depending on their nature they can be divided into three classes: i) vacancies, removing an atom from the lattice, ii) substitutional defects, substituting one atom for another type, and iii) interstitials, replacing an atom from the pristine structure in an unoccupied site.[124]

The production of point defects in any metal-oxide semiconductor occurs unintentionally during their structural formation. However, the introduction of intentionally native defects has been suggested to be involved in the photoelectrocatalytic performance of metal oxide semiconductors. For this reason, in recent years, the research has been focus on the physical and chemical processes involved in the population and energy distribution of point defects.

Among the most studied point defects in metal oxide semiconductors, are oxygen vacancies (OV_s). Such defects are generated by the removal of an oxygen atom from the crystal structure. Specifically, the creation of OV_s in $BiVO_4$, is associated with the formation of V^{4+} occasioned by the loss of an oxygen in the tetrahedral structure of VO_4 units. As a result of this process the structure is left charged with two extra electrons,[125,126] which can be structured in localized V centers (**Figure 11a)** or delocalized in a bridge V_a-O-V_b (**Figure 11b**), because of the versatile chemistry of the tetrahedral subunits of VO_4.[127]

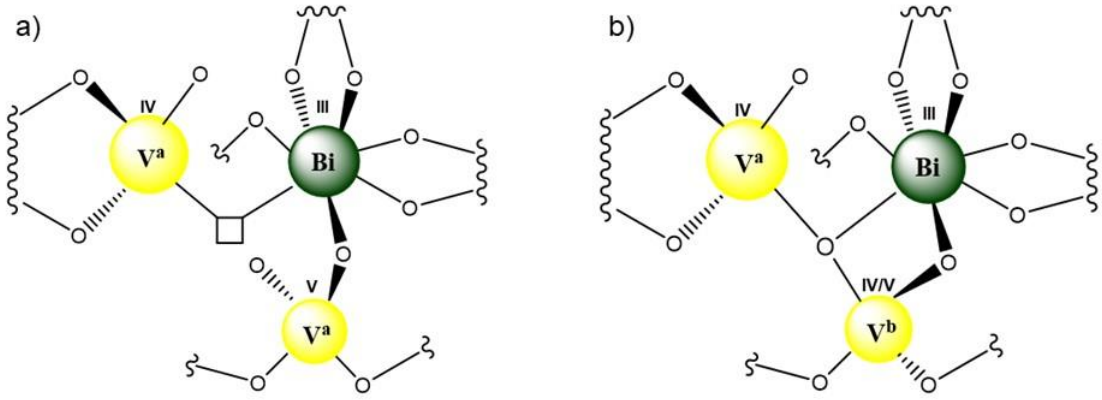

Figure 11. Structure of OVs created in $BiVO_4$. (a) Localized in V centers and (b) delocalized in a bridge V^a-O-V^b.[127]

The production of oxygen vacancies is capable of transforming the electronic structure of $BiVO_4$, although its real effect is quite controversial. In fact, their influence has been traditionally associated with the introduction of shallow intragap states collocated inside the bandgap of the material, near the conduction band.[128,129] For this reason, the presence of OV_s have long been considered responsible for the intrinsic n-type behaviour of $BiVO_4$ as a semiconductor.[130,131] Alternatively, recent publication suggests that the presence of hydrogen in the interstitial and

substitutional sites of $BiVO_4$ structure is dominant in determining the n-type conductivity of $BiVO_4$, instead of oxygen vacancies.[132]

1.4.3.4. Synthesis and deposition techniques

Several methods for the synthesis and deposition of $BiVO_4$ layer are reported in literature, depending on the crystalline structure desired. For instance, monoclinic crystalline phase $BiVO_4$ is obtained by solid state and melting reactions at high temperature and tetragonal $BiVO_4$ is prepared by a precipitation method in aqueous media at room temperature. But the details of each synthesis are beyond the focus of this thesis. Regarding the deposition techniques, the variety is wide, depending as well on the morphology, size and shape desired for the final material itself. Some of the most used deposition techniques reported in literature include spin-coating, drop casting, electrodeposition, laser deposition, hydrothermal processes and so on.[109]

1.4.3.5. Strategies to improve the photoelectrocatalytic performance

The fast development of $BiVO_4$-based photoanodes has been due to the introduction of modifications in the fabrication of the photoelectrocatalyst. These modifications include changes in the morphology and in the electronic structure of the material, involving the insertion of new species to enhance its optoelectronic properties. These modifications are carried out by means of different strategies that are described below:

(a) Morphology and size control

As we mentioned at the beginning of this section, $BiVO_4$ has been suggested as one of the best PEC performances photocatalyst for solar light driven water oxidation reactions.[133] However, intrinsic weakness of this photocatalyst such as slow charge mobility and fast charge recombination, result in limitations during practical applications, leading to a much lower current density than the theoretical one.[134]

The introduction of porosity to increase surface area, together with the decoration techniques of the cocatalyst, have been proposed as successful approaches to improve its solar light conversion efficiency (η). Being defined as the product of the solar light absorption efficiency (η_{abs}), charge separation efficiency (η_{sep}), and surface charge transfer efficiency (η_{trans}), it seems clear that an increase in porosity as well as changes in morphology, size and connectivity between particles, can have a significant impact on the performance of PEC systems using $BiVO_4$ as a photoelectrode.[135]

First, the photoabsorber must be sufficiently thick to absorb all the incident light, possessing good structural properties to allow the photogenerated minority carriers to diffuse towards the surface.[136,137] As compare with planar morphology, the mesoporous structured $BiVO_4$ surfaces provides larger active surface area per electrode volume, leading to higher number of active sites.[138,139]

On the other hand, ordered porosity allows to reduce electron-hole recombination processes, by providing the minority carriers a readily access channel where they must travel before reaching the surface.[133] Therefore, the synthesis of $BiVO_4$ with self-assembly of nanometer-sized building blocks, including nanowires, nanobelts, nanosheets and nanotubes, have shown improved photon to current conversion efficiencies (IPCEs) with respect to the planar structure.[140] Contrary, if the introduction of porosity is not accurately optimized, it can also have negative effects on charge separation and transport properties, as it can lead to an increase in surface states, defective sites and grain boundaries.[141] By introducing photocatalytic crystal facet engineering and co-catalyst, the design of $BiVO_4$ microcrystals have been highlighted in the literature to produce solar fuel products with enhanced solar light conversion efficiency. For instance, a (040) crystal facet results in an accumulation of photogenerated charges, delaying the charge recombination rate and favouring the charge separation and charge transport efficiency.[142]

(b) Application of overlayers and underlayers

Electron transport has been recognized as one the main limiting factor for the performance of $BiVO_4$, attributed to its crystalline structure, where the VO_4 tetrahedral units are not interconnected.[143] In addition, it has been reported that the charge transfer kinetics at the semiconductor–liquid junction is sluggish, leading to different strategies to enhance the optoelectronic/catalytic properties. The heterostructuring with different materials to exploit synergistic interactions between them has been successfully reported for that purpose, using the overlaying and underlaying techniques as the main approaches. Regarding overlaying, two different catalytic overlayers (FeOOH and NiOOH) have been used to obtain $BiVO_4$/NiOOH and $BiVO_4$/FeOOH, allowing to minimize the recombination losses at the $BiVO_4$/electrolyte interface by boosting the hole injection efficiency into the solution.[133] As underlayers, SnO_2 and WO_3 are the best performers so far. SnO_2 as an underlayer between fluorine-doped tin oxide (FTO) and $BiVO_4$ improved the electron transfer by reducing recombination pathways at the back contact.[144] On the other hand, WO_3 has attracted major attention, due to the highest water oxidation photocurrents obtained close to the theoretical maximum.[145] This heterojunction combines the high conductivity of WO_3 with the good absorption properties of $BiVO_4$. The suitable type II band alignment created promotes good charge separation, leading to a significant reduction of charge recombination processes.[146]

(c) Surface co-catalysts

Two main issues of $BiVO_4$ as photoelectrode are addressed with surface co-catalysts treatments: (i) the poor surface charge transfer at the semiconductor/electrolyte interface and (ii) the low stability of the material. The co-catalyst is aimed to decrease the activation energy of water oxidation by providing a better pathway for holes, instead of the semiconductor itself. A variety of co-catalysts and surface overlayers have been reported to effectively improve hole

transfer on the surface of $BiVO_4$ by following mechanisms: i) reduction of overpotential, ii) increasing stability, and iii) enhancing J_{ph}. One of the most popular and widely effective co-catalysis is Co–Pi and not only for $BiVO_4$ but also for other photoanode materials.[147] The use of catalytic layers to overcome the large overpotential required for the water oxidation reaction can be performed by sequential addition of these layers. For instance, Zr and Fe precursors can be converted into monoclinic ZrO_2 and α-Fe_2O_3 nanoparticles upon a heat treatment cycle. They act as catalysts, leading to a five-fold increase of the water oxidation photocurrent of $BiVO_4$.[32]

(d) Surface post-treatments

Unlike the surface co-catalyst treatments above mentioned, post-synthetic treatments occur after the synthesis of the electrodes. Such post-treatments can be based on illumination steps, chemical or electrochemical methods or even combinations of them. Here we will address the illumination post-treatments and their mechanistic advantages, highlighting the benefits related with the findings of this thesis.

Photochemical treatments have been demonstrated with both visible and ultraviolet light, and the resulting effects can be achieved either in or out of the electrolyte. The main advantage of these treatments is the no-requirement of an additional coating to enhance the optoelectronic properties of the system. For instance, the combination of alkaline electrolyte and visible light illumination, led to the conclusion that photogenerated holes (h•) and hydroxide ions cause two main effects: (i) hydrogenation of the near-surface region, proposed as the formation of interstitial positively charged defects (H_{int}) and resulting in V^{4+} and oxygen vacancies (OV_s), and (ii) saturation of the electrode surface with hydroxyl groups, which act as intermediates in the OER.[148] The reaction below described the self-doping of the V_2O_5 sublattice with reduced VO_2 species, in alkaline conditions (OH^-) and under illumination ($h^\bullet$) using the Kröger−Vink notation. Here, vanadium site (V'_v) and an oxygen vacancy site ($v_o^{\bullet\bullet}$) has to be distinguish. Furthermore, the ($O^x{}_o$) denotes the oxygen atoms occupying the regular oxygen sites. These surface and near-surface alterations result in a record high photocurrent for undoped and uncatalyzed $BiVO_4$.[149]

$$2VO_2 + 2OH^- + 2h^\bullet \xrightarrow{V_2O_5} 2V'_v + 4O^x{}_o + v_o^{\bullet\bullet} + H^\bullet_{int} + 0.5O_2 \quad (12)$$

In addition of visible light treatments, UV-curing exposure can produce morphological changes with an improvement in photo-electrocatalytic efficiency for water splitting reaction.[150] The UV-curing can enhance the performance even when illuminated in air, however, photocharging could be performed only in an aqueous solution, or so it was thought until we proved otherwise in one of the works presented in this thesis (Chapter 5).

References

(1) Intergovernmental Panel on Climate Change (IPCC). *Sixth Assessment Report of the Intergovernmental Panel on Climate Change*; 2021.

(2) United Nations Sustainable Development Goals https://www.un.org/sustainabledevelopment/energy/ (accessed Dec 14, 2021).

(3) Züttel, A.; Remhof, A.; Borgschulte, A.; Friedrichs, O. Hydrogen: The Future Energy Carrier. *Philos. Trans. R. Soc. A Math. Phys. Eng. Sci.* **2010**, *368* (1923), 3329–3342.

(4) Armaroli, N.; Balzani, V. The Hydrogen Issue. *ChemSusChem* **2011**, *4* (1), 21–36.

(5) Global Energy Infrastructure. Hydrogen – data telling a story | Global Energy Infrastructure https://globalenergyinfrastructure.com/articles/2021/03-march/hydrogen-data-telling-a-story/ (accessed Jan 30, 2023).

(6) Montoya, J. H.; Seitz, L. C.; Chakthranont, P.; Vojvodic, A.; Jaramillo, T. F.; Nørskov, J. K. Materials for Solar Fuels and Chemicals. *Nat. Mater.* **2016**, *16* (1), 70–81.

(7) Nian-Tzu, S.; Sung-Fu, H.; Quan, Q.; Zhang, N.; Xu, Y.-J.; Ming, C. H. Electrocatalysis for the Oxygen Evolution Reaction: Recent Development and Future Perspectives. *Chem. Soc. Rev* **2017**, *46*, 337–365.

(8) Hong, W. T.; Risch, M.; Stoerzinger, K. A.; Grimaud, A.; Suntivich, J.; Shao-Horn, Y. Toward the Rational Design of Non-Precious Transition Metal Oxides for Oxygen Electrocatalysis. *Energy Environ. Sci.* **2015**, *8* (5), 1404–1427.

(9) Doyle, A. D.; Montoya, J. H.; Vojvodic, A. Improving Oxygen Electrochemistry through Nanoscopic Confinement. *ChemCatChem* **2015**, *7* (5), 738–742.

(10) Fei, H.; Dong, J.; Feng, Y.; Allen, C. S.; Wan, C.; Volosskiy, B.; Li, M.; Zhao, Z.; Wang, Y.; Sun, H.; et al. General Synthesis and Definitive Structural Identification of MN4C4 Single-Atom Catalysts with Tunable Electrocatalytic Activities. *Nat. Catal.* **2018**, *1* (1), 63–72.

(11) Fabbri, E.; Schmidt, T. J. Oxygen Evolution Reaction - The Enigma in Water Electrolysis. *ACS Catal.* **2018**, *8* (10), 9765–9774.

(12) Reier, T.; Oezaslan, M.; Strasser, P. Electrocatalytic Oxygen Evolution Reaction (OER) on Ru, Ir, and Pt Catalysts: A Comparative Study of Nanoparticles and Bulk Materials. *ACS Catal.* **2012**, *2* (8), 1765–1772.

(13) Frydendal, R.; Paoli, E. A.; Knudsen, B. P.; Wickman, B.; Malacrida, P.; Stephens, I. E. L.; Chorkendorff, I. Benchmarking the Stability of Oxygen Evolution Reaction Catalysts: The Importance of Monitoring Mass Losses. *ChemElectroChem* **2014**, *1* (12), 2075–2081.

(14) McCrory, C. C. L.; Jung, S.; Ferrer, I. M.; Chatman, S. M.; Peters, J. C.; Jaramillo, T. F. Benchmarking Hydrogen Evolving Reaction and Oxygen Evolving Reaction Electrocatalysts for Solar Water Splitting Devices. *J. Am. Chem. Soc.* **2015**, *137* (13), 4347–4357.

(15) Gasteiger, H. A.; Kocha, S. S.; Sompalli, B.; Wagner, F. T. Activity Benchmarks and Requirements for Pt, Pt-Alloy, and Non-Pt Oxygen Reduction Catalysts for PEMFCs. *Appl. Catal. B Environ.* **2005**, *56* (1–2), 9–35.

(16) European Chemical Society. Element Scarcity https://www.euchems.eu/euchems-periodic-table/ (accessed May 15, 2020).

(17) Galán-Mascarós, J. R. Water Oxidation at Electrodes Modified with Earth-Abundant Transition-Metal Catalysts. *ChemElectroChem* **2015**, *2* (1), 37–50.

(18) Suryanto, B. H. R.; Wang, Y.; Hocking, R. K.; Adamson, W.; Zhao, C. Overall Electrochemical Splitting of Water at the Heterogeneous Interface of Nickel and Iron Oxide. *Nat. Commun. 2019 101* **2019**, *10* (1), 1–10.

(19) Swierk, J. R.; Klaus, S.; Trotochaud, L.; Bell, A. T.; Tilley, T. D. Electrochemical Study of the Energetics of the Oxygen Evolution Reaction at Nickel Iron (Oxy)Hydroxide Catalysts. *J. Phys. Chem. C* **2015**, *119*, 19022–19029.

(20) Friebel, D.; Louie, M. W.; Bajdich, M.; Sanwald, K. E.; Cai, Y.; Wise, A. M.; Cheng, M. J.; Sokaras, D.; Weng, T. C.; Alonso-Mori, R.; et al. Identification of Highly Active Fe Sites in (Ni,Fe)OOH for Electrocatalytic Water Splitting. *J. Am. Chem. Soc.* **2015**, *137* (3), 1305–1313.

(21) Klaus, S.; Cai, Y.; Louie, M. W.; Trotochaud, L.; Bell, A. T. Effects of Fe Electrolyte Impurities on Ni(OH)2/NiOOH Structure and Oxygen Evolution Activity. *J. Phys. Chem. C* **2015**, *119*, 7243–7254.

(22) Li, N.; Bediako, D. K.; Hadt, R. G.; Hayes, D.; Kempa, T. J.; Cube, F. Von; Bell, D. C.; Chen, L. X.; Nocera, D. G. Influence of Iron Doping on Tetravalent Nickel Content in Catalytic Oxygen Evolving Films. *PNAS* **2016**, *114*, 1486–1491.

(23) Gorlin, M.; De Araujo, J. F.; Schmies, H.; Bernsmeier, D.; Dresp, S.; Gliech, M.; Jusys, Z.; Chernev, P.; Kraehnert, R.; Dau, H.; et al. Tracking Catalyst Redox States and Reaction Dynamics in Ni-Fe Oxyhydroxide Oxygen Evolution Reaction Electrocatalysts: The Role of Catalyst Support and Electrolyte PH. *J. Am. Chem. Soc.* **2017**, *139* (5), 2070–2082.

(24) Lee, S.; Banjac, K.; Lingenfelder, M.; Hu, X. Oxygen Isotope Labeling Experiments Reveal Different Reaction Sites for the Oxygen Evolution Reaction on Nickel and Nickel Iron Oxides. *Angew. Chemie - Int. Ed.* **2019**, *58* (30), 10295–10299.

(25) Sivula, K.; Van De Krol, R. Semiconducting Materials for Photoelectrochemical Energy Conversion. *Nat. Rev. Mater.* **2016**, *1* (2), 1–16.

(26) Grätzel, M. Photoelectrochemical Cells. *Nature*. Nature Publishing Group November 15, 2001, pp 338–344.

(27) Cardenas-Morcoso, D.; García-Tecedor, M.; Merdzhanova, T.; Smirnov, V.; Finger, F.; Kaiser, B.; Jaegermann, W.; Gimenez, S. An Integrated Photoanode Based on Non-Critical Raw Materials for Robust Solar Water Splitting. *Mater. Adv.* **2020**.

(28) Valdés, A.; Brillet, J.; Grätzel, M.; Gudmundsdóttir, H.; Hansen, H. A.; Jónsson, H.; Klüpfel, P.; Kroes, G. J.; Le Formal, F.; Man, I. C.; et al. Solar Hydrogen Production with Semiconductor Metal Oxides: New Directions in Experiment and Theory. *Phys. Chem. Chem. Phys.* **2011**, *14* (1), 49–70.

(29) Tachibana, Y.; Vayssieres, L.; Durrant, J. R. Artificial Photosynthesis for Solar Water-Splitting. *Nat. Photonics* **2012**, *6* (8), 511–518.

(30) Jiang, C.; Moniz, S. J. A.; Wang, A.; Zhang, T.; Tang, J. Photoelectrochemical Devices for Solar Water Splitting – Materials and Challenges. *Chem. Soc. Rev.* **2017**, *46* (15), 4645–4660.

(31) Hegner, F. S.; Herraiz-Cardona, I.; Cardenas-Morcoso, D.; López, N.; Galán-Mascarós, J.-R.; Gimenez, S. Cobalt Hexacyanoferrate on BiVO4 Photoanodes for Robust Water Splitting. *ACS Appl. Mater. Interfaces* **2017**, *9* (43), 37671–37681.

(32) Shaddad, M. N.; Ghanem, M. A.; Almayouf, A. M.; Gimenez, S.; Bisquert, J.; Herraiz-Cardona, I. Cooperative Catalytic Effect of ZrO2 and A-Fe2O3 Nanoparticles on BiVO4 Photoanodes for Enhanced Photoelectrochemical Water Splitting. *Chem. Sustain. Energy Mater.* **2016**, *9*, 1–7.

(33) Toma, F. M.; Cooper, J. K.; Kunzelmann, V.; McDowell, M. T.; Yu, J.; Larson, D. M.; Borys, N. J.; Abelyan, C.; Beeman, J. W.; Yu, K. M.; et al. Mechanistic Insights into Chemical and Photochemical Transformations of Bismuth Vanadate Photoanodes. *Nat. Commun.* **2016**, *7* (1), 1–11.

(34) FUJISHIMA, A.; HONDA, K. Electrochemical Photolysis of Water at a Semiconductor Electrode. *Nature* **1972**, *238* (5358), 37–38.

(35) Liu, C.; Colón, B. C.; Ziesack, M.; Silver, P. A.; Nocera, D. G. Water Splitting-Biosynthetic System with CO2 Reduction Efficiencies Exceeding Photosynthesis. *Science (80-.).* **2016**, *352* (6290), 1210–1213.

(36) Wang, J.; Yang, H.; Li, F.; Li, L.; Wu, J.; Liu, S.; Cheng, T.; Xu, Y.; Shao, Q.; Huang, X. Single-Site Pt-Doped RuO 2 Hollow Nanospheres with Interstitial C for High-

Performance Acidic Overall Water Splitting. *Sci. Adv.* **2022**, *8* (9), 9271.

(37) Dinh, C. T.; Burdyny, T.; Kibria, G.; Seifitokaldani, A.; Gabardo, C. M.; Pelayo García De Arquer, F.; Kiani, A.; Edwards, J. P.; De Luna, P.; Bushuyev, O. S.; et al. CO2 Electroreduction to Ethylene via Hydroxide-Mediated Copper Catalysis at an Abrupt Interface. *Science (80-.).* **2018**, *360* (6390), 783–787.

(38) Arquer, F. P. G. de; Dinh, C.-T.; Ozden, A.; Wicks, J.; McCallum, C.; Kirmani, A. R.; Nam, D.-H.; Gabardo, C.; Seifitokaldani, A.; Wang, X.; et al. CO2 Electrolysis to Multicarbon Products at Activities Greater than 1 A Cm−2. *Science (80-.).* **2020**, *367* (6478), 661–666.

(39) Lhermitte, C. R.; Sivula, K. Alternative Oxidation Reactions for Solar-Driven Fuel Production. *ACS Catal.* **2019**, *9* (3), 2007–2017.

(40) Francke, R.; Gonzalez, L.; Little, R. D.; Moeller, K. D. Electrons, Electrodes, and the Transformation of Organic Molecules. In *Surface and Interface Science*; Wiley, 2020; pp 827–891.

(41) Cha, H. G.; Choi, K.-S. Combined Biomass Valorization and Hydrogen Production in a Photoelectrochemical Cell. *Nat. Chem.* **2015**, *7*, 328–333.

(42) You, B.; Liu, X.; Jiang, N.; Sun, Y. A General Strategy for Decoupled Hydrogen Production from Water Splitting by Integrating Oxidative Biomass Valorization. *J. Am. Chem. Soc.* **2016**, *138* (41), 13639–13646.

(43) Davis, S. E.; Ide, M. S.; Davis, R. J. Selective Oxidation of Alcohols and Aldehydes over Supported Metal Nanoparticles. *Green Chem.* **2012**, *15* (1), 17–45.

(44) Li, R.; Xiang, K.; Peng, Z.; Zou, Y.; Wang, S. Recent Advances on Electrolysis for Simultaneous Generation of Valuable Chemicals at Both Anode and Cathode. *Adv. Energy Mater.* **2021**, *11* (46), 2102292.

(45) Wang, F.; Stahl, S. S. Electrochemical Oxidation of Organic Molecules at Lower Overpotential: Accessing Broader Functional Group Compatibility with Electron−Proton Transfer Mediators. *Acc. Chem. Res.* **2020**, *53*, 561–574.

(46) Herold, S.; Bafaluy, D.; Muñiz, K. Anodic Benzylic C(Sp3)–H Amination: Unified Access to Pyrrolidines and Piperidines. *Green Chem.* **2018**, *20* (14), 3191–3196.

(47) Horn, E. J.; Rosen, B. R.; Chen, Y.; Tang, J.; Chen, K.; Eastgate, M. D.; Baran, P. S. Scalable and Sustainable Electrochemical Allylic C-H Oxidation. *Nature* **2016**, *533* (7601), 77–81.

(48) Hu, X.; Zhang, G.; Bu, F.; Nie, L.; Lei, A. Electrochemical-Oxidation-Induced Site-Selective Intramolecular C(Sp3)-H Amination. *ACS Catal.* **2018**, *8* (10), 9370–9375.

(49) Sayama, K. Production of High-Value-Added Chemicals on Oxide Semiconductor Photoanodes under Visible Light for Solar Chemical-Conversion Processes. *ACS Energy Letters*. American Chemical Society May 11, 2018, pp 1093–1101.

(50) Tilley, D. Recent Advances and Emerging Trends in Photo-Electrochemical Solar Energy Conversion. *Adv. Energy Mater.* **2019**, *9*, 1802877.

(51) Lhermitte, C. R.; Plainpan, N.; Canjura, P.; Boudoire, F.; Sivula, K. Direct Photoelectrochemical Oxidation of Hydroxymethylfurfural on Tungsten Trioxide Photoanodes. *RSC Adv.* **2020**, *11* (1), 198–202.

(52) Kawde, A.; Sayed, M.; Shi, Q.; Uhlig, J.; Pullerits, T.; Hatti-Kaul, R. Photoelectrochemical Oxidation in Ambient Conditions Using Earth-Abundant Hematite Anode: A Green Route for the Synthesis of Biobased Polymer Building Blocks. *Catal. 2021, Vol. 11, Page 969* **2021**, *11* (8), 969.

(53) Luo, L.; Wang, Z.-J.; Xiang, X.; Yan, D.; Ye, J. Selective Activation of Benzyl Alcohol Coupled with Photoelectrochemical Water Oxidation via a Radical Relay Strategy. **2020**.

(54) Tateno, H.; Miseki, Y.; Sayama, K. Photoelectrochemical Oxidation of Benzylic Alcohol Derivatives on BiVO4 /WO3 under Visible Light Irradiation. *ChemElectroChem* **2017**, *4*, 3283–3287.

(55) Tateno, H.; Miseki, Y.; Sayama, K. Photoelectrochemical Dimethoxylation of Furan via a Bromide Redox Mediator Using a BiVO 4 /WO 3 Photoanode †. *Chem. Commun.* **2017**, *53*, 4378–4381.

(56) Li, T.; Kasahara, T.; He, J.; Dettelbach, K. E.; Sammis, G. M.; Berlinguette, C. P. Photoelectrochemical Oxidation of Organic Substrates in Organic Media. *Nat. Commun.* **2017**, *8* (1), 1–5.

(57) Tateno, H.; Iguchi, S.; Miseki, Y.; Sayama, K. Photo-Electrochemical C-H Bond Activation of Cyclohexane Using a WO3 Photoanode and Visible Light. *Angew. Chemie* **2018**, *57*, 11238–11241.

(58) Tateno, H.; Miseki, Y.; Sayama, K. PINO/NHPI-Mediated Selective Oxidation of Cycloalkenes to Cycloalkenones via a Photo-Electrochemical Method †. *Chem. Commun* **2019**, *55*, 9339.

(59) Tateno, H.; Chen, S. Y.; Miseki, Y.; Nakajima, T.; Mochizuki, T.; Sayama, K. Photoelectrochemical Oxidation of Glycerol to Dihydroxyacetone Over an Acid-Resistant Ta:BiVO4Photoanode. *ACS Sustain. Chem. Eng.* **2022**, *10* (23), 7586–7594.

(60) Liu, Y.; Wang, M.; Zhang, B.; Yan, D.; Xiang, X. Mediating the Oxidizing Capability of Surface-Bound Hydroxyl Radicals Produced by Photoelectrochemical Water Oxidation to

Convert Glycerol into Dihydroxyacetone. *ACS Catal.* **2022**, *12* (12), 6946–6957.

(61) Liu, J.; Li, J.; Shao, M.; Wei, M. Directed Synthesis of SnO2 @BiVO4 /Co-Pi Photoanode for Highly Efficient Photoelectrochemical Water Splitting and Urea Oxidation. *J. Mater. Chem. A* **2019**, *7*, 6327–6336.

(62) Ohta, H.; Nomura, K.; Hiramatsu, H.; Ueda, K.; Kamiya, T.; Hirano, M.; Hosono, H. Frontier of Transparent Oxide Semiconductors. *Solid. State. Electron.* **2003**, *47* (12), 2261–2267.

(63) Van De Krol, R.; Grätzel, M. *Photoelectrochemical Hydrogen Production*; Springer, 2012.

(64) Akanda, R.; Sohail, M.; Aziz, A.; Kawde, A. Recent Advances in Nanomaterial-Modified Pencil Graphite Electrodes for Electroanalysis. *Electroanalysis* **2016**, *28*, 408–424.

(65) Alipour, E.; Majidi, M. R.; Saadatirad, A.; Golabi, S. M.; Alizadeh, A. M. Simultaneous Determination of Dopamine and Uric Acid in Biological Samples on the Pretreated Pencil Graphite Electrode. *Electrochim. Acta* **2013**, *91*, 36–42.

(66) Kawde, A. N.; Baig, N.; Sajid, M. Graphite Pencil Electrodes as Electrochemical Sensors for Environmental Analysis: A Review of Features, Developments, and Applications. *RSC Adv.* **2016**, *6* (94), 91325–91340.

(67) Nathani, A.; Sharma, C. S. Pencil Graphite Electrodes as Platform for Enzyme and Enzyme-like Protein Immobilization for Electrochemical Detection. *J. Electrochem. Soc.* **2020**, *167*, Article ID: 037520.

(68) Karimi-Maleh, H.; Tahernejad-Javazmi, F.; Atar, N.; Yola, M. L.; Gupta, V. K.; Ensafi, A. A. A Novel DNA Biosensor Based on a Pencil Graphite Electrode Modified with Polypyrrole/Functionalized Multiwalled Carbon Nanotubes for Determination of 6-Mercaptopurine Anticancer Drug. *Ind. Eng. Chem. Res.* **2015**, *54* (14), 3634–3639.

(69) Yao, B.; Yuan, L.; Xiao, X.; Zhang, J.; Qi, Y.; Zhou, J.; Zhou, J.; Hu, B.; Chen, W. Paper-Based Solid-State Supercapacitors with Pencil-Drawing Graphite/Polyaniline Networks Hybrid Electrodes. *Nano Energy* **2013**, *2* (6), 1071–1078.

(70) Vishnu, N.; Gopalakrishnan, A.; Badhulika, S. Impact of Intrinsic Iron on Electrochemical Oxidation of Pencil Graphite and Its Application as Supercapacitors. *Electrochim. Acta* **2018**, *269*, 274–281.

(71) Baysal, G.; Uzun, D.; Hasdemir, E. The Fabrication of a New Modified Pencil Graphite Electrode for the Electrocatalytic Reduction of 2-Nitrophenol in Water Samples. *J. Electroanal. Chem.* **2020**, 113893.

(72) Kayan, D. B.; Koçak, D.; İlhan, M.; Koca, A. Electrocatalytic Hydrogen Production on a

Modified Pencil Graphite Electrode. *Int. J. Hydrogen Energy* **2017**, *42* (4), 2457–2463.

(73) Tsuji, R.; Masutani, H.; Haruyama, Y.; Niibe, M.; Suzuki, S.; Honda, S. I.; Matsuo, Y.; Heya, A.; Matsuo, N.; Ito, S. Water Electrolysis Using Flame-Annealed Pencil-Graphite Rods. *ACS Sustain. Chem. Eng.* **2019**, *7* (6), 5681–5689.

(74) Tsuji, R.; Koshino, Y.; Masutani, H.; Haruyama, Y.; Niibe, M.; Suzuki, S.; Nakashima, S.; Fujisawa, H.; Ito, S. Water Electrolysis Using Thin Pt and RuO x Catalysts Deposited by a Flame-Annealing Method on Pencil-Lead Graphite-Rod Electrodes. *ACS Omega* **2020**, *5*, 6090–6099.

(75) Bode, H.; Dehmelt, K.; Witte, J. Zur Kenntnis Der Nickelhydroxidelektrode—I.Über Das Nickel (II)-Hydroxidhydrat. *Electrochim. Acta* **1966**, *11* (8), 1079–1087.

(76) OLIVA, P.; LEONARD, J.; LAURENT, J. F.; DELMAS, C.; BRACONNIER, J. J.; FIGLARZ, M.; FIEVET, F.; GUIBERT, A. de. Review of the Structure and the Electrochemistry of Nickel Hydroxides and Oxy-Hydroxides. *J. Power Sources* **1982**, *8*, 229–255.

(77) Louie, M. W.; Bell, A. T. An Investigation of Thin-Film Ni-Fe Oxide Catalysts for the Electrochemical Evolution of Oxygen. *J. Am. Chem. Soc.* **2013**, *135* (33), 12329–12337.

(78) Doyle, R. L.; Godwin, I. J.; Brandon, M. P.; Lyons, M. E. G. Redox and Electrochemical Water Splitting Catalytic Properties of Hydrated Metal Oxide Modified Electrodes. *Phys. Chem. Chem. Phys.* **2013**, *15*, 13737–13783.

(79) Trotochaud, L.; Young, S. L.; Ranney, J. K.; Boettcher, S. W. Nickel-Iron Oxyhydroxide Oxygen-Evolution Electrocatalysts: The Role of Intentional and Incidental Iron Incorporation. *J. Am. Chem. Soc.* **2014**, *136* (18), 6744–6753.

(80) Gong, M.; Li, Y.; Wang, H.; Liang, Y.; Wu, J. Z.; Zhou, J.; Wang, J.; Regier, T.; Wei, F.; Dai, H. An Advanced Ni−Fe Layered Double Hydroxide Electrocatalyst for Water Oxidation. *J. Am. Chem. Soc* **2013**, *135*, 8455.

(81) Zhou, Y.; López, N. The Role of Fe Species on NiOOH in Oxygen Evolution Reactions. *ACS Catal.* **2020**, *10* (11), 6254–6261.

(82) Lu, Z.; Xu, W.; Zhu, W.; Yang, Q.; Lei, X.; Liu, J.; Li, Y.; Sun, X.; Duan, X. Three-Dimensional NiFe Layered Double Hydroxide Film for High-Efficiency Oxygen Evolution Reaction. *Chem. Commun* **2014**, *50*, 6479.

(83) Lu, Z.; Qian, L.; Xu, W.; Tian, Y.; Jiang, M.; Li, Y.; Sun, X.; Duan, X. Dehydrated Layered Double Hydroxides: Alcohothermal Synthesis and Oxygen Evolution Activity. *Nano Res. 2016 910* **2016**, *9* (10), 3152–3161.

(84) Park, J. H.; Seo, J.; Park, S.; Shin, S. S.; Kim, Y. C.; Jeon, N. J.; Shin, H. W.; Ahn, T. K.;

Noh, J. H.; Yoon, S. C.; et al. Efficient CH3NH3PbI3 Perovskite Solar Cells Employing Nanostructured P-Type NiO Electrode Formed by a Pulsed Laser Deposition. *Adv. Mater.* **2015**, *27* (27), 4013–4019.

(85) Miller, E. L.; Rocheleau, R. E. Electrochemical Behavior of Reactively Sputtered Iron-Doped Nickel Oxide. *J. Electrochem. Soc.* **1997**, *144* (9), 3072–3077.

(86) Park, I. J.; Kang, G.; Park, M. A.; Kim, J. S.; Seo, S. W.; Kim, D. H.; Zhu, K.; Park, T.; Kim, J. Y. Highly Efficient and Uniform 1 Cm2 Perovskite Solar Cells with an Electrochemically Deposited NiOx Hole-Extraction Layer. *ChemSusChem* **2017**, *10* (12), 2660–2667.

(87) Katumba, G.; Lu, J.; Olumekor, L.; Westin, G.; Wäckelgård, E. Low Cost Selective Solar Absorber Coatings: Characteristics of Carbon-In-Silica Synthesized with Sol-Gel Technique. *J. Sol-Gel Sci. Technol. 2005 361* **2005**, *36* (1), 33–43.

(88) Cai, Z.; Zhou, D.; Wang, M.; Bak, S. M.; Wu, Y.; Wu, Z.; Tian, Y.; Xiong, X.; Li, Y.; Liu, W.; et al. Introducing Fe2+ into Nickel–Iron Layered Double Hydroxide: Local Structure Modulated Water Oxidation Activity. *Angew. Chemie Int. Ed.* **2018**, *57* (30), 9392–9396.

(89) Ng, J. W. D.; García-Melchor, M.; Bajdich, M.; Chakthranont, P.; Kirk, C.; Vojvodic, A.; Jaramillo, T. F. Gold-Supported Cerium-Doped NiOx Catalysts for Water Oxidation. *Nat. Energy 2016 15* **2016**, *1* (5), 1–8.

(90) Joya, K. S.; Joya, Y. F.; De Groot, H. J. M. Ni-Based Electrocatalyst for Water Oxidation Developed In-Situ in a HCO3−/CO2 System at Near-Neutral PH. *Adv. Energy Mater.* **2014**, *4* (9), 1301929.

(91) Fu, G.-R.; Hu, Z.-A.; Xie, L.-J.; Jin, X.-Q.; Xie, Y.-L.; Wang, Y.-X.; Zhang, Z.-Y.; Yang, Y.-Y.; Wu, H.-Y. Electrodeposition of Nickel Hydroxide Films on Nickel Foil and Its Electrochemical Performances for Supercapacitor. *Int. J. Electrochem. Sci* **2009**, *4*, 1052–1062.

(92) Kong, D. S.; Wang, J. M.; Shao, H. B.; Zhang, J. Q.; Cao, C. N. Electrochemical Fabrication of a Porous Nanostructured Nickel Hydroxide Film Electrode with Superior Pseudocapacitive Performance. *J. Alloys Compd.* **2011**, *509* (18), 5611–5616.

(93) Subbaiah, T.; Mallick, S. C.; Mishra, K. G.; Sanjay, K.; Das, R. P. Electrochemical Precipitation of Nickel Hydroxide. *J. Power Sources* **2002**, *112* (2), 562–569.

(94) Murthy, M.; Nagarajan, G. S.; Weidner, J. W.; Van Zee, J. W. A Model for the Galvanostatic Deposition of Nickel Hydroxide. *J. Electrochem. Soc.* **1996**, *143* (7), 2319–2327.

(95) Streinz, C. C.; Hartman, A. P.; Motupally, S.; Weidner, J. W. The Effect of Current and Nickel Nitrate Concentration on the Deposition of Nickel Hydroxide Films. *J. Electrochem. Soc.* **1995**, *142* (4), 1084–1089.

(96) Streinz, C. C.; Motupally, S.; Weidner, J. W. The Effect of Temperature and Ethanol on the Deposition of Nickel Hydroxide Films. *J. Electrochem. Soc.* **1995**, *142* (12), 4051–4056.

(97) Liu, H.; Yan, G.; Liu, F.; Zhong, Y.; Feng, B. Structural, Electrochemical and Optical Properties of NiOxHy Thin Films Prepared by Electrochemical Deposition. *J. Alloys Compd.* **2009**, *481* (1–2), 385–389.

(98) Fantini, M.; Gorenstein, A. Electrochromic Nickel Hydroxide Films on Transparent/Conducting Substrates. *Sol. Energy Mater.* **1987**, *16* (6), 487–500.

(99) Lyons, M. E. G.; Cakara, A.; O'brien, P.; Godwin, I.; Doyle, R. L. Redox, PH Sensing and Electrolytic Water Splitting Properties of Electrochemically Generated Nickel Hydroxide Thin Films in Aqueous Alkaline Solution. *Int. J. Electrochem. Sci* **2012**, *7*, 11768–11795.

(100) MacArthur, D. M. The Proton Diffusion Coefficient for the Nickel Hydroxide Electrode. *J. Electrochem. Soc.* **1970**, *117* (6), 729.

(101) MacArthur, D. M. The Hydrated Nickel Hydroxide Electrode Potential Sweep Experiments. *J. Electrochem. Soc.* **1970**, *117* (4), 422.

(102) Louër, M.; Louër, D.; Grandjean, D.; Weigel, D.; IUCr. Etude Structurale Des Hydroxynitrates de Nickel et de Zinc. III. Etude Structurale Des Nitrates Basiques Zn(OH)2.Zn(NO3)2.2H2O et Ni(OH)2.Ni(NO3)2.2H2O. *Acta Crystallogr. Sect. B* **1973**, *29* (8), 1707–1710.

(103) Louër, M.; Louër, D.; Grandjean, D. Etude Structurale Des Hydroxynitrates de Nickel et de Zinc. I. Classification Structurale. *urn:issn:0567-7408* **1973**, *29* (8), 1696–1703.

(104) Glemser, O.; Einerhand, J. Über Höhere Nickelhydroxyde. *Zeitschrift für Anorg. Chemie* **1950**, *261* (1–2), 26–42.

(105) Lu, X.; Zhao, C. Electrodeposition of Hierarchically Structured Three-Dimensional Nickel–iron Electrodes for Efficient Oxygen Evolution at High Current Densities. *Nat. Commun.* **2015**, *6*, Article ID: 6616.

(106) Pérez-Alonso, F. J.; Adán, C.; Rojas, S.; Peña, M. A.; Fierro, J. L. G. Ni/Fe Electrodes Prepared by Electrodeposition Method over Different Substrates for Oxygen Evolution Reaction in Alkaline Medium. *Int. J. Hydrogen Energy* **2014**, *39* (10), 5204–5212.

(107) Ma, W.; Ma, R.; Wang, C.; Liang, J.; Liu, X.; Zhou, K.; Sasaki, T. A Superlattice of Alternately Stacked Ni-Fe Hydroxide Nanosheets and Graphene for Efficient Splitting of

Water. *ACS Nano* **2015**, *9* (2), 1977–1984.

(108) Marini, S.; Salvi, P.; Nelli, P.; Pesenti, R.; Villa, M.; Berrettoni, M.; Zangari, G.; Kiros, Y. Advanced Alkaline Water Electrolysis. *Electrochim. Acta* **2012**, *82*, 384–391.

(109) Kim, J. H.; Lee, J. S. Elaborately Modified BiVO4 Photoanodes for Solar Water Splitting. *Adv. Mater.* **2019**, *31* (20), 1806938.

(110) Long, M.; Cai, W.; Kisch, H. Visible Light Induced Photoelectrochemical Properties of N-BiVO4 and n-BiVO4/p-Co3O4. *J. Phys. Chem. C* **2008**, *112* (2), 548–554.

(111) Kudo, A.; Ueda, K.; Kato, H.; Mikami, I. Photocatalytic O 2 Evolution under Visible Light Irradiation on BiVO 4 in Aqueous AgNO 3 Solution. *Catal. Letters* **1998**, *53*, 229–230.

(112) Han, H. S.; Shin, S.; Kim, D. H.; Park, I. J.; Kim, J. S.; Huang, P.-S.; Lee, J.-K.; Cho, I. S.; Zheng, X. Boosting the Solar Water Oxidation Performance of a BiVO 4 Photoanode by Crystallographic Orientation Control †. *Energy Environ. Sci* **2018**, *11*, 1299.

(113) Favaro, M.; Artiglia, L.; Mun, B. S. In Situ/Operando Investigation of Catalytic and Electrocatalytic Interfaces. *J. Phys. D. Appl. Phys.* **2021**, *55* (6), 060201.

(114) Zhang, S.; Ahmet, I.; Kim, S. H.; Kasian, O.; Mingers, A. M.; Schnell, P.; Kölbach, M.; Lim, J.; Fischer, A.; Mayrhofer, K. J. J.; et al. Different Photostability of BiVO4in Near-PH-Neutral Electrolytes. *ACS Appl. Energy Mater.* **2020**, *3* (10), 9523–9527.

(115) Lee, D. K.; Choi, K. S. Enhancing Long-Term Photostability of BiVO4 Photoanodes for Solar Water Splitting by Tuning Electrolyte Composition. *Nat. Energy 2017 31* **2017**, *3* (1), 53–60.

(116) Giménez, S.; Bisquert, J. *Photoelectrochemical Solar Fuel Production. From Basic Principles to Advanced Devices*; Springer Nature, 2016.

(117) Sleight, A. W.; Chen, H. -y.; Ferretti, A.; Cox, D. E. Crystal Growth and Structure of BiVO4. *Mater. Res. Bull.* **1979**, *14* (12), 1571–1581.

(118) Zhao, Z.; Luo, W.; Li, Z.; Zou, Z. Density Functional Theory Study of Doping Effects in Monoclinic Clinobisvanite BiVO4. *Phys. Lett. A* **2010**, *374* (48), 4919–4927.

(119) Kudo, A.; Omori, K.; Kato, H. A Novel Aqueous Process for Preparation of Crystal Form-Controlled and Highly Crystalline BiVO 4 Powder from Layered Vanadates at Room Temperature and Its Photocatalytic and Photophysical Properties. *J. Am. Chem. Soc.* **1999**, *121* (49), 11459–11467.

(120) Ding, Y.; Wang, Y. Density Functional Theory Study of the Silicene-like Six and XSi 3 (X = B, C, N, Al, P) Honeycomb Lattices: The Various Buckled Structures and Versatile Electronic Properties. *J. Phys. Chem. C* **2013**, *117* (35), 18266–18278.

(121) Cooper, J. K.; Gul, S.; Toma, F. M.; Chen, L.; Glans, P. A.; Guo, J.; Ager, J. W.; Yano,

J.; Sharp, I. D. Electronic Structure of Monoclinic BiVO4. *Chem. Mater.* **2014**, *26* (18), 5365–5373.

(122) Cooper, J. K.; Gul, S.; Toma, F. M.; Chen, L.; Liu, Y. S.; Guo, J.; Ager, J. W.; Yano, J.; Sharp, I. D. Indirect Bandgap and Optical Properties of Monoclinic Bismuth Vanadate. *J. Phys. Chem. C* **2015**, *119* (6), 2969–2974.

(123) Zhao, Z.; Li, Z.; Zou, Z. Electronic Structure and Optical Properties of Monoclinic Clinobisvanite BiVO4. *Phys. Chem. Chem. Phys.* **2011**, *13* (10), 4746–4753.

(124) Österbacka, N.; Ambrosio, F.; Wiktor, J. Charge Localization in Defective BiVO4. *J. Phys. Chem. C* **2022**, *126* (6), 2960–2970.

(125) Wang, S.; Chen, P.; Yun, J. H.; Hu, Y.; Wang, L. An Electrochemically Treated BiVO4 Photoanode for Efficient Photoelectrochemical Water Splitting. *Angew. Chemie - Int. Ed.* **2017**, *56* (29), 8500–8504.

(126) Zhang, Y.; Guo, Y.; Duan, H.; Li, H.; Sun, C.; Liu, H. Facile Synthesis of V4+ Self-Doped, [010] Oriented BiVO4 Nanorods with Highly Efficient Visible Light-Induced Photocatalytic Activity. *Phys. Chem. Chem. Phys.* **2014**, *16* (44), 24519–24526.

(127) Hegner, F. S.; Forrer, D.; Joséramó, J.; Galán, J.; Mascarós, G.-M.; Núria Lópezlópez, N.; Selloni, A. Versatile Nature of Oxygen Vacancies in Bismuth Vanadate Bulk and (001) Surface. *J. Phys. Chem. Lett.* **2019**, *10*, 6672–6678.

(128) Yuan, Y.; Huang, Y.; Ma, F.; Zhang, Z.; Wei, X. Effects of Oxygen Vacancy on the Mechanical, Electronic and Optical Properties of Monoclinic BiVO4. *J. Mater. Sci.* **2017**, *52* (14), 8546–8555.

(129) Yin, W. J.; Wei, S. H.; Al-Jassim, M. M.; Turner, J.; Yan, Y. Doping Properties of Monoclinic BiVO4 Studied by First-Principles Density-Functional Theory. *Phys. Rev. B - Condens. Matter Mater. Phys.* **2011**, *83* (15), 155102.

(130) Zhang, W.; Song, L.; Cen, J.; Liu, M. Mechanistic Insights into Defect-Assisted Carrier Transport in Bismuth Vanadate Photoanodes. *J. Phys. Chem. C* **2019**, *123* (34), 20730–20736.

(131) Kim, T. W.; Ping, Y.; Galli, G. A.; Choi, K. S. Simultaneous Enhancements in Photon Absorption and Charge Transport of Bismuth Vanadate Photoanodes for Solar Water Splitting. *Nat. Commun. 2015 61* **2015**, *6* (1), 1–10.

(132) Cooper, J. K.; Scott, S. B.; Ling, Y.; Yang, J.; Hao, S.; Li, Y.; Toma, F. M.; Stutzmann, M.; Lakshmi, K. V.; Sharp, I. D. Role of Hydrogen in Defining the N-Type Character of BiVO4 Photoanodes. *Chem. Mater.* **2016**, *28* (16), 5761–5771.

(133) Kim, T. W.; Choi, K. S. Nanoporous BiVO4 Photoanodes with Dual-Layer Oxygen

Evolution Catalysts for Solar Water Splitting. *Science (80-.).* **2014**, *343* (6174), 990–994.

(134) Abdi, F. F.; Savenije, T. J.; May, M. M.; Dam, B.; Van De Krol, R. The Origin of Slow Carrier Transport in BiVO4 Thin Film Photoanodes: A Time-Resolved Microwave Conductivity Study. *J. Phys. Chem. Lett.* **2013**, *4* (16), 2752–2757.

(135) Huang, Z. F.; Pan, L.; Zou, J. J.; Zhang, X.; Wang, L. Nanostructured Bismuth Vanadate-Based Materials for Solar-Energy-Driven Water Oxidation: A Review on Recent Progress. *Nanoscale* **2014**, *6* (23), 14044–14063.

(136) Choi, K.-S. Shape Effect and Shape Control of Polycrystalline Semiconductor Electrodes for Use in Photoelectrochemical Cells. *J. Phys. Chem. Lett* **2010**, *1*, 2244–2250.

(137) Walter, M. G.; Warren, E. L.; McKone, J. R.; Boettcher, S. W.; Mi, Q.; Santori, E. A.; Lewis, N. S. Solar Water Splitting Cells. *Chem. Rev.* **2010**, *110* (11), 6446–6473.

(138) Sinclair, T. S.; Hunter, B. M.; Winkler, J. R.; Gray, H. B.; Müller, A. M. Factors Affecting Bismuth Vanadate Photoelectrochemical Performance. *Mater. Horizons* **2015**, *2* (3), 330–337.

(139) McDonald, K. J.; Choi, K. S. A New Electrochemical Synthesis Route for a BiOI Electrode and Its Conversion to a Highly Efficient Porous BiVO4 Photoanode for Solar Water Oxidation. *Energy Environ. Sci.* **2012**, *5* (9), 8553–8557.

(140) Xi, G.; Ye, J. Synthesis of Bismuth Vanadate Nanoplates with Exposed {001} Facets and Enhanced Visible-Light Photocatalytic Properties. *Chem. Commun.* **2010**, *46* (11), 1893–1895.

(141) Berglund, S. P.; Flaherty, D. W.; Hahn, N. T.; Bard, A. J.; Mullins, C. B. Photoelectrochemical Oxidation of Water Using Nanostructured BiVO 4 Films. *J. Phys. Chem. C* **2011**, *115* (9), 3794–3802.

(142) Kim, C. W.; Son, Y. S.; Kang, M. J.; Kim, D. Y.; Kang, Y. S. (040)-Crystal Facet Engineering of BiVO4 Plate Photoanodes for Solar Fuel Production. *Adv. Energy Mater.* **2016**, *6* (4).

(143) Ravensbergen, J.; Abdi, F. F.; Van Santen, J. H.; Frese, R. N.; Dam, B.; Van De Krol, R.; Kennis, J. T. M. Unraveling the Carrier Dynamics of BiVO4: A Femtosecond to Microsecond Transient Absorption Study. *J. Phys. Chem. C* **2014**, *118* (48), 27793–27800.

(144) Byun, S.; Kim, B.; Jeon, S.; Shin, B. Effects of a SnO2 Hole Blocking Layer in a BiVO4-Based Photoanode on Photoelectrocatalytic Water Oxidation. *J. Mater. Chem. A* **2017**, *5* (15), 6905–6913.

(145) Pihosh, Y.; Turkevych, I.; Mawatari, K.; Uemura, J.; Kazoe, Y.; Kosar, S.; Makita, K.; Sugaya, T.; Matsui, T.; Fujita, D.; et al. Photocatalytic Generation of Hydrogen by Core-

Shell WO3/BiVO4 Nanorods with Ultimate Water Splitting Efficiency. *Sci. Reports 2015 51* **2015**, *5* (1), 1–10.

(146) Hong, S. J.; Lee, S.; Jang, J. S.; Lee, J. S. Heterojunction BiVO4/WO3 Electrodes for Enhanced Photoactivity of Water Oxidation. *Energy Environ. Sci.* **2011**, *4* (5), 1781–1787.

(147) Ma, Y.; Kafizas, A.; Pendlebury, S. R.; Le Formal, F.; Durrant, J. R. Photoinduced Absorption Spectroscopy of CoPi on BiVO4: The Function of CoPi during Water Oxidation. *Adv. Funct. Mater.* **2016**, *26* (27), 4951–4960.

(148) Zhong, D. K.; Choi, S.; Gamelin, D. R. Near-Complete Suppression of Surface Recombination in Solar Photoelectrolysis by "Co-Pi" Catalyst-Modified W:BiVO4. *J. Am. Chem. Soc.* **2011**, *133* (45), 18370–18377.

(149) Lamm, B.; Trześniewski, B. J.; Döscher, H.; Smith, W. A.; Stefik, M. Emerging Postsynthetic Improvements of BiVO4 Photoanodes for Solar Water Splitting. *ACS Energy Lett.* **2017**, *3* (1), 112–124.

(150) Li, T.; He, J.; Peña, B.; Berlinguette, C. P. Curing BiVO4 Photoanodes with Ultraviolet Light Enhances Photoelectrocatalysis. *Angew. Chemie - Int. Ed.* **2016**, *55* (5), 1769–1772.

2. Experimental methods

In this chapter, a comprehensive overview of the electrodes preparation, the main techniques used to analyse and characterise these electrodes and the photoelectrochemical (PEC) conditions are described. First, a complete description of electrodes, photoelectrodes and PEC preparation are detailed, including the main deposition techniques used to prepare the different catalysts on substrate electrodes and the main steps for PEC set up prior to any electrochemical measurement. Then, the basics of the structural, morphological, and analytical techniques will be described, specifying in each case the corresponding measurement conditions. Finally, the experimental set-ups and the fundamental background of the electrical measurements used to study in detail the performance and electrochemical properties of the electrochemical or photoelectrochemical systems are explained.

2.1. Electrodes and photoelectrodes preparation

2.1.1. Activated pencil graphite rods

In this thesis, commercial pencil graphite rods (PGRs) have been used as supporting electrodes in Chapter 3. These PGRs were purchased from Mitsubishi Pencil Co., Ltd. company in Japan. The hardness code selected was 4B which is the PGR with more graphite content. Their dimensions were 2.0 mm diameter and 13.0 mm length. Since the commercial PGRs were not electrochemically active, two activation steps were performed prior to the preparation of the electrodes.

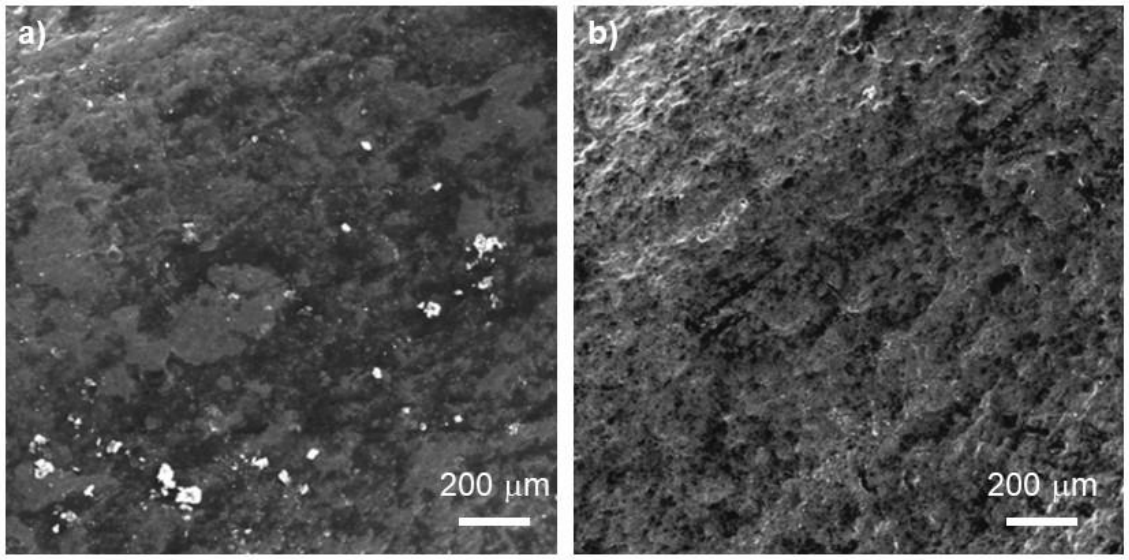

Figure 1. Top view SEM images of 4B PGR **(a)** before and **(b)** after FA treatment.

1) To control the surface area of the rods, the tips were polished with a polishing machine (LaboPol Struers) until a completely flat and homogeneous surface was reached.
2) A flame annealing (FA) treatment was used to remove the coating polymer on the PGR surface. This process, inspired on the FA process proposed by Tsuji et al.[1] consists of burning the whole rod in flame using liquefied petroleum gas (LPG) until the PGR became red because of the heat. After 1 min in flame, the PGR was air-cooled until room temperature. This process was repeated 10 times, leading to a polymer-free porous structure of carbon (**Figure 1**).

2.1.2. Ni, Fe and NiFe decorated pencil graphite rod

Several strategies have been developed for the design of new Ni and NiFe catalysts in order to achieve the oxygen evolution reaction. Among these techniques, pulsed laser deposition, sputtering, chemical vapor deposition and sol-gel methodologies are some of the most commonly used for this purpose.[2,3] However, in most cases, these strategies involve the use of very unusual experimental processes, with lack of reproducibility.

In order to achieve low-cost and reproducible electrochemical systems, the decoration of the PGR with Ni, Fe hydroxides and NiFe layered double hydroxide was based on flame annealing and electrodeposition techniques. In a general way, both techniques offer the possibility to directly grow the metal over the conductive substrate under ambient conditions. Moreover, the experimental procedure is very simple which lead to highly active, low-cost and reproducible electrocatalysts. The experimental conditions employed in each technique are as follows.

Catalyst (co)-deposition on PGR by flame annealing strategy. Flame annealing (FA) deposition was based on the thermal procedure proposed by Tsuji et al.[4] The process consists of three steps: (1) First, the PGR was flame heated until it became red. (2) Immediately, PGR was withdrawn of the flame and 2 seconds after it was dipped for 5 seconds into a vial which contained 8 mL of the precursor solution. (3) these steps are repeated 10 times, after which the flame annealing was applied to the electrode for 20 seconds. For an even annealing of the catalyst, the PGR is slid in the direction of the rod axis and then turned 180° to the left and right by hand. Using this technique, FA@Ni/PGR and FA@NiFe/PGR electrodes were prepared.

Ni electrodeposition on PG. The electrodeposition (ED) of nickel on PGR electrodes was performed by cyclic voltammetry. A mixture of 0.1 M Na_2SO_4 and 0.02 M $NiCl_2x6H_2O$ in water was used as the electrolyte solution and Ag/AgCl and Pt were used as reference and counter electrodes, respectively. After PGR pre-deposition treatment, cyclic voltammetries, consisted of 25 cycles from -1.2 to 0.2 V vs Ag/AgCl, with a scan rate of 50 $mV \cdot s^{-1}$, were performed. Using this technique, ED@Ni/PGR electrodes were prepared.

2.1.3. Zr decorated $BiVO_4$

To perform the oxygen evolution reaction directly driven with sunlight as introduced in Chapter 1 and studied in Chapters 4 and 5, Zr-decorated $BiVO_4$ (Zr:$BiVO_4$) photoanodes were prepared following a two-step method also described by Choi et al.[5] The first step is to electrodeposit a dendritic Bismuth metal film on the FTO substrate using a non-aqueous bath solution containing the oxidized Bi^{3+} species (from $Bi(NO_3)_3$-$5H_2O$) in ethylene glycol. A negative applied potential provides electrons to the FTO surfaces, where the reduction of Bi^{3+} occurs, leading to the formation and deposition of metallic Bismuth, as a result of the reaction:

$$Bi^{3+} + 3e^- \rightarrow Bi^0 \qquad E^\circ = 0.308\,V \qquad (1)$$

The reason for using a non-aqueous ethylene glycol solution is to increase the solubility of Bi^{3+} and, at the same time, to avoid dissolution of the deposited Bismuth, favouring good coating and attachment of the resulting films. For the preparation of Zr-containing $BiVO_4$ photoelectrode, $ZrCl_2O$-$8H_2O$ was added to the solution. The second step is to drop a solution of $VO(acac)_2$ in dimethyl sulfoxide (DMSO) onto the deposited Bi metal film, immediately followed by a low-temperature conditioning (around 80 °C) to evaporate the solvent. Lastly, the sample is annealed at 450 °C for 2 hours, during which the metallic Bismuth and VO_2^+ are oxidized and mutually reacted to form the crystalline $BiVO_4$ and amorphous V_2O_5. For a pure $BiVO_4$ film, the exceeding V_2O_5 is removed by dipping the films in a 1M NaOH solution with agitation for 30 min.

2.2. Characterization techniques

2.2.1. Morphological and structural techniques

2.2.1.1. X-ray diffraction (XRD)

X-ray diffraction (XRD) is one of the most effective techniques for the qualitative and quantitative analysis of crystalline phases of any type of material.[6] The fundamentals of this technique are based on the interference of a crystal in an X-ray beam. The wavelengths of the X-rays are of the same order as the interatomic distances of the components of the crystal lattices. When irradiated on the sample to be analysed, X-rays diffract with angles that depend on the interatomic distances. The interplanar distances (d) are related with the glancing angle (θ) by the Bragg's law (**Figure 2**).[7]

$$n \cdot \lambda = 2 \cdot d \cdot sen\theta \qquad \textit{Eq. 1}$$

Where n is the diffraction order (n = 1, 2, 3 …) and λ is the radiation wavelength comparable to atomic spacings.

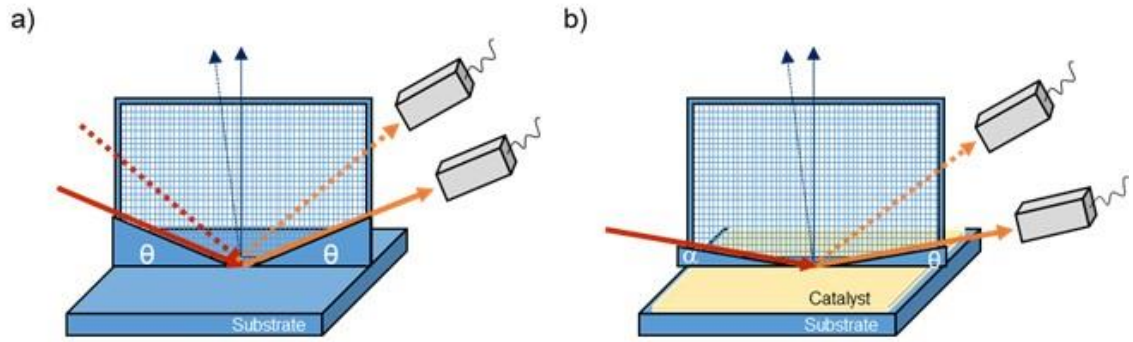

Figure 2. Schematic diagrams of glancing angle XRD geometry for **(a)** conventional XRD and **(b)** GIXRD systems.

The configuration diagram for conventional XRD employs the usual Bragg-Brentano (or θ-2θ) connection. In this case, the detector is arranged at the same angle at which the X-rays are incident upon the sample (**Figure 2a**). This configuration guarantees a highly diffracted beam detection for any crystallographic plane in the sample.

Conventional XRD systems, however, suffer from certain drawbacks when they are used in the analysis of thin films, since the depth of X-ray penetration on the surface can be greater than the film thickness. For polycrystalline thin films, the solution to the problem is to apply the grazing angle geometry where the angle of the incident beam on the sample surface is small (typically 1-5º) and remains fixed during the analysis (**Figure 2b**). This method is known as grazing beam X-ray diffraction (GIXRD) and it is mainly used to characterize materials deposited or grown on amorphous and single-crystalline substrates, being able to perform phase identification, phase changes, grain size calculation, lattice deformations, profile studies, oxidation state, surface mechanical properties, and so on.

XRD technique was employed as part of the structural characterization made for $BiVO_4$ in chapters 4 and 5. The measurements were developed in the x-ray diffraction service of the Servei Central d'Investigacions Científiques (SCIC) at the University Jaume I. A Rigaku Miniflex 600 from Rigaku Corporation diffractometer operating at a grazing incidence of 1º and scan rated at $3^{o} \cdot min^{-1}$ was employed in any case. The equipment configuration contains copper Ka radiation (λ = 1.5418 Å) and a scintillation detector.

2.2.1.2. X-ray photoelectron spectroscopy

X-ray photoelectron spectroscopy (XPS) is a spectroscopic technique, which is widely used in the surface characterization of solids.[8] Based on the photoelectric effect, this technique is able to determine the kinetic energy of the electrons that are photoemitted from the material when it is irradiated with a beam of ionizing X-rays (**Figure 3**). Depending on the incident irradiation to the sample, different photoemission-based techniques are obtained: X-ray photoelectron spectroscopy (XPS), ultraviolet photoelectron spectroscopy (UPS) and synchrotron radiation x-ray photoelectron spectroscopy (SXPS).

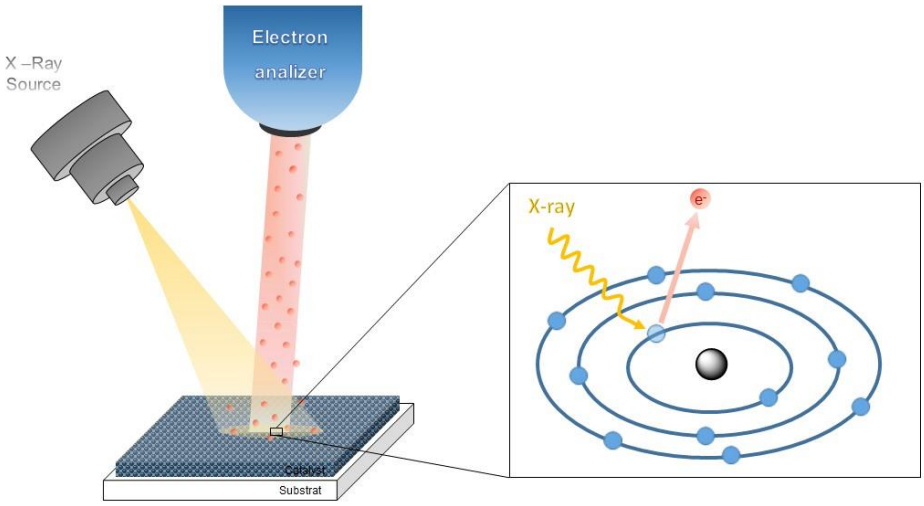

Figure 3. Schematic diagram representation of the photoelectric effect upon the sample surface.

The kinetic energy (E_c) of the emitted electrons is described by the Einstein photoelectric equation (**Figure 3**).

$$E_c = E_{h\nu} - E_B - \Phi \qquad Eq.\ 2$$

where E_B is the binding energy of the electron in the atom, $E_{h\nu}$ is the monochromatic x ray source energy and Φ is the work function of the analyser. During the measurement preparation, the XPS spectrometer is referenced and calibrated setting the fermi edge emission of Au film to obtain the work function of the spectrometer.

The binding energy of the photoemitted electrons is characteristic of the energy for each electronic level and of the chemical nature for each emitting atom. Therefore, by means of this technique it is possible to obtain both information on the nature of the atoms (elemental composition) and their oxidation state on the surface. As a general rule it should be noted that the binding energy increases with increasing oxidation state of the atom. Moreover, the depth of sampling depends, among other factors, on the energy of the ionizing beam. However, the photoemitted electrons do not pass through solids, being the measured ones those at a distance close to the surface. On this way, for an incident beam with an energy of 1 keV (as the one used for this technique), the mean free path of a stripped electron is between 30 and 50 Å, this being the range of depths typically analysed.

XPS has been employed in the surface characterization of pencil graphite decorated electrodes in the chapter 3. The measurements presented here were carried out by our collaborators at University of Hyogo (Japan). Details of further experimental information could be found in the corresponding chapter.

2.2.1.3. Scanning electron microscopy

Scanning electron microscopy (SEM) is a technique that allows the structural and morphological characterization of a sample.[9] An image is obtained by scanning with an electron beam. In this technique, a filament (usually tungsten or lanthanum) is used to emit electrons and, through an electric field, these electrons are accelerated towards the sample. As the electron beam hits the surface of the sample, an interaction takes place and different types of signals are produced, including: backscattered electrons, secondary electrons, auger and X-ray fluorescence. The detectors are able to collect the different types of radiation and convert each type into a final image, whose characteristics are determined according to the type of radiation and are discussed below.

Backscattered electrons: are those produced by the elastic collision of the beam electrons with the nucleus of an atom of the sample. The intensity of this phenomenon depends on the atomic number of the atom. For this reason, this type of radiation is used to acquire images with information about the composition of the sample.

Secondary electrons: these are the electrons resulting from the inelastic collision of the electron beam with the electrons in the atoms. When the beam pass very close to the nucleus of the atoms in the sample and interact with their electrons, these may acquire enough energy to escape from the atom and can be detected in a sensor. These are low energy electrons and are mainly originated at the surface of the sample. Therefore, the image provided by the secondary electrons shows a very detailed picture of the sample surface.

X-ray fluorescence: in the process described above, the ionized electrons from the deeper levels are regenerated by the electrons from the shallower orbitals. The excess of energy is emitted as X-rays. This is the basis for the X-ray analysis in SEM or, more precisely, by the technique known as energy dispersive X-ray spectroscopy (EDX or EDS). In EDX, the energy of the emitted photons depends on the nature of the emitting atom and the number of photons emitted is a function of the relative amount of each element. For this reason, EDX allows both qualitative and quantitative characterization of the elements that make-up the surface of the sample.

In the sample preparation requirements, conductivity within the sample is desirable. Therefore, when it is not, a thin layer of thickness between 10 and 25 nm is deposited on the sample. The materials used to make the sample conductive are mainly heavy metals as they produce higher electron emission.

SEM and EDX techniques are employed as part of the surface morphological characterization of the corresponding electrode in chapters 3 and 5. The corresponding measurements were developed in the SEM service of the SCIC in the University Jaume I. The equipment employed was a scanning electron microscopy JEOL 7001F from JEOL Company which is equipped with

an INCA 350 software for the EDX measurements. The equipment uses a field emission gun between 0.1-30 kV. For the metal deposition, a Baltec SCD500 sputter coater from BAL-TEC company was employed for the 10 nm layer of Pt deposition.

2.2.1.4. Transmission electron microscopy

Transmission electron microscopy (TEM) is a structural and morphological characterization technique that allows the formation of high-resolution images from high-energy electron (100-200 keV) passing through the sample.[10] Due to the high intensity of the electron beam, TEM offers the possibility to characterize solid organic and inorganic samples at the nanometer level.

Similar to SEM, the incidence of the electron beam upon the specimen generates different types of radiation which are employed to generate different types of images. In detail, the transmission mode in high-resolution (HRTEM) allows images with spatial resolution of the order of Å or even lower, depending on the sample and observation conditions. In this way it is possible to study atomic arrangements, crystalline planes and defects present in the structures. In addition, by means of selected area electron diffraction (SAED) it is possible to study the reciprocal space. This technique analyses the beams diffracted by the different crystalline planes, yielding information on the orientation and crystalline structure of the sample. Finally, the electron kinetic energy loss after interacting with the sample (EELS) is used to determine the atomic structure and some chemical properties of the sample, including the identification and quantification of the elements present, the chemical state of this atoms, as well as information on the interactions of the atoms with their neighbours.

The most important condition for the transmission of electrons through the sample is that the specimen must be thin, that is, transparent to electrons. In general, it is recommended not to use samples thicker than 10 nm, since the thinner the sample, the better the quality of the images obtained. Then, the preparation of the samples is very important for their following analysis. In this work, the film layer of the electrode was scratched to obtain a powder of the material, which is further dispersed with ultrasonication in ethanol or isopropanol. Subsequently, the suspension is placed on a Ni grid for their analysis

HRTEM, SAED and EELS techniques have been employed for the structural and morphological analysis of $BiVO_4$ samples in chapter 5. Our collaborators in the Catalan Institute of Nanoscience and Nanotechnology (ICN2) conducted the measurements presented in this work. They employed a high angle annular dark-field (HAADF) STEM combined with EELS in the Tecnai F20 microscope. A field emission gun FEI Tecnai F20 microscope at 200 kV provides a point-to-point resolution of 0.19 nm.

2.2.1.5. Raman spectroscopy

Raman spectroscopy is a spectroscopic technique that studies the vibrational and rotational modes of molecules when low-frequency radiation is focused on a sample.[11] Raman effect is based on the inelastic dispersion of the light due to the interaction of the light with the vibrational or rotational energy states of the molecules.[12]

In the Raman effect the stokes transition occurs when the energy of the incident photon is greater than that of the scattered photon, generating an excess of energy that results in the creation of a phonon. In contrast, an anti-stokes transition occurs when a phonon is neutralized to compensate the energy difference between the incident photon and the scattered photon.

In general, the Raman spectrum is interpreted as a vibrational spectrum that provides very similar information to the infrared spectroscopy, although the vibrations reflected in Raman are not always the same as in the infrared, as the selection rules of the spectroscopies are different.

Raman spectroscopy was carried out for the structural characterization of the $BiVO_4$ surface in chapter 5. The measurements were performed at the Raman spectroscopy facilities of the SCIC spectroscopy section at University Jaume I. A WiTec apyron system, equipped with a 300 mm focal length UHTS 300 spectrometer system, was used for the measurements. The scanning area of the combined spectra was 40 x 24 m^2 with a laser power of 2 mW and an integration time of 0.5 s.

2.2.2. Analytical techniques

2.2.2.1. Nuclear magnetic resonance spectroscopy (NMR)

Nuclear magnetic resonance (NMR) is the main technique for the determination of molecular structures, whether organic, organometallic or biological molecules.[13] Fundamentally, NMR is based on the nuclear absorbance properties of some atoms to absorb energy when they are subjected to the action of a magnetic field. The intense magnetic fields created by powerful magnets cause the atoms to behave like small dipoles and to orient themselves according to the magnetic field created. The response to the transition between these energetic levels can be detected, amplified and recorded in what would be a spectral line or resonance signal.

In this way, NMR spectra are generated for compounds with non-zero magnetic nuclear moment, among which are the proton (^1H), and others such as ^{13}C, ^{14}N, ^{15}N, ^{19}F, ^{31}P. Once the frequency at which it is worked has been chosen and, therefore, the type of nuclei under study has been selected, the NMR experiments allow to distinguish all and each of the nuclei of the same type that are differentiated only and exclusively by their magnetic environment. Then, the chemical shift (δ) is then defined as the separation between successive spectral lines. Moreover, the spectral lines are not always simple, but as a result of couplings between nuclear spins of

neighboring nuclei, signal splitting occurs and the characteristic lines conform doublets, triplets and so on, which are separated by a characteristic frequency or coupling constant (J).

NMR spectroscopy has been employed for the elemental quantification and detection of organic products and H_2O_2 in chapter 3. NMR spectra were recorded at room temperature on a Bruker 400/300 MHz instrument in possession of the NMR spectroscopy section of SCIC at University Jaume I.

2.2.3. Electrochemical and Photoelectrochemical techniques

Electrochemical (EC) and photoelectrochemical (PEC) measurements are the key tool in the development and the understanding of PEC systems. In these techniques, an electrical signal is introduced into the system and the information is obtained by the analysis of the electrical response generated. From (photo)electrochemical measurements, it is possible to measure from the performance of the PEC system to understanding the properties and mechanisms by which an electron transfer is taking place either in the electrode or in the electrolyte. In the following lines the explanation of the J-V measurements, Chronoamperometries and Impedance Spectroscopy fundamentals as well as the explanation of most relevant measurements performed in this thesis are detailed.

2.2.3.1. PEC design for (photo)electrochemical measurements

Photoelectrochemical measurements were performed in a PEC system, a schematic illustration of PEC system is shown and it involves three parts, as represented in **Figure 4**: (a) a simulated sunlight source; (b) a PEC cell consisted in: a quartz cell, the electrolyte, a working electrode (WE), a counter electrode (CE) and a reference electrode (RE) and (c) a potentiostat station coupled to a computer with the software for data acquisition and analysis. In the case of electrochemical measurements, the working electrode has no light response, for this reason electrochemical measurements only needs the EC cell and the potentiostat station.

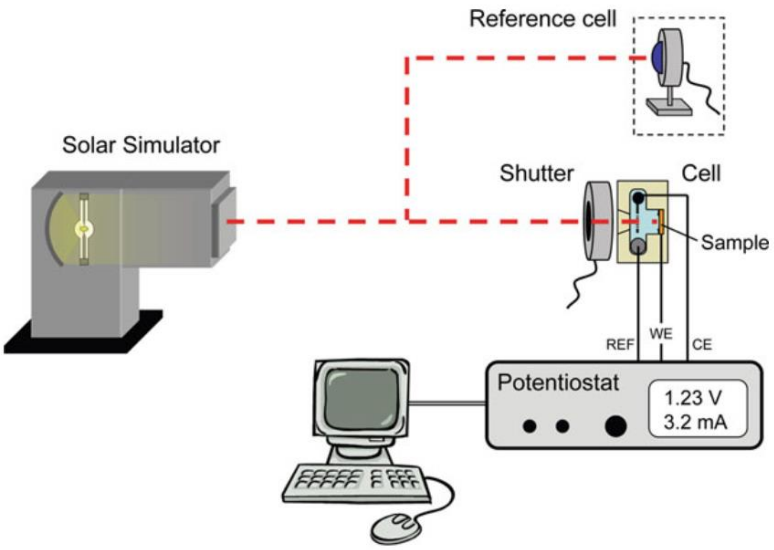

Figure 4. Experimental set up for electrochemical and photoelectrochemical measurements for EC and PEC systems.

a) Simulated sunlight source

Measurements under light illumination need a constant light source, which provide meaningful radiation similarly to real sun spectra. The standard solar spectrum AM1.5G is employed as a reference. It includes ultraviolet (UV), visible and infrared (IR) radiation and it has a total integrated power of 100 $mW \cdot cm^{-2}$ including the direct beam and the diffusion. Frequently, xenon lamps are broadly recognized as illumination source of photoelectrochemical devices as they provide a spectral irradiance similar to sunlight spectra. Some intense emission peaks of xenon lamps at ~764 and ~825 nm could be ignored as they are out of range outside the band gap of metal oxides typically employed for these measurements.

The lamp employed in this thesis is a Xe arc lamp (ozone free) from Newport company. The power of the lamp is 300 W and it has a protection from toxic ozone by suppressing the ultraviolet radiation below 260 nm.

b) EC or PEC cell

The EC or PEC cell is the place where the electrochemical process takes place. In a laboratory scale, it generally consists of a container holding the electrolyte, three electrodes including the working electrode (WE), the counter electrode (CE) and the reference electrode (RE) and external facilities to connect the cables.

A standard electrochemical cell made of quartz is used for photoelectrochemical measurements. Quartz is stable in acid and basic medias and is transparent in the entire range from UV which prevent the absorption of light showed in other materials like glass at 350 nm which could affects the performance of the PEC.

The electrolyte is the liquid media in which the active species are dissolved and also provide a conductive media that ensure the current flow by the cell. Depending on the desired reaction, the electrolyte is chosen to accomplish some specific characteristics, including solubility of the active species, pH and conductivity. In general, a high concentration of supporting electrolyte is essential to avoid ohmic voltage losses in the PEC cell. For this reason, traditionally highly concentrated buffer systems have been employed as electrolytes. Buffer systems, constituted by a redox pair, provide the specific conductivity in the cell as well as avoid local pH fluctuations. However, sometimes the stability of the electrodes is critical in the selection of the electrolytic solution. For example, electrodes containing nickel or iron oxides are commonly active for oxygen evolution reaction at strong alkaline pH (13-14); in contrast, WO_3 and TiO_2 are often used in high acidic solutions for the same reactions.

In the case of organic reactions, the solvent and electrolyte selection becomes more difficult. Additional to the stability of the electrodes, the solubility and the stability of the substrate are two additional parameters to consider. In general, polar solvents have demonstrated a higher reactivity in organic synthesis. Thus, solvents with a high (H_2O) or intermediate (acetonitrile, methanol) polarity are mostly employed for this purpose. However, the employment of H_2O as solvent could compete with the electrochemical oxidation performed in the anode affecting in the formation of undesired products. In addition, organic substrates are unsolvable or partially soluble in water, the incorporation of organic solvents to water or the use of pure organic solvents lead to higher concentration of the substrate in the PEC cell.[14] Regarding the electrolyte in organic solvents, organic salts have been extensible used as they provide high ion mobility and conductivity, chemical inertness towards the cell components and oxidative and reductive stability.[15]

Concerning to the electrodes, the WE and CE are the two electrodes to drive the oxidation and reduction reactions in the PEC cell. Each electrode is alternately named according to the reaction that is considered to be of interest, being WE the electrode of interest and CE the one in charge of performing the reaction in the counter side. In this thesis, oxidation reaction is considered as the main interest and the different considerations for this reaction are widely explained in the different parts of this thesis. Contrary, reaction in CE, where the reduction of H^+ to H_2 takes place, is completed avoiding performance limitations. Thus, the reaction should be fast and the electrode should have an excellent catalytic activity. In this regard, Pt film with a high surface area is an excellent material as it combines good chemical stability with a very small overpotential for hydrogen evolution reaction (HER).

Next, in order to study the electrochemistry in the PEC it is necessary to control the applied potential and ensure that any change in the applied potential is reflected only in the electrochemical properties of the WE. For this reason, it is mandatory to use a reference electrode (RE), which presents negligible potential variations, independently of current fluctuations. There

are a large number of reference electrodes restricted to very specific uses, however because of their simplicity and practicality, silver-based electrodes are mainly used in PEC applications. In the case of aqueous electrolytes, silver/silver chloride electrodes (Ag/AgCl/KCl salt) provide a pH-dependent metric, then in order to be able to compare the measured potentials it must be converted to the reversible hydrogen electrode (V_{RHE}), using the Nernst equation.

$$V_{RHE} = V_{Ag/AgCl} + V^0{}_{Ag/AgCl} + \frac{RT}{nF} \cdot pH \qquad Eq.\ 3$$

Where $V_{Ag/AgCl}$ is the measured potential versus the reference, $V^0{}_{Ag/AgCl}$ is the standard potential of the Ag/AgCl redox couple (at room temperature, $\frac{RT}{nF}$ is 0.0592) and the pH is the one of the electrolyte selected.

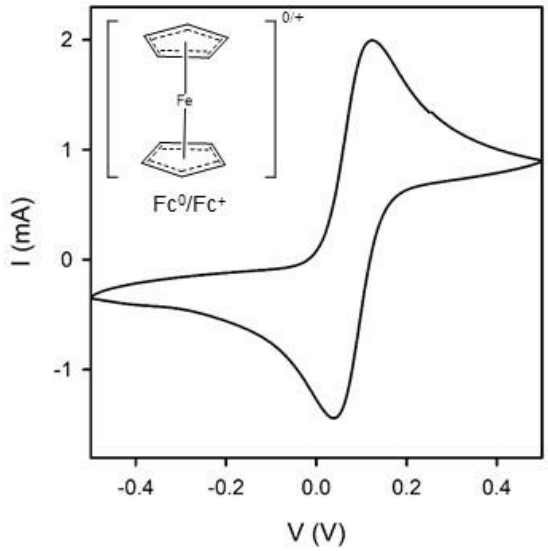

Figure 5. Ferrocene/Ferrocenium (Fc/Fc^+) redox couple as a potential internal reference in organic solvents. Measurement conditions: 1.9mM Ferrocene in 0.1M $TBAClO_4$ in acetonitrile using Pt as WE and CE.

On the other side, when organic or non-aqueous electrolyte is employed, (Ag/Ag^+) electrode provide the RE. This system consists on an Ag wire immersed in $AgNO_3$ and tetrabutylammonium hexafluorophosphate ($TBAPF_6$) salt solution of acetonitrile as organic solvent. The Ag/Ag^+ electrode is a pseudo reference electrode which means that the applied potential could differ depending on the concentration of the Ag^+ as well as the nature and concentration of the supporting salt. With the aim to calibrate the electrode, an internal reference should be incorporated to further specify the applied potential to the redox potential of internal reference compound. Ferrocene/Ferrocenium (Fc/Fc^+) couple is stable and easy to use compound which is soluble in most organic solvents. Moreover, their redox peak it is very characteristic using cyclic voltammetry, see **Figure 5**. For this reason, it is frequently used as an internal reference. The

measured potentials compared to the Fc/Fc^+ redox couple could be converted to the normal hydrogen electrode (NHE).

Finally, external facilities to accommodate the cables are very important when performing electrochemical and photoelectrochemical measurements. These parts are designed to prevent their corrosion during the electrical measurements; therefore, stainless steel is used for this purpose. In general, they allow the direct connection of the PEC with the potentiostat, making possible high quality electrochemical measurements and preventing the appearance of electrical noise.

c) Potentiostat

The potentiostat is the central unit in the electrochemical and photoelectroelectrochemical cells. By employing four leads, WE, CE, RE and sense electrode (S), these apparatus control and measure voltages and currents. In the potentiostat, supplementary modules are required for specific measurements. For example, in impedance spectroscopy it is necessary the incorporation of a module FRA in order to control the small perturbation signal. During this thesis different manufacturers were employed as a potentiostat, including the well know industries: Methrom Autolab, Gamry and Palm Sense. All were equipped with the corresponding FRA module for impedance spectroscopy measurements.

d) Other components in the PEC

In some cases, the photoelectrochemical design could contains other components, which helps in some specific measurements as follows:

Infrared diode laser. It allows steady state photoelectrochemical measurements under infrared radiation as the diode produces continue illumination over the sample. An infrared diode laser (MDLIII-980-2W) from Roithner LaserTechnik (980 nm ± 5 nm, 2 W cw, stability < 5%, beam aperture of 5 x 8 mm^2) was employed in this thesis

Calibrated photodiodes. They are employed to calibrate the white light radiation from the solar simulator. In general, a thermopile was used and it consists in a black body material which is able to convert the incident radiation into heat. The temperature registered in the thermocouples is proportional to the absolute power of the incident light (in $W \cdot cm^{-2}$) and its response covers a wide range of the electromagnetic spectra.

Long pass filter. It is designed to have a sharped transition from reflection to transmission. Then, it is used to cut off the transmission of light below a certain wavelength. The UV long pass filter employed blocks the ultraviolet light (above 365 nm) avoiding the generation of free radicals in mechanistic reaction due to the UV light (**Figure 6**).

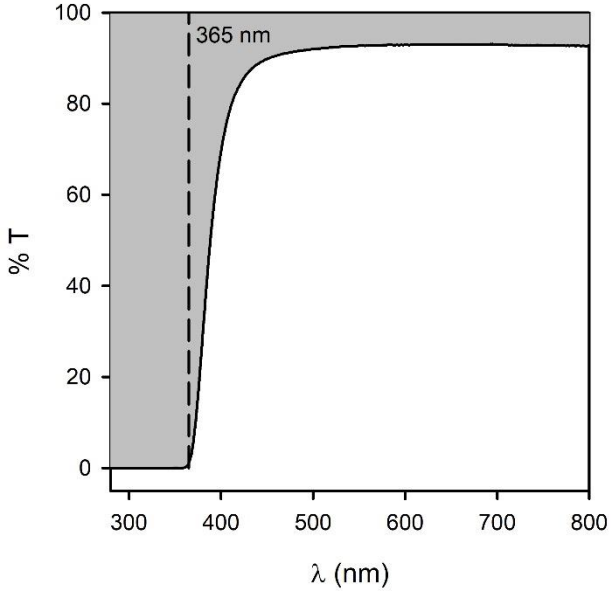

Figure 6. Absorbance spectra of UV long pass filter.

Band pass filters. They are available as colored glass filters and are designed to selectively transmit a portion of the spectrum while discarding all other wavelengths. The band pass filters employed (400 + 475 nm) in **Figure 7** blocks the visible portion in the electromagnetic spectra where the semiconductors absorbs (400-600 nm).

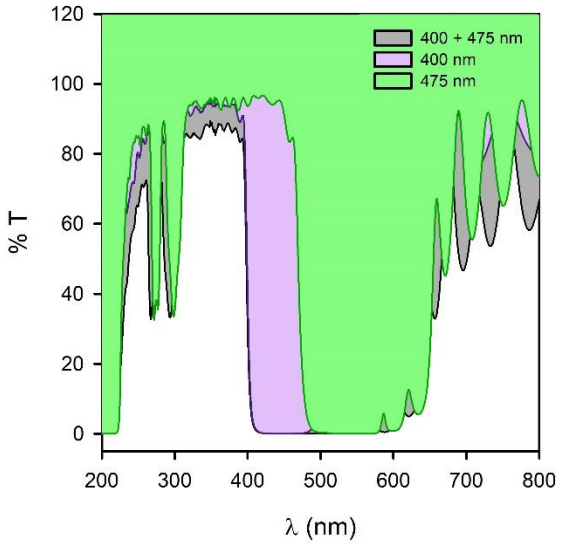

Figure 7. Absorbance spectra of band pass filters.

Faraday cage. Avoiding the electromagnetic interferences produced by any electrical equipment is necessary during the (photo)electrochemical measurements. It helps during the data acquisition, above all, in small perturbation measurements like impedance spectroscopy.

2.2.3.2. Cyclic voltammetry (CV)

Current-voltage measurements offers an optimal relationship between simplicity and operation versatility, and it provides a huge amount of information about the performance characteristics of the electrodes and photoelectrodes for (photo)electrosynthesis.[16,17] Fundamentally, this technique is a potentiodynamic method in which the applied potential (V_{ap}) runs at a constant rate between two potential limit values (V_{max}, V_{min}), following the next equation, where V_o is the initial potential and s is the scan rate ($V \cdot s^{-1}$).

$$V_{ap} = V_o + s \cdot t \qquad Eq.\ 4$$

The response in the electrochemical cell to this potential change affects both the mobility of ionic species in the solution and the interface between the electrode and the solution, resulting in changes in the measured current density.[18] A typical CV response of a commonly studied electrocatalyst and a photoelectrocatalyst upon oxidative potential is presented in **Figure 8**. As shown in the figure, the CV plot is a qualitative measure in which an excellent insight into the performance of different (photo)electrocatalysts measured under the same conditions is obtained. Moreover, parameters such as the onset potential (V_{onset}), the overpotentials at which current density is 10 (η_{10}) and 100 (η_{100}) $mA \cdot cm^{-2}$ and the tafel slope can be obtained by this technique. The estimation of these parameters provide preliminary information about the kinetics and electrochemistry related to the (photo)electrochemical cell performance and serves as comparison with other (photo)electrochemical cells reported in the literature.

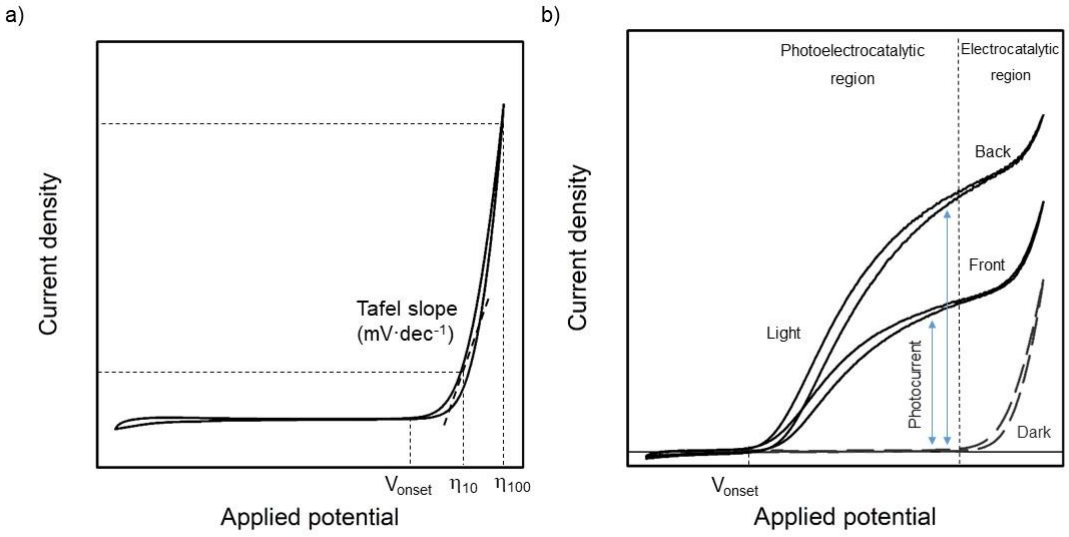

Figure 8. Characteristic current-voltage measurements of (a) an electrocatalyst and (b) a photoelectrocatalyst upon oxidative potential.

In addition, the use of CV measurements in photoelectrochemistry are generally employed to understand the absorption and conversion of sunlight into photocurrent. For this purpose, it is necessary to make measurements in dark and under illumination. The resulting plot represented

in **Figure 8b** provides valuable information relative to the photocurrent including the onset potential at which the photocurrent starts and the saturated photocurrent density for front and back side illumination.

Cyclic voltammetries (CV) are not typically steady state measurements because the measured current density is constantly adapting to the change in the applied potential. When CV is working, two possible contributions to the current density as a function of potential can be measured. Firstly, a capacitive component (j_c) is related with the interface electrode-solution, and it is measured without an electron exchange. By contrast, faradaic contribution (j_f) occurs when there is electron exchange with the electrolyte. Then, the capacitive component has no contribution to faraday processes and it is mandatory reduce for accurate measurement. According to the equation below, j_c is proportional to the scanning rate and therefore its component is minimized at low scanning rates.

$$j_t = j_c + j_f = s \cdot C_d + j_f \qquad \textit{Eq. 5}$$

Therefore, for accurate measurements in which steady state conditions are needed, CV measurements are not the recommended measures. In this case, Impedance Spectroscopy measurements offers the necessary steady state conditions as will be indicated below.

- *Tafel slope*

As mentioned above, in electrocatalysis, the measurement of kinetic experimental parameters allow the understanding of the electrocatalyst from a certain reaction. In these systems, the measurement of the density current is a manifestation of the rate of the interfacial reaction and it is dependent on the applied potential. This relationship could be expressed as a general form according to the Butler-Volmer equation.[16]

$$j = j_o \exp\left(\frac{\alpha_a F \eta}{RT}\right) \qquad \textit{Eq. 6}$$

In this case, j_o is the exchange current density at the equilibrium potential, α_a is the transfer coefficient for the anodic reaction, η is the ovepotential, F the Faraday constant, R is the universal gas constant and T is temperature. If the above current density is expressed in logarithm form, the following equation is obtained.

$$\log(j) = \log(j_o) + {}^{\eta}/_{b} \qquad \textit{Eq. 7}$$

Rearranging equation 8, then a linear relationship between the overpotential and the logarithm of current density is predicted. On this way, the original format of Tafel expression is obtained.

$$\eta = a + b \log(j) \qquad \textit{Eq. 8}$$

From this equation, the tafel slope (b) derived from the representation of η vs log(j) is expressed in units of millivolts (mV) per decade of current density (dec^{-1}) and their significance

possess great relevance in multiple areas such as electrocatalysis, corrosion among others. At its most basic level, it represents the rate of change of current density with the applied potential and low Tafel slope values are highly recognized as an indicator of the effectiveness of electrocatalytic performance.

From a more theoretical background, the elucidation of tafel slopes can be useful for the identification of the possible mechanism leading a reaction. For this purpose, it is necessary to consider the electrocatalytic reaction as a sequence of elementary steps in which one stage is determining the reaction rate. The mechanistic analysis of the elementary steps and the study of rate limiting process predict different tafel slopes and reaction order values.[19]

2.2.3.3. Chronoamperometry

Chronoamperometry is an electrochemical technique that studies the changes in the current response for a specified time in a potentiostatic mode.[16] Normally, at the beginning of the chronoamperometry, an initial potential is applied at which no faradaic processes occur. After a few seconds of stabilization of the sample, a second potential value is applied at which the oxidation/reduction of the species to be analyzed occurs.

The characteristic response of $BiVO_4$ upon experimental chronoamperometry is represented in **Figure 9**. In this graph, the photoelectrochemical oxidation of benzyl alcohol is the faradaic process represented. Initially, the photocurrent response of **Figure 9** shows a period in which the substrate delivery to the electrode is constant and then the conversion of benzyl alcohol is proportional to time. After some time, a current control by diffusion appears and then, the substrate contribution to the electrode is no longer constant and side reactions begin to occur. Finally, when the substrate is depleted or there is no input to the electrode, side reactions become the only reaction at the electrode being responsible of losses in Faraday efficiency.

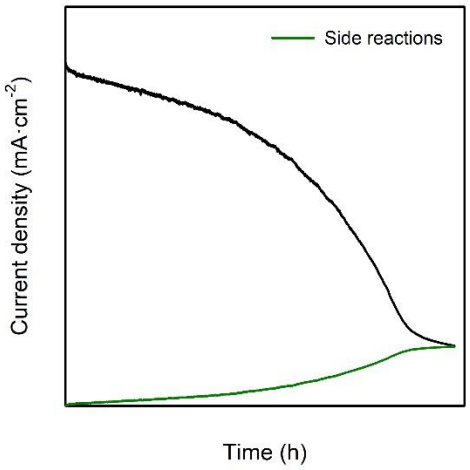

Figure 9. Characteristic chronoamperometry of benzyl alcohol oxidation using $BiVO_4$ electrode as photoanode.

- *Faraday's Laws and Faraday Efficiency*

In electrochemistry, Faraday's Laws are described to quantify the chemical transformations occurred in an interface during an electrocatalytic process.[16] The first law states that the amount of chemical change produced by a current at an electrode-electrolyte interface is proportional to the charge of current used, whereas the second law establishes that the amounts of chemical change produced by the same amount of electricity in different substances are proportional to their equivalent weights. Following these two laws, the equivalent weight of a chemical specie is associated with the gain or loss of an electron and therefore the Faraday expression is obtained.

$$n_i = \frac{Q}{n_e \cdot F} \qquad \textit{Eq. 9}$$

In this equation, n is the number of moles of a specie produced or consumed at the electrode, Q is the total electric charge measured during the electrocatalytic process and F is the equivalent electricity needed to transform 1 mole of electrons (96485 $C \cdot mol^{-1}$).

For the estimation of the Faradaic efficiency, first we employ the Faraday's Laws to estimate the theoretical amount of product converted during the electrolysis. For this purpose, we assume that the number of electrons that are exchanged in the transformation from benzyl alcohol to aldehyde is 2, and carrying out different transformations we obtain:

$$n_t = \frac{Q_T}{n_e \cdot F} = \frac{\int I \cdot t}{2F} = \frac{\sum I \Delta t}{2F} \qquad \textit{Eq. 10}$$

where (n_t) represents the number of moles that theoretically may be converted into a product when a certain charge (Q_T) is injected in the electrode. If we consider the initial moles of the substrate (n_o), the Faraday Yield is given by the ratio between these two amounts and the expression is represented in equation 12.

$$F_{yield} = \frac{n_t}{n_o} \cdot 100 \qquad \textit{Eq. 11}$$

In this expression it is assumed that only one product is formed during the electrolysis. Similarly, the Faraday efficiency can be obtained by the ratio of the real number of moles of the converted product measured by an analytical technique, for instance NMR spectroscopy and the theoretical moles of product converted theoretically (n_t), as follow in the below expression.

$$F_{eff} = \frac{n_{NMR}}{n_t} \cdot 100 \qquad \textit{Eq. 12}$$

2.2.3.4. Impedance Spectroscopy

Impedance spectroscopy (IS) is a powerful and non-destructive technique usually employed in the electrical characterization of energy conversion devices, including the electrochemical and photoelectrochemical systems studied in this work. Generally, IS is especially useful to provide

an integral understanding of the mechanistic operation of electrical devices which lead to identify the causes for efficiency or failure of their electrical response and it can always be ascribed to chemical, physical and mechanical phenomenon produced in the sample during operation.

In this electrochemical approach, the sample is monitored by a small AC signal that is imposed on steady-state electrochemical conditions. For this approach, a small modulated AC voltage is applied on the sample, which is a function of frequency ranges, as defined in Equation 14, from given steady-state conditions of dc voltage $\bar{V}$ and light intensity.

$$\tilde{V} = V_{AC} e^{i\omega t} \qquad \textit{Eq. 13}$$

In this equation V_{AC} is the amplitude of the wave typically (10-20 mV) and the value of frequency ranges (ω) oscillates between the time order of the electrical process generally 1MHz (microseconds) to 10 mHz (seconds).

The output signal in IS is the modulated current response $\tilde{J}(\omega)$ and the ratio of the AC voltage to the output current forms a transfer function which is known as impedance Z ($\Omega \cdot cm^2$), see equation 15. The value of Z is a complex number defined in the frequency domain which gives rise to the DC resistance in the low frequency limit. The small disturbance $\bar{V} \gg \tilde{V}$, is required to obtain a linear impedance meaning Z(ω) independent of the amplitude of the disturbance.

$$Z(\omega) = \frac{\tilde{V}(\omega)}{\tilde{J}(\omega)} \qquad \textit{Eq. 14}$$

The representation of the IS response in the frequency range is usually done according to two different graphs, represented in **Figure 10**. **Figure 10a** is the Nyquist plot where the real impedance (Z') is plotted against the imaginary part of the impedance (Z''). Similarly, **Figure 10b** represents the bode plot, in this case the capacitance modulus is plotted as a function of frequency range. The information contained in the complementary plots are key to the analysis of the IS and their interpretation is analysed by using an appropriate equivalent circuit model (ECM).

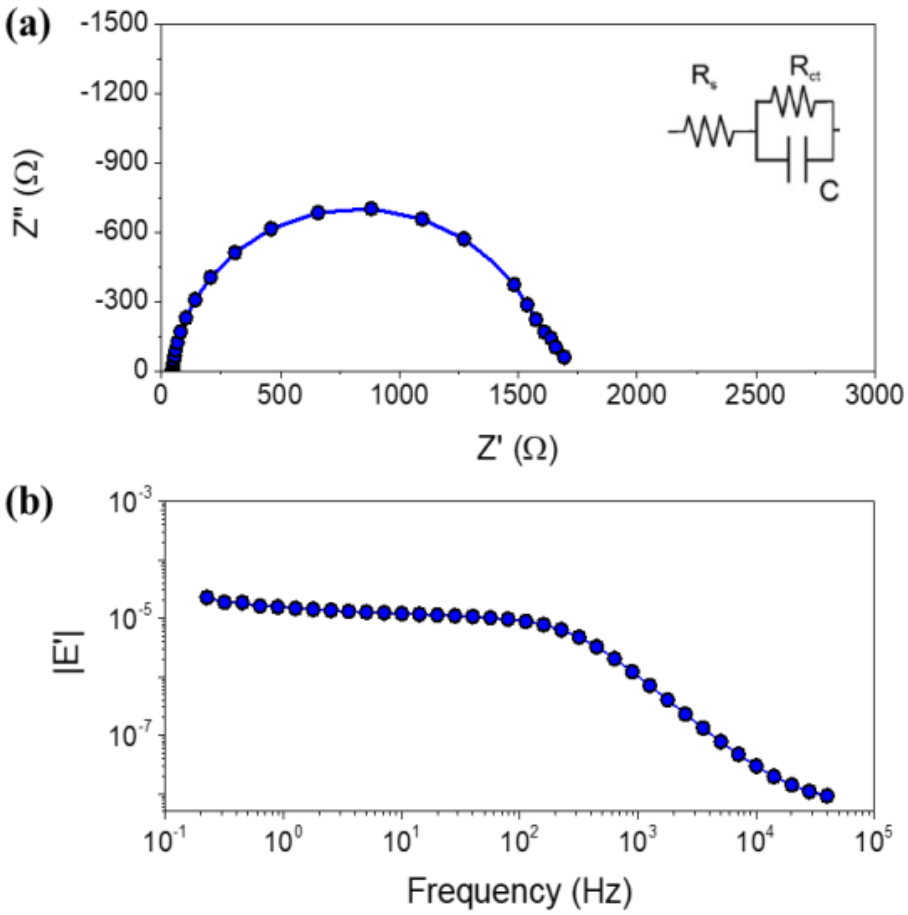

Figure 10. (a) Complex plane of imaginary impedance Z'' versus its real-value counterpart Z' (Nyquist plot) and (b) real part of the capacitance vs frequency (Bode plot) representations of an IS data measurement on a metal oxide photoanode. The inset represent the ECM (randles circuit) used for the fitting of the IS measurement represented.

The elements contained in the ECM have been extensively discussed in the literature, where many different ECMs have been proposed. Broadly summarized, the ECM should include capacitances and resistances to account for the basic electronic processes occurring in the electronic device, including charge accumulation at the electrode-solution interface, surface recombination, and charge transfer to solution. In a theoretical approach, the ECM is transformed into a physico-chemical transport and conservation equation and solved for the frequency dependence condition to give the impedance model. Finally, capacitance identification, as well as resistances, usually proceeds by adapting the compiled data at different voltages to a single EC. As these elements progress through the voltage variations, they provide valuable information on the significance of individual components and the overall characteristics of the system.

References

(1) Tsuji, R.; Masutani, H.; Haruyama, Y.; Niibe, M.; Suzuki, S.; Honda, S. I.; Matsuo, Y.; Heya, A.; Matsuo, N.; Ito, S. Water Electrolysis Using Flame-Annealed Pencil-Graphite Rods. *ACS Sustain. Chem. Eng.* **2019**, *7* (6), 5681–5689.

(2) Wu, Z.; Lu, X. F.; Zang, S.; Wen, X.; Lou, D. Non-Noble-Metal-Based Electrocatalysts toward the Oxygen Evolution Reaction. *Adv. Funct. Mater.* **2020**, *30*, Article ID: 1910274.

(3) Wang, Y.; Chen, Z.; Zhang, M.; Liu, Y.; Luo, H.; Yan, K. Green Fabrication of Nickel-Iron Layered Double Hydroxides Nanosheets Efficient for the Enhanced Capacitive Performance. *Green Energy Environ.* **2022**, *7* (5), 1053–1061.

(4) Tsuji, R.; Koshino, Y.; Masutani, H.; Haruyama, Y.; Niibe, M.; Suzuki, S.; Nakashima, S.; Fujisawa, H.; Ito, S. Water Electrolysis Using Thin Pt and RuO x Catalysts Deposited by a Flame-Annealing Method on Pencil-Lead Graphite-Rod Electrodes. *ACS Omega* **2020**, *5*, 6090–6099.

(5) Seabold, J. A.; Choi, K. S. Efficient and Stable Photo-Oxidation of Water by a Bismuth Vanadate Photoanode Coupled with an Iron Oxyhydroxide Oxygen Evolution Catalyst. *J. Am. Chem. Soc.* **2012**, *134* (4), 2186–2192.

(6) Bunaciu, A. A.; Udriştioiu, E. gabriela; Aboul-Enein, H. Y. X-Ray Diffraction: Instrumentation and Applications. *Anal. Chem.* **2015**, *45* (4), 289–299.

(7) Bragg, W. L. The Specular Reflection of X-Rays. *Nature* **1912**, *90* (2250), 410–410.

(8) Watts, J. F.; Wolstenholme, J. *An Introduction to Surface Analysis by XPS and AES*; Wiley, 2003.

(9) Zhou, W.; Apkarian, R.; Wang, Z. L.; Joy, D. *Fundamentals of Scanning Electron Microscopy (SEM)*; Zhou, W., Wang, Z. L., Eds.; Springer, 2006.

(10) Williams, D. B.; Carter, B. C. *Transmission Electron Microscopy. Part 1: Basics*, Second Edition.; Springer, 2009.

(11) Jones, R. R.; Hooper, D. C.; Zhang, L.; Wolverson, D.; Valev, V. K. Raman Techniques: Fundamentals and Frontiers. *Nanoscale Res. Lett. 2019 141* **2019**, *14* (1), 1–34.

(12) Long, D. A. *The Raman Effect: A Unified Treatment of the Theory of Raman Scattering by Molecules*; Wiley, 2002.

(13) Roberts, J. D. *Nuclear Magnetic Resonance: Applications to Organic Chemistry*; McGraw-Hill Book Company, Inc, 1959.

(14) Reid, L. M.; Li, T.; Cao, Y.; Berlinguette, C. P. Organic Chemistry at Anodes and Photoanodes. *Sustain. Energy Fuels* **2018**, *2* (9), 1905–1927.

(15) Chen, R.; Bresser, D.; Saraf, M.; Gerlach, P.; Balducci, A.; Kunz, S.; Schröder, D.; Passerini, S.; Chen, J. A Comparative Review of Electrolytes for Organic-Material-Based Energy-Storage Devices Employing Solid Electrodes and Redox Fluids. *ChemSusChem* **2020**, *13* (9), 2205.

(16) Lefrou, C.; Fabry, P.; Poignet, J.-C. *Electrochemistry. The Basics, with Examples*; Springer, 2012.

(17) Van De Krol, R.; Grätzel, M. *Photoelectrochemical Hydrogen Production*; Springer, 2012.

(18) Climent, V.; Feliu, J. M. *Encyclopedia of Interfacial Chemistry. Cyclic Voltammetry*; Elsevier, 2018.

(19) Shinagawa, T.; Garcia-Esparza, A. T.; Takanabe, K. Insight on Tafel Slopes from a Microkinetic Analysis of Aqueous Electrocatalysis for Energy Conversion. *Sci. Rep.* **2015**, *5*, 1–21.

3. Publication 1

"Pencil Graphite Rods Decorated with Nickel and Nickel-Iron as Low-Cost Oxygen Evolution Reaction Electrodes"

Ramón Arcas[a]*, Yuuki Koshino[b], Elena Mas-Marzá[a], Ryuki Tsuji[b], Hideaki Masutani[b], Eri Miura-Fujiwara[b], Yuichi Haruyama[c], Seiji Nakashima[d] Seigo Ito[b]* and Francisco Fabregat Santiago[a]*

a. Institute of Advanced Materials (INAM), Universitat Jaume I, 12006 Castelló, Spain.

b. Department of Materials and Synchrotron Radiation Engineering, Graduate School of Engineering, University of Hyogo, 2167 Shosha, Himeji, Hyogo 671-2280, Japan.

c. Laboratory of Advanced Science and Technology for Industry, University of Hyogo, 3-1-2 Kouto, Ako, Hyogo 678-1205, Japan.

d. Department of Electronics and Computer Science, Graduate School of Engineering, University of Hyogo, 2167 Shosha, Himeji, Hyogo 671-2280, Japan.

Sustainable Energy Fuels, 2021, **5**, 3929-3938

3.1. Candidate's contribution

Nature of Contribution	Extent of Contribution
✓ Contribution to the execution of experimental procedures ✓ Design and execution of electrochemical characterization ✓ Contribution to the analysis of results ✓ Figures and manuscript preparation ✓ Writing of the manuscript ✓ Contribution to the corrections on the manuscript according to the reviewer's comments.	70 %

3.2. Published manuscript

"Pencil Graphite Rods Decorated with Nickel and Nickel-Iron as Low-Cost Oxygen Evolution Reaction Electrodes"

Ramón Arcas[a*], Yuuki Koshino[b], Elena Mas-Marzá[a], Ryuki Tsuji[b], Hideaki Masutani[b], Eri Miura-Fujiwara[b], Yuichi Haruyama[c], Seiji Nakashima[d], Seigo Ito[b*] and Francisco Fabregat Santiago[a*]

a. Institute of Advanced Materials (INAM), Universitat Jaume I, 12006 Castelló, Spain

b. Department of Materials and Synchrotron Radiation Engineering, Graduate School of Engineering, University of Hyogo, 2167 Shosha, Himeji, Hyogo 671-2280, Japan

c. Laboratory of Advanced Science and Technology for Industry, University of Hyogo, 3-1-2 Kouto, Ako, Hyogo 678-1205, Japan.

d. Department of Electronics and Computer Science, Graduate School of Engineering, University of Hyogo, 2167 Shosha, Himeji, Hyogo 671-2280, Japan.

E-mail: rarcas@uji.es, itou@eng.u-hyogo.ac.jp, fabresan@uji.es

Abstract

Society is demanding clean energy to substitute the greatly pollutant carbon-based fuels. As an alternative, the green hydrogen produced by electrocatalysis constitutes a nice strategy as its products and reactants are not toxic to the environment. However, the use of scarce materials and the high overpotentials to accomplish the Oxygen Evolution Reaction (OER) make electrocatalysis an uncompetitive process. To solve these challenges, a low-cost procedure for the preparation of earth-abundant Ni, Fe and NiFe decorated electrodes has been developed. For this purpose, Pencil Graphite Rods have been selected as highly porous substrates. A reasonable performance is achieved when they are employed for OER. Furthermore, for the first time, a detailed analysis of Impedance Spectroscopy allows the association of the Ni redox transitions Ni^{2+}/Ni^{3+} and Ni^{3+}/Ni^{4+} (including the identification of the hydrated α-γ and the non-hydrated β phases) with an electrochemical redox capacitance response. Additionally, the Ni^{3+}/Ni^{4+} redox peak capacitance together with a quick decrease in the charge transfer resistance remarks the implication of Ni^{4+} in the OER. These results show the utility of impedance spectroscopy as a non-destructive and non-invasive technique to study in detail of these electrochemical systems in operating conditions.

Table of content

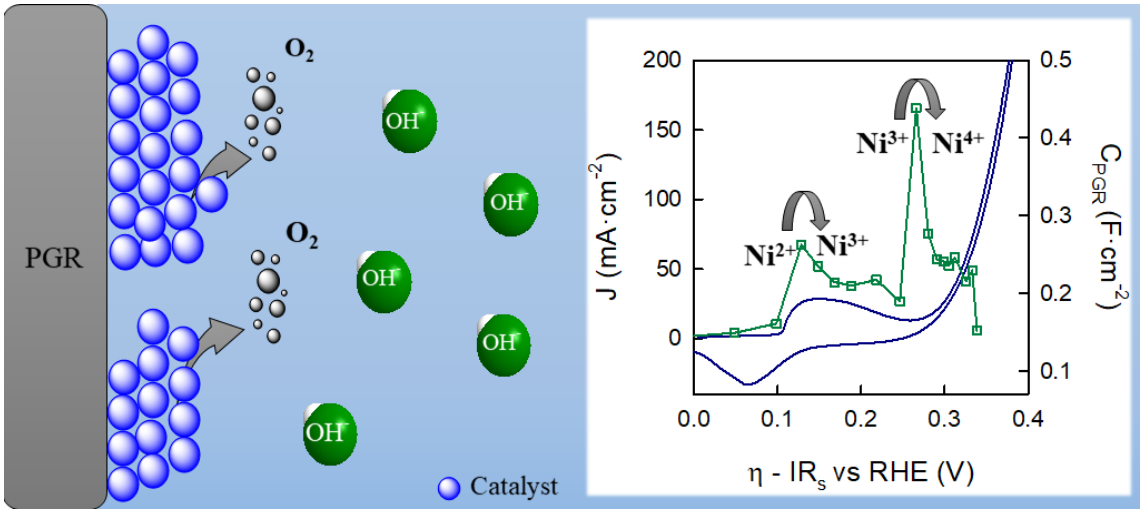

Ni and NiFe decorated Pencil Graphite Rods have good performance for the oxygen evolution reaction. Capacitance data describes the redox processes of Nickel and shows the OER activation after Ni^{4+} formation.

Introduction

Limitations in the use of fossil fuels like oil, carbon or natural gas are one of the main challenges that humanity must face in the next few decades. Dependence of the economy upon cheap energy urges environmentally friendly energy sources to satisfy the continuous growth in energy demand around the world.[1] Renewable energies are increasing their importance in the global share of energy production very quickly, but problems regarding the continuity in their availability still limit their spread to attain a carbon-free society, with an affordable and scalable way of storing the energy needed. One of the lines under development, to make this scenario possible, is focused on the use of molecular hydrogen as an energy storage system. H_2 is not only the most efficient energy source (due to its large energetic power per unit mass) but also one of the greenest technologies as its sub-products, essentially water, have no impact on human health and the environment.[2]

Electrocatalysis is regarded as an appropriate technique to produce pure hydrogen by water splitting.[3] To do this, external electric power is employed which, ideally, may be obtained from natural sources, e.g. solar or wind power.[4] To have an efficient energy conversion, the overpotentials needed to produce the oxygen evolution reaction (OER) and the hydrogen evolution reaction (HER) must be minimized. From a thermodynamic and kinetic point of view, OER is the limiting reaction as it involves four electrons and a bigger overpotential.[5,6] Traditionally, noble metals oxides such as RuO_x, IrO_x, have been employed as anodes due to their high performance for the OER.[7,8] Recently, RuO_x has been deposited on Pencil Graphite Rods (PGR) to obtain high-performance porous electrodes.[9] However, the cost of these noble metals is high as they are not earth-abundant, which makes water splitting an uncompetitive process if using them.[10] In addition, RuO_x catalyst shows low stability in alkaline solutions. In this study, high OER activity was achieved using only inexpensive base metal materials without using expensive precious metal materials.

Earth-abundant Ni-based material has risen as an attractive alternative to noble metal for water oxidation.[11] Among the different Ni electrocatalysts, nickel oxide NiO_x and Ni oxide hydroxide (NiOOH) have attracted great attention mainly due to their efficiency and robustness.[12] Since Corrigan discovered the higher activity and the decrease in the overpotential of OER when Fe is incorporated onto a NiOOH layer,[13] a noteworthy effort has been developed to understand and design new electrodes with better OER performances. Thus, becoming $Ni_{1-x}Fe_xOOH$ layered double hydroxides (LDH) the best catalyst based on earth-abundant materials for water oxidation in alkaline media since today.[14] However, the performance of this material is strongly dependent on different issues, such as the chemical and electronic structure of the electrode, the electrochemical environment, the electrode preparation method, etc.[15–21] It has recently been reported a graphene-nanoplatelets-supported (Ni,Fe) metal–organic framework (MOF) with

outstanding performance for water splitting in alkaline media and high stability.[22] It is well-known that NiFe catalysts are more stable in alkaline aqueous solutions than other noble metal catalysts such as RuO_x. It has been shown that the combination of Ru and Ni, in a compressed metallic Ru-core and oxidized Ru-shell with Ni single atoms (SAs,) led to low overpotentials and high current densities in strong acidic media for water oxidation[23]

In this paper, we study the electrochemical response of pencil graphite rods decorated with nickel and nickel-iron alloys to perform the oxygen evolution reaction. Techniques such as flame annealing (FA) or electrodeposition were used to decorate the PGR obtaining reasonable results for OER. Structural analysis was used to identify oxidation states of nickel and iron contents in the samples while electrochemical measurements allowed us to associate the differences in electrical response of the Ni^{2+}/Ni^{3+} transition to the presence of hydrated and non hydrated phases and to show-up the activation of OER after Ni^{4+} formation.

Experimental section

PGR pre-deposition treatment. Pencil Graphite Rods (4B hardness, 2.0 mm diameter and 13.0 mm length, Mitsubishi Pencil Co., Ltd., Japan) were used as supporting electrode. To control the area of the PGRs, tips were polished with a polishing machine (LaboPol Struers) until the surface was completely flat and homogeneous. PGR have a coating polymer on the surface which makes it stronger. In order to remove this coating, the whole rod was burned for 1 min until it became red because of the heat. This process was repeated 10 times and led to a porous structure of carbon with traces (0.2-0.4 %) of iron as checked by SEM.[9]

Catalyst (co)-deposition on PGR by flame annealing. Flame annealing (FA) deposition was based on the thermal procedure proposed by Tsuji et al.[9] To prepare Ni and Fe decorated PGR rods, a 10 mg/mL precursor solution ($NiCl_2x6H_2O$ for Ni-based electrocatalyst and $FeCl_3x6H_2O$ for Fe-based electrocatalysts) in ethanol was prepared. The thermal treatment process consists of three steps which are 10 times repeated (1) First, the PGR was flame heated until it became red. (2) Immediately, PGR was retired from the flame and two seconds after it was dipped for five seconds into a vial which contained 8 mL of the precursor solution. (3) Finally, flame annealing was applied to the electrode for 20 s. To anneal, the PGR is slid in the direction of the rod axis, then turned 180° to the left and right by hand so that the catalyst can be annealed evenly.

Ni electrodeposition on PG. The electrodeposition (ED) of nickel on PGR electrodes was performed by cyclic voltammetry. A mixture of 0.1 M Na_2SO_4 and 0.02 M $NiCl_2x6H_2O$ in water was used as the electrolyte solution and Ag/AgCl and Pt were used as reference and counter electrode respectively. After PGR pre-deposition treatment, cyclic voltammetries consisted of 25 cycles from -1.2 to 0.2 V vs $V_{Ag/AgCl,}$ with a scan rate of 50 $mV \cdot s^{-1}$ were performed.

Scanning electron microscopy (SEM). The morphological characterization of the samples was performed in a Field Emission Scanning Electron Microscopy performed with a JSM-7000F

JEOL FEG-SEM system (Tokyo, Japan) equipped with an INCA 400 Oxford EDS analyzer (Oxford, U.K.) and operating at 15 kV.

X-ray photoemission spectroscopy (XPS). A photoelectron spectroscopy apparatus installed at a beamline 07B end station of New SUBARU synchrotron radiation facility performed the chemical states and surface characterization by XPS technique. The XPS peaks were fitting by attributing the oxidation state found in the bibliography to the corresponding binding energy. Ni (2p) was adjusted by 6 peaks at 855.5 eV, 856.9 eV, 873.5 eV, and 875 eV, 852.7 eV and 871.4 eV which are attributed to Ni^{2+} (2p3 / 2), Ni^{3+} (2p3 / 2), Ni^{2+} (2p1 / 2), Ni^{2+} (2p1 / 2), Ni^{0} (2p3/2) and Ni^{0} (2p1/2) respectively. Fe (2p) peak was adjusted by 4 peaks at 725,4 eV, 723.5 eV, 714 eV and 711 eV which are attributed to Fe^{3+} (2p3 / 2), Fe^{2+} (2p3 / 2), Fe^{3+} (2p1 / 2), Fe^{2+} (2p1 / 2). O (1s) was adjusted by 5 peaks at 529.4 eV, 530.7 eV, 530 eV, 531.5 eV and 533.3 which are attributed to nickel oxide, nickel hydroxide, iron oxide, C = O and C-O, respectively.

Electrochemical measurements. All the electrochemical measurements were performed on a PGSTAT302N potentiostat (Methrom-Autolab) equipped with a FRA32 Module. The electrochemical performance and electrochemical characterization were carried out by using a homemade polypropylene one-compartment three electrodes electrochemical cell (EC). No corrosion effects were observed on the material after use. In the EC, an aqueous Ag/AgCl electrode was used as a reference electrode and Pt mesh was employed as counter electrode. To ensure high basicity during the experiments 8 M KOH in water was used as electrolyte. Cyclic Voltammetries (CV) were taken at a scan rate of 25 $mV \cdot s^{-1}$. Impedance Spectroscopy (IS) measurements were carried out at selected bias with a perturbation of 20 mV and a frequency range from 1 MHz to 10 mHz. CV and IS measurements are represented as a function of the overpotential: ($\eta = V_{app}$ vs RHE – 1.23 V), and the interfacial overpotential (i.e. the applied potential corrected by the voltage drop at the external series resistances ($\eta - IR_s$).

The CV and IS measurements of the ED@Ni/PGR sample was performed under Fe free KOH electrolyte. The KOH employed in this experiment was treated by following the procedure reported by Boettcher et. al.[24] $Ni(NO_3)_2$ x $6H_2O$ salt was dissolved in high purity KOH 1M solution in order to precipitate $Ni(OH)_2$. Once the salt was precipitated, the solution was centrifugated and the supernatant was decanted. This procedure was repeated three times until $Ni(OH)_2$ was completely pure. Then, the pure $Ni(OH)_2$ was redissolved in high purity 8 M KOH and stirred for 1h. Then, the purified electrolyte was centrifuged and decanted into a polypropylene bottle for their electrochemical use.

Electrochemically Active Surface Area (ECSA). ECSA of PGR was calculated by Impedance Spectroscopy following equation 1.

$$ECSA = \frac{C_{dl}}{C_s} \qquad Eq.\ 1$$

where C_s is the capacitance of a planar glassy carbon microelectrode that was used as reference and C_{dl} stands for the double-layer capacitance of the PGR electrodes (C_{PGR}) obtained at an overpotential of -0.20V *vs* V_{RHE}, where neither redox process nor Faraday current were observed. Both capacitances were normalized to the geometric area of the electrode.

Results and discussion

Pencil Graphite Rods are made up of a graphite structure mixed by a polymer assembly which makes them harder (**Figure 1a**).[9] After a flame annealing (FA) treatment, part of the polymer is removed and the FA@PGR is transformed in a network of branches of crystalline graphite (**Figure 1b**). The space between graphite branches provides the high porosity of the rods. 'Previous data by SEM and BET showed that flame annealing treatment improves the porosity of PGR.[25]

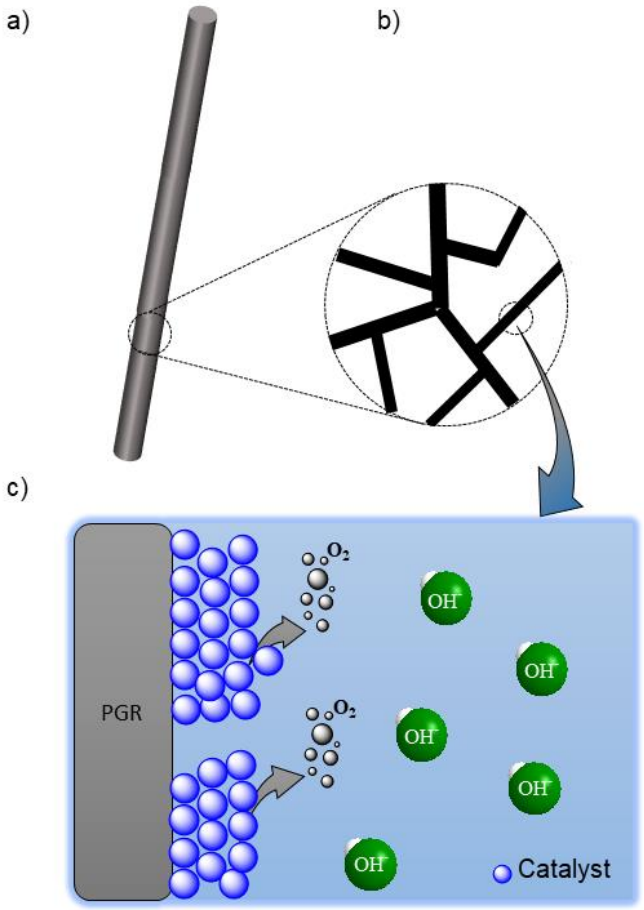

Figure 1. Schematic structure of a) PGR, b) graphite branches, c) detail of graphite branches decorated with catalyst for OER.

We tested FA@PGRs for OER, however, they were not good catalysts by themselves yet. For this reason, in order to improve the performance of PGR, we developed new electrodes by the deposition of Ni and NiFe on the PGR (**Figure 1c**). Ni was deposited following two different methodologies, namely flame annealing (FA) and electrodeposition (ED), obtaining the corresponding electrodes FA@Ni/PGR ED@Ni/PGR (see the experimental section for experimental details). To prepare the PGR decorated with NiFe we followed only the FA procedure (FA@NiFe/PGR).

The morphology and the composition of the decorated PGR were studied by SEM and EDX techniques (see **Figure S1, S2 and S3** in supporting information [SI]). The SEM image of the ED@Ni/PGR sample showed an ordered and homogeneous surface composed of Ni particles of variable size, around 200 nm on top of the PGR. Compared to the ED sample, FA samples present smaller particles on the top of a disordered and non-homogeneous PGR surface. From the microanalysis made at SEM, we could conclude that the amount of Ni deposited by ED is bigger than by FA (see **Figure S1** and **Figure S2** in SI). Moreover, we could also determine the Ni/Fe ratio of each sample. For the FA@NiFe/PGR, the Ni:Fe ratio was ~3:2. In the case of FA@Ni/PGR and ED@Ni/PGR iron was also detected (9:1 and 24:1, respectively). The presence of iron in these two samples was due to contamination of iron of the bare PGR (~0.2%)[9]. The presence of iron, even in small amounts, has implications for the performance of the electrodes as will be explained.

XPS measurements were performed to investigate the chemical environment in the electrodes at the surface level (see **Figure S4** in SI). The analysis of the high resolution XPS spectra and the data fitting of Ni (2p) peak in each sample confirms the non-homogeneity environment of these samples. The Ni (2p) peak in FA@Ni/PGR and FA@NiFe/PGR electrodes show the presence of Ni in two different oxidation states, Ni^{2+} and Ni^{3+}.[26,27] The proportion of each oxidation state was quantify as a function of the peak area (Table S2, SI) and not differences were observed between this two samples. By contrast, Ni (2p) peak in the ED@Ni/PGR sample points to the presence of Ni in the electrode as a mixed phase between metallic and oxidized Ni. The quantification of each state indicates the same concentration of Ni^{2+} species, pointing that ED led to Ni^{0} species instead of Ni^{3+}."

The presence of Fe could be also observed by XPS as a Fe (2p) peak. The presence of Fe in the samples was detected as oxidized state species of Fe^{2+} and Fe^{3+}. This peak was already found for the bare PGR treated by FA (FA@PGR), confirming that impurities of Fe came from the PGR. Additionally, **Figure S4c** shows the high resolution XPS spectra of O (1s) for the electrodes. The presence of C-O interactions either as a double or singlet bond dominates in the sample response.

The differences in the O (1s) spectra in the samples have been attributed to Ni-O and FeO interactions.[28,29]

Electrochemical oxygen evolution reaction on Ni and NiFe PGR.

We performed studies of the performance in the OER of FA@PGR electrodes and the corresponding electrodes decorated with Ni and NiFe (ED@Ni/PGR, FA@Ni/PGR and FA@NiFe/PGR, respectively (**Figure 1c**). These tests were performed with 8 M KOH solution. The reason why the KOH concentration is 8M is that the activity of water electrolysis is higher in a higher concentration of KOH aqueous solution. We sought to obtain higher catalytic activity by testing at a concentration of 8 M KOH higher than 6M. **Figure S5** in supporting information shows the cyclic voltammetry for the oxidation of water using FA@NiFe/PGR in 1M and 8M. It can be observed how the activity and onset for this reaction is improve by increasing the pH of the electrolyte. **Figure 2** shows the cyclic voltammetries and the Tafel plots obtained. For a better analysis of the electrode behaviour, the plots in **Figure 2** have been corrected from potential drop at series resistance.

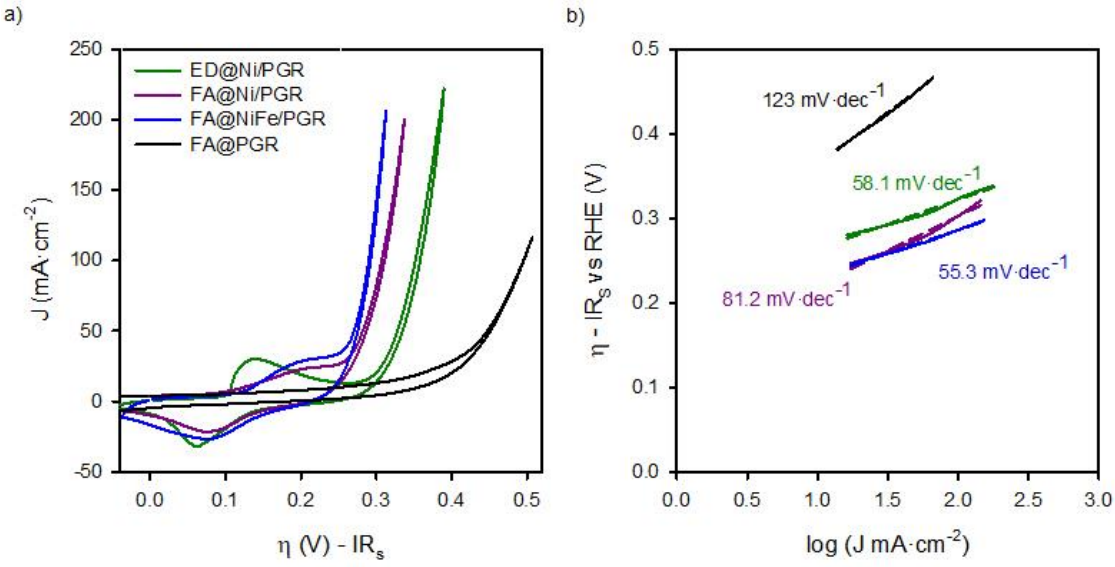

Figure 2. a) Cyclic voltammetries of FA@PGR, ED@Ni/PGR, FA@Ni/PGR and FA@NiFe/PGR and (b) Tafel Plots of FA@PGR, ED@Ni/PGR, FA@Ni/PGR and FA@NiFe/PGR electrodes measured in KOH 8 M. Scan rate: 25 $mV \cdot s^{-1}$. Tafel plots were obtained from J-V curves in stationary conditions.

The analysis of FA@PGR sample in **Figure 2a** shows a hysteretic behaviour in the flat area of the CV. This capacitive behaviour could be associated with the microporous structure of the rods and the ability of carbon to absorb small cations.[30] In the case of the catalyst decorated samples, the hysteresis cannot be clearly observed mainly due to the presence of the $Ni(OH)_2$/NiOOH redox peak, which appears preceding to the region corresponding to OER.

The potential at which the Ni^{2+}/Ni^{3+} redox peak appears, depends on both the Fe content in the catalyst and the Ni phase segregation. It has been reported that the presence of more than 10 % of Fe produces that Ni redox peak appear close to OER. By contrast, lower amount of Fe in the Ni electrode separates both phenomena. Thereby, the Ni redox peak is displaced to lower overpotentials while, at the same time, the OER overpotential is higher.[13,24] In our case, as can be seen in **Figure 2a**, we observe the same trend. Thus, for ED@Ni/PGR with a Ni:Fe ratio of 24:1 (estimated by EDX) the wide redox peak for Ni^{2+}/Ni^{3+} appear at an overpotential of 0.12 V vs RHE in the forward direction (0.08V vs RHE in the reverse direction) with the onset overpotential for the OER occurring at 0.26 V.

Table 1. Overpotential at the current density of 10 $mA \cdot cm^{-2}$ was found in this paper and compared with previous studies. In brackets the value of $n@10mA \cdot cm^{-2}$ after correcting the potential drop at the R_s. Abbreviations: NW (nanowires), EG (Exfoliated Graphene), DG (Doped Graphene), ANHA (Alloy Nanowire Array) and GNP (Graphene-Nanoplatelets).

Catalyst	Electrode Support	Electrolyte	η_{10}@10 mA·cm^{-2} (mV)	References
NiFe	PGR	8 M KOH	252 (240)	this work
Ni	PGR	8 M KOH	290 (270)	this work
RuO_x	PGR	1 M KOH	312	(9)
$Ni_{0.8}Fe_{0.2}$-AHNA	NiFe NW	1 M KOH	180	(14)
NiFe	EG	1 M KOH	214	(31)
NiFe	DG	1 M KOH	310	(32)
NiFe	Ni Foam	1 M KOH	240	(27)
NiFe	Pt	1 M NaOH	340	(33)
NiFe	GNP	1 M KOH	280	(22)
Ni-Ru	RuO_x	0.5M H_2SO_4	184	(23)
Ru	Pt	1 M NaOH	290	(33)

However, for FA samples, FA@Ni/PGR and FA@NiFe/PGR with Ni:Fe ratios 9:1 and 3:2, respectively (see **Figure S2** and **Figure S3** in SI), both the redox peak and the OER onset are so close that the two phenomena approach each other and overlap in the CV. From the steady-state J-V curves of the electrodes in **Figure 5d**, (and **Figure S6d** in SI) we could determine with better

accuracy both the onset of OER and, after substracting the Faradaic contribution, the peaks of the overpotentials of the redox states. Thus, for the two FA samples that have Ni:Fe ratios above 9:1, the same values are obtained for the Ni^{2+}/Ni^{3+} redox peak, ~0.20V vs RHE in forward (and 0.09V in the reverse direction) and for the onset overpotential for OER, 0.22 V vs RHE.

Focusing now on the performance of the electrodes, the interfacial overpotential needed to deliver 10 $mA \cdot cm^2$ (of the geometrical area) is ~270 mV for ED@Ni/PGR and ~ 240 mV for FA@NiFe/PG, see **Table 1** and **Table S1**. These values are in line with the ones reported for NiFe deposited onto graphene and exfoliated graphite as supporting electrode and improve some of the published values shown in **Table 1**.[31,32] Therefore, these materials provide top performance electrodes for OER while keeping an easy and low-cost processing method. We believe that the performance of our electrodes is due to their high surface area and the interaction between Ni and Fe. As can be seen from the data in **Table 1**, there is still room to improve the performance of the electrodes if those are designed to minimize series resistance, including carbon doping to improve its conductivity.

Tafel plots in **Figure 2b** also showed the increase in the OER catalytic activities of PGR by the addition of the catalysts. Furthermore, the decrease of the onset potential observed for the decorated samples vs the bare one, the Tafel slope is reduced ~ 60 $mV \cdot dec^{-1}$ when the catalyst is deposited on top of the PGR, which has a slope 120 $mV \cdot dec^{-1}$ when uncoated. Tafel slopes of 60 $mV \cdot dec^{-1}$ have been associated with proton-coupled electron transfer mechanism for OER.[34]

Impedance Spectroscopy on Ni and NiFe PGRs.

We completed the study of FA@PGR electrodes and the corresponding electrodes decorated with Ni and NiFe (ED@Ni/PGR, FA@Ni/PGR and FA@NiFe/PGR, respectively) by Impedance Spectroscopy (IS) measurements. In order to determine the electrocatalytic active surface area (ECSA) of PGR during the FA, through IS, we compared the capacitance of glassy carbon and PGR at low voltages (-0.2V), where neither redox nor faradaic currents were performed. The resulting ECSA obtained shows a huge increase in the electrocatalytic active area of around 700 and 1000 times in ED and FA samples respectively (**Table S1**), being these ECSA values responsible for the improvement in the OER performance achieved by PGR after FA treatment.

For a better understanding of the performance of Ni and NiFe on PGR electrodes, IS analysis in the area of Ni^{2+}/Ni^{3+} redox peak and the OER onset was performed. **Figure 3** shows the N-quist and bode plot data of FA@PGR and FA@NiFe/PGR obtained at overpotentials before and after OER onset (-0.05 and 0.35V vs RHE). The plots obtained for ED@Ni/PGR are omitted here as their plots have minimum differences with the FA@NiFe/PGR sample. IS shapes are characterized by two features. At high frequencies (**Figure 3b**), a 45º line appears which is followed by an arc at medium-low frequencies. This behaviour is described with a transmission

line in two different situations: (i) when transport resistance (R_t) of electrons in the porous material is smaller than charge transfer resistance (R_{ct}) towards the solution, the transmission line presents the shape obtained at low potentials (**Figure 3**, line black and blue); (ii) in the opposite case, when $R_t > R_{ct}$, the transmission line has the shape shown at high voltages (**Figure 3**, line gray and cyan) which is given by a Gerischer element.[35–38]

The first situation is observed at low potentials when there is no current flow to the electrolyte. In this case, R_{ct} is very large (>> R_{tr}) and the two samples show very similar impedance. When the current flow is activated at higher overpotentials (0.35V vs RHE), R_{ct} becomes smaller than R_{tr} and the arc width (=$[R_{tr} \cdot R_{ct}]^{1/2}$) becomes smaller. The incorporation of the catalysts on the PGRs favours the OER performance, being this effect also observed on the IS measurements by the smaller arc in the NiFe case, indicating a better charge transfer (smaller R_{ct}) for the decorated PGRs.

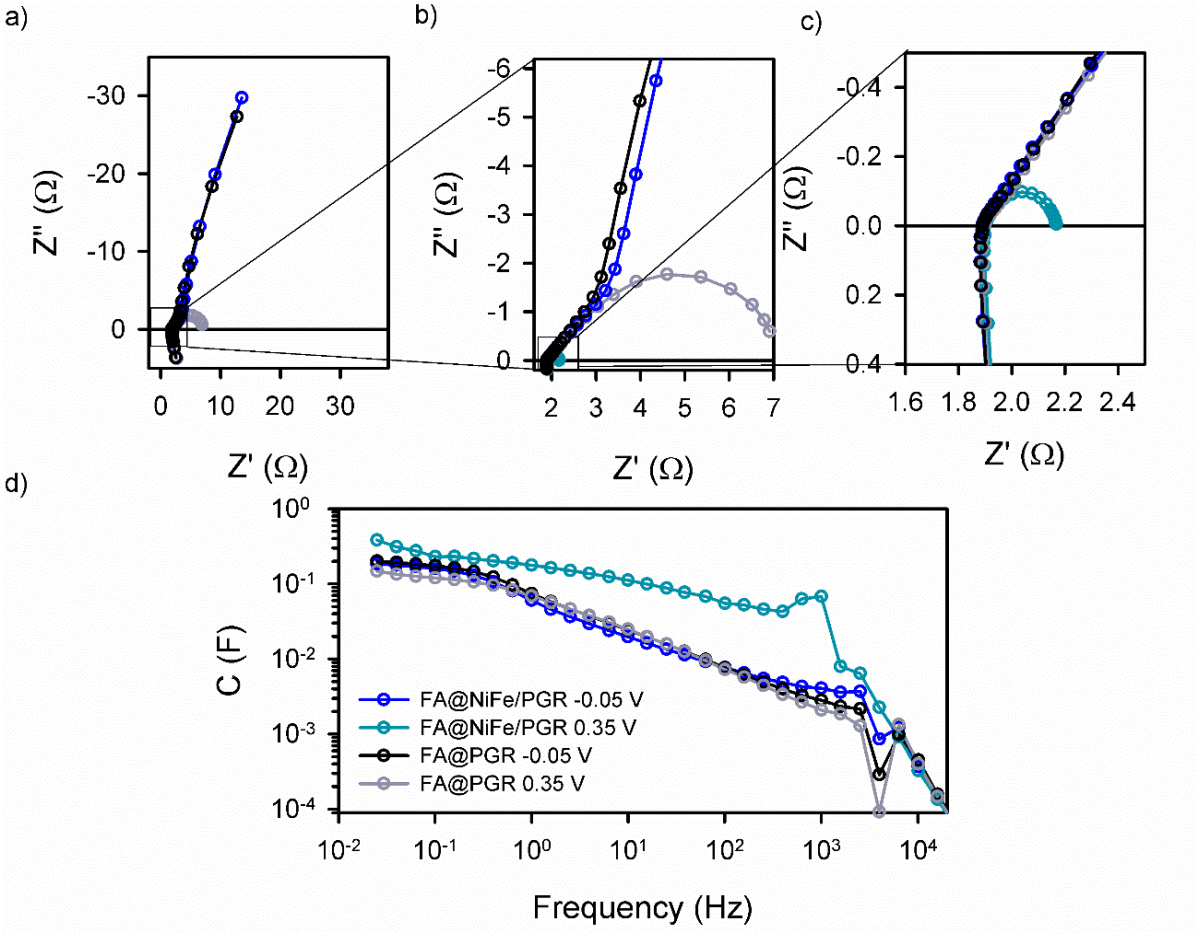

Figure 3. Experimental **(**a), (b) and (c) N-Quist and (d) Ohmic Drop corrected Bode plot obtained by impedance spectroscopy of OER in KOH 8M using FA@NiFe/PGR and FA@PGR as working electrodes. The dark lines show IS at low potential (-0.05 V *vs* RHE) and the light lines at high potential (0.35 V vs RHE).

Detailed analysis of IS measurements at overpotentials between -0.2 and 0.4 V vs RHE was performed by fitting the experimental data with the equivalent circuits (EC) proposed in **Figure 4**. The EC suggested for these porous electrodes consists of a transmission line, where electrons are regularly distributed around the PGR (**Figure 4a**). However, when the metal catalyst is incorporated into the PGR, the electron conduction occurs along the PGR catalyst line, i.e where the catalyst is in contact with the PGR. In this new EC, (**Figure 4b**) a new capacitance is incorporated to describe the OER in the not catalyst covered area.[39] The elements employed in these two EC are described as:

- R_s is the series resistance, which includes the resistance of the carbon rod out of the electrolyte together with the resistances of the bulk of the electrolyte and at the contacts.
- r_{tr} is the electron transport resistance per unit length of the PGR electrode immersed in the electrolyte, which yields a total transport resistance $R_{tr} = r_{tr} \cdot L$
- $r_{ct,G}$ is the charge transfer resistance at the graphite/electrolyte interface. In the case of the ED@Ni/PGR and FA@NiFe/PGR samples, it accounts for the charge transfer at the surface of the PGR which is not coated by the catalyst. At the macroscopic level, the total charge transfer at this interface is given by $R_{ct,G} = r_{ct,G}/L$
- c_G is the capacitance given by the graphite/electrolyte interface. In the case of the decorated samples, it accounts for the uncoated PGR/electrolyte surface. The total capacitance of the graphite is given by $C_G = c_G \cdot L$.
- $r_{ct,cat}$ is the charge transfer resistance associated to Ni or NiFe catalyst. The total contribution to the total charge transfer resistance of the catalyst is given by $R_{ct,cat} = r_{ct,cat}/L$.
- c_{cat} is the capacitance associated to the catalysts (Ni and NiFe) deposited on the PGRs and includes the contribution of their redox states. The total contribution of the catalyst capacitance is given by $C_{cat} = c_{cat} \cdot L$.
- Z_D is the impedance diffusion associated with the reactive species at the diffusion layer in the solution.

With these definitions, the charge transfer resistance and the capacitance of the PGR are given by the parallel combination of the graphite and the catalyst contributions, $R_{ct}^{-1} = R_{ct,cat}^{-1} + R_{ct,G}^{-1}$ and $C_{PGR} = C_{cat} + C_G$, which are the effective values we measure.

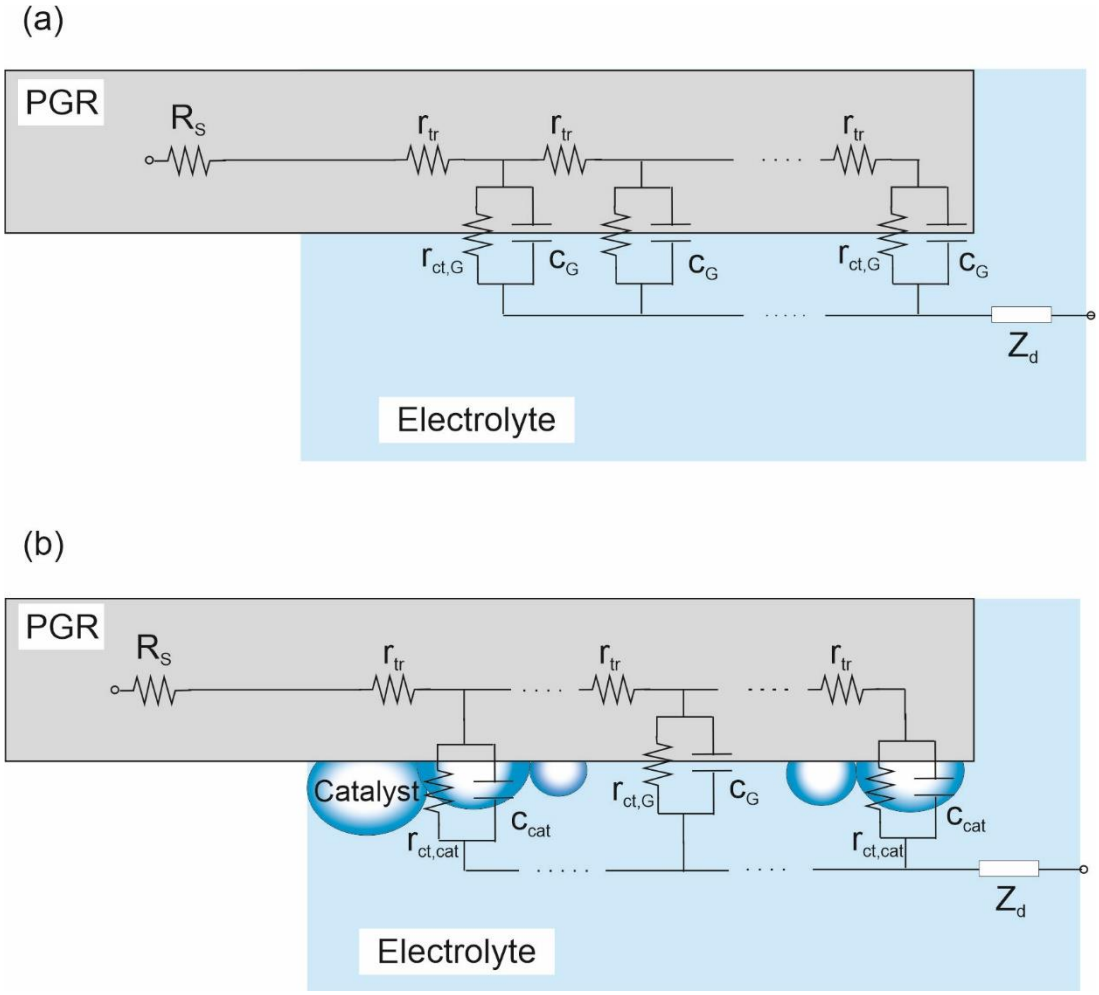

Figure 4. Transmission line based equivalent circuits selected for IS analysis. (a) FA@PGR, (b) ED@Ni/PGR, and FA@NiFe/PGR electrodes. The meaning of the different elements is described in the main text.

When the Ni and NiFe are deposited on the PGR, three capacitance peaks are observed, what suggest a more complex explanation for the peaks observed in the cyclic voltammetry of **Figure 2a**, given above. In fact and according to the literature, the two peaks observed at low overpotentials are attributed to two different Ni^{2+}/Ni^{3+} redox transitions.[40,41] As commented before, the energy of these transitions depends on the Fe content but also to the phase segregation in the sample, which is a function of the deposition environment and the flame annealing treatment.[42] There are two possible phases for $Ni(OH)_2$ molecules present at Ni surface: the β–$Ni(OH)_2$, which is the normal and stable phase and the α–phase, a hydrated form of the nickel hydroxide, $3Ni(OH)_2 \cdot 2H_2O$. The formation of the α–phase is related to the ability of incorporating water between the layers during the nickel deposition on the PGR. We expect that the thermal annealing conducts to a larger proportion of de-hydrated phase while electrodeposition, which is not thermally treated, becomes more hydrated. In any case, α to β conversion phase could happen as a consequence of aging and temperature.[43]

The oxidation of Ni^{2+} to Ni^{3+} by the application of a potential lead to the formation of γ– and β–NiOOH (hydrated and de-hydrated) respectively. According to literature, α–$Ni(OH)_2$ oxidizes to γ–NiOOH (α/γ) at η = 0.12 V (E^0 = 1.35 V vs RHE) and β–$Ni(OH)_2$ oxidizes to β–NiOOH (β/β) at η = 0.20 V (E^0 =1.43 V vs RHE),[43–46] which match very well with the peaks found in the capacitance of the ED@Ni/PGR electrode in **Figure 5a**. This result confirms that the small load of Fe still present in the ED sample, has a minimal effect in the Ni oxidation states, as discussed above. The larger height on the first peak indicates that the α/γ transition is the most important one in this sample and dominates the peak in the CV. The β/β transition also occurs, causing the wide peak measured in the CV curve.

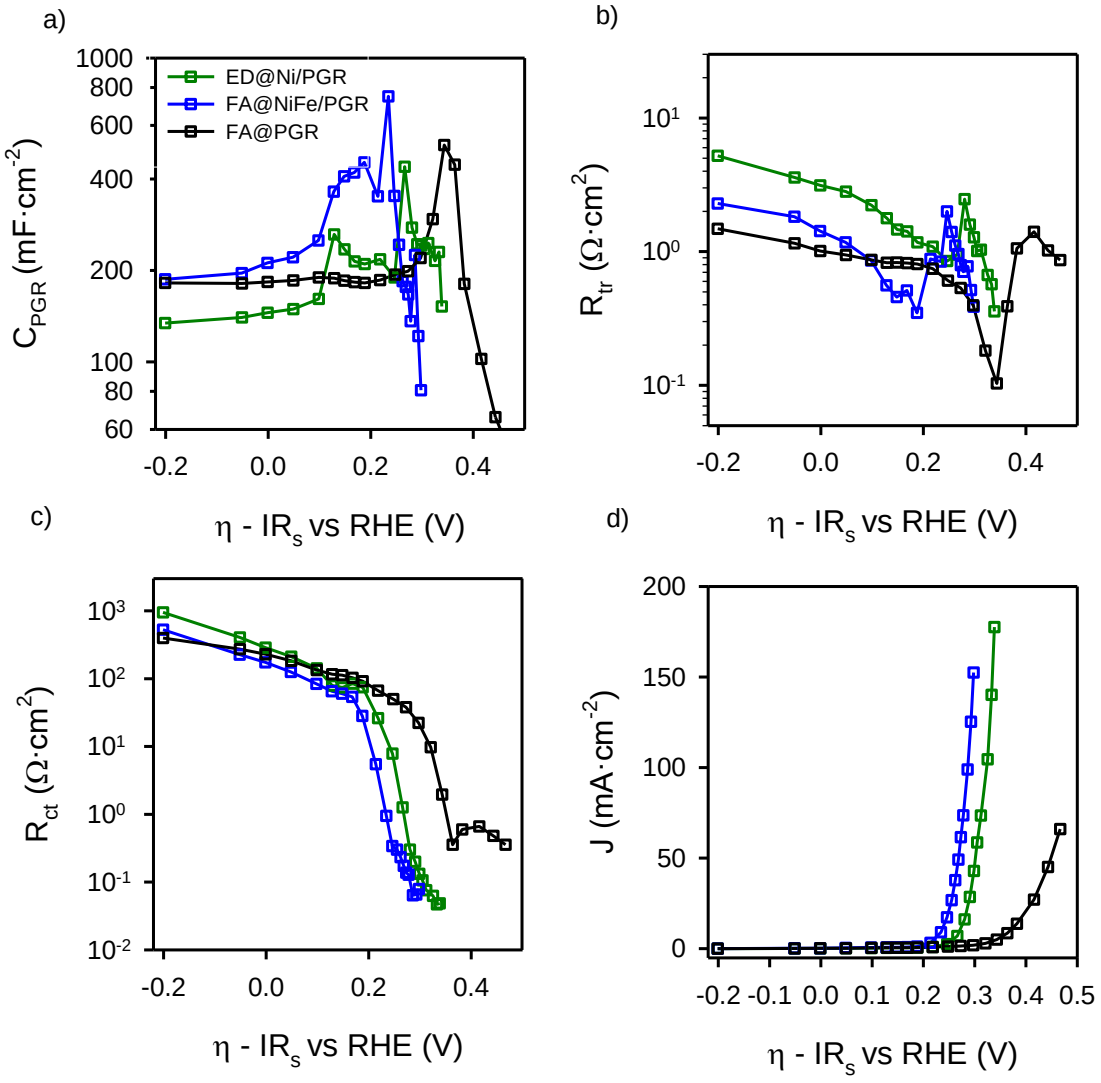

Figure 5. Results from the IS measurements data for FA@PGR(Black), ED@Ni/PGR(Green) and FA@NiFe/PGR(Blue) as a function of the interfacial overpotential (a) Electrode capacitance, (b) *transport* resistance, (c) charge transfer resistance and (d) *J-V curve*.

The third peak, that appears in **Figure 5a** at the overpotential of ~0.26 V (E^0 = 1.49 vs RHE), corresponds to the redox transformation between Ni^{3+}/Ni^{4+},[43,47,48.] which some studies have associated with the formation of $NiOO^-$ after deprotonation of NiOOH.[12] This peak is strongly affected by the iron concentration of the electrode and marks the starting of the quick decrease of R_{ct} observed in **Figure 5c**. R_{ct} is related to the activation of the charge transfer mechanism that yields to the onset of the OER in the CV and the J-V curve in **Figure 2a** and **Figure 5d**, respectively.

For the FA@NiFe/PGR, a clear peak at an overpotential of 0.19 V vs RHE is observed. We associated this peak to the β/β transitions of Ni^{2+}/Ni^{3+} which is much larger than in the case of the ED and slightly displaced to more negative potentials. In this case, the data suggest that the α/γ transition contribution to the capacitance is much smaller than in the ED@Ni/PGR case, and only produces a distortion of the Ni^{2+}/Ni^{3+} peak. Consequently, the peak observed in the CV of **Figure 2** is displaced towards positive values. This result matches well with results obtained in many previous papers.[49,50,51] Therefore, these data suggest that the effect of Fe rather than displacing the Ni^{+3}/Ni^{+2} peaks is favouring the presence of the β phases of Nickel rather than the α/γ.

For the third peak of the capacitance associated with Ni^{3+}/Ni^{4+}, now we see a reduction in the overpotential needed to make the redox transition to the Ni^{3+}/Ni^{4+} which now occurs at 0.23 V, see **Figure 5d**. Consequently, OER activates at an overpotential 30 mV smaller, in good agreement with literature data. Associated with this effect, we can see that the abrupt drop R_{ct} matches very well with the OER activation in the CV (**Figure 5d**). The analysis of R_{ct} shows even more clearly how the onset decrease in R_{ct} is displaced towards smaller overpotentials as we move from the FA@PGR sample to the ED@Ni/PGR and then to the FA@NiFe/PGR, in perfect agreement with the J-V response observed in **Figure 5d**.

Non-electrochemical techniques have been used to correlate the detection of the different Ni phase transitions for $Ni(OH)_2$/NiOOH (α/γ and β/β) and the Ni^{3+}/Ni^{4+} transition with the-electrochemical techniques.[41,45] However, the IS analysis made here have successfully demonstrated for the first time, to our knowledge, the availability of IS for that purpose, being a low cost, easy and useful tool to characterize these kind of samples.

Finally, the transport resistances of FA@NiFe/PGR and FA@PGR present similar values at low voltages, while the ED@Ni/PGR sample presents slightly larger values see **Figure 5b**. This result suggests that larger Fe concentrations produce larger conductivity of the Ni/PGR, but deeper analysis, outside the scope of this paper, is needed to fully understand this behaviour. At the potentials of the Ni^{+2}/Ni^{+3} redox transition, R_{tr} diminishes until a valley is formed, what we associate to the contribution of the redox species to the overall conductivity of the film.

Conclusions

We present herein a low-cost procedure to obtain porous Ni-decorated electrodes based on graphite rods, that provided a reasonable performance. For the study of their electrochemical response, we proposed an impedance model based on a transmission line and made a detailed analysis of the capacitance. This allowed to deconvolute the contributions of α-γ and β-β phases in the Ni^{2+}/Ni^{3+} redox transitions. Through this analysis, we could identify the most prominent phases present in each of the electrodes measured here. Thus, we found that in the electrodeposited sample the predominant phases are α-$Ni(OH)_2$ and γ-NiOOH associated with hydrated Ni, while in the case of the sample with flame annealing treatment, the dominant are the non-hydrated β phases. Rather than the Fe content, the dominant Ni-phase in the electrode is the origin of the position of the Ni^{2+}/Ni^{3+} redox peaks found. Finally, we show the direct relationship between the capacitance peak associated to Ni^{3+}/Ni^{4+} redox transition and the activation of charge transfer resistance and, consequently the oxygen evolution reaction.

Supporting information

ECSA data, SEM, XPS and complementary impedance spectroscopy plots are included in supporting information

Author contributions

YK and RA fabricated the samples and made the measurements, YK and YH made XPS analysis. RA contributed with cyclic voltammetry and impedance spectroscopy analysis. RT, HM and found the improvement attained by NiFe for flame-annealed catalysts. SI provided the initial idea of the paper, completed later by FFS and EMM. FFS made interpretation of impedance spectroscopy data. EMM and FFS directed the experiments done and selected the contents for the paper and RA wrote first version of the paper. All authors revised and improved the paper with their contributions.

Acknowledgements

The authors want to acknowledge the Ministerio de Economía y Competitividad (MINECO) from Spain (ENE2017-85087-C3-1-R), University Jaume I (UJI-B2019-20) and Generalitat Valenciana (PROMETEO/2020/028) for financial support. Serveis Centrals d'Instrumentació Científica from UJI are acknowledged for SEM measurements.

References

(1) Gielen, D.; Miranda, R.; Taibi, E. *Hydrogen: A Renewable Energy Perspective*; Japan, 2019.

(2) Züttel, A.; Remhof, A.; Borgschulte, A.; Friedrichs, O. Hydrogen: The Future Energy Carrier. *Philos. Trans. R. Soc. A Math. Phys. Eng. Sci.* **2010**, *368* (1923), 3329–3342.

(3) Walter, M. G.; Warren, E. L.; McKone, J. R.; Boettcher, S. W.; Mi, Q.; Santori, E. A.; Lewis, N. S. Solar Water Splitting Cells. *Chem. Rev.* **2010**, *110* (11), 6446–6473.

(4) Cardenas-Morcoso, D.; García-Tecedor, M.; Merdzhanova, T.; Smirnov, V.; Finger, F.; Kaiser, B.; Jaegermann, W.; Gimenez, S. An Integrated Photoanode Based on Non-Critical Raw Materials for Robust Solar Water Splitting. *Mater. Adv.* **2020**.

(5) Cook, T. R.; Dogutan, D. K.; Reece, S. Y.; Surendranath, Y.; Teets, T. S.; Nocera, D. G. Solar Energy Supply and Storage for the Legacy and Nonlegacy Worlds. *Chem. Rev.* **2010**, *110* (11), 6474–6502.

(6) Suntivich, J.; May, K. J.; Gasteiger, H. A.; Goodenough, J. B.; Shao-Horn, Y. A Perovskite Oxide Optimized for Oxygen Evolution Catalysis from Molecular Orbital Principles. *Science (80-.).* **2011**, *334* (6061), 1383–1385.

(7) Trasatti, S. Physical Electrochemistry of Ceramic Oxides. *Electrochim. Acta* **1991**, *36* (2), 225–241.

(8) Matsumoto, Y.; Sato, E. Electrocatalytic Properties of Transition Metal Oxides for Oxygen Evolution Reaction. *Mater. Chem. Phys.* **1986**, *14* (5), 397–426.

(9) Tsuji, R.; Koshino, Y.; Masutani, H.; Haruyama, Y.; Niibe, M.; Suzuki, S.; Nakashima, S.; Fujisawa, H.; Ito, S. Water Electrolysis Using Thin Pt and RuO x Catalysts Deposited by a Flame-Annealing Method on Pencil-Lead Graphite-Rod Electrodes. *ACS Omega* **2020**, *5*, 6090–6099.

(10) European Chemical Society. Element Scarcity https://www.euchems.eu/euchems-periodic-table/ (accessed May 15, 2020).

(11) Vij, V.; Sultan, S.; Harzandi, A. M.; Meena, A.; Tiwari, J. N.; Lee, W.-G.; Yoon, T.; Kim, K. S. Nickel-Based Electrocatalysts for Energy-Related Applications: Oxygen Reduction, Oxygen Evolution, and Hydrogen Evolution Reactions. *ACS Catal.* **2017**, *7*, 7196–7225.

(12) Diaz-Morales, O.; Ferrus-Suspedra, D.; Koper, M. T. M. The Importance of Nickel Oxyhydroxide Deprotonation on Its Activity towards Electrochemical Water Oxidation. *Chem. Sci.* **2016**, *7* (4), 2639–2645.

(13) Corrigan, D. A. The Catalysis of the Oxygen Evolution Reaction by Iron Impurities in Thin Film Nickel Oxide Electrodes. *J. Electrochem. Soc.* **1987**, *134* (2), 377.

(14) Liang, C.; Zou, P.; Nairan, A.; Zhang, Y.; Liu, J.; Liu, K.; Kang, F.; Fan, H. J.; Yang, C. Exceptional Performance of Hierarchical Ni–Fe Oxyhydroxide@NiFe Alloy Nanowire Array Electrocatalysts for Large Current Density Water Splitting. *Energy Environ. Sci.* **2020**, *13*, 86–95.

(15) Park, Y. Bin; Kim, J. H.; Jang, Y. J.; Lee, J. H.; Lee, M. H.; Lee, B. J.; Youn, D. H.; Lee, J. S. Exfoliated NiFe Layered Double Hydroxide Cocatalyst for Enhanced Photoelectrochemical Water Oxidation with Hematite Photoanode. *ChemCatChem* **2019**, *11* (1), 443–448.

(16) Hunter, B. M.; Hieringer, W.; Winkler, J. R.; Gray, H. B.; Müller, A. M. Effect of Interlayer Anions on [NiFe]-LDH Nanosheet Water Oxidation Activity. *Energy Environ. Sci.* **2016**, *9* (5), 1734–1743.

(17) Carrasco, J. A.; Sanchis-Gual, R.; Silva, A. S.-D.; Abellán, G. A.; Coronado, E. Influence of the Interlayer Space on the Water Oxidation Performance in a Family of Surfactant-Intercalated NiFe-Layered Double Hydroxides. *Cite This Chem. Mater* **2019**, *31*, 6807.

(18) Gong, M.; Li, Y.; Wang, H.; Liang, Y.; Wu, J. Z.; Zhou, J.; Wang, J.; Regier, T.; Wei, F.; Dai, H. An Advanced Ni−Fe Layered Double Hydroxide Electrocatalyst for Water Oxidation. *J. Am. Chem. Soc* **2013**, *135*, 8455.

(19) Long, X.; Li, J.; Xiao, S.; Yan, K.; Wang, Z.; Chen, H.; Yang, S. A Strongly Coupled Graphene and FeNi Double Hydroxide Hybrid as an Excellent Electrocatalyst for the Oxygen Evolution Reaction. *Angew. Chemie Int. Ed.* **2014**, *53* (29), 7584–7588.

(20) Tang, D.; Liu, J.; Wu, X.; Liu, R.; Han, X.; Han, Y.; Huang, H.; Liu, Y.; Kang, Z. Carbon Quantum Dot/NiFe Layered Double-Hydroxide Composite as a Highly Efficient Electrocatalyst for Water Oxidation. *ACS Appl. Mater. Interfaces* **2014**, *6*, 7918–7925.

(21) Lu, Z.; Xu, W.; Zhu, W.; Yang, Q.; Lei, X.; Liu, J.; Li, Y.; Sun, X.; Duan, X. Three-Dimensional NiFe Layered Double Hydroxide Film for High-Efficiency Oxygen Evolution Reaction. *Chem. Commun* **2014**, *50*, 6479.

(22) Thangavel, P.; Ha, M.; Kumaraguru, S.; Meena, A.; Singh, A. N.; Harzandi, A. M.; Kim, K. S. Graphene-Nanoplatelets-Supported NiFe-MOF: High-Efficiency and Ultra-Stable Oxygen Electrodes for Sustained Alkaline Anion Exchange Membrane Water Electrolysis. *Energy Environ. Sci.* **2020**, *13* (10), 3447–3458.

(23) Harzandi, A. M.; Shadman, S.; Nissimagoudar, A. S.; Kim, D. Y.; Lim, H. D.; Lee, J. H.; Kim, M. G.; Jeong, H. Y.; Kim, Y.; Kim, K. S. Ruthenium Core–Shell Engineering with Nickel Single Atoms for Selective Oxygen Evolution via Nondestructive Mechanism. *Adv. Energy Mater.* **2021**, *11* (10), 1–12.

(24) Trotochaud, L.; Young, S. L.; Ranney, J. K.; Boettcher, S. W. Nickel-Iron Oxyhydroxide Oxygen-Evolution Electrocatalysts: The Role of Intentional and Incidental Iron Incorporation. *J. Am. Chem. Soc.* **2014**, *136* (18), 6744–6753.

(25) Tsuji, R.; Masutani, H.; Haruyama, Y.; Niibe, M.; Suzuki, S.; Honda, S. I.; Matsuo, Y.; Heya, A.; Matsuo, N.; Ito, S. Water Electrolysis Using Flame-Annealed Pencil-Graphite Rods. *ACS Sustain. Chem. Eng.* **2019**, *7* (6), 5681–5689.

(26) Dubey, P.; Kaurav, N.; Devan, R. S.; Okram, G. S.; Kuo, Y. K. The Effect of Stoichiometry on the Structural, Thermal and Electronic Properties of Thermally Decomposed Nickel Oxide. *RSC Adv.* **2018**, *8* (11), 5882–5890.

(27) Song, Q.; Zhai, X.; Yu, F.; Li, J.; Ren, X.; Zhang, H.; Zhu, M.; Dai, B.; Ge, G.; Zhang, J. Defect-Rich Nickel Nanoparticles Supported on SiC Derived from Silica Fume with Enhanced Catalytic Performance for CO Methanation. *Catalysts* **2019**, *9* (3), 295.

(28) Wright, K.; Barron, A. Catalyst Residue and Oxygen Species Inhibition of the Formation of Hexahapto-Metal Complexes of Group 6 Metals on Single-Walled Carbon Nanotubes. *C* **2017**, *3* (4), 17.

(29) Xiong, D.; Li, W.; Liu, L. Vertically Aligned Porous Nickel(II) Hydroxide Nanosheets Supported on Carbon Paper with Long-Term Oxygen Evolution Performance. *Chem. - An Asian J.* **2017**, *12* (5), 543–551.

(30) Guo, Y.; Smith, R. B.; Yu, Z.; Efetov, D. K.; Wang, J.; Kim, P.; Bazant, M. Z.; Brus, L. E. Li Intercalation into Graphite: Direct Optical Imaging and Cahn-Hilliard Reaction Dynamics. *J. Phys. Chem. Lett.* **2016**, *7* (11), 2151–2156.

(31) Ye, Y. J.; Zhang, N.; Liu, X. X. Amorphous NiFe(Oxy)Hydroxide Nanosheet Integrated Partially Exfoliated Graphite Foil for High Efficiency Oxygen Evolution Reaction. *J.*

Mater. Chem. A **2017**, *5* (46), 24208–24216.

(32) Wang, J.; Gan, L.; Zhang, W.; Peng, Y.; Yu, H.; Yan, Q.; Xia, X.; Wang, X. In Situ Formation of Molecular Ni-Fe Active Sites on Heteroatom-Doped Graphene as a Heterogeneous Electrocatalyst toward Oxygen Evolution. *Sci. Adv.* **2018**, *4* (March), Article ID: 3.

(33) McCrory, C. C. L.; Jung, S.; Ferrer, I. M.; Chatman, S. M.; Peters, J. C.; Jaramillo, T. F. Benchmarking Hydrogen Evolving Reaction and Oxygen Evolving Reaction Electrocatalysts for Solar Water Splitting Devices. *J. Am. Chem. Soc.* **2015**, *137* (13), 4347–4357.

(34) Joya, K. S.; Sinatra, L.; Abdulhalim, L. G.; Joshi, C. P.; Hedhili, M. N.; Bakr, O. M.; Hussain, I. Atomically Monodisperse Nickel Nanoclusters as Highly Active Electrocatalysts for Water Oxidation. *Nanoscale* **2016**, *8* (18), 9695–9703.

(35) Gimenez, S.; Dunn, H. K.; Rodenas, P.; Fabregat-Santiago, F.; Miralles, S. G.; Barea, E. M.; Trevisan, R.; Guerrero, A.; Bisquert, J. Carrier Density and Interfacial Kinetics of Mesoporous TiO2 in Aqueous Electrolyte Determined by Impedance Spectroscopy. *J. Electroanal. Chem.* **2012**, *668*, 119–125.

(36) Fabregat-Santiago, F.; Bisquert, J.; Garcia-Belmonte, G.; Boschloo, G.; Hagfeldt, A. Influence of Electrolyte in Transport and Recombination in Dye-Sensitized Solar Cells Studied by Impedance Spectroscopy. *Sol. Energy Mater. Sol. Cells* **2005**, *87* (1–4), 117–131.

(37) Bisquert, J. Influence of the Boundaries in the Impedance of Porous Film Electrodes. *Phys. Chem. Chem. Phys.* **2000**, *2*, 4185–4192.

(38) Bisquert, J.; Grätzel, M.; Wang, Q.; Fabregat-Santiago, F. Three-Channel Transmission Line Impedance Model for Mesoscopic Oxide Electrodes Functionalized with a Conductive Coating. *J. Phys. Chem. B* **2006**, *110* (23), 11284–11290.

(39) Helmenstine, A. M. Table of Electrical Resistivity and Conductivity https://www.thoughtco.com/table-of-electrical-resistivity-conductivity-608499 (accessed Jul 1, 2020).

(40) Corby, S.; Tecedor, M. G.; Tengeler, S.; Steinert, C.; Moss, B.; Mesa, C. A.; Heiba, H. F.; Wilson, A. A.; Kaiser, B.; Jaegermann, W.; et al. Separating Bulk and Surface Processes in NiOxelectrocatalysts for Water Oxidation. *Sustain. Energy Fuels* **2020**, *4* (10), 5024–

5030.

(41) Francàs, L.; Corby, S.; Selim, S.; Lee, D.; Mesa, C. A.; Godin, R.; Pastor, E.; Stephens, I. E. L.; Choi, K. S.; Durrant, J. R. Spectroelectrochemical Study of Water Oxidation on Nickel and Iron Oxyhydroxide Electrocatalysts. *Nat. Commun.* **2019**, *10* (1), 1–10.

(42) Bernard, M. C.; Bernard, P.; Keddam, M.; Senyarich, S.; Takenouti, H. Characterisation of New Nickel Hydroxides during the Transformation of α Ni(OH)2 to β Ni(OH)2 by Ageing. *Electrochim. Acta* **1996**, *41* (1), 91–93.

(43) Klaus, S.; Cai, Y.; Louie, M. W.; Trotochaud, L.; Bell, A. T. Effects of Fe Electrolyte Impurities on Ni(OH)2/NiOOH Structure and Oxygen Evolution Activity. *J. Phys. Chem. C* **2015**, *119*, 7243–7254.

(44) Juodkazis, K.; Juodkazytė, J.; Vilkauskaitė, R.; Jasulaitienė, V. Nickel Surface Anodic Oxidation and Electrocatalysis of Oxygen Evolution. *J. Solid State Electrochem.* **2008**, *12* (11), 1469–1479.

(45) Trzešniewski, B. J.; Diaz-Morales, O.; Vermaas, D. A.; Longo, A.; Bras, W.; Koper, M. T. M.; Smith, W. A. In Situ Observation of Active Oxygen Species in Fe-Containing Ni-Based Oxygen Evolution Catalysts: The Effect of PH on Electrochemical Activity. *J. Am. Chem. Soc.* **2015**, *137* (48), 15112–15121.

(46) Yeo, B. S.; Bell, A. T. In Situ Raman Study of Nickel Oxide and Gold-Supported Nickel Oxide Catalysts for the Electrochemical Evolution of Oxygen. *J. Phys. Chem. C* **2012**, *116* (15), 8394–8400.

(47) Marrani, A. G.; Novelli, V.; Sheehan, S.; Dowling, D. P.; Dini, D. Probing the Redox States at the Surface of Electroactive Nanoporous NiO Thin Films. *ACS Appl. Mater. Interfaces* **2014**, *6*, 8.

(48) Huang, J.; Li, Y.; Zhang, Y.; Rao, G.; Wu, C.; Hu, Y.; Wang, X.; Lu, R.; Li, Y.; Xiong, J. Identification of Key Reversible Intermediates in Self-Reconstructed Nickel-Based Hybrid Electrocatalysts for Oxygen Evolution. *Angew. Chemie Int. Ed.* **2019**, *58* (48), 17458–17464.

(49) Cappadonia, M.; Divisek, J.; Von Der Heyden, T.; Stimming, U. Oxygen Evolution Reaction at Nickel Anodes in Concentrated Alkaline Solution. *Electrochim. Acta* **1994**, *39*, 1559–1564.

(50) Louie, M. W.; Bell, A. T. An Investigation of Thin-Film Ni-Fe Oxide Catalysts for the Electrochemical Evolution of Oxygen. *J. Am. Chem. Soc.* **2013**, *135* (33), 12329–12337.

(51) Zhou, Y.; López, N. The Role of Fe Species on NiOOH in Oxygen Evolution Reactions. *ACS Catal.* **2020**, *10* (11), 6254–6261.

3.3. Supporting information

"Pencil Graphite Rods Decorated with Nickel and Nickel-Iron as Low-Cost Oxygen Evolution Reaction Electrodes"

Ramón Arcas[a*], Yuuki Koshino[b], Elena Mas-Marzá[a], Ryuki Tsuji[b], Hideaki Masutani[b], Eri Miura-Fujiwara[b], Yuichi Haruyama[c], Seiji Nakashima[d], Seigo Ito[b*] and Francisco Fabregat Santiago[a*]

a. Institute of Advanced Materials (INAM), Universitat Jaume I, 12006 Castelló, Spain
b. Department of Materials and Synchrotron Radiation Engineering, Graduate School of Engineering, University of Hyogo, 2167 Shosha, Himeji, Hyogo 671-2280, Japan
c. Laboratory of Advanced Science and Technology for Industry, University of Hyogo, 3-1-2 Kouto, Ako, Hyogo 678-1205, Japan.
d. Department of Electronics and Computer Science, Graduate School of Engineering, University of Hyogo, 2167 Shosha, Himeji, Hyogo 671-2280, Japan.

Table 1. ECSA and overpotential referred to RHE data for the different samples studied. In brackets the value of the interfacial overpotential, i.e. after subtracting the potential drop at series resistance.

Electrode	C_{dl}@-0.05V (mF·cm^{-2})	ECSA	R_s (Ω)	η (η – IR_S) @10 mA·cm^{-2} (mV)	η (η – IR_S) @100 mA·cm^{-2} (mV)
ED@Ni/PGR	134	768	1.8	290 (270)	380 (325)
FA@Ni/PGR	191	1093	2.5	252 (240)	440 (300)
FA@NiFe/PGR	186	1071	2.5	250 (240)	450 (290)
FA@PGR	182	1042	1.9	400 (370)	620 (500)
Glassy Carbon	0.174	1	-	-	-

SEM and EDX analysis

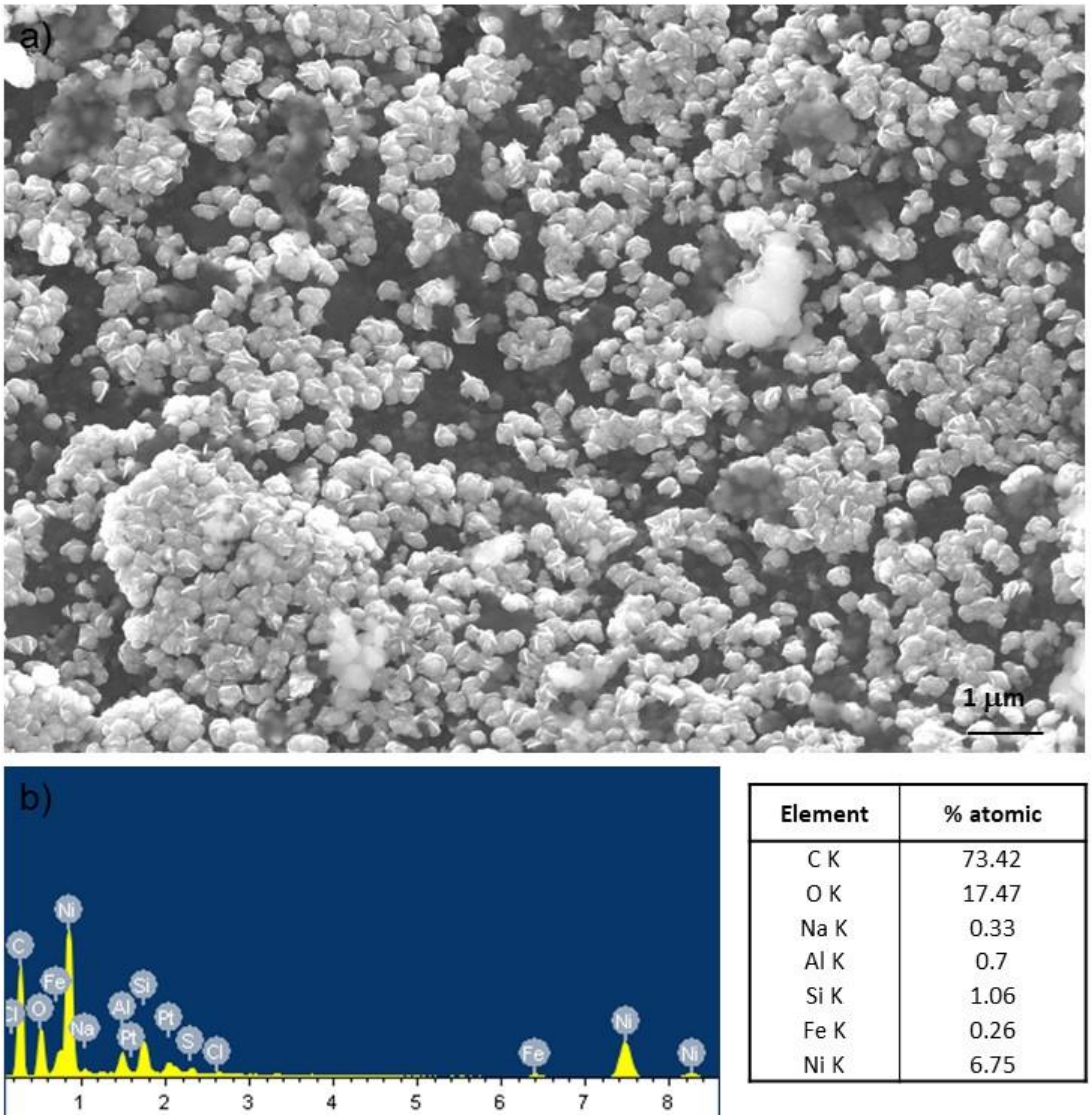

Element	% atomic
C K	73.42
O K	17.47
Na K	0.33
Al K	0.7
Si K	1.06
Fe K	0.26
Ni K	6.75

Figure S1. a) SEM and b) EDX analysis of ED@Ni/PGR.

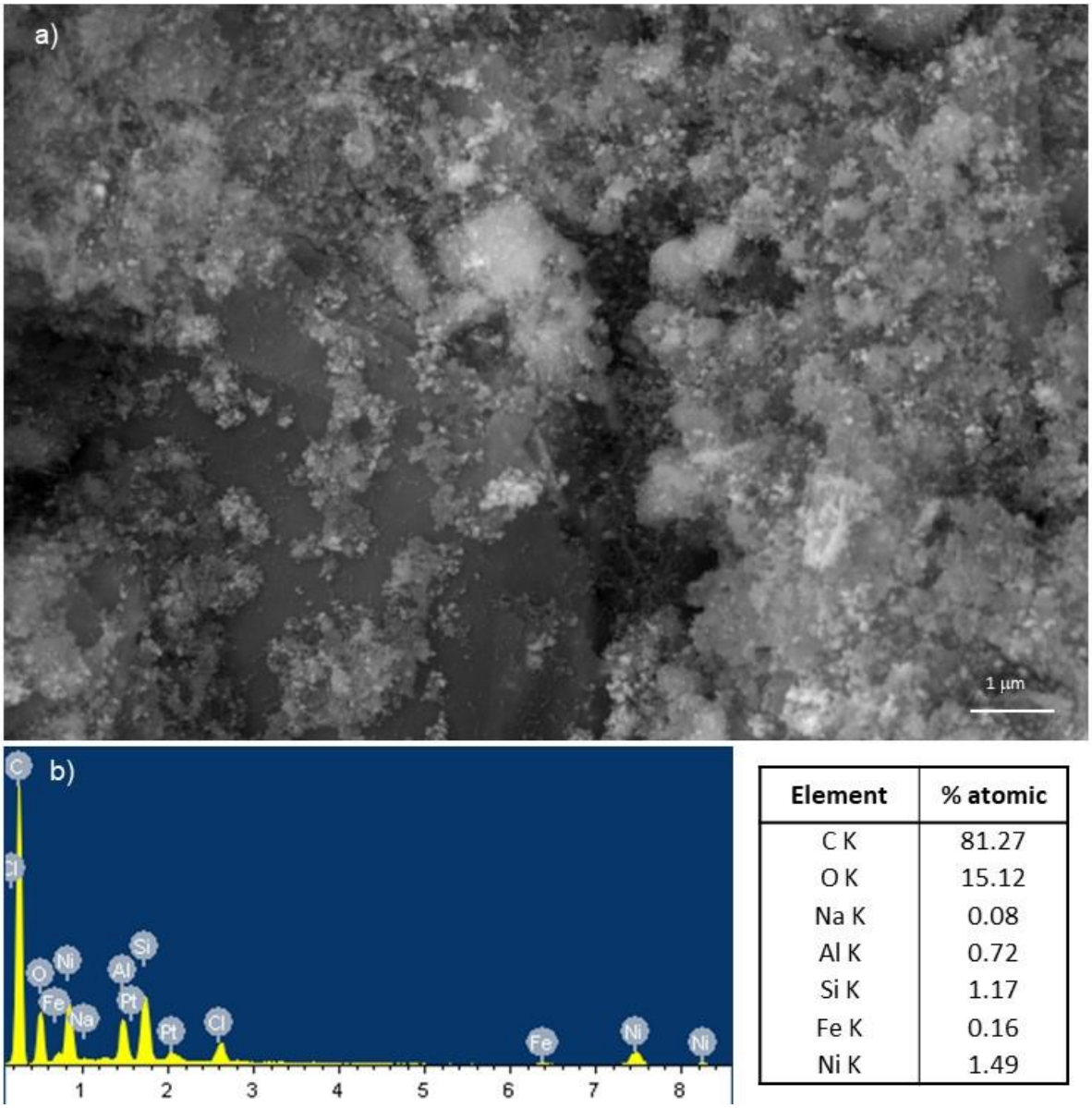

Element	% atomic
C K	81.27
O K	15.12
Na K	0.08
Al K	0.72
Si K	1.17
Fe K	0.16
Ni K	1.49

Figure S2. a) SEM and b) EDX analysis of FA@Ni/PGR.

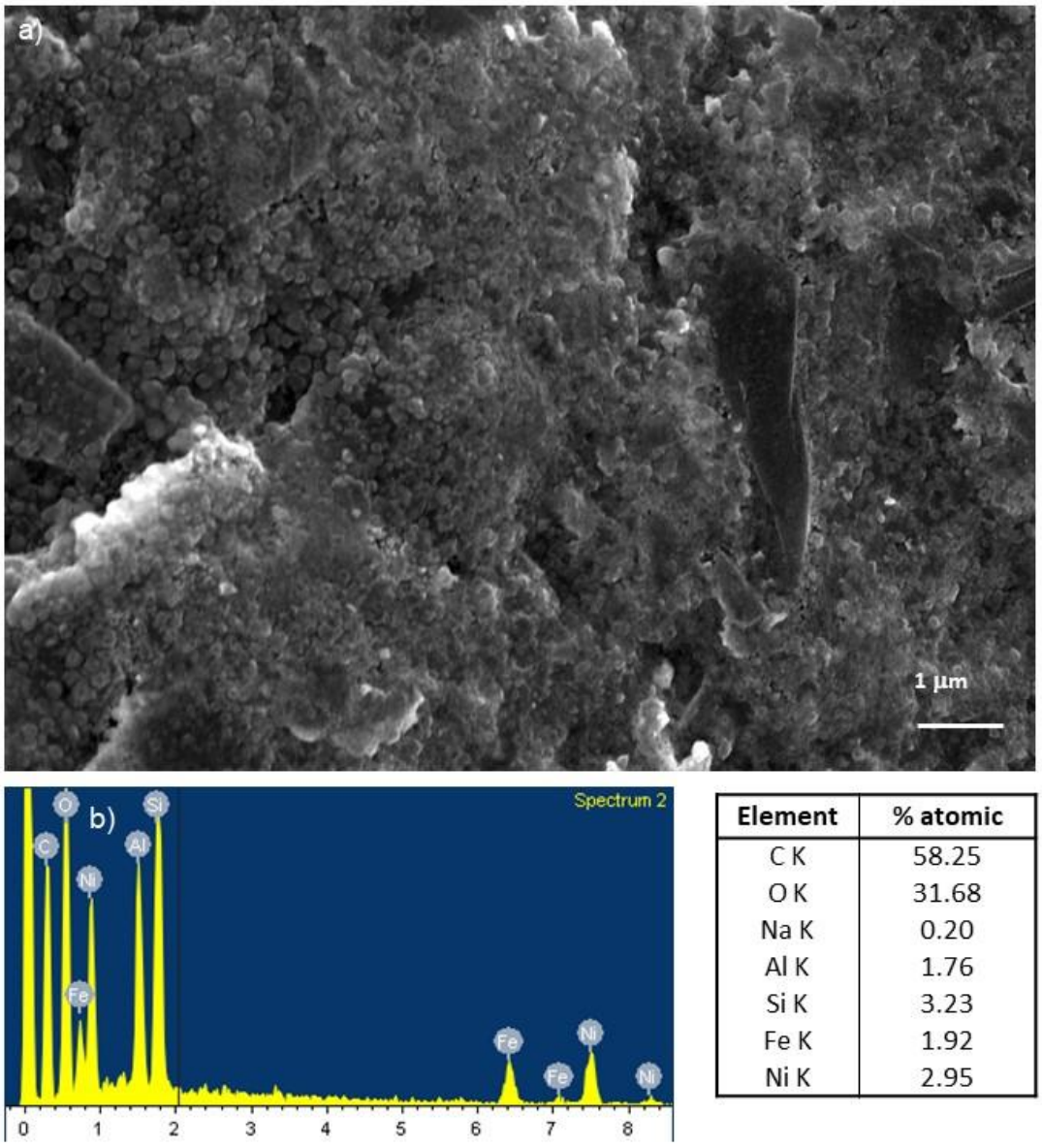

Element	% atomic
C K	58.25
O K	31.68
Na K	0.20
Al K	1.76
Si K	3.23
Fe K	1.92
Ni K	2.95

Figure S3. a) SEM and b) EDX analysis of FA@NiFe/PGR.

XPS

Table S2. Quantification of Ni and Fe species in each sample.

a)

Sample	Ni^{0}	Ni^{2+}	Ni^{3+}
ED@Ni/PGR	14.6	66.1	19.2
FA@Ni/PGR	-	65.9	34.1
FA@NiFe/PGR	-	65.7	34.3

b)

Sample	Fe^{2+}	Fe^{3+}
FA@PGR	88.7	11.3
FA@NiFe/PGR	70.3	29.7

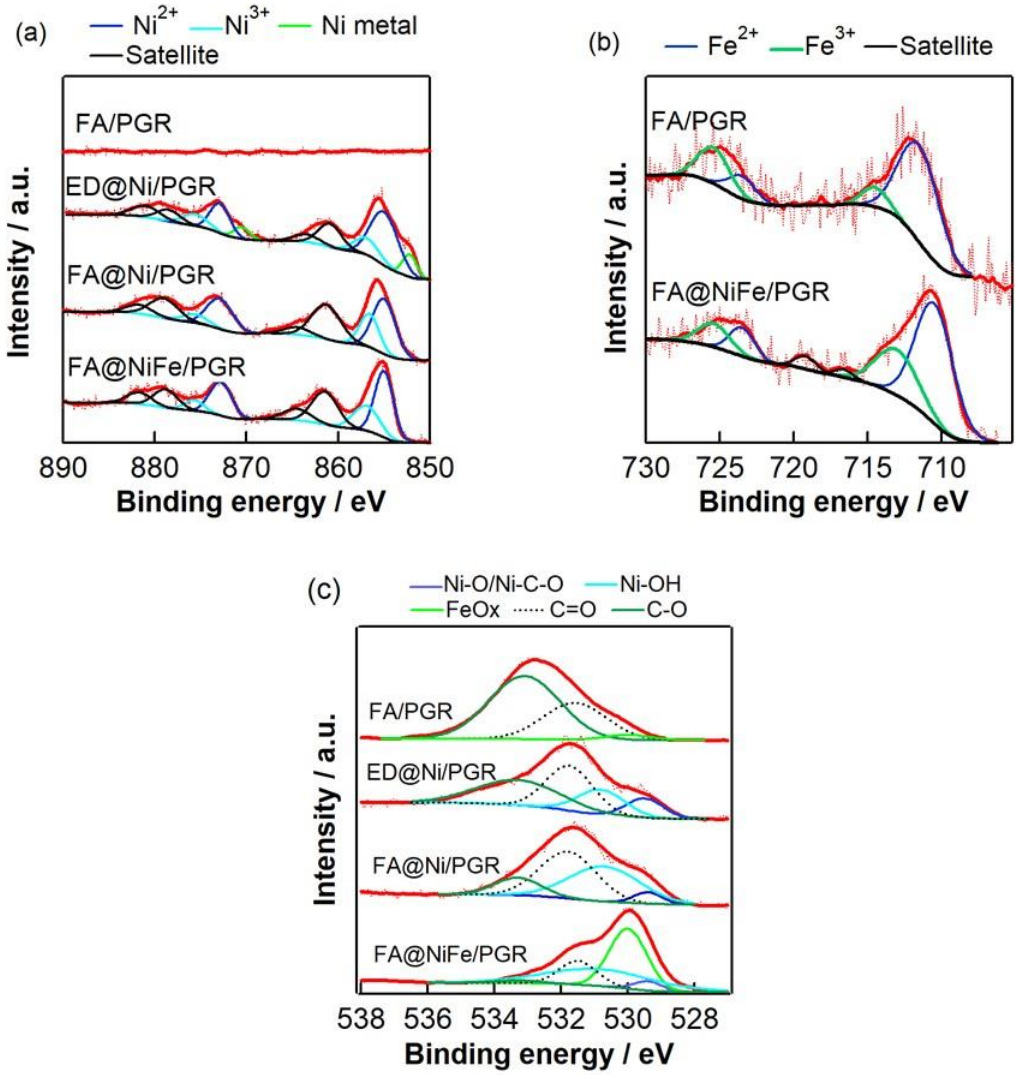

Figure S4. XPS spectra of (a)Ni2p and (b)O1s in FA@NiFe/PGR, ED@Ni/PGR and FA/PGR electrodes. The dotted line is the measurement data, and the solid line is the smoothed data and fitting data.

Cyclic voltammetry measurements at different pH

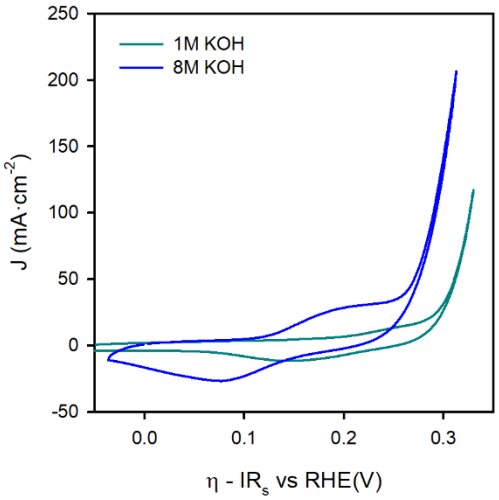

Figure S5. FA@NiFe/PGR measured at 1M and 8M KOH.

Impedance parameters at the applied overpotential

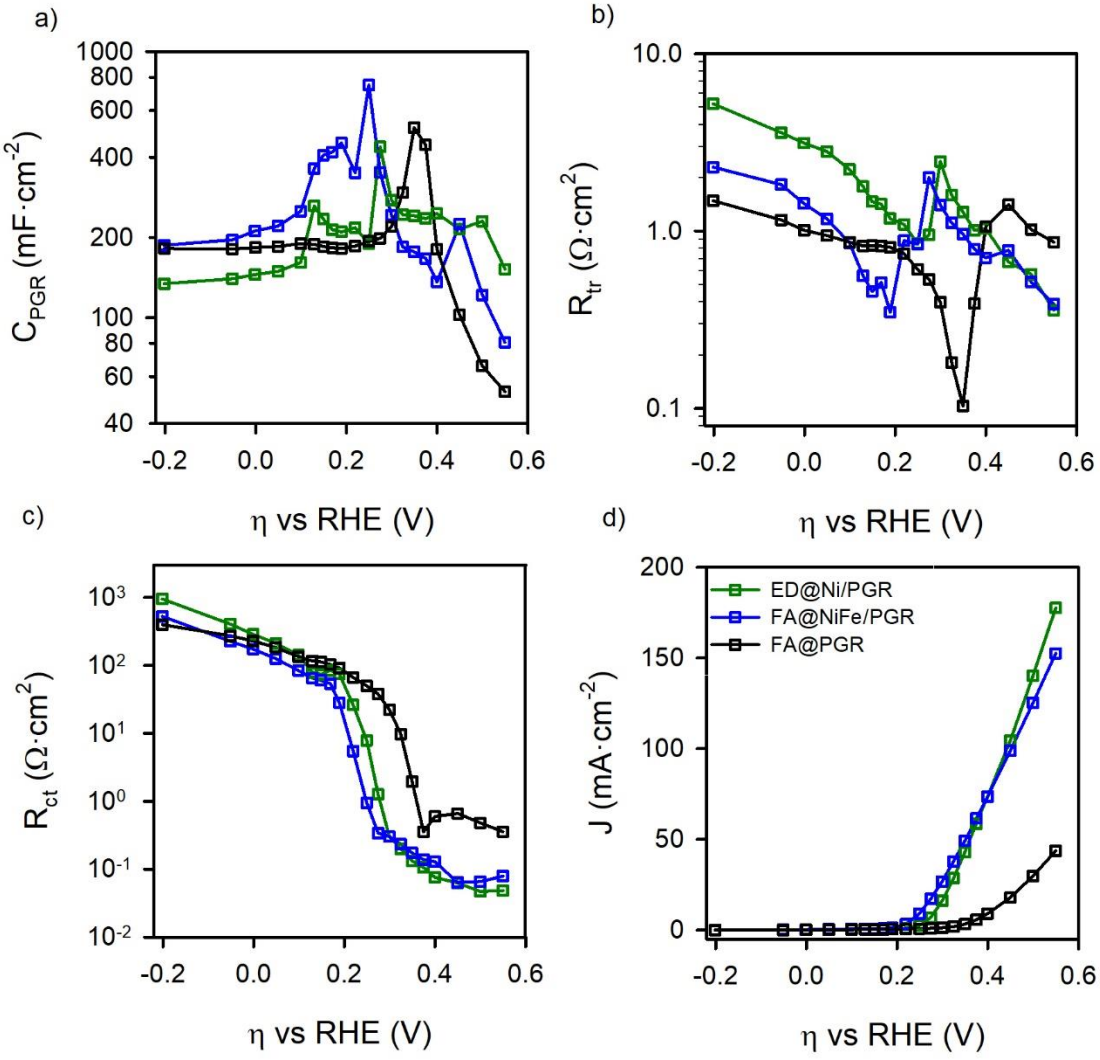

Figure S6. Results from the IS measurements data as a function of the overpotential for FA@PGR (Black), ED@Ni/PGR (Green), and FA@NiFe/PGR (Blue). (a) Electrode capacitance, (b) transport resistance, (c) Charge transfer resistance, and (d) *J*-*V* curve obtained during IS measurements.

Comparison of impedance parameters with Fe decorated PGR

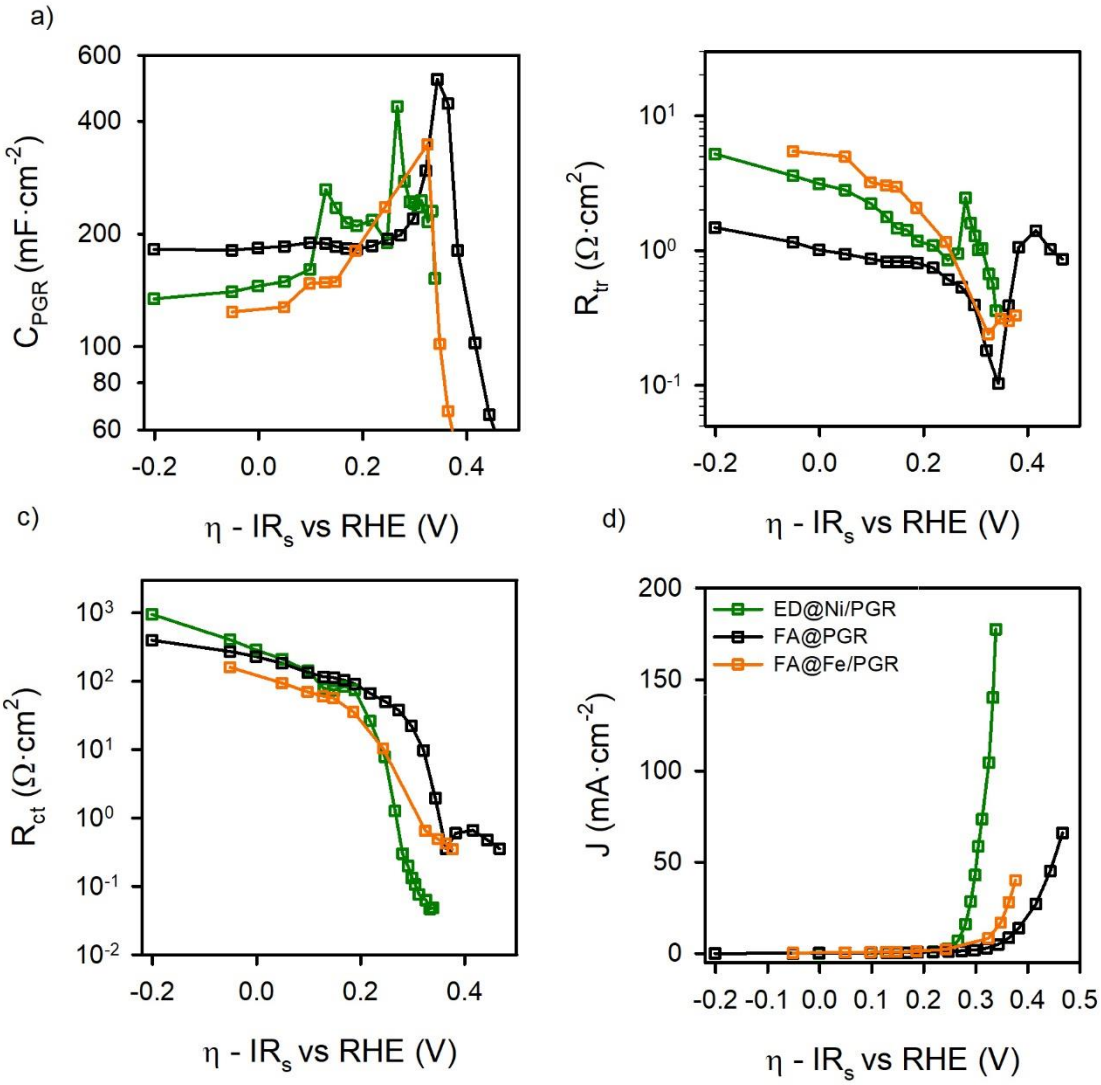

Figure S7. IS measurements as a function of the interfacial overpotential for FA@PGR (Black), ED@Ni/PGR (Green), and FA@Fe/PGR (Orange). (a) Electrode capacitance, (b) transport resistance, (c) Charge transfer resistance, and (d) *J-V* curve obtained during IS measurements.

4. Publication 2

"Revealing the contribution of singlet oxygen in the photoelectrochemical oxidation of benzyl alcohol"

Ramón Arcas, Eduardo Peris, Elena Mas-Marzá* and Francisco Fabregat-Santiago*

Sustainable Energy Fuels, 2021, **5**, 956-962

4.1. Candidate's contribution

Nature of Contribution	Extent of Contribution
✓ Preparation of the $BiVO_4$ photoelectrodes ✓ Execution of experimental procedures ✓ Execution of analytical and electrochemical characterization ✓ Contribution of the figures and manuscript preparation ✓ Contribution on the analysis of results ✓ Contribution of the corrections on the manuscript according to the reviewer's comments.	50 %

4.2. Published manuscript

"Revealing the contribution of singlet oxygen in the photoelectrochemical oxidation of benzyl alcohol"

Ramón Arcas, Eduardo Peris, Elena Mas-Marzá* and Francisco Fabregat-Santiago*

Institute of Advanced Materials (INAM), Universitat Jaume I, Av. Vicente Sos Baynat s/n, Castellon E-12006, Spain

E-mail: emas@uji.es, fabresan@uji.es

Abstract

Photoelectrochemical approaches are finding their use for the transformation of organic molecules beyond water oxidation and CO_2 reduction. Among the different reactions that can be performed, the selective oxidation of alcohols to aldehydes is a transformation of great interest, as aldehydes are the starting materials for the preparation of more complex organic molecules with high added value. In order to develop efficient photoelectrochemical methodologies for this reaction, it is crucial to unravel all the different parameters that are involved in such light-driven process. Herein we analyse in detail the effect of light wavelength and atmosphere in the photoelectrochemical oxidation of benzyl alcohol to benzaldehyde using $BiVO_4$ electrodes. Our studies demonstrate that an important contribution to the oxidation of the alcohol is due to a UV light-induced production of singlet oxygen, which is also responsible for the formation of hydrogen peroxide in the reaction media. These findings are key for identifying and evaluating the underlying mechanism involved in this type of photoelectrochemically-induced oxidation, in order to avoid misinterpretations of the efficiencies.

Table of content

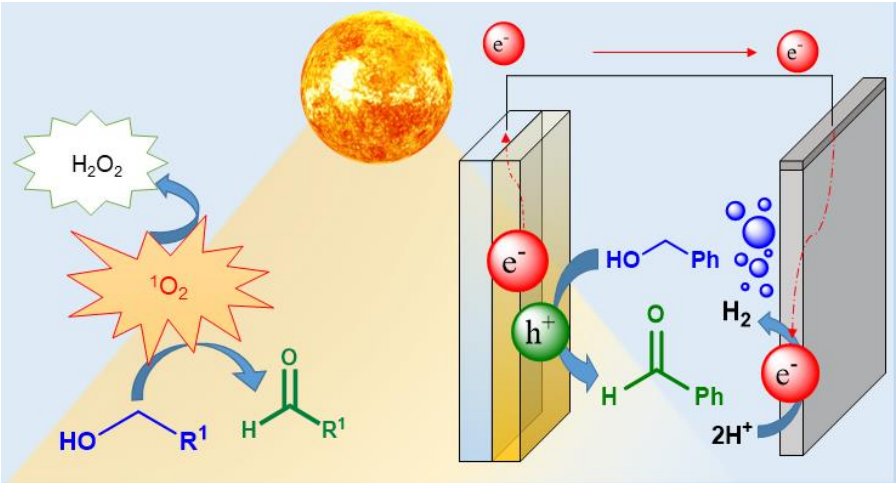

Introduction

During the last decade, photolectrocatalysis mostly devoted to the study of the oxidation of H_2O and the reduction of CO_2[1–3], and disregarded its use for the synthesis of more complex organic molecules with high added value.[4] Given the high potentials that can be attained in a photoelectrochemical cell (PEC), these should be considered suitable for the preparation of organic products *via* redox transformations that would be difficult to achieve by chemical means. Just recently, a few examples have been described where photoanodes are used to generate added-value organic species.[5,6] For example, $BiVO_4$ and WO_3 anodes were recently used for the photoelectrochemical oxidation of 5-hydroxymethylfurfural,[7] benzylic alcohols,[8–11] furan,[12] tetralines,[9] cyclohexane,[13,14] glycerol[15] and urea.[16] Also of interest is the synthesis of 5,5'-azotetrazolate-based salts using W, Mo co-doped $BiVO_4$ photoanodes,[17] and the amination of arenes assisted by α-Fe_2O_3 electrodes.[18]

The selective oxidation of alcohols to aldehydes is a key transformation in organic synthesis. Traditionally, this reaction involves the use of stoichiometric amounts of inorganic and organic oxidants and harsh reaction conditions. Consequently, efforts have been made in order to perform this transformation in a cleaner and environmentally friendly method using homogeneous or heterogeneous catalysts and oxygen.[19–25] Photolectrocatalysis constitutes an eco-friendly and smart approach for this transformation. When this reaction is performed in a PEC, the oxidation of the substrate is accompanied by the release of H_2 at the cathode.

In many cases, the photooxidation of alcohols requires that the photocatalyst is irradiated with UV light,[26] but this sometimes makes that the product is formed together with over-oxidized compounds.[27,28] Some studies suggest that the irradiation with UV light may increase the efficiency in the oxidation of benzyl alcohol to benzaldehyde;[29] although the reasons to justify the role of UV light in the process are still unclear. Recently, Mokari and co-workers proposed that, in the photocatalytic oxidation of benzyl alcohol under UV irradiation using heterogeneous catalysts, there is a competition between the photocatalytic process and a so-called 'autooxidation process'. This autooxidation was suggested to be a consequence of the photoactivation of small amounts of benzaldehyde present in the reaction media.[30] Aiming to shed some light on the role of UV irradiation in the photocatalytic oxidation of alcohols, herein we carried out a study considering all plausible mechanistic pathways. In a first set of experiments, we detected a photoelectrode-free oxidation of benzyl alcohol, with concomitant formation of H_2O_2 as a persistent side-product. After performing a series of control experiments, we concluded that this photoelectrode-free oxidation process is a consequence of the formation of singlet oxygen in the reaction media, which is formed upon irradiating O_2-containing solutions with UV light. In addition, we also found that this photoelectrode-free oxidation pathway has an important share in the total efficiency of the system.

Experimental section

All reagents and solvents were employed as received. Bismuth(III) nitrate pentahydrate (≥98.0%), zirconyl chloride octahydrate (98.0%), Vanadium(IV)-oxy acetylacetonate (98.0%), Sodium hydroxide (pellets for analysis), Tetrabutylammonium perchlorate (≥99.0% electrochemical degree), Benzyl alcohol (anhydrous 99.8%), Ferrocene (98.0%,), Anisole (≥99.0%), tert-butyl alcohol (≥99.0%), 1,4-Diazabicyclo{2.2.2}octane (DABCO, ≥ 99.0%) and Dimethylsulfoxide (anhydrous) were purchase from Sigma Aldrich; Ethyleneglycol (technical degree) and Acetonitrile (HPLC) were purchase from Scharlab; Deuterated acetonitrile (99.8%D) was purchase from Eurisotop. Anhydrous acetonitrile (HPLC, SPS M BRAUN) was obtained from an SPS M Braum System.

Preparation and characterization of Zr decorated BiVO4 photoanodes

The synthesis and fabrication of 2.5 % zirconium $BiVO_4$ electrodes was performed following the literature procedure.[31] This procedure consists of an electrodeposition of a $Bi(NO_3)_3 \cdot 5H_2O$ (20mM) and $ZrCl_2O \cdot 8H_2O$ (0.5 mM) solution in ethylenglycol followed by drop-coating of a solution of $VO(acac)_2$ (0.15M) in DMSO. Absorbance spectra of the $BiVO_4$ photoanodes were measured on a Varian Cary 300 Bio spectrophotometer. Powder X-ray diffraction data was acquired on a Rigaku Miniflex 600, (Rigaku Corporation, Tokyo, Japan) with copper Kα radiation (λ = 1.5418 Å) at a scan speed of 3°·min-1. Finally, scanning electron microscopy (SEM) images were recorded with a Leica-Zeiss LEO 440 microscopy. To improve the quality of the images, the top of the samples was covered with platinum. UV-vis spectra, X-Ray diffraction (XRD) data and surface morphology were consistent with the ones described in the literature (see Figure S1).

(Photo)electrochemical measurements

Photoelectrochemical and electrochemical measurements were performed on a PGSTAT302N potentiostat (Metrohm-Autolab, The Netherlands) in a one-compartment, three-electrode configuration photoelectrochemical solar cell (PEC). Non-aqueous $Ag/AgNO_3$ (ALS, Japan) and platinum foil (0.1 mm thick, Alfa Aesar) constitutes the reference and counter electrodes and a solution of 0.1 M of tetrabutylammonium perchlorate ($TBAClO_4$) in CH_3CN was the non-aqueous electrolyte selected as supporting electrolyte. PECs were illuminated using an ozone-free 300 W Xenon (Xe) lamp and the illumination of the working photoelectrode was adjusted with a thermopile to 100 $mW \cdot cm^{-2}$. CV measurements were carried out at 50 $mV \cdot s^{-1}$ and all the electrochemical measurements were referred to the reference electrode $Ag/AgNO_3$. Experiments were performed at V_{oc}, 0.4, 0.8, 1.2 and 1.6V vs $Ag/AgNO_3$, being V_{oc} the potential reached when illuminating the sample in open circuit conditions, i.e. without applying a potential (typically -0.2V vs $Ag/AgNO_3$).

To refer the photoelectrochemical potentials to the reversible hydrogen electrode (RHE), Ferrocene/Ferrocenium (Fc/Fc^+) couple was used as an internal reference by adding 2.0 mM of ferrocene after the electrochemical tests (see Figure S2).

In a typical chronoamperometry (CA), the corresponding concentration of benzyl alcohol (**1**) was added to a solution of 30 mL of electrolyte. Half of the solution was kept in a vial and labelled as a blank sample. The other half was introduced in a transparent quartz PEC, with dimensions 5 x 3 x 5 cm^3, and was used for the chronoamperometry. Before the CA measurement, CV in dark and light was used as a measurement to test the performance of the electrode. CA measurements were run under soft stirring and constant potential for 13 hours. The CA measurements were taken each 5 s and the Faradaic yield has been estimated by integration of the current, adapting the Faraday law of electrolysis to our case (equation 1).

$$F_{yield} = \frac{n_2}{n_{1,o}} \cdot 100 = \frac{Q}{n_e \cdot F \cdot n_{1,o}} \cdot 100 = \frac{\int I dt}{n_e \cdot F \cdot n_{1,o}} \approx \frac{\sum I \cdot \Delta t}{2 \cdot F \cdot n_{1,o}} \qquad Eq.\ 1$$

Where $n_{1,o}$ is the initial number of mols of **1**, n_2 is the number of mols of benzaldehyde produced (**2**), n_e the number of electrons needed in the reaction (n_e = 2 in this case), F Faraday constant, I the current and Δt the time step.

As Xe lamp has visible and UV light, bandpass filters were used to select the wavelength of incident light when needed. Experiments with visible light were done using a long wavelength pass UV filter (S&K); experiments with UV light were done using two coupled short wavelength pass filters of 400 nm and 475 nm (Edmund Optics). Filters were placed in the middle of the lamp and PEC. Considering the part of light absorbed by filters, the final illumination power in the photoelectrode was 100 $mW \cdot cm^{-2}$, measured with a thermopile, unless explicitly indicated.

Electrode-free reactions with light

Studies under inert atmosphere were performed using anhydrous CH_3CN (N_2 atmosphere), in a Schlenk flask with 100 mM of **1**, illuminating with an ozone-free Xe lamp (100 $mW \cdot cm^{-2}$). Reaction under O_2 was performed similarly but saturating the solution with O_2.

Photocatalytic endoperoxidation of Anthracene

A solution of anthracene (0.5 $mg \cdot mL^{-1}$) CD_3CN was illuminated with an ozone-free Xe lamp (100 $mW \cdot cm^{-2}$) in the absence and presence of O_2. Reactions were monitored by ^1H NMR. When needed, DABCO (0.5 $mg \cdot mL^{-1}$) was used as $^1O_2$ quencher.

Analytical measurements

The analytical performance of the reactions was measured by ^{1}H NMR spectroscopy. NMR spectra were recorded, under ambient temperature, on a Bruker 400/300 MHz instrument. For this purpose, CD_3CN and anisole were used as a solvent and integration reference standard.

Results and discussion

With the aim of investigating the photoelectrochemical oxidation of primary alcohols, we used a Zr-decorated BiVO4 photoanode, due to its proven oxidation capabilities.[31] In order to avoid competition with water oxidation, and aiming to ensure solubility of reagents and products while maximizing the stability of our BiVO4 electrodes, we used acetonitrile as solvent.[9] We studied the photoelectrooxidation of benzyl alcohol (**1**) to benzaldehyde (**2**) (Scheme 1), which constitutes a convenient model reaction for study because the reaction can be easily monitored by 1H NMR spectroscopy and gas chromatography (GC).

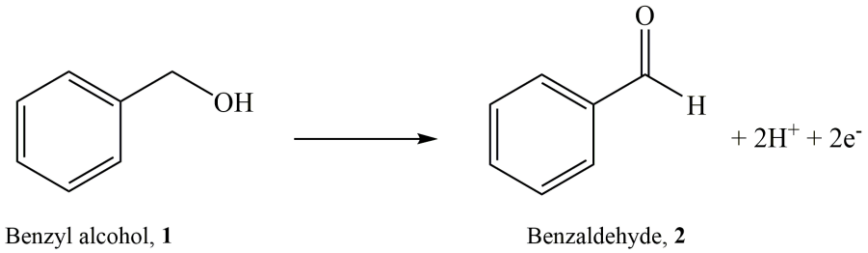

Scheme 1. Oxidation of benzyl alcohol (**1**) to benzaldehyde (**2**).

The electrooxidation of **1** (2 mM in CH_3CN) was performed using a Pt microelectrode for oxidation as working electrode (WE), Pt film as counter electrode (CE), and 0.1M tetrabutylammonium perchlorate ($TBAClO_4$) as electrolyte. All measurements were referenced against $Ag/AgNO_3$. The cyclic voltammetry shown in Figure 1a shows an oxidation wave at 1.94 V, which is attributed to the oxidation of **1** to **2**.[32] When the working electrode is replaced by $BiVO_4$, in the absence of **1** under dark conditions, no current was detected below 2V. However, a photocurrent was observed upon illumination (ozone-free Xe lamp 100 $mW \cdot cm^{-2}$) (Figure 1b). This photocurrent observed in the absence of **1** can be attributed to the presence of traces of water in the system (see Figure S3). In the presence of **1** and in the dark, almost negligible differences in the oxidation potential for both electrodes (Pt and $BiVO_4$, see Figure S4) are observed. However, under illumination, a significant shift to lower potentials (+0.45 V) was observed when using $BiVO_4$, due to the photoelectroactivity of the electrode. This potential is similar to the ones reported previously when $BiVO_4/WO_3$ photoanodes were used for the oxidation of benzylic alcohols.[10]

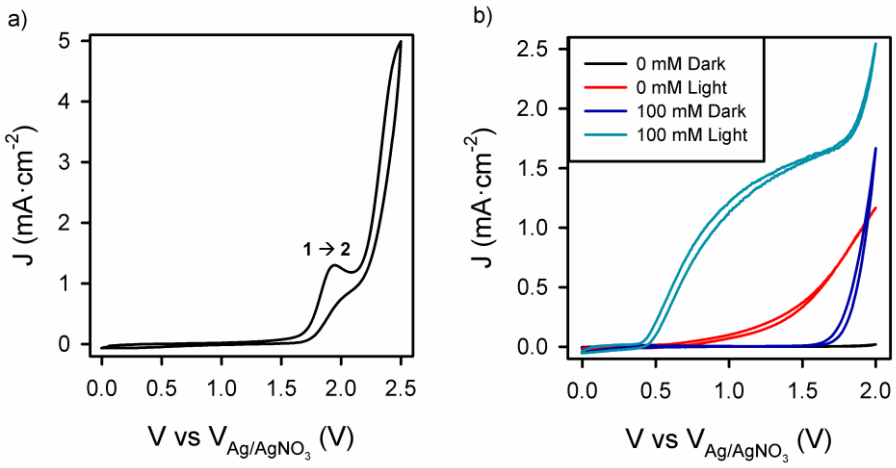

Figure 1. Cyclic voltammetry of benzyl alcohol (**1**). a) 2 mM of **1** in 0.1 M $TBAClO_4$ in CH_3CN, using Pt microelectrode as WE, Pt film as counter electrode (CE) and $Ag/AgNO_3$ as reference electrode (RE). Oxidation peak of **1** into benzaldehyde (**2**) is observed (1 → 2). b) 0 and 100 mM of **1** (benzyl alcohol), in 0.1 M $TBAClO_4$ in CH_3CN, using Zr decorated $BiVO_4$ as WE, Pt film as CE and $Ag/AgNO_3$ as RE. The cyclic voltammetries in this case were performed in dark and light conditions. Illumination was done with an ozone-free Xe lamp 100 $mW \cdot cm^{-2}$.

We next performed a series of chronoamperometry experiments with light for the oxidation of **1** (100 mM) at different voltages (open circuit voltage V_{oc}, 0.4, 0.8, 1.2 and 1.6 V vs $Ag/AgNO_3$) during 13h, illuminating with an ozone-free Xe lamp 100 $mW \cdot cm^{-2}$. At the end of each experiment, the product yield was determined by 1H NMR spectroscopy. As can be observed in Figure 2a, together with the formation of benzaldehyde (**2**), a significative amount of benzoic acid (**3**) was also detected at each potential. The production of **3** is a consequence of the overoxidation of **1**. The combined yield of both, **2** and **3**, increased with the potential, with no significant changes upon potentials above 1.2V. Surprisingly, at V_{oc}, non-negligible yields of 25 and 5% were obtained for **2** and **3**, respectively. Moreover, chronoamperometry at V_{oc} led to the formation of H_2O_2 in a 1:1 molar ratio with respect to **2**. Identification and quantification of H_2O_2 was done by 1H NMR, by comparing with the 1H NMR spectrum of H_2O_2 in the same deuterated solvent and integrating against anisole as integration reference standard (see Supporting information Figure S5 for further details). It is worth mentioning that the detection of H_2O_2 in the photoelectrochemical oxidation of alcohols has previously been reported, although its origin remains unclear.[33]

The Faraday yield (obtained from Faraday law, equation 1) was also determined at each potential, being negligible at V_{oc} (as expected) and showing no significant changes above 1.2V (Figure 2b). Interestingly, we also observed that, at all potentials, the amount of product determined by NMR was larger than the expected according to the Faraday yield. In addition, the difference between these two yields (NMR and Faraday) remained virtually constant for each

potential. This result strongly suggests that a parallel pathway, different from the photoelectrochemical oxidation of **1**, is occurring during the chronoamperometric oxidation of **1**.

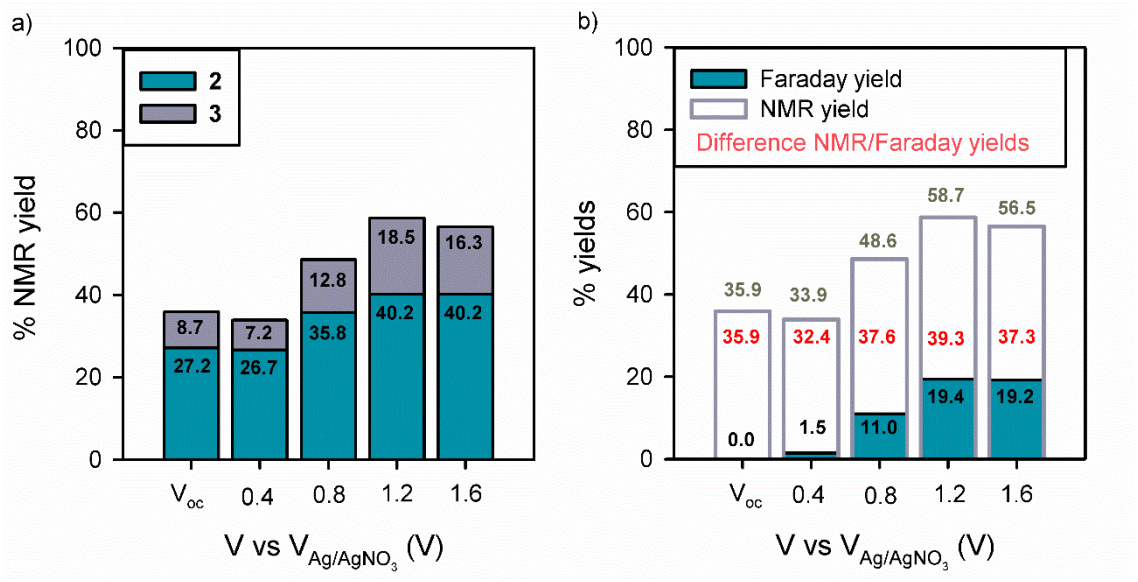

Figure 2. Chronoamperometry experiments for the oxidation of benzyl alcohol (**1**) at different potentials, under illumination with an ozone-free Xe lamp 100 mW·cm^{-2}. Conditions:100 mM of **1**, in 0.1 M $TBAClO_4$ in CH_3CN, using Zr decorated $BiVO_4$ as WE, Pt film as CE and $Ag/AgNO_3$ as RE. a) Yield of oxidation of **1** into benzaldehyde (**2**) and benzoic acid (**3**) calculated by ^1H NMR, using 100 mM of anisole as the integration reference standard. b) Comparison between total product yield (yield of **2** + yield of **3**) obtained by ^1H NMR and Faraday yield. Details for calculation of Faradays yield are in Experimental Section.

We thought that this non-electrochemical oxidation could be due to the following reasons: i) thermal effect, ii) photocatalytic activity of $BiVO_4$, iii) activation by·OH radicals,[8] iv) light-driven photooxidation, or v) autocatalytic oxidation of benzyl alcohol, as suggested in previous studies.[30] Considering that in the chronoamperometries, after illuminating for 13 hours, the solutions reach a temperature of 313K, we performed the reaction at this temperature, without applying bias or illuminating. Under these conditions, no reaction was detected (Table 1, entry 2), therefore, the overoxidation due to a thermal process can be discarded.

When the reaction was carried out with $BiVO_4$ at V_{oc}, without applying bias, illuminating with visible light, no oxidation of **1** was detected. This experiment made us discard that the photocatalytic activity of $BiVO_4$ was responsible for the overoxidation of the alcohol (Table 1, entry 3).

Ye and co-workers recently pointed out that benzyl alcohol can be oxidized through a radical relay strategy coupled to water oxidation.[8] In this process, ·OH radicals are formed and are responsible for the oxidation of the alcohol. Considering that we have traces of water in our system (Figure1b and Figure S3), we decided to check whether ·OH radicals could be responsible

for the oxidation of **1**. For this purpose, we performed the chronoamperometry experiment in the presence of tert-butyl alcohol, a ·OH scavenger. Under these conditions, we did not observe any modification in the amount of **2** formed, thus the participation ·OH radicals can be discarded, in our case (Table 1, compare entries 1 and 4).

In the absence of $BiVO_4$, after illuminating with UV light for 13 hours in the presence of air, **2** and **3** were obtained (see Table 1, entries 5 and 6), with the concomitant production of H_2O_2. The differences found between the yields in entries 5 and 6 are due to a larger UV power used in the case of illuminating only with UV light. Moreover, in the absence of $BiVO_4$, but illuminating with visible light, or under inert atmosphere, no reaction was observed (Table 1, entries 7 and 8). These observations indicate that the non-electrochemical oxidation reaction is observed only for samples irradiated with UV-light under air.

Table 1. Reactions under different conditions

Entry	Light conditions	$BiVO_4$	Applied bias (V)	Atmosphere	Yield (%)[a]	
					2	**3**
1[b]	UV-vis	yes	1.6	O_2	40.2	16.3
2[c]	dark	yes	V_{oc}	O_2	0.0	0.0
3	vis	yes	V_{oc}	O_2	0.0	0.0
4[d]	UV-vis	yes	1.6	O_2	40	16
5	UV-vis	no	-	O_2	22.7	2.2
6	UV	no	-	O_2	27.8	3.3
7	vis	no	-	O_2	0.0	0.0
8	UV	no	-	N_2	0.0	0.0

Reaction conditions: 100 mM of **1** in 15 mL of CH_3CN during 13 hours, illumination with an ozone-free Xe lamp 100 $mW \cdot cm^{-2}$, with filters used when needed. [a] ^1H NMR using 100 mM anisole as the integration reference standard. [b] Data from Figure 2a. [c] Temperature 313K. [d] Using 5mM terc-butyl alcohol as ·OH scavenger

Photocatalyzed processes involving reactive oxygen species (ROS), such as $^1O_2$, constitute an effective method for the oxidation of many organic species, as well as for synthesizing oxygenated molecules by facilitating carbon-oxygen and heteroatom-oxygen bond formation.[34–37] Considering that from our results in Table 1 we can conclude that the combination of UV light and O_2 leads to a non-electrochemical path for the oxidation of **1**, we decided to explore whether singlet oxygen ($^1O2$, $^1\Delta g$) could be formed under our reaction conditions and provoke the non-electrochemical oxidation of **1**. Anthracenes have widely been used for the detection and quantification of singlet oxygen production.[38–42] In order to determine if $^1O2$ is formed when illuminating with UV light, we illuminated an oxygenated solution of anthracene (3 mM) in

CD_3CN with a Xe lamp, and we monitored the reaction by 1H NMR spectroscopy. After 10 minutes, anthracene was converted into 9,10-dihydro-9,10-epidioxyanthracene (anthracene-endoperoxide) in 58% yield, (Figure 3a and 3b).

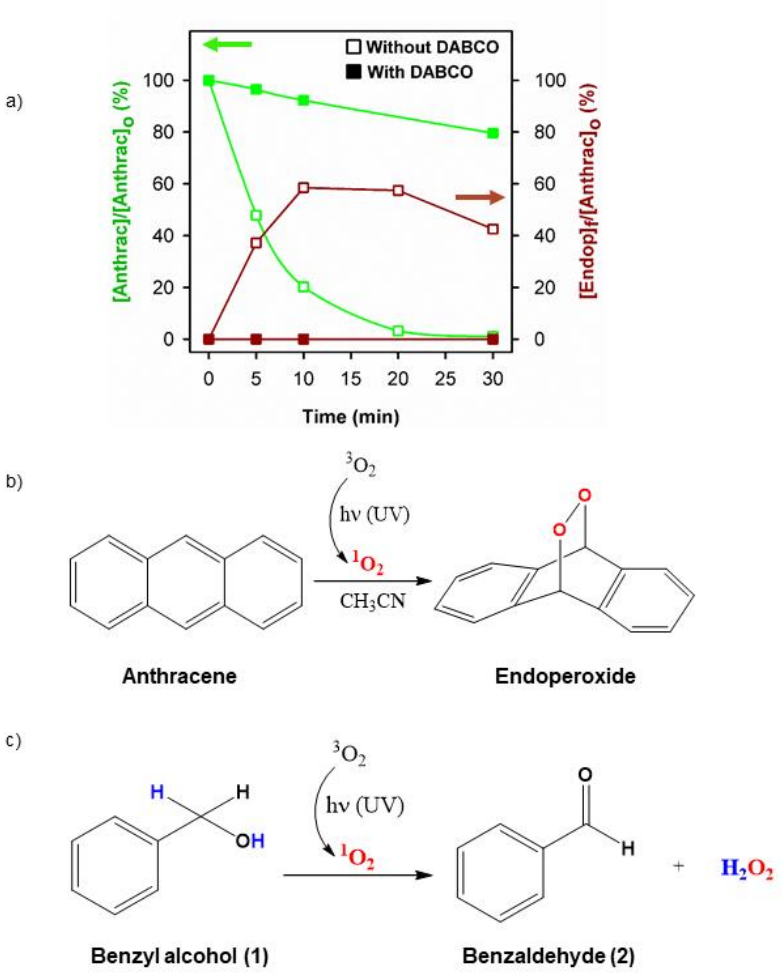

Figure 3. a) Time evolution of the conversion of anthracene (left axis) and formation of endoperoxide, during the illumination of a solution of anthracene (0.5 mg·mL-1) in CD_3CN, in the absence or presence of DABCO (1:1 molar ratio with anthracene). Illumination was done with an ozone-free Xe lamp 100 mW·cm^{-2}. % conversion of anthracene and % formation of endoperoxide were calculated by 1H NMR. After 20 min of illumination, without DABCO a degradation of endoperoxide was detected, explaining the decrease in the concentration of endoperoxide at 30 min. b) Scheme of endoperoxide formation by reaction of anthracene and $^1O_2$. c) Proposed reaction scheme for the oxidation of benzyl alcohol (**1**) with $^1O_2$, leading to the formation of H_2O_2.

Under the same reaction conditions, but using an oxygen-free solution, anthracene-endoperoxide was not detected. In addition, when the reaction was performed in the presence of a singlet oxygen quencher, such as 1,4-diazabicyclo{2.2.2}octane (DABCO), under aerobic conditions and under UV irradiation, again, anthracene-endoperoxide was not formed (Figure 3a).[43] Interestingly, when a solution of **1** was irradiated with UV light in the presence of DABCO

no conversion of **1** into **2** was observed (Table S1 entry 5). All these experiments clearly demonstrate that $^1O_2$ is formed when illuminating with UV light. This formation of $^1O_2$ explains the non-electrochemical oxidation of **1**, depicted in Figure 3c, therefore we can exclude that other pathways, such as the autocatalytic oxidation of **1** reported previously,[30] is taking place in our case. The reaction depicted in Figure 3c also explains the formation of H_2O_2 that we detect in our process.

Once we confirmed the generation of $^1O_2$ under UV light irradiation, we carried out a series of chronoamperometry experiments illuminating with visible light (Table 2), in order to eliminate the contribution of the non-electrochemical reaction. At V_{oc} no conversion of **1** was observed (Table 2, entry 1), confirming that no photocatalytic conversion at the surface of $BiVO_4$ occurs in this system. When applying external bias, **1** was selectively oxidized to **2**, without formation of the over-oxidized species **3** or H_2O_2. This result corroborates that the over-oxidation of the aldehyde and formation of H_2O_2 are both exclusively due to a UV-induced generation of $^1O_2$. Furthermore, we observed that under visible light, the oxidation of benzyl alcohol takes place exclusively through the photoelectrochemical conversion path, as the Faraday yield matched perfectly with the NMR yield.

Table 2. Chronoamperometry experiments under visible light at different voltages

Entry	V (V) vs $V_{Ag/AgNO_3}$	NMR Yield[a]	Faradaic efficiency (%)[b]	H_2O_2
1	V_{oc}	0.0	-	No
2	0.4	2.8	100	No
3	0.8	10.2	100	No
4	1.2	13.1	100	No
5	1.6	13.4	100	No

Reaction conditions: 100 mM of benzyl alcohol in 0.1 M $TBAClO_4$ in CH_3CN solution, using Zr decorated $BiVO_4$ as WE, Pt film as CE and $Ag/AgNO_3$ as RE. Illumination with an ozone-free Xe lamp 100 $mW \cdot cm^{-2}$ using a long wavelength pass UV filter, to ensure only illumination with visible light. Irradiance over the sample was 85 $mW \cdot cm^{-2}$. [a] ^1H NMR yield of benzyladehyde (**2**) using 100 mM of anisole as integration reference standard. [b] Faradaic efficiency calculated as 'NMR yield/Faraday yield'.

As can be seen in Table 2, an enhancement on the yield of **2** was observed at higher voltages, in agreement with the increase of photocurrent observed in cyclic voltammetry under visible light (see Figure S6 in the SI), which by other side, has the same shape as the one with UV-vis (Figure 1b). Under these conditions, the Faraday yield matched perfectly with the NMR yield. In addition, no H_2O_2 was detected at V_{oc} (or any other applied voltage), demonstrating that H_2O_2 is exclusively produced by the UV-induced generation of $^1O_2$.

The data shown in Tables 1 and 2 allowed us to quantify the contribution of the formation of **2** due to UV light/singlet oxygen in the process. Thus, of the 40% yield achieved for the oxidation of **1** into **2** (Table 1 entries 1 and 4), 22.7% can be directly attributed to the oxidation produced by singlet oxygen under UV irradiation that occurs in the absence of the photoanode (Table 1 entry 5), and 13.4% of the yield is due to the activity of the $BiVO_4$ under illumination with visible (not UV) light (Table 2, entry 5). This leaves just 3.9% yield that can be assigned to the contribution of the activity of the photoanode. By other side, the number of photons in the UV region of the spectrum of a Xe lamp (after filtered by glass and electrolyte) is smaller than in the visible. As the absorbance of $BiVO_4$ is nearly constant from 200 to 550 nm[44] the number of absorbed photons effectively transformed into electrons is still larger in the visible than in the UV region of the spectra.

Conclusions

In conclusion, the photoelectrochemical oxidation of benzyl alcohol to benzaldehyde using $BiVO_4$ anodes was studied, and the factors affecting this transformation were analysed. A non-electrochemical path for the oxidation of the alcohol has been found for the first time. We demonstrated that this alternative oxidation process is due to the formation of singlet oxygen in the reaction media, as a consequence of the use of UV light and the presence of oxygen. The formation of $^1O_2$ explains the formation of hydrogen peroxide, which leads to the over-oxidation of the alcohol. In fact, we observed that $^1O_2$-mediated production of **2** is dominant over the photoelectrocatalytic process, while the contribution of the direct photocatalytic reaction is almost negligible. This additional oxidation path justifies the strong activation of the reaction under UV light that remarkably enhances the amount of aldehyde obtained with respect to the photoelectrochemical oxidation. Our findings demonstrate that any studies using photoelectrocatalytic oxidation under UV light irradiation should seriously consider the results published herein, in order to avoid the misinterpretations of the photoanode's efficiency, which can lead to the overestimation of the activity.

Acknowledgements

Authors want to acknowledge the Ministerio de Economía y Competitividad (MINECO) from Spain (ENE2017-85087-C3-1-R and PGC2018-093382-B-I00) University Jaume I (UJI-B2019-20 and UJI-B2017-07). Serveis Centrals d'Instrumentació Científica from UJI are acknowledged for NMR measurements.

References

(1) Tachibana, Y.; Vayssieres, L.; Durrant, J. R. Artificial Photosynthesis for Solar Water-Splitting. *Nat. Photonics* **2012**, *6* (8), 511–518.

(2) Grätzel, M. Photoelectrochemical Cells. *Nature*. Nature Publishing Group November 15, 2001, pp 338–344.

(3) FUJISHIMA, A.; HONDA, K. Electrochemical Photolysis of Water at a Semiconductor Electrode. *Nature* **1972**, *238* (5358), 37–38.

(4) Song, J. What Else Can Photoelectrochemical Solar Energy Conversion Do Besides Water Splitting and CO 2 Reduction? *ACS Energy Lett.* **2018**, *3*, 2610–2612.

(5) Sayama, K. Production of High-Value-Added Chemicals on Oxide Semiconductor Photoanodes under Visible Light for Solar Chemical-Conversion Processes. *ACS Energy Letters*. American Chemical Society May 11, 2018, pp 1093–1101.

(6) Tilley, D. Recent Advances and Emerging Trends in Photo-Electrochemical Solar Energy Conversion. *Adv. Energy Mater.* **2019**, *9*, 1802877.

(7) Cha, H. G.; Choi, K.-S. Combined Biomass Valorization and Hydrogen Production in a Photoelectrochemical Cell. *Nat. Chem.* **2015**, *7*, 328–333.

(8) Luo, L.; Wang, Z.-J.; Xiang, X.; Yan, D.; Ye, J. Selective Activation of Benzyl Alcohol Coupled with Photoelectrochemical Water Oxidation via a Radical Relay Strategy. **2020**.

(9) Li, T.; Kasahara, T.; He, J.; Dettelbach, K. E.; Sammis, G. M.; Berlinguette, C. P. Photoelectrochemical Oxidation of Organic Substrates in Organic Media. *Nat. Commun.* **2017**, *8* (1), 1–5.

(10) Tateno, H.; Miseki, Y.; Sayama, K. Photoelectrochemical Oxidation of Benzylic Alcohol Derivatives on BiVO4 /WO3 under Visible Light Irradiation. *ChemElectroChem* **2017**, *4*, 3283–3287.

(11) Fang, W.; Tao, R.; Jin, Z.; Sun, Z.; Li, F.; Xu, L. Sandwich-Type Cobalt-Polyoxometalate as an Effective Hole Extraction Layer for Enhancing BiVO4-Based Photoelectrochemical Oxidation. *J. Alloys Compd.* **2019**, *797*, 140–147.

(12) Tateno, H.; Miseki, Y.; Sayama, K. Photoelectrochemical Dimethoxylation of Furan via a Bromide Redox Mediator Using a BiVO 4 /WO 3 Photoanode †. *Chem. Commun.* **2017**, *53*, 4378–4381.

(13) Tateno, H.; Iguchi, S.; Miseki, Y.; Sayama, K. Photo-Electrochemical C-H Bond Activation of Cyclohexane Using a WO3 Photoanode and Visible Light. *Angew. Chemie* **2018**, *57*, 11238–11241.

(14) Tateno, H.; Miseki, Y.; Sayama, K. PINO/NHPI-Mediated Selective Oxidation of Cycloalkenes to Cycloalkenones via a Photo-Electrochemical Method †. *Chem. Commun* **2019**, *55*, 9339.

(15) Huang, L. W.; Vo, T. G.; Chiang, C. Y. Converting Glycerol Aqueous Solution to Hydrogen Energy and Dihydroxyacetone by the BiVO4 Photoelectrochemical Cell. *Electrochim. Acta* **2019**, *322*, 134725.

(16) Liu, J.; Li, J.; Shao, M.; Wei, M. Directed Synthesis of SnO2 @BiVO4 /Co-Pi Photoanode for Highly Efficient Photoelectrochemical Water Splitting and Urea Oxidation. *J. Mater. Chem. A* **2019**, *7*, 6327–6336.

(17) He, H.; Du, J.; Wu, B.; Duan, X.; Zhou, Y.; Ke, G.; Huo, T.; Ren, Q.; Bian, L.; Dong, F. Photoelectrochemical Driving and Clean Synthesis of Energetic Salts of 5,5'-Azotetrazolate at Room Temperature . *Green Chem.* **2018**, *20*, 3722–3726.

(18) Zhang, L.; Liardet, L.; Luo, J.; Ren, D.; Grätzel, M.; Hu, X. Photoelectrocatalytic Arene C–H Amination. *Nat. Catal.* **2019**, *2* (4), 366–373.

(19) Mallat, T.; Baiker, A. Oxidation of Alcohols with Molecular Oxygen on Solid Catalysts. *Chem. Rev.* **2004**, *104* (6), 3037–3058.

(20) Su, F.; Mathew, S. C.; Lipner, G.; Fu, X.; Antonietti, M.; Blechert, S.; Wang, X. Mpg-C3N4-Catalyzed Selective Oxidation of Alcohols Using O2 and Visible Light. *J. Am. Chem. Soc.* **2010**, *132*, 16299–16301.

(21) Parmeggiani, C.; Cardona, F. Transition Metal Based Catalysts in the Aerobic Oxidation of Alcohols. *Green Chem.* **2012**, *14* (3), 547–564.

(22) Shi, Z.; Zhang, C.; Tang, C.; Jiao, N. Recent Advances in Transition-Metal Catalyzed Reactions Using Molecular Oxygen as the Oxidant. *Chem. Soc. Rev.* **2012**, *41* (8), 3381–3430.

(23) Davis, S. E.; Ide, M. S.; Davis, R. J. Selective Oxidation of Alcohols and Aldehydes over Supported Metal Nanoparticles. *Green Chem.* **2012**, *15* (1), 17–45.

(24) Wertz, S.; Studer, A. Nitroxide-Catalyzed Transition-Metal-Free Aerobic Oxidation Processes. *Gree* **2013**, *15*, 3116–3134.

(25) Guo, Z.; Liu, B.; Zhang, Q.; Deng, W.; Wang, Y.; Yang, Y. Recent Advances in Heterogeneous Selective Oxidation Catalysis for Sustainable Chemistry. *Chem. Soc. Rev* **2014**, *43*, 3480–3524.

(26) Colmenares, J. C.; Ouyang, W.; Ojeda, M.; Kuna, E.; Chernyayeva, O.; Lisovytskiy, D.; De, S.; Luque, R.; Balu, A. M. Mild Ultrasound-Assisted Synthesis of TiO2 Supported on Magnetic Nanocomposites for Selective Photo-Oxidation of Benzyl Alcohol. *Appl. Catal.*

B Environ. **2016**, *183*, 107–112.

(27) Kim, S.; Choi, W. Visible-Light-Induced Photocatalytic Degradation of 4-Chlorophenol and Phenolic Compounds in Aqueous Suspension of Pure Titania: Demonstrating the Existence of a Surface-Complex-Mediated Path. *J. Phys. Chem. B* **2005**, *109*, 5143–5149.

(28) Palmisano, G.; Scandura, G.; Augugliaro, V.; Loddo, V.; Pace, A.; Tek, B. S.; Yurdakal, S.; Palmisano, L. Unexpectedly Ambivalent O2 Role in the Autocatalytic Photooxidation of 2-Methoxybenzyl Alcohol in Water. *J. Mol. Catal. A Chem.* **2015**, *403*, 37–42.

(29) Li, H.; Qin, F.; Yang, Z.; Cui, X.; Wang, J.; Zhang, L. New Reaction Pathway Induced by Plasmon for Selective Benzyl Alcohol Oxidation on BiOCl Possessing Oxygen Vacancies. *J. Am. Chem. Soc.* **2017**, *139*, 3513–3521.

(30) Pavan, M. J.; Ridman, H.; Segalovich, G.; Shames, A. I.; Lemcoff, N. G.; Lebm Okari, T. Photoxidation of Benzyl Alcohol with Heterogeneous Photocatalysts in the UV Range:T He Complex Interplay with the Autoxidative Reaction. *ChemCatChem* **2018**, *10*, 2541–2545.

(31) Shaddad, M. N.; Ghanem, M. A.; Almayouf, A. M.; Gimenez, S.; Bisquert, J.; Herraiz-Cardona, I. Cooperative Catalytic Effect of ZrO2 and A-Fe2O3 Nanoparticles on BiVO4 Photoanodes for Enhanced Photoelectrochemical Water Splitting. *Chem. Sustain. Energy Mater.* **2016**, *9*, 1–7.

(32) Lund, H. Electroorganic Preparations. II. Oxidation of Carbinols. *Acta Chem.Scand.* **1957**, *11*, 491–498.

(33) Liu, D.; Liu, J. C.; Cai, W.; Ma, J.; Yang, H. Bin; Xiao, H.; Li, J.; Xiong, Y.; Huang, Y.; Liu, B. Selective Photoelectrochemical Oxidation of Glycerol to High Value-Added Dihydroxyacetone. *Nat. Commun.* **2019**, *10* (1).

(34) Ghogare, A. A.; Greer, A. Using Singlet Oxygen to Synthesize Natural Products and Drugs. *Chem. Rev.* **2016**, *116* (17), 9994–10034.

(35) Nosaka, Y.; Nosaka, A. Y. Generation and Detection of Reactive Oxygen Species in Photocatalysis. *Chem. Rev.* **2017**, *117* (17), 11302–11336.

(36) Greer, A. Christopher Foote's Discovery of the Role of Singlet Oxygen [1O2 (1Δg)] in Photosensitized Oxidation Reactions. *Acc. Chem. Res.* **2006**, *39* (11), 797–804.

(37) Martínez-Agramunt, V.; Peris, E. Photocatalytic Properties of a Palladium Metallosquare with Encapsulated Fullerenes via Singlet Oxygen Generation. *Inorg. Chem.* **2019**, *58*, 11836–11842.

(38) Vankayala, R.; Sagadevan, A.; Vijayaraghavan, P.; Kuo, C.-L.; Chu Hwang, K. Metal Nanoparticles Sensitize the Formation of Singlet Oxygen. *Angew. Chemie* **2011**, *50*,

10640–10644.

(39) Xu, S.; Zhou, P.; Zhang, Z.; Yang, C.; Zhang, B.; Deng, K.; Bottle, S.; Zhu, H. Selective Oxidation of 5-Hydroxymethylfurfural to 2,5-Furandicarboxylic Acid Using O2 and a Photocatalyst of Co-Thioporphyrazine Bonded to g-C3N4. *J. Am. Chem. Soc.* **2017**, *139*, 14775–14782.

(40) Sagadevan, A.; Hwang, K. C.; Su, M. Der. Singlet Oxygen-Mediated Selective C–H Bond Hydroperoxidation of Ethereal Hydrocarbons. *Nat. Commun.* **2017**, *8* (1), 1–8.

(41) De Souza, J. M.; Brocksom, T. J.; McQuade, D. T.; De Oliveira, K. T. Continuous Endoperoxidation of Conjugated Dienes and Subsequent Rearrangements Leading to C-H Oxidized Synthons. *J. Org. Chem.* **2018**, *83* (15), 7574–7585.

(42) You, Y. Chemical Tools for the Generation and Detection of Singlet Oxygen. *Org. Biomol. Chem.* **2018**, *16*, 4044–4060.

(43) Kwak, J.; Freunberger, S. A.; Kim, H.; Park, J.; Nguyen, T. T.; Jung, H.-G.; Byon, H. R.; Sun, Y.-K. Mutual Conservation of Redox Mediator and Singlet Oxygen Quencher in Lithium−Oxygen Batteries. *ACS Catal.* **2019**, *9*, 9914–9922.

(44) Han, J.; Li, K.; Cheng, H.; Zhang, L. A Green Desulfurization Technique: Utilization of Flue Gas SO2 to Produce H2 via a Photoelectrochemical Process Based on Mo-Doped BiVO4. *Front. Chem.* **2017**, *5* (DEC), 114.

4.3. Supporting information

"Revealing the contribution of singlet oxygen in the photoelectrochemical oxidation of benzyl alcohol"

Ramón Arcas, Eduardo Peris, Elena Mas-Marzá* and Francisco Fabregat-Santiago*

Institute of Advanced Materials (INAM), Universitat Jaume I, Av. Vicente Sos Baynat s/n, Castellon E-12006, Spain

1. Zr decorated BiVO4 photoanodes characterization

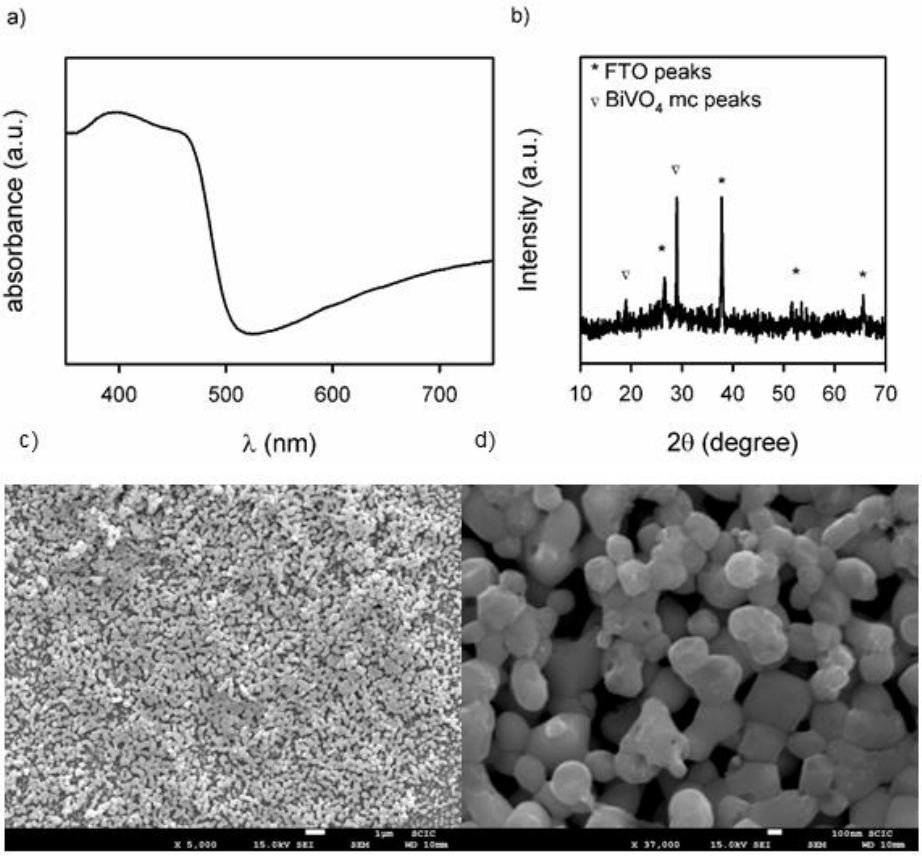

Figure S1. Optical and structural characterization of Zr decorated $BiVO_4$ photoanodes. a) UV-vis Absorption. b) XRD data. c) and d) SEM images.

2. Ferrocene/Ferrocenium (Fc/Fc+) couple used as an internal reference

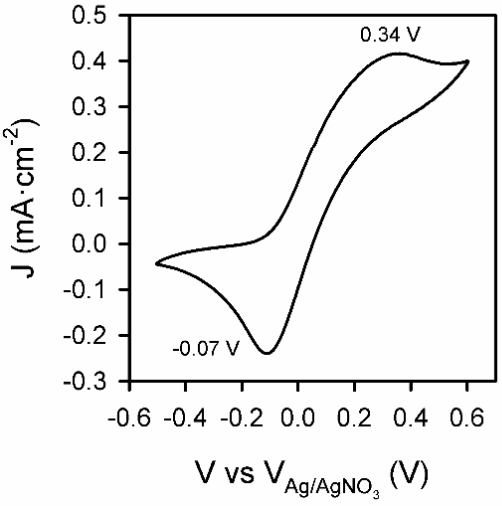

Figure S2. Cyclic voltammetry peak of Ferrocene/Ferrocenium (Fc/Fc^{+}). 2mM of ferrocene was used to calibrate the voltage of the reference electrode. Conditions: 100 mM of benzyl alcohol (**1)**, in 0.1 M $TBAClO_4$ in CH_3CN, using Zr decorated BiVO4 as WE, Pt film as CE, and $Ag/AgNO_3$ as *RE*.

3. Effect of water in photoelectrochemical measurements

The effect of water in the CV measurements is shown in Figure S3. Experimental conditions: cyclic voltammetry in 0.1 M $TBAClO_4$ CH_3CN solution, Zr decorated $BiVO_4$ as WE, Pt as CE and $Ag/AgNO_3$ as RE, illumination with an ozone-free Xe lamp 100 $mW \cdot cm^{-2}$. In dry condition the solvent was dried, $TBAClO_4$ was dried by heating at 80ºC for 2 days and Zr decorated $BiVO_4$ was pre-heated at 300ºC for 6 days. In not dried condition, the solvent and $TBAClO_4$ were obtained from ambient conditions, without previous treatment, and the Zr decorated $BiVO_4$ was the same sample used previously under dry condition. In not dried conditions there is an increase of the photocurrent due to the oxidation of water.

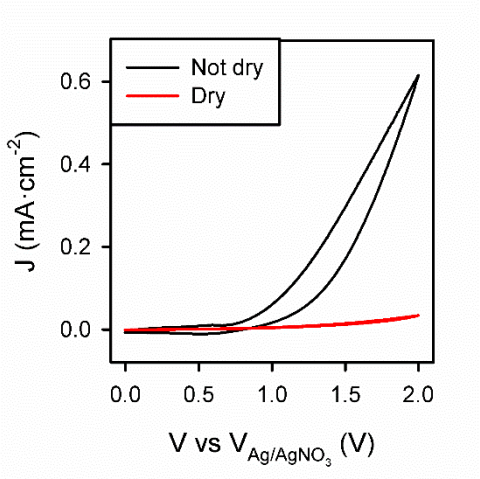

Figure S3. Cyclic voltammetry measurements, humid and dried electrolyte (black and red line, respectively).

4. Electrocatalytic oxidation of benzyl alcohol (1) with Pt and BiVO4 electrodes in dark

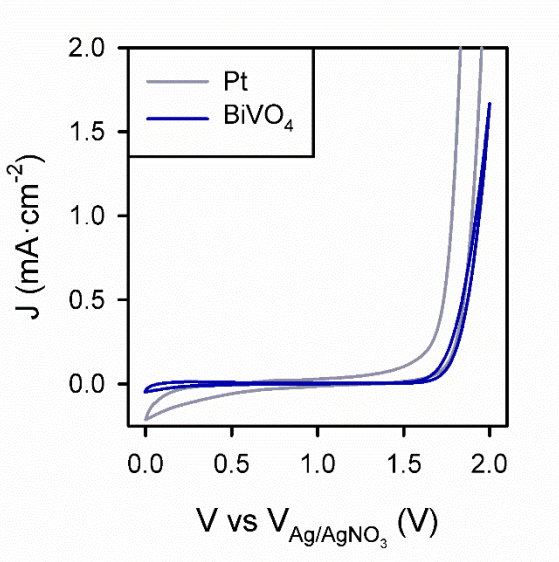

Figure S4. Cyclic voltammetry, of (**1**), using Pt (grey) or Zr decorated $BiVO_4$ (blue) as WE electrodes in the dark. The photoelectrode response for the oxidation of **1** is not so far from the one obtained using Pt as WE. Conditions: 100 mM of **1**, in 0.1 M $TBAClO_4$ in CH_3CN, using Pt film as CE and $Ag/AgNO_3$ as RE.

5. Detection and quantification of H_2O_2

Detection and quantification of H_2O_2 were done by ^1H NMR. The signal of H_2O_2 in the ^1H NMR spectrum of the chronoamperometry experiments was assigned by comparison with the signal of pure H_2O_2 in the same deuterated solvent. The quantification was done using anisole as an integration reference standard.

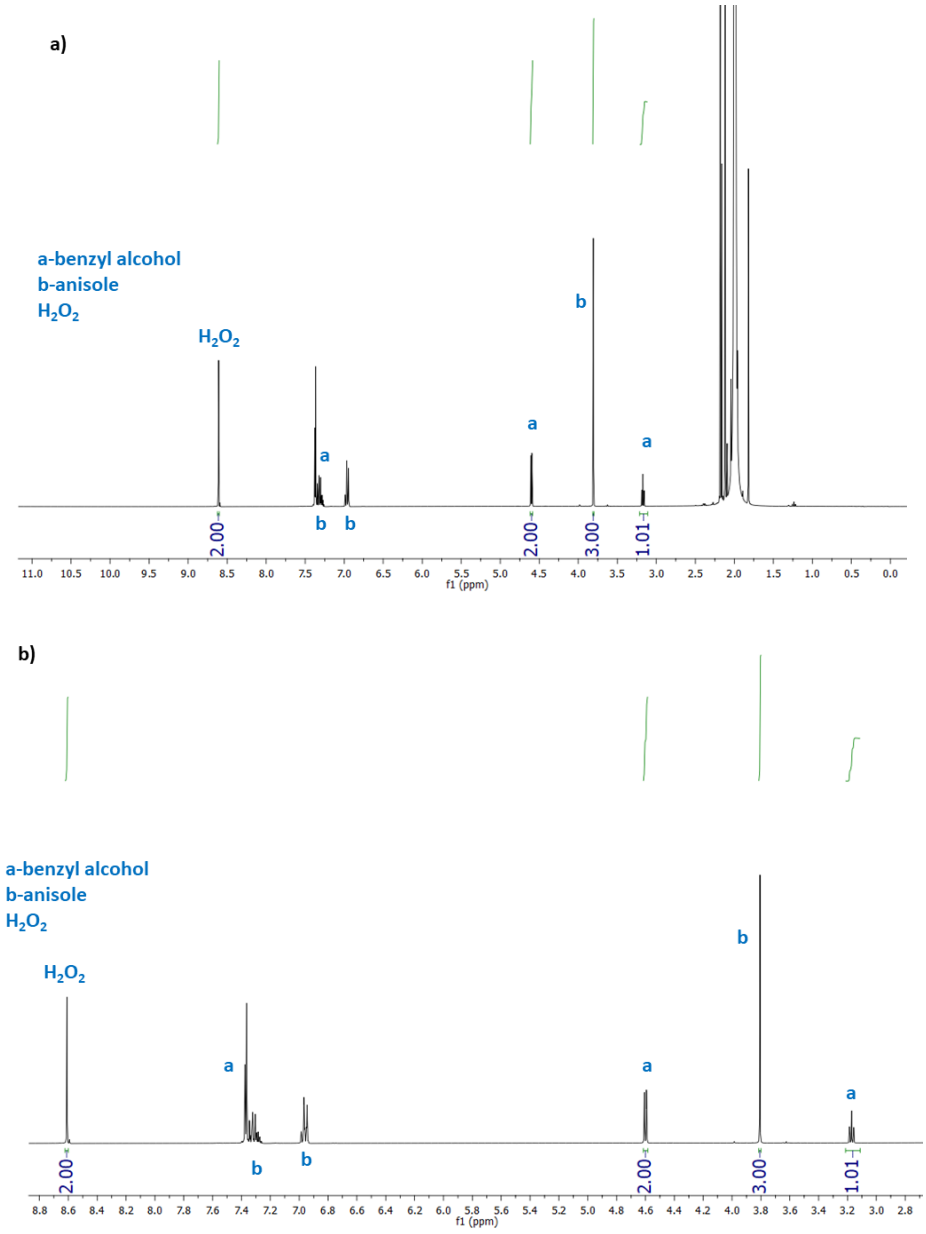

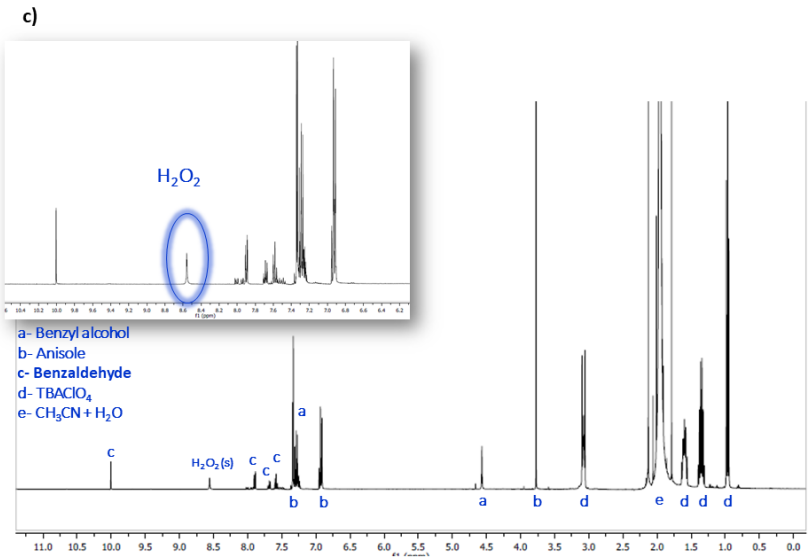

Figure S5. a) and b)[1]H NMR of H_2O_2, benzyl alcohol and anisole, in a molar ratio 1:1:1, in CD_3CN. From this data, it can clearly be observed the signal for H_2O_2, and its integration using anisole as an integration reference standard; c) [1]H NMR of a chronoamperometry experiment at V_{oc}, where H_2O_2 can be detected and quantified.

6. Cyclic voltammetry of benzyl alcohol (1) using Zr decorated $BiVO_4$ as WE under visible light

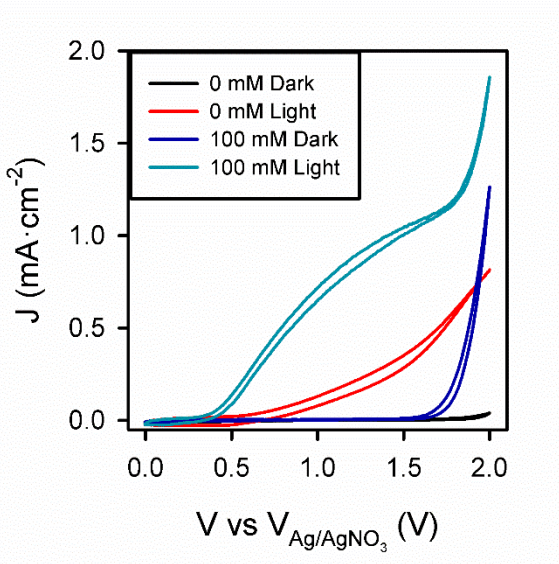

Figure S6 Cyclic voltammetry in dark or illuminating only with visible light, in the absence or presence of **1** (100 mM), in 0.1 M $TBAClO_4$ in CH_3CN, using Zr decorated $BiVO_4$ as WE, Pt film as CE and $Ag/AgNO_3$ as RE.

7. Effect of atmosphere, light and DABCO, a $^1O_2$ quencher, in anthracene and 1 solution under illumination

Solutions of anthracene or **1** illuminated with different light conditions under different atmospheres, in the presence or absence of DABCO as $^1O_2$ quencher. The reactions do not occur in the absence of UV light, O_2 or under the presence of DABCO.

Table S1. The reaction of solutions of anthracene or **1** under different conditions

Entry	Substrate	Light conditions	Atmosphere	DABCO	Conversion[a]
1	**anthracene**	UV	O_2	×	✓
2	**anthracene**	vis	O_2	×	very low
3	**anthracene**	UV	N_2	×	×
4	**anthracene**	UV	O_2	✓	×
5[b]	**1**	UV	N_2	×	×
6[b]	**1**	vis	O_2	×	×
7[b]	**1**	UV	O_2	✓	×

Reaction conditions: 3 mM of the substrate in 2 mL of CD_3CN, during 30 min. DABCO added in a 1:1 molar ratio with respect to the substrate. [a]^{1}H NMR conversion. [b]100 mM of the substrate in 15 mL of CH_3CN.

5. Publication 3

"Direct observation of the chemical transformations in $BiVO_4$ photoanodes upon prolonged light-aging treatments"

Ramón Arcas,[a] Drialys Cardenas-Morcoso, [b] Maria Chiara Spadaro,[c] Miguel García-Tecedor,[d] Camilo A. Mesa,*[a] Jordi Arbiol,[c,e] Francisco Fabregat-Santiago,[a] Sixto Giménez,*[a] and Elena Mas-Marzá,*[a]

a. Institute of Advanced Materials (INAM), Universitat Jaume I, 12006 Castelló, Spain.

b. Material Research and Technology (MRT) Department, Luxembourg Institute of Science and Technology (LIST), 41 Rue du Brill L-4422 Belvaux, (Luxembourg)

c. Catalan Institute of Nanoscience and Nanotechnology (ICN2), CSIC and BIST Campus UAB, Bellaterra, Barcelona, Catalonia, 08193, (Spain)

d. Unidad de Procesos Fotoactivados, Instituto IMDEA Energía, Avda. Ramón de la Sagra, 3 Parque Tecnológico de Móstoles E-28935 Móstoles, Madrid, (Spain)

e. ICREA, Pg. Lluís Companys 23, 08010 Barcelona, Catalonia, (Spain).

Sol. RRL 2022, **6**, 2200132

5.1. Candidate's contribution

Nature of Contribution	Extent of Contribution
✓ Contribution to the execution of experimental procedures ✓ Design and execution of electrochemical characterization ✓ Contribution to the analysis of results ✓ Figures and manuscript preparation ✓ Writing of the manuscript ✓ Contribution to the corrections on the manuscript according to the reviewer's comments.	60 %

5.2. Published manuscript

"Direct observation of the chemical transformations in $BiVO_4$ photoanodes upon prolonged light-aging treatments"

Ramón Arcas,[a] Drialys Cardenas-Morcoso, [b] Maria Chiara Spadaro,[c] Miguel García-Tecedor,[d] Camilo A. Mesa,*[a] Jordi Arbiol,[c,e] Francisco Fabregat-Santiago,[a] Sixto Giménez,*[a] and Elena Mas-Marzá,*[a]

a. Institute of Advanced Materials (INAM), Universitat Jaume I, 12006 Castelló, Spain.

b. Material Research and Technology (MRT) Department, Luxembourg Institute of Science and Technology (LIST), 41 Rue du Brill L-4422 Belvaux, (Luxembourg)

c. Catalan Institute of Nanoscience and Nanotechnology (ICN2), CSIC and BIST Campus UAB, Bellaterra, Barcelona, Catalonia, 08193, (Spain)

d. Unidad de Procesos Fotoactivados, Instituto IMDEA Energía, Avda. Ramón de la Sagra, 3 Parque Tecnológico de Móstoles E-28935 Móstoles, Madrid, (Spain)

e. ICREA, Pg. Lluís Companys 23, 08010 Barcelona, Catalonia, (Spain).

Abstract

Exposing $BiVO_4$ photoanodes to light-aging treatments is known to produce a significant photocurrent enhancement. Until now, the interpretation given to this phenomenon has been associated to the formation of oxygen vacancies and little has been reported about chemical changes in the material. Here, we demonstrate the chemical segregation of Bi species toward the surface upon light-aging treatment, which takes place with the concomitant formation of intra-band gap states associated to the oxygen vacancies. We further demonstrate that these intra-band gap states are photoactive and generate photocurrent under infra-red excitation. These results highlight the importance of understanding light-induced effects while employing multinary metal oxide photoelectrodes.

Table of content

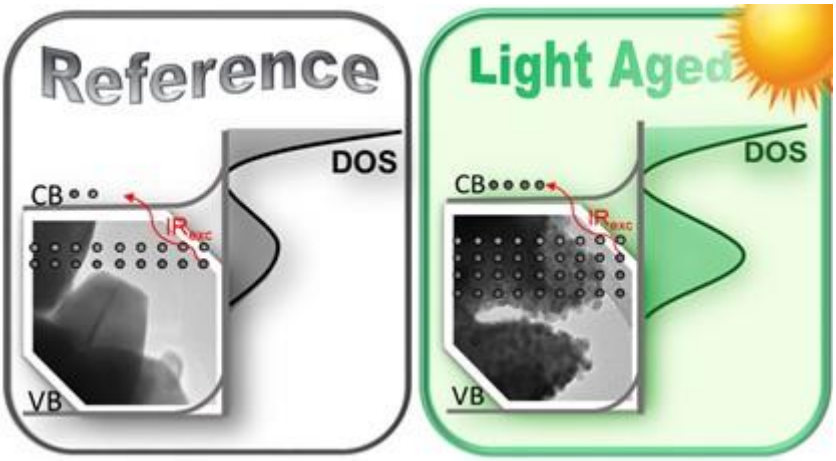

Prolonged light treatments over $BiVO_4$ photoanodes under air conditions induces Bi segregation in the surface, new intra-band gap states, as well as the formation of oxygen vacancies

Introduction

Photoelectrocatalysis (PEC) has emerged as an attractive route to store solar energy involving photoelectro-oxidation and photoelectro-reduction processes. To date, most of the PEC applications developed have been mainly focused either on water splitting to obtain molecular hydrogen[1] or on the reduction of CO_2 to C1 and C2 derivatives.[2] However, there is a growing interest to exploit alternative reactions to obtain compounds with higher added-value for the chemical industry.[3,4] Among the different transformations proposed, the PEC oxidation of primary alcohols to the corresponding aldehydes or acids has attracted significant attention.[5,6,7,8] $BiVO_4$ is a promising material for the development of PEC devices, mainly due to its suitable band gap (2.4 eV), which allows visible light absorption (up to 516 nm)[9] leading to a theoretical photocurrent of ~7.5 $mA \cdot cm^{-2}$ under 1 sun illumination.[10] Furthermore its band structure (i.e. the position of the valence and conduction bands) leads to large photovoltages for driving organic transformations.[11–13] In contrast, the low electron mobility has been identified as the main bottleneck for the PEC performance of this material.[14,15]

The crystal structure of $BiVO_4$ is composed by Bi^{3+} and V^{5+} cations in coordination with O^{2-}.[16] During structural arrangement, the inherent formation of structural defects takes place and their concentration can be controlled by either modifying the synthetic conditions[17] or by post-synthetic treatments.[18,19] The most common defects in this material are oxygen vacancies (OV_s), which are the result of removing O atoms from the lattice.[20–22] It has been shown that these OV_s have a huge impact on the PEC behavior of different photoanodes for the oxygen evolution reaction (OER).[23–26] Specifically, the effect of OV_s on $BiVO_4$ for OER is based on the ability of these defects to increase the bulk carrier concentration and conductivity.[27] Furthermore, an excessive density of OV_s has been correlated to the decrease of performance.[28] The formation of OV_s also creates intra-band gap states, mainly related to V species, where the electrons are located closer to the conduction band.[29] These new electronic states lead to enhanced light absorption and have been related to the reduction of the nearby vanadium atoms from V_{ov}^{5+} to V_{ov}^{4+}.[30] The attempts to directly excite these intra-band gap states associated with oxygen vacancies in $BiVO_4$ have been limited, and only a recent study by Selim et al. reports the use of a transient infrared light to modulate the electrical response of the photoanode.[30] Consequently, infrared excitation of OV_s could clarify the role of these chemical defects on the PEC performance of $BiVO_4$.

On the other hand, prolonged light-aging treatments have been reported to improve the PEC performance of $BiVO_4$ towards OER. Trzésniewski *et al*. showed the enhancement of both photocurrent and photovoltage for undoped and uncatalyzed $BiVO_4$ photoanodes due to a process the authors refer as photocharging (10 hours under illumination at open-circuit conditions).[31] Similar results were reported by Li *et al*. after 20 hours of curing under UV illumination.[32] In both studies, the authors attributed the increase in photocurrent to the reduction of surface

recombination processes as a consequence of the decrease of the defect sites at the surface.[33] The effects of the light-aging treatments were also analyzed by Liu *et al*. using Intensity Modulated Photocurrent Spectroscopy (IMPS).[34] The authors found that after three hours of light treatment, a complex interaction between charge transfer and surface recombination takes place, dominating the suppression of surface recombination at more positive applied potentials. More recently, Feng *et al*. reported the beneficial effects of a photoetching treatment, consisting of 10 minutes illumination at open circuit conditions. This treatment revealed that short illumination periods generates OV_s at the surface, which double the $BiVO_4$ photocurrent due to the significant enhancement of the charge separation efficiency.[35] All these studies demonstrated that short periods (10 min – 20 hours) of light-aging preferentially modify the $BiVO_4$ surface; however, illumination periods longer than 30 hours have not been reported yet.

Few works have tried to analyze the influence of light-aging treatments on $BiVO_4$ using in situ spectroelectrochemical measurements. Particularly, Firet et al. employing a sequence of XPS, UV-Vis and XRS techniques[36] and Venugopal et al. using infrared spectroscopy[37] revealed a dynamic nature of the light treatments on $BiVO_4$/electrolyte interface, however, in these cases the effect of the electrolyte could mask the true effects of light into the material during the light-aging process.

In the present study, we report the effect of prolonged light treatments on the PEC behavior of $BiVO_4$ photoelectrodes for the benzyl alcohol oxidation under air conditions for 48 hours. We have selected this reaction as a model platform for more complex organic transformations, opening the door to more sustainable and environmentally friendly synthetic strategies. Morphological, structural, and electrical measurements allowed us to unravel the different chemical processes taking place in the material during the light treatment and correlate them with the changes observed in PEC response. Moreover, we show for the first time, to the best of our knowledge, steady-state photocurrent generation upon continuous infra-red excitation, confirming the photoactivity of these light-induced electronic states.

Results and discussion

$BiVO_4$ photoanodes were prepared by electrodeposition on FTO substrates, as detailed in the Supporting Information (S.I.) and were illuminated in air to elucidate the influence of prolonged light-aging treatments for the oxidation of benzyl alcohol. Our $BiVO_4$ photoanodes were illuminated at two different light intensities (1 and 3 suns for 1LA-$BiVO_4$ and 3LA-$BiVO_4$, respectively) for 48 h while the other films were kept under dark conditions (Reference). All samples were tested using the operational conditions normally used to oxidize selectively benzyl alcohol to benzaldehyde.[6] A 0.1 M tetrabutylammonium perchlorate ($TBAClO_4$) in CH_3CN solution served as non-aqueous electrolyte in order to avoid the competing water oxidation reaction. A UV filter was incorporated to the ozone free Xe lamp in order to avoid the singlet

oxygen generation and the non-faradaic oxidation of benzyl alcohol, previously reported for a similar system.[5] **Figure 1** compares the photocurrent of 1LA-$BiVO_4$ and 3LA-$BiVO_4$ to that for the Reference, showing a performance enhancement after the light-aging treatment. Similarly, the light-aging (LA) treatment produced films with higher photocurrents towards the oxygen evolution reaction (OER) as shown in S.I., **Figure S2**. The difference in the onset potential between LA and Reference sample observed for OER and not present in ROH oxidation demonstrates the higher catalytic activity of $BiVO_4$ photoanodes towards alcohol oxidation compared to OER.

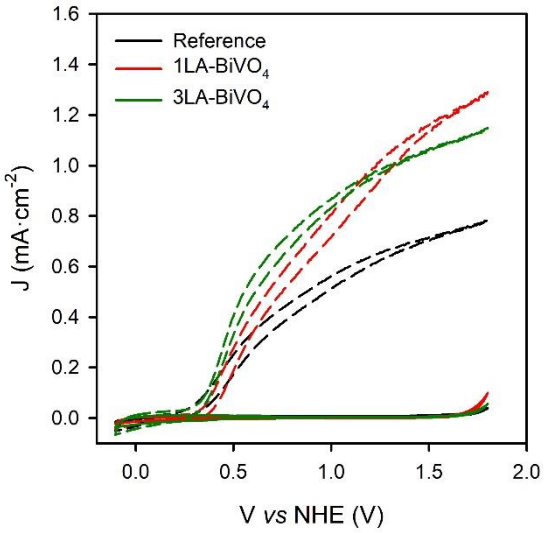

Figure 1. Cyclic Voltammograms of Reference (black), 1LA-$BiVO_4$ (red) and 3LA-$BiVO_4$ (green) photoanodes measured at 20 $mV \cdot s^{-1}$ in 0.1M benzyl alcohol in acetonitrile solution with 0.1M $TBAClO_4$ in the dark (solid lines) and under illumination (100 $mW \cdot cm^{-2}$) [dashed lines].

To study the nature of the LA treatment on $BiVO_4$, we firstly analyzed the morphology and crystalline structure of $BiVO_4$ by scanning electron microscopy (SEM), see **Figures 2a**, **2b** and **Figure S3** in S.I. A clear change in the surface of the $BiVO_4$ photoanodes is observed after LA. More precisely, while the Reference $BiVO_4$ exhibits a homogenous surface (**Figure 2a**), the LA samples are characterized by the presence of several islands (region B in **Figure 2b**) formed by small nanoparticles surrounding the regular $BiVO_4$ grains. Interestingly, EDS analysis for the different samples (**Figure 2c**), revealed that, upon LA treatment, the stoichiometric Bi/V concentration ratio of the Reference $BiVO_4$ divides into Bi deficient (zone A in **Figure 2b**) and Bi enriched domains (zone B in **Figure 2b**). These observations evidence the morphological and chemical modification of the $BiVO_4$ photoanodes due to LA and are directly related to the photocurrent increase shown in **Figure 1**.

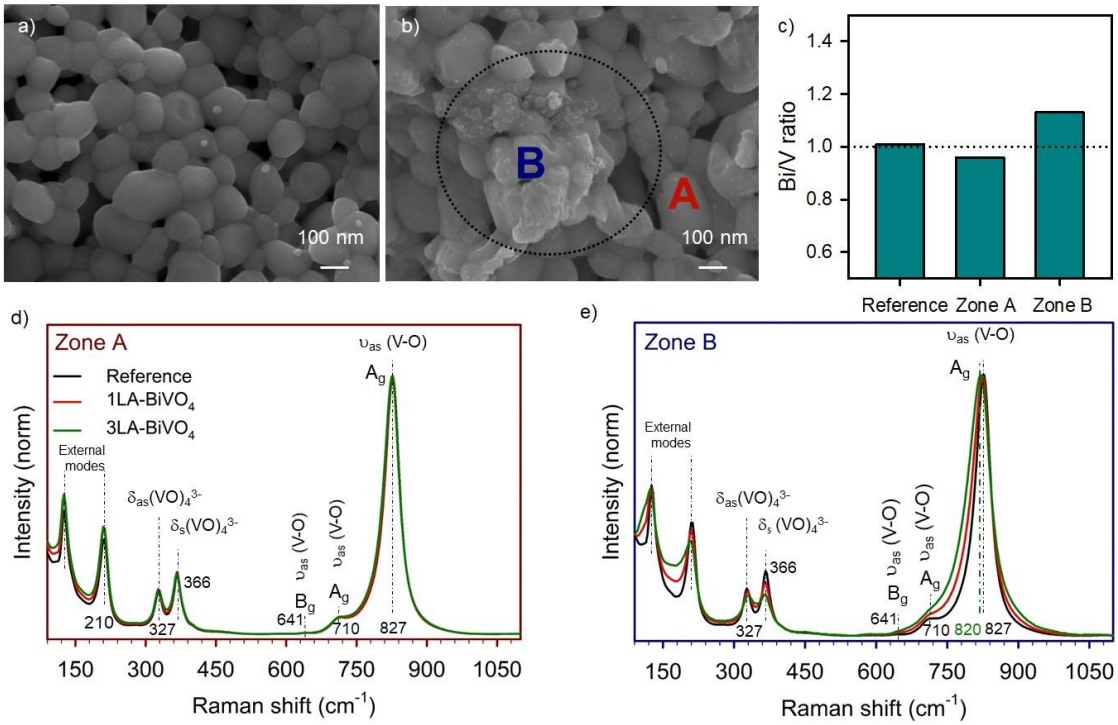

Figure 2. Top-view SEM images of (a) Reference and (b) 1LA-$BiVO_4$. (c) Bi/V concentration ratio for Reference and A and B zones measured by EDS in (b). Raman spectra of (d) Zone A and (e) Zone B.

To further analyze the morphological and chemical modifications of $BiVO_4$ photoanodes induced by LA treatment, we performed Raman spectroscopy on all samples in both zones A and B in **Figure 2b**. As depicted in **Figures 2d** and **2e**, Raman bands perfectly matched with the vibrational modes of $BiVO_4$.[38,39] Comparing the different samples, Raman bands were practically independent of LA in zone A. However, a significant band broadening is observed in zone B after LA, in particular for both the external and A_g modes. This has been previously attributed to the formation of defects, such as oxygen vacancies or hydrogen impurities.[40,41] We note that that oxygen vacancies in metal oxides can also be monitored by other techniques like electron paramagnetic resonance (EPR), [42,43] cathodoluminescence,[44] transient absorption spectroscopy (TAS)[28] and spectroelectrochemistry.[45] On the other hand, XRD measurements did not evidence any relevant modification of the crystalline structure due to LA (**Figure S4** in S.I.).

We move now to investigate the morphological transformation upon light-aging by transmission electron microscopy (TEM). Indeed, compared to the homogeneous surface of the Reference $BiVO_4$ sample (**Figure 3a**), 1LA-$BiVO_4$ evidenced the development of a thin amorphous layer, as the origin of the growth of small nanoparticles, as observed in **Figure 3b**, on the $BiVO_4$ crystallites which results in a granulated surface (**Figure 3c**). Additionally, scanning transmission electron microscopy combined with electron energy loss spectroscopy (STEM-EELS) proved the increase of Bi species on the surface of $BiVO_4$ crystallites after LA (**Figure S5** in S.I.). It is apparent from **Figure 3** that prolonged electron beam irradiation undergoes in a dramatic morphological transformation of our $BiVO_4$. Interestingly, the migration of some atomic

species from the bulk to form particles at the surface could be recorded during the electron beam irradiation (the complete sequence can be visualized in the video freely available at 10.5281/zenodo.5643642) and the final morphology presented the segregation of a significant number of nanoparticles on top of the $BiVO_4$ grains (**Figures 3c** and **3d**).

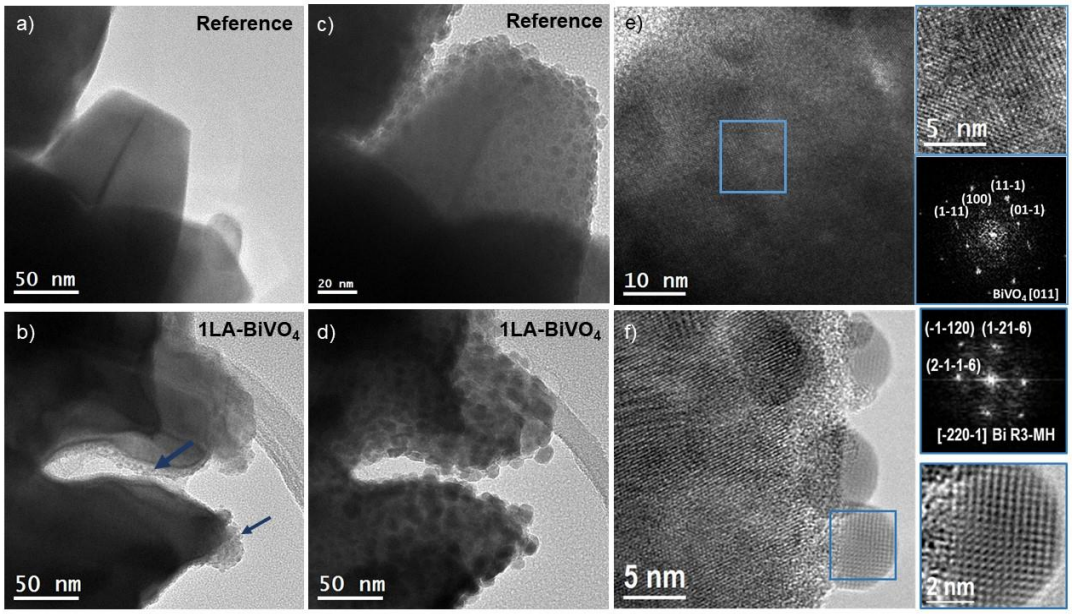

Figure 3. TEM images (a) - (b) before and (c) - (d) after electron beam irradiation. (a) and (c) correspond to the Reference and (b) and (d) correspond to the 1LA-$BiVO_4$, demonstrating that the $BiVO_4$ morphology transforms during either light or electron beam irradiation. (e) and (f) HR-TEM and power spectra images of bulk and surface $BiVO_4$ grains respectively after electron beam irradiation.

To understand the nature and composition of these aggregates, we carried out a detailed HR-TEM characterization. **Figure 3e** shows the HR-TEM image of the bulk area of a $BiVO_4$ grain. The power spectrum (Fast Fourier Transform) analysis of this area (inset in **Figure 3e**) confirms the clinobisvanite $BiVO_4$ phase I112/B (s.g. 15) oriented along its [011] zone axis. However, focusing the electron beam on the segregated nanoparticles (**Figure 3f**), the power spectrum analysis clearly indicates the presence of Bi species. The results of the power spectra analysis in different areas matched with two different Bi structures: metallic Bi with hexagonal structure (R3-MH s.g. 166) oriented along [241] and [5-51] and monoclinic Bi_2O_3 oriented along [110] and [-114] zone axis, indicating the plausible chemical composition of this segregated particles (see **Figure S6** in S.I.).

We note that the electron beam in both SEM and TEM measurements is clearly different in wavelengths and intensities compared to sunlight (LA treatment). However, the morphology and presence of Bi-rich particles at the surface on the LA treated sample (**Figure S5** in S.I.) suggests that the localized structural modification induced by LA is alike to that presented after electron beam irradiation, involving in both cases the segregation of Bi species.

Summarizing, we have shown by different spectroscopic and microscopic techniques, that LA induces OV_S and a Bi segregation process. These processes have been reported previously in different studies, where $BiVO_4$ has undergone prolonged exposure to light, including light treatments studies at open circuit conditions and stability tests under operational conditions.[18,25,31,33,35,36,46] In all cases different morphological and compositional processes take place at the electrode in different electrolytes and in different structures of $BiVO_4$ converging in a higher proportion of Bi compared to V.

Now, we turn to investigate plausible mechanistic insights of the effect of LA on the functional performance of the photoanodes (as showed in **Figure 1**). To this end, we perform Impedance Spectroscopy (IS) measurements under illumination to extract Nyquist plots, at different potentials, relevant for the selective oxidation of benzyl alcohol to benzaldehyde. **Figure 4a** shows one of the experimentally obtained Nyquist plot and the selected equivalent circuit (inset) used to fit the data, which has been generally employed for different metal oxide photoanodes.[47] This equivalent circuit is commonly used to separate the contribution of bulk and surface processes in the photoanodes.[33] The elements employed are: R_s (series resistance), C_{bulk} (bulk capacitance), R_{bulk} (bulk resistance), R_{ct} (charge transfer resistance) and C_s (surface capacitance). The obtained capacitances and resistances as a function of the applied potential are reported in **Figures S7** and **S8** in S.I.

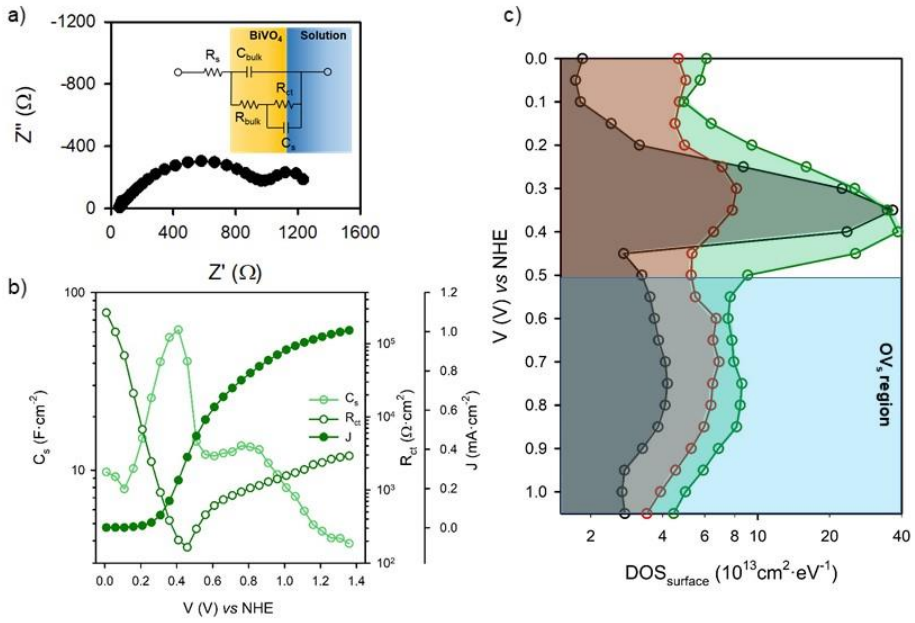

Figure 4. (a) Nyquist plot of Reference sample and selected equivalent circuit to fit the experimental data of the Reference and LA samples. (b) Surface capacitance (C_s), charge transfer resistance (R_{ct}) and photocurrent (J) of Reference $BiVO_4$. (c) Density of surface states as a function of applied potential. Reference (Black), 1LA-$BiVO_4$ (Red) and 3LA-$BiVO_4$ (Green). Measurements were performed under illumination, in 0.1 M benzyl alcohol oxidation conditions.

Figures 4b and **S7a** show the presence of two peaks at 0.35 V and 0.75 V vs NHE, for the surface capacitance (C_s light green empty circles in **Figure 4b**) of all tested samples. The peak at 0.35 V is coincident with the valley of the R_{ct} (dark green empty circles in **Figure 4b**), and both features take place at the same potential associated to the benzyl alcohol oxidation onset (dark green full cycles). A similar behavior has been already observed in different metal oxides, where a surface capacitance peak is observed just before the onset for OER. This behavior on hematite photoanodes was assigned to charge transfer controlled by surface state charging associated to intermediate species in the reaction process.[47] Consequently, we suggest that ROH oxidation is controlled by a surface state, which dictates the hole transfer process from the electrode to the substrate. We note that this DOS is lower for the 1LA-$BiVO_4$ sample compared to the Reference material. A more detailed study of the influence of this surface capacitance on the photoelectrooxidation of benzyl alcohol remains beyond the scope of the present work.

On the other hand, the broader peak at 0.75 V vs NHE either in C_s and C_{bulk} is assigned to the V^{4+}/V^{5+} redox process, which has previously been related to the presence of OV_s in $BiVO_4$ films.[33,48,49] The presence of this peak in the reference sample suggests the intrinsic formation of this defects during the crystallization step.

Considering the C_s, the energetic distribution of these surface states, $g(E_{Fn})$ or DOS, can be estimated by equation 1

$$C_s = q \cdot g(E_{F_n}) \qquad Eq.\ 1$$

where q is the elementary charge ($1.6x10^{-19}$ C). **Figure 4c** shows that the calculated DOS associated to OV_s scales with the irradiation intensity, confirming the increase of the V^{4+} species during the light-aging process as mentioned previously in Raman. This result confirms the modification of the electronic environment of $BiVO_4$ during the LA. These observations are consistent with the results reported by Feng et al.[35] although, the higher concentration of OV_s, reflected on the bulk capacitance suggests that prolonged LA affects not only the bulk but also the surface of the film. Such higher OV_s concentration could also be responsible for the slightly lower photocurrent density found for the 3LA-$BiVO_4$ sample in **Figure 1**. This is supported by the detrimental role of a "too high" concentration of OV_s in $BiVO_4$ photoanodes as suggested in references,[23,41] which is also consistent with a recent report by Corby et al. in which an excessive concentration of OV_s could be negative for the PEC performance of WO_3 photoanodes,[28] suggesting that this effect may be general for metal oxide photoelectrodes. Furthermore, we have performed a long light aging treatment for 3 weeks (LT-1LA-$BiVO_4$, **Figure S9** in SI), which compared to 1LA-$BiVO_4$ leads to an increased DOS of OV_s, and lower photocurrent, also in good agreement with this hypothesis. Collectively, our observations also suggest the possibility that above certain levels, Bi segregation at the surface of the $BiVO_4$ could impede the charge transfer

of holes to the solution. In this case, the Bi species on the surface of $BiVO_4$ could operate as a blocking layer for surface states as shown in **Figure S7** in S.I.

Finally, to confirm the generation of new intra-band gap electronic states associated with OV_s in $BiVO_4$, we used an infra-red (IR) continuous-wave laser as light source to extract steady-state photocurrents for the oxidation of benzyl alcohol. Upon sub-bandgap excitation, photocurrent generation can only be due to the activation of intra-bandgap transitions in the semiconductor material (see **Figure S10** in SI). This approach, to the best of our knowledge, uses for the first-time infrared radiation (980 nm, 1.26 eV) to selectively excite the trapped electrons from the intra-bandgap states to the conduction band. **Figure 5a** shows the IR chopped chronoamperometry measurements for Reference and 3LA-$BiVO_4$ samples at 0.8 V vs NHE. The measured photocurrent stems from the excitation of the intra-bandgap states. The highest photocurrent of the 3LA-$BiVO_4$ sample is fully consistent with its increased density of intra-bandgap states, associated with OV_s (**Figure 5b**). Surprisingly, the photocurrent of the 3LA-$BiVO_4$ sample almost doubled compared to that for the Reference (from ~50 to ~90 nA cm^{-2}). This is in excellent agreement with the equivalent increase of the DOS (from ~4 to ~$8 \cdot 10^{13}$ cm^2 eV^{-1}) associated to OV_s (**Figure 4c**).

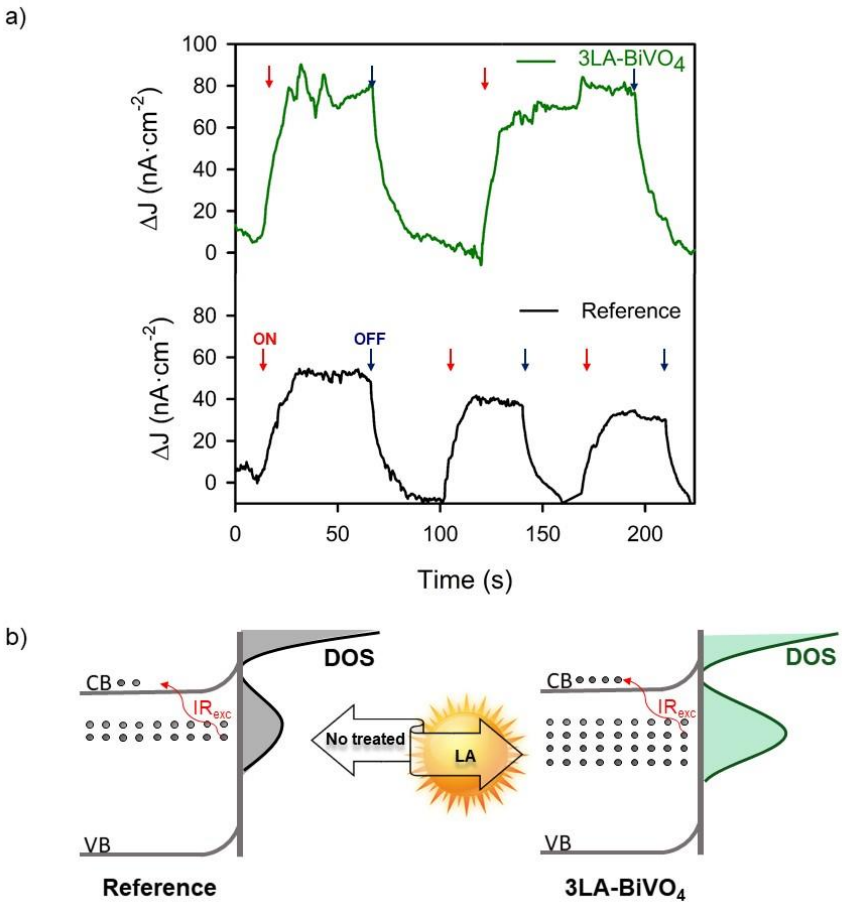

Figure 5. (a) Infra-red (IR) chopped chronoamperometry measurements of Reference (Black) and 3LA-$BiVO_4$ (green). (b) Band diagrams representation of the fresh and light-aged treated $BiVO_4$ samples.

We note that, although surface reduction of $BiVO_4$[50] and the increase of surface Bi species[25,51] have been previously reported, both effects have been characterized either after or during operando conditions and, consequently, they were attributed to vanadium dissolution.[37] On the contrary, the light-aging treatments and the structural characterization performed here take place in the absence of electrolyte. Therefore, the bismuth-rich surface observed is a direct consequence of the incidence of light on $BiVO_4$. Moreover, we demonstrate the correlation between the segregation of small Bi-rich nanoparticles and the formation of new intra-bandgap states associated to oxygen vacancies. The photoactivity of these intra-bandgap states observed under infra-red illumination opens new perspectives for the development of competitive $BiVO_4$ photoanodes.

Conclusions

Herein, we have investigated the effect of prolonged light-aging on $BiVO_4$ photoanodes, providing a direct observation of the chemical and structural modifications after light-aging treatments. We showed that light-assisted treatments under air conditions led to the chemical transformation of the material, being more pronounced upon increased light intensity used during LA. Electrical, PEC and HR-TEM characterizations allowed assigning the chemical transformations observed to the segregation of Bi species on top of $BiVO_4$ grains, leading to the formation of new intra-bandgap states associated to oxygen vacancies. Moreover, effective photocurrent generation from these intra-bandgap states was demonstrated by infra-red light excitation, confirming the formation of oxygen vacancies during the light-aging treatment and their implications on the generation of infra-red photocurrent. These results highlight the importance of understanding the light-induced effects while employing multinary metal oxide photoelectrodes either for OER or for the synthesis of high added-value chemicals.

Acknowledgements

The authors want to acknowledge the Ministerio de Economía y Competitividad (MINECO) from Spain (ENE2017-85087-C3-1-R and PID2020-116093RB-C41 and C43), University Jaume I (UJI-B2019-20) and Generalitat Valenciana (PROMETEO/2020/028) for financial support. Serveis Centrals d'Instrumentació Científica from UJI are also acknowledged for SEM, TEM Raman and XRD measurements. M. C. S and J. A. acknowledge funding from Generalitat de Catalunya 2017 SGR 327. ICN2 is supported by the Severo Ochoa program from Spanish MINECO (Grant No. SEV-2017-0706) and is funded by the CERCA Programme / Generalitat de Catalunya. M.C.S. has received funding from the European Union's Horizon 2020 research and innovation programme under the Marie Skłodowska-Curie grant agreement No. 754510 (PROBIST) and the Severo Ochoa programme. C.A.M acknowledges the University Jaume I for the postdoc fellowship POSDOC/2019/20 and Generalitat Valenciana for the APOSTD/2021/251

fellowship. Dr. Beatriz Julián-López and Laura Montañés are also acknowledged for their help with the measurements with the infrared laser beam and some electrodes preparation.

References

(1) Grätzel, M. Photoelectrochemical Cells. *Nature*. Nature Publishing Group November 15, 2001, pp 338–344.

(2) Kumar, B.; Llorente, M.; Froehlich, J.; Dang, T.; Sathrum, A.; Kubiak, C. P. Photochemical and Photoelectrochemical Reduction of CO2 . *Annu. Rev. Phys. Chem.* **2012**, *63* (1), 541–569.

(3) Sayama, K. Production of High-Value-Added Chemicals on Oxide Semiconductor Photoanodes under Visible Light for Solar Chemical-Conversion Processes. *ACS Energy Letters*. American Chemical Society May 11, 2018, pp 1093–1101.

(4) Lhermitte, C. R.; Sivula, K. Alternative Oxidation Reactions for Solar-Driven Fuel Production. *ACS Catal.* **2019**, *9* (3), 2007–2017.

(5) Arcas, R.; Peris, E.; Mas-Marzá, E.; Fabregat-Santiago, F. Revealing the Contribution of Singlet Oxygen in the Photoelectrochemical Oxidation of Benzyl Alcohol. *Sustain. Energy Fuels* **2021**, *5* (4), 956–962.

(6) Li, T.; Kasahara, T.; He, J.; Dettelbach, K. E.; Sammis, G. M.; Berlinguette, C. P. Photoelectrochemical Oxidation of Organic Substrates in Organic Media. *Nat. Commun.* **2017**, *8* (1), 1–5.

(7) Cha, H. G.; Choi, K. S. Combined Biomass Valorization and Hydrogen Production in a Photoelectrochemical Cell. *Nat. Chem.* **2015**, *7* (4), 328–333.

(8) Liu, D.; Liu, J. C.; Cai, W.; Ma, J.; Yang, H. Bin; Xiao, H.; Li, J.; Xiong, Y.; Huang, Y.; Liu, B. Selective Photoelectrochemical Oxidation of Glycerol to High Value-Added Dihydroxyacetone. *Nat. Commun.* **2019**, *10* (1).

(9) Long, M.; Cai, W.; Kisch, H. Visible Light Induced Photoelectrochemical Properties of N-BiVO4 and n-BiVO4/p-Co3O4. *J. Phys. Chem. C* **2008**, *112* (2), 548–554.

(10) Kim, J. H.; Lee, J. S. Elaborately Modified BiVO4 Photoanodes for Solar Water Splitting. *Adv. Mater.* **2019**, *31* (20), 1806938.

(11) Cooper, J. K.; Gul, S.; Toma, F. M.; Chen, L.; Liu, Y. S.; Guo, J.; Ager, J. W.; Yano, J.; Sharp, I. D. Indirect Bandgap and Optical Properties of Monoclinic Bismuth Vanadate. *J. Phys. Chem. C* **2015**, *119* (6), 2969–2974.

(12) Cooper, J. K.; Gul, S.; Toma, F. M.; Chen, L.; Glans, P. A.; Guo, J.; Ager, J. W.; Yano, J.; Sharp, I. D. Electronic Structure of Monoclinic BiVO4. *Chem. Mater.* **2014**, *26* (18), 5365–5373.

(13) Zhao, Z.; Li, Z.; Zou, Z. Electronic Structure and Optical Properties of Monoclinic Clinobisvanite BiVO4. *Phys. Chem. Chem. Phys.* **2011**, *13* (10), 4746–4753.

(14) Abdi, F. F.; Savenije, T. J.; May, M. M.; Dam, B.; Van De Krol, R. The Origin of Slow Carrier Transport in BiVO4 Thin Film Photoanodes: A Time-Resolved Microwave Conductivity Study. *J. Phys. Chem. Lett.* **2013**, *4* (16), 2752–2757.

(15) Ziwritsch, M.; Müller, S.; Hempel, H.; Unold, T.; Abdi, F. F.; Krol, R. van de; Friedrich, D.; Eichberger, R. Direct Time-Resolved Observation of Carrier Trapping and Polaron Conductivity in BiVO4. *ACS Energy Lett.* **2016**, *1* (5), 888–894.

(16) Luo, W.; Wang, J.; Zhao, X.; Zhao, Z.; Li, Z.; Zou, Z. Formation Energy and Photoelectrochemical Properties of BiVO4 after Doping at Bi3+ or V5+ Sites with Higher Valence Metal Ions. *Phys. Chem. Chem. Phys.* **2013**, *15* (3), 1006–1013.

(17) Wu, J. M.; Chen, Y.; Pan, L.; Wang, P.; Cui, Y.; Kong, D. C.; Wang, L.; Zhang, X.; Zou, J. J. Multi-Layer Monoclinic BiVO4 with Oxygen Vacancies and V4+ Species for Highly Efficient Visible-Light Photoelectrochemical Applications. *Appl. Catal. B Environ.* **2018**, *221*, 187–195.

(18) Lamers, M.; Fiechter, S.; Friedrich, D.; Abdi, F. F.; Van De Krol, R. Formation and Suppression of Defects during Heat Treatment of BiVO4 Photoanodes for Solar Water Splitting. *J. Mater. Chem. A* **2018**, *6* (38), 18694–18700.

(19) Lamm, B.; Trześniewski, B. J.; Döscher, H.; Smith, W. A.; Stefik, M. Emerging Postsynthetic Improvements of BiVO4 Photoanodes for Solar Water Splitting. *ACS Energy Lett.* **2017**, *3* (1), 112–124.

(20) Wang, Z.; Mao, X.; Chen, P.; Xiao, M.; Monny, S. A.; Wang, S.; Konarova, M.; Du, A.; Wang, L. Understanding the Roles of Oxygen Vacancies in Hematite-Based Photoelectrochemical Processes. *Angew. Chemie Int. Ed.* **2019**, *58* (4), 1030–1034.

(21) Gan, J.; Lu, X.; Wu, J.; Xie, S.; Zhai, T.; Yu, M.; Zhang, Z.; Mao, Y.; Wang, S. C. I.; Shen, Y.; et al. Oxygen Vacancies Promoting Photoelectrochemical Performance of In2O3 Nanocubes. *Sci. Rep.* **2013**, *3*.

(22) Crespillo, M. L.; Graham, J. T.; Agulló-López, F.; Zhang, Y.; Weber, W. J. Isolated Oxygen Vacancies in Strontium Titanate Shine Red: Optical Identification of Ti3+ Polarons. *Appl. Mater. Today* **2018**, *12*, 131–137.

(23) Fernández-Climent, R.; Giménez, S.; García-Tecedor, M. The Role of Oxygen Vacancies in Water Splitting Photoanodes. *Sustain. Energy Fuels* **2020**, *4* (12), 5916–5926.

(24) Wang, W.; Strohbeen, P. J.; Lee, D.; Zhou, C.; Kawasaki, J. K.; Choi, K.-S.; Liu, M.; Galli, G. The Role of Surface Oxygen Vacancies in BiVO4 . *Chem. Mater.* **2020**, *32* (7), 2899–2909.

(25) Gao, R.; Wang, L. Stable Cocatalyst-Free BiVO4 Photoanodes with Passivated Surface States for Photocorrosion Inhibition. *Angew. Chemie Int. Ed.* **2020**, *59* (51), 23094–23099.

(26) Mesa, C. A.; Steier, L.; Moss, B.; Francàs, L.; Thorne, J. E.; Grätzel, M.; Durrant, J. R. Impact of the Synthesis Route on the Water Oxidation Kinetics of Hematite Photoanodes. *J. Phys. Chem. Lett.* **2020**, *11* (17), 7285–7290.

(27) Seo, H.; Ping, Y.; Galli, G. Role of Point Defects in Enhancing the Conductivity of BiVO4. *Chem. Mater.* **2018**, *30* (21), 7793–7802.

(28) Sacha Corby; Laia Francàs; Andreas Kafizas; R. Durrant, J. Determining the Role of Oxygen Vacancies in the Photoelectrocatalytic Performance of WO 3 for Water Oxidation. *Chem. Sci.* **2020**, *11* (11), 2907–2914.

(29) Walsh, A.; Yan, Y.; Huda, M. N.; Al-Jassim, M. M.; Wei, S.-H. Band Edge Electronic Structure of BiVO 4 : Elucidating the Role of the Bi s and V d Orbitals. *Chem. Mater.* **2009**, *21*, 547–551.

(30) Selim, S.; Pastor, E.; García-Tecedor, M.; Morris, M. R.; Francàs, L.; Sachs, M.; Moss, B.; Corby, S.; Mesa, C. A.; Gimenez, S.; et al. Impact of Oxygen Vacancy Occupancy on Charge Carrier Dynamics in BiVO4 Photoanodes. *J. Am. Chem. Soc.* **2019**, *141* (47), 18791–18798.

(31) Trześniewski, B. J.; Smith, W. A. Photocharged BiVO4 Photoanodes for Improved Solar Water Splitting. *J. Mater. Chem. A* **2016**, *4* (8), 2919–2926.

(32) Li, T.; He, J.; Peña, B.; Berlinguette, C. P. Curing BiVO4 Photoanodes with Ultraviolet Light Enhances Photoelectrocatalysis. *Angew. Chemie - Int. Ed.* **2016**, *55* (5), 1769–1772.

(33) Trześniewski, B. J.; Digdaya, I. A.; Nagaki, T.; Ravishankar, S.; Herraiz-Cardona, I.;

Vermaas, D. A.; Longo, A.; Gimenez, S.; Smith, W. A. Near-Complete Suppression of Surface Losses and Total Internal Quantum Efficiency in BiVO4 Photoanodes. *Energy Environ. Sci.* **2017**, *10* (6), 1517–1529.

(34) Liu, E. Y.; Thorne, J. E.; He, Y.; Wang, D. Understanding Photocharging Effects on Bismuth Vanadate. *ACS Appl. Mater. Interfaces* **2017**, *9* (27), 22083–22087.

(35) Feng, S.; Wang, T.; Liu, B.; Hu, C.; Li, L.; Zhao, Z.; Gong, J. Enriched Surface Oxygen Vacancies of Photoanodes by Photoetching with Enhanced Charge Separation. *Angew. Chemie Int. Ed.* **2020**, *59* (5), 2044–2048.

(36) Firet, N. J.; Venugopal, A.; Blommaert, M. A.; Cavallari, C.; Sahle, C. J.; Longo, A.; Smith, W. A. Chemisorption of Anionic Species from the Electrolyte Alters the Surface Electronic Structure and Composition of Photocharged BiVO4. *Chem. Mater.* **2019**, *31* (18), 7453–7462.

(37) Venugopal, A.; Kas, R.; Hau, K.; Smith, W. A. Operando Infrared Spectroscopy Reveals the Dynamic Nature of Semiconductor−Electrolyte Interface in Multinary Metal Oxide Photoelectrodes. *J. Am. Chem. Soc.* **2021**, *143*, 18581–18591.

(38) Zhou, D.; Pang, L. X.; Qu, W. G.; Randall, C. A.; Guo, J.; Qi, Z. M.; Shao, T.; Yao, X. Dielectric Behavior, Band Gap, in Situ X-Ray Diffraction, Raman and Infrared Study on (1 - X)BiVO4-x(Li0.5Bi 0.5)MoO4 Solid Solution. *RSC Adv.* **2013**, *3* (15), 5009–5014.

(39) Wang, S.; Chen, P.; Yun, J. H.; Hu, Y.; Wang, L. An Electrochemically Treated BiVO4 Photoanode for Efficient Photoelectrochemical Water Splitting. *Angew. Chemie - Int. Ed.* **2017**, *56* (29), 8500–8504.

(40) Xu, X.; Xu, Y.; Xu, F.; Jiang, G.; Jian, J.; Yu, H.; Zhang, E.; Shchukin, D.; Kaskel, S.; Wang, H. Black BiVO4: Size Tailored Synthesis, Rich Oxygen Vacancies, and Sodium Storage Performance. *J. Mater. Chem. A* **2020**, *8* (4), 1636–1645.

(41) Wang, G.; Ling, Y.; Lu, X.; Qian, F.; Tong, Y.; Zhang, J. Z.; Lordi, V.; Rocha Leao, C.; Li, Y. Computational and Photoelectrochemical Study of Hydrogenated Bismuth Vanadate. *J. Phys. Chem. C* **2013**, *117* (21), 10957–10964.

(42) Zhang, X.; Du, X. Oxygen Vacancies Confined in Nickel Oxide Nanoprism Arrays for Promoted Electrocatalytic Water Splitting. *New J. Chem.* **2020**, *44* (5), 1703–1706.

(43) Eichel, R. A. Structural and Dynamic Properties of Oxygen Vacancies in Perovskite

Oxides—analysis of Defect Chemistry by Modern Multi-Frequency and Pulsed EPR Techniques. *Phys. Chem. Chem. Phys.* **2010**, *13* (2), 368–384.

(44) Prades, J. D.; Arbiol, J.; Cirera, A.; Morante, J. R.; Avella, M.; Zanotti, L.; Comini, E.; Faglia, G.; Sberveglieri, G. Defect Study of SnO2 Nanostructures by Cathodoluminescence Analysis: Application to Nanowires. *Sensors Actuators B Chem.* **2007**, *126* (1), 6–12.

(45) Francàs, L.; Corby, S.; Selim, S.; Lee, D.; Mesa, C. A.; Godin, R.; Pastor, E.; Stephens, I. E. L.; Choi, K. S.; Durrant, J. R. Spectroelectrochemical Study of Water Oxidation on Nickel and Iron Oxyhydroxide Electrocatalysts. *Nat. Commun.* **2019**, *10* (1), 1–10.

(46) Lee, D. K.; Choi, K. S. Enhancing Long-Term Photostability of BiVO4 Photoanodes for Solar Water Splitting by Tuning Electrolyte Composition. *Nat. Energy 2017 31* **2017**, *3* (1), 53–60.

(47) Klahr, B.; Gimenez, S.; Fabregat-Santiago, F.; Hamann, T.; Bisquert, J. Water Oxidation at Hematite Photoelectrodes: The Role of Surface States. *J. Am. Chem. Soc* **2012**, *134*, 36.

(48) Yalavarthi, R.; Zbořil, R.; Schmuki, P.; Naldoni, A.; Kment, Š. Elucidating the Role of Surface States of BiVO4 with Mo Doping and a CoOOH Co-Catalyst for Photoelectrochemical Water Splitting. *J. Power Sources* **2021**, *483*, 229080.

(49) Shi, Q.; Murcia-López, S.; Tang, P.; Flox, C.; Morante, J. R.; Bian, Z.; Wang, H.; Andreu, T. Role of Tungsten Doping on the Surface States in BiVO4 Photoanodes for Water Oxidation: Tuning the Electron Trapping Process. *ACS Catal.* **2018**, *8* (4), 3331–3342.

(50) Hermans, Y.; Murcia-López, S.; Klein, A.; Jaegermann, W. BiVO4 Surface Reduction upon Water Exposure. *ACS Energy Lett.* **2019**, *4* (10), 2522–2528.

(51) Toma, F. M.; Cooper, J. K.; Kunzelmann, V.; McDowell, M. T.; Yu, J.; Larson, D. M.; Borys, N. J.; Abelyan, C.; Beeman, J. W.; Yu, K. M.; et al. Mechanistic Insights into Chemical and Photochemical Transformations of Bismuth Vanadate Photoanodes. *Nat. Commun.* **2016**, *7* (1), 1–11.

5.3. Supporting information

"Direct observation of the chemical transformations in BiVO4 photoanodes upon prolonged light-aging treatments"

Ramón Arcas,[a] Drialys Cardenas-Morcoso, [b] Maria Chiara Spadaro,[c] Miguel García-Tecedor,[d] Camilo A. Mesa,*[a] Jordi Arbiol,[c,e] Francisco Fabregat-Santiago,[a] Sixto Giménez,*[a] and Elena Mas-Marzá,*[a]

a. Institute of Advanced Materials (INAM), Universitat Jaume I, 12006 Castelló, Spain.

b. Material Research and Technology (MRT) Department, Luxembourg Institute of Science and Technology (LIST), 41 Rue du Brill L-4422 Belvaux, (Luxembourg)

c. Catalan Institute of Nanoscience and Nanotechnology (ICN2), CSIC and BIST Campus UAB, Bellaterra, Barcelona, Catalonia, 08193, (Spain)

d. Unidad de Procesos Fotoactivados, Instituto IMDEA Energía, Avda. Ramón de la Sagra, 3 Parque Tecnológico de Móstoles E-28935 Móstoles, Madrid, (Spain)

e. ICREA, Pg. Lluís Companys 23, 08010 Barcelona, Catalonia, (Spain).

Experimental Section

Preparation of Zr doped $BiVO_4$ photoanodes

All reagents and solvents employed were purchased and used as received, without extra purification. Bismuth(III) nitrate pentahydrate (≥98.0%), zirconyl chloride octahydrate (98.0%), Vanadium(IV)-oxy acetylacetonate (98.0%), Sodium hydroxide (pellets for analysis), Tetrabutylammonium perchlorate (≥99.0% electrochemical degree), Benzyl alcohol (anhydrous 99.8%), Ferrocene (98.0%,), and Dimethylsulfoxide (anhydrous) were purchased from Sigma Aldrich; Acetonitrile (HPLC) were purchased from Scharlab. Fluorine-doped tin oxide (FTO)-coated glass slides were purchased from Hartford glass (sheet resistance 15 Ω/cm^2).

The synthesis and fabrication of 2.5 % zirconium doped $BiVO_4$ electrodes over fluorine-doped tin oxide (FTO) coated glass substrates were performed following a reported procedure.[1] This method consists of electrodeposition of a $Bi(NO_3)_3 \cdot 5H_2O$ (20mM) and $ZrCl_2O \cdot 8H_2O$ (0.5 mM) solution in ethylene glycol followed by drop-casting of a solution of $VO(acac)_2$ (0.15 M) in DMSO. The electrodes were calcined at 500ºC for 2 h with a heating rate of 2 $ºC \cdot min^{-1}$. Finally, the excess of V_2O_5 was removed by immersing the electrodes in a KOH 1 M solution for 20-30 min.

Prolonged light-aging treatments.

The $BiVO_4$ photoelectrodes were illuminated for 48 h directly using an ozone-free 300 W Xenon (Xe) lamp under ambient conditions. Note that, during the light-aging treatment the photoelectrode is exposed to ambient conditions, without being in contact to the electrolyte. We termed this process as Light-Aging treatment (LA). The power of the lamp was calibrated to 100 $mW \cdot cm^{-2}$ or 300 $mW \cdot cm^{-2}$, corresponding to 1 sun (1LA-$BiVO_4$) and 3 sun (3LA-$BiVO_4$) irradiated samples, respectively.

Morphological and structural characterization.

Field Emission Scanning Electron Microscopy (SEM) was performed with a JSM-7000F JEL FEG-SEM system (Tokyo, Japan) equipped with an INCA 400 Oxford EDS analyzer (Oxford, U.K.) and operating at 25 kV. Raman spectroscopy was carried out with a WiTec apyron system, equipped with a 300 mm focal length UHTS 300 spectrometer system. The scanned area of combined spectra was 40 x 24 m^2 with a laser power of 2 mW and an integration time of 0.5 s. The crystalline structure of $BiVO_4$ was assessed by X-ray diffraction (XRD) collected on a Rigaku Miniflex 600, (Rigaku Corporation, Tokyo, Japan) with copper Kα radiation (l = 1.5418 Å) operating at a grazing incidence of 1º, at a scan rate of 3º min^{-1}. High-resolution transmission electron microscopy (HRTEM) together with scanning transmission electron microscopy (STEM) investigation was performed on a field emission gun FEI Tecnai F20 microscope at 200 kV with a point-to-point resolution of 0.19 nm. High angle annular dark-field (HAADF) STEM was

combined with electron energy loss spectroscopy (EELS) in the Tecnai F20 microscope by using a GATAN QUANTUM energy filter. To prepare the TEM samples, a $BiVO_4$ photoanode was scratched and the obtained powder was deposited on a TEM grid. After deposition, the grid was illuminated at 1 sun following the same procedure to perform the light treatment in 1LA-$BiVO_4$.

(Photo)electrochemical characterization.

Cyclic voltammetry (CV) and Impedance Spectroscopy (IS) measurements were performed on a PGSTAT302N potentiostat (Metrohm-Autolab, The Netherlands). The photoelectrochemical cell consisted of a one-compartment, three-electrode configuration quartz cell. Non-aqueous $Ag/AgNO_3$ electrode (ALS, Japan) and a platinum foil (25x25 mm, 0.1 mm thick, Alfa Aesar) were employed as reference and counter electrodes respectively, while a 0.1 M tetrabutylammonium perchlorate ($TBAClO_4$) in CH_3CN solution served as non-aqueous electrolyte. An ozone-free 300 W Xenon (Xe) lamp calibrated with a thermopile to 100 $mW \cdot cm^{-2}$ was used for the photoelectrochemical experiments. CV measurements were carried out at 50 $mV \cdot s^{-1}$. IS measurements were performed at selected applied bias with a sinusoidal perturbation of 20 mV and a frequency range from 100 kHz to 50 mHz. We have homogenized all potentials against NHE when measurements are performed in an organic electrolyte and against RHE when measurements are performed in water. For this purpose, we estimate the $E_{1/2}$ of the Ferrocene/Ferrocinium couple redox peak (see Figure S1) in our experimental conditions (in organic electrolytes) and compare with the reported $E_{1/2}$ (0.4V vs NHE).[2-3] Finally, the Nernst equation was employed to normalize aqueous systems following equation 1.

$$V_{RHE} = V_{Ag/AgCl} + V^0_{Ag/AgCl} + 0.059 \cdot pH \qquad \text{Eq.1}$$

Infra-red (IR) photoelectrochemical characterization.

Chronoamperometry measurements under IR were performed using a mobile Palmsens3 potentiostat (Compact electrochemical interfaces). For these measurements, identical experimental conditions as those described above were employed. An infrared diode laser (MDL-III-980-2W) from Roithner LaserTechnik (980 nm ± 5 nm, 2 W cw, stability < 5%, beam aperture of 5 x 8 mm^2) was employed to illuminate the $BiVO_4$ photoanodes, focusing the beam as close as possible to the photoanode. Manual chopping was carried out.

Cyclic voltammetries measurements

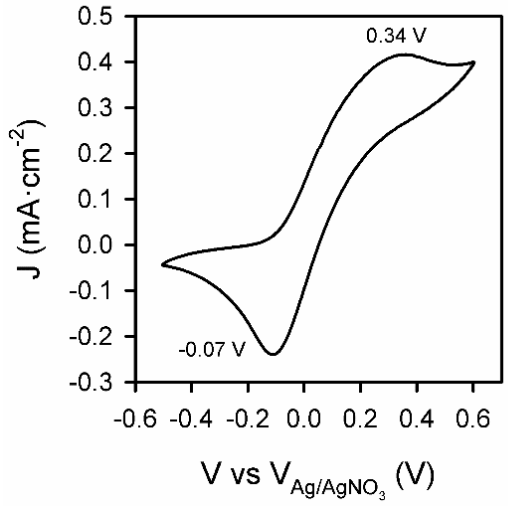

Figure S1. Cyclic voltammetry peak of Ferrocene/Ferrocenium (Fc/Fc^{+}). 1.9 mM of ferrocene was used to calibrate the applied voltage to the normal hydrogen electrode (NHE). Conditions: 100 mM of benzyl alcohol, in 0.1 M $TBAClO_4$ in CH_3CN, using $BiVO_4$ as WE, Pt film as CE, and $Ag/AgNO_3$ as RE.

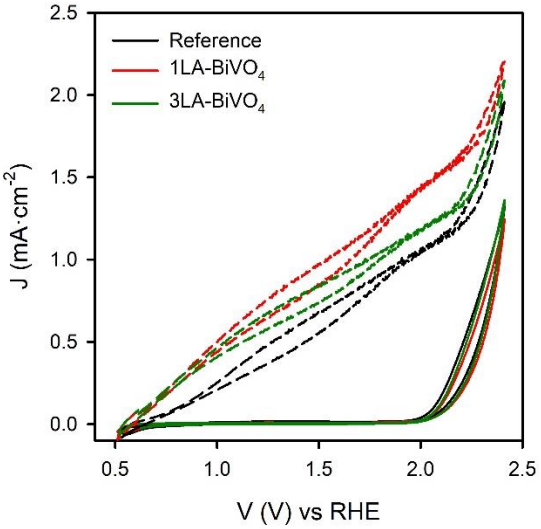

Figure S2. CV of Reference (black) and 1LA-$BiVO_4$ (red) measured at scan rates of 20 $mV \cdot s^{-1}$ in a 0.1M KPi buffered aqueous solution (pH 7.8) in the dark (solid lines) and under 100 $mW \cdot cm^{-2}$ illumination (dashed lines).

Morphological and structural characterisation data (SEM, XRD, TEM, SAED and STEM-EELS)

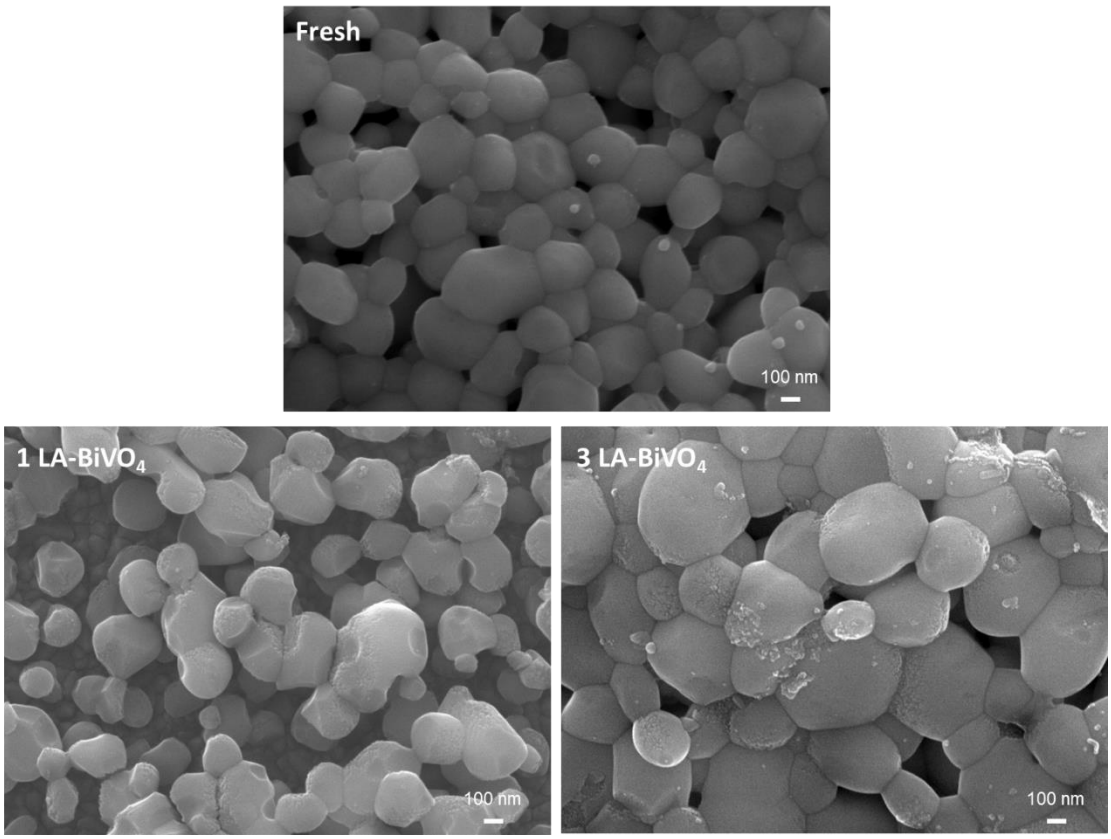

Figure S3. Top-view SEM images of Reference, 1LA-$BiVO_4$ and 3LA-$BiVO_4$ samples.

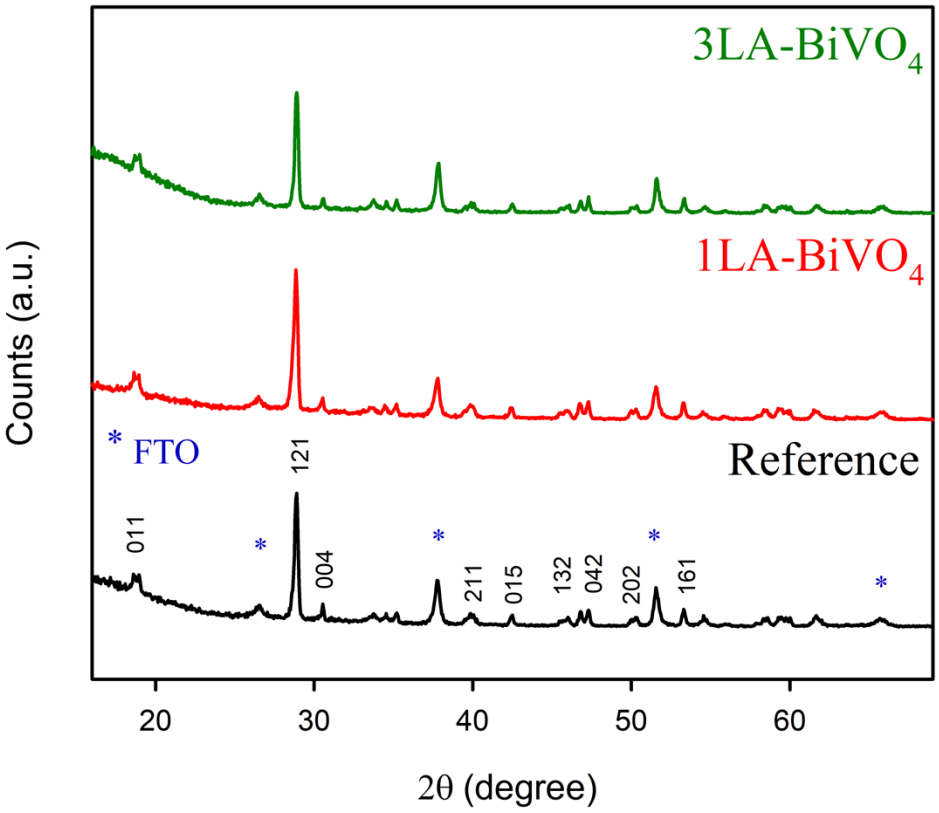

Figure S4. XRD spectra for Reference (black), 1LA-$BiVO_4$ (red) and 3LA-$BiVO_4$ (green) photoanodes.

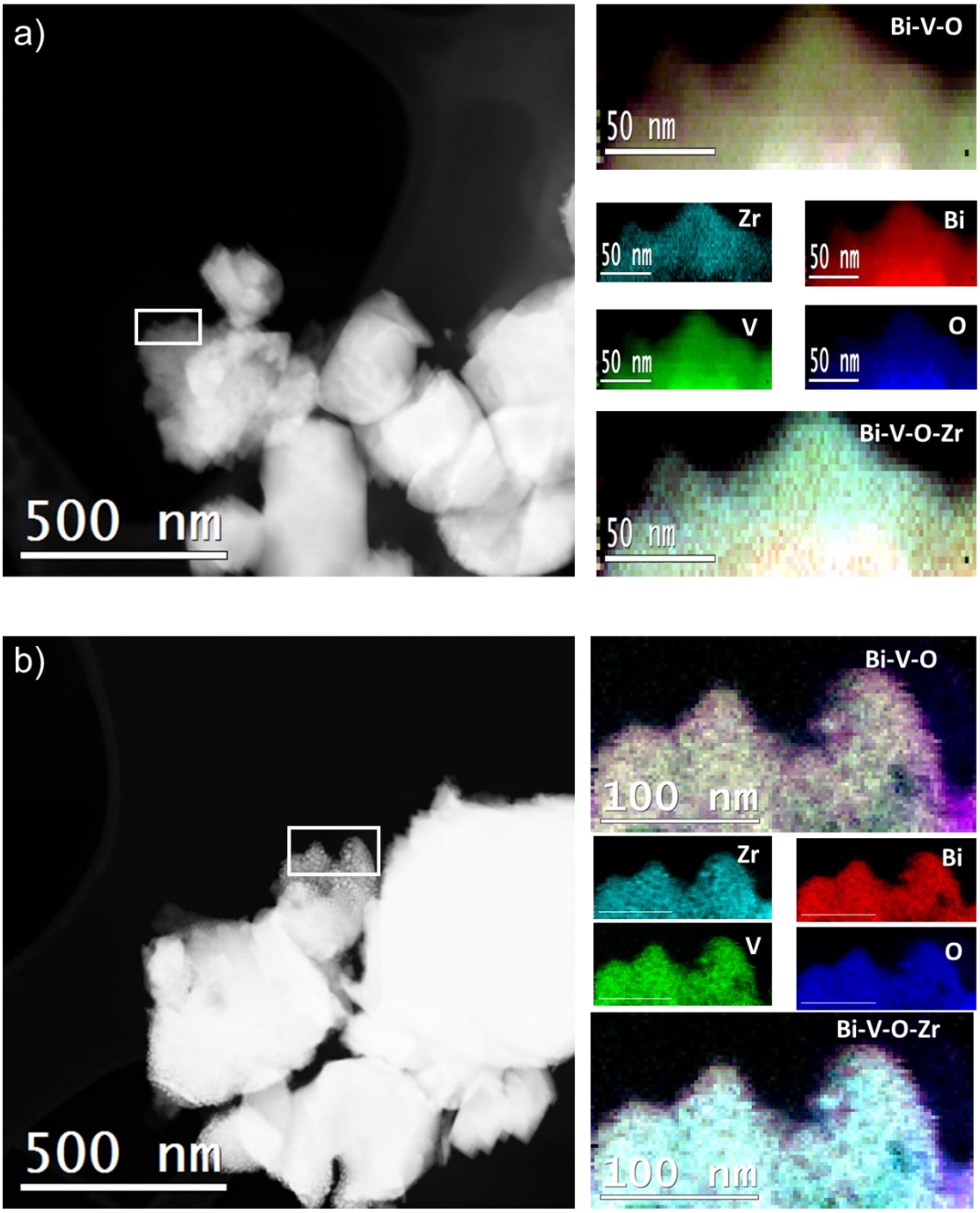

Figure S5. STEM-EELS measurements of Zr, Bi, V and O of a $BiVO_4$ section in (a) Reference and (b) 1LA-$BiVO_4$ samples.

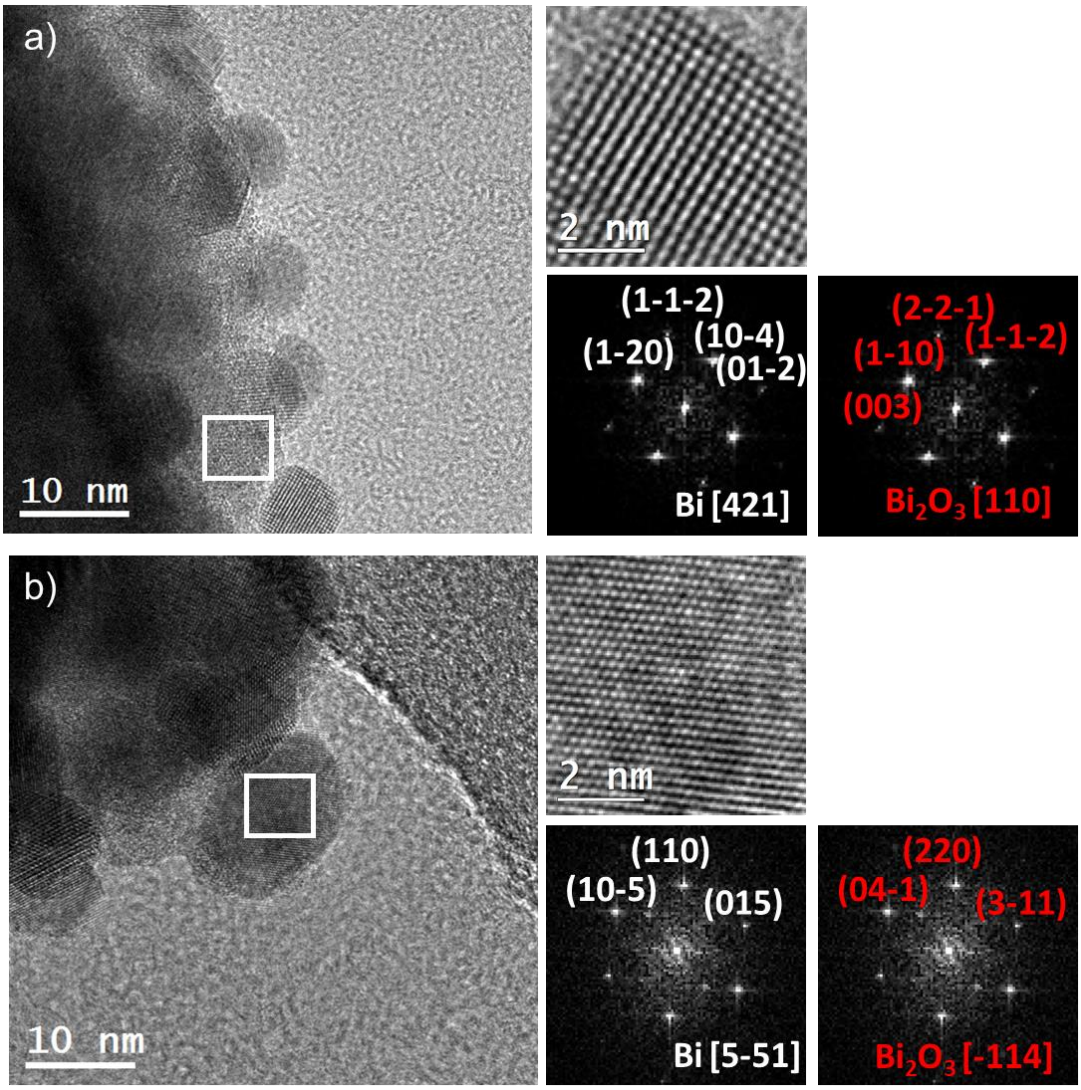

Figure S6. HRTEM images evidencing the particle segregation after electron beam irradiation of $BiVO_4$ samples. The power spectra analysis confirms that two possible structures consisting of metallic Bi or Bi_2O_3 could be possible and compatible with the structural indexation of the power spectra obtained on the HRTEM image.

The migration of atomic species from the bulk forming new particles at the surface of the $BiVO_4$ can be visualized at 10.5281/zenodo.5643642.

Electrochemical characterisation by impedance spectroscopy

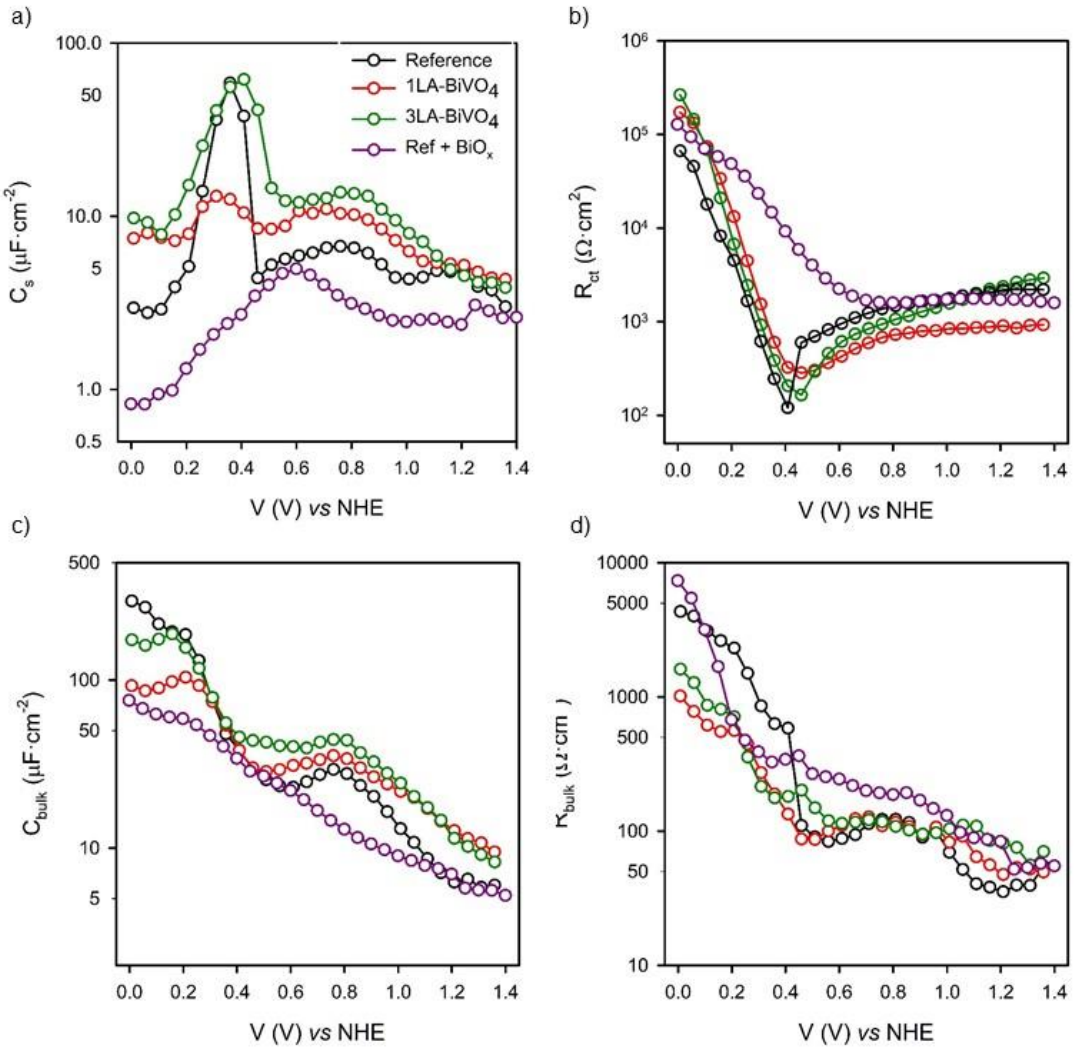

Figure S7. Impedance spectroscopy parameters extracted from fitting the experimental data with the selected equivalent circuit showed in Figure 3, (a) surface capacitance, C_s (b) charge transfer resistance, R_{ct} (c) bulk capacitance, C_{bulk} and (d) bulk resistance, R_{bulk} in $BiVO_4$ as a function of the light intensity during LA. Reference (Black), 1LA-$BiVO_4$ (Red), 3LA-$BiVO_4$ (Green), Reference with electrodeposited BiO_x on top (purple). Measurements were performed under illumination at 0.1 M benzyl alcohol oxidation conditions

Coating the fresh $BiVO_4$ with electrodeposited Bismuth species yields to the suppression of surface states associated to charge transfer Figure S7a and to an increase in R_{ct} in Figure S7b. The Bi coating seems to hinder the contribution of OV_s to C_{bulk} in Figure S6c.

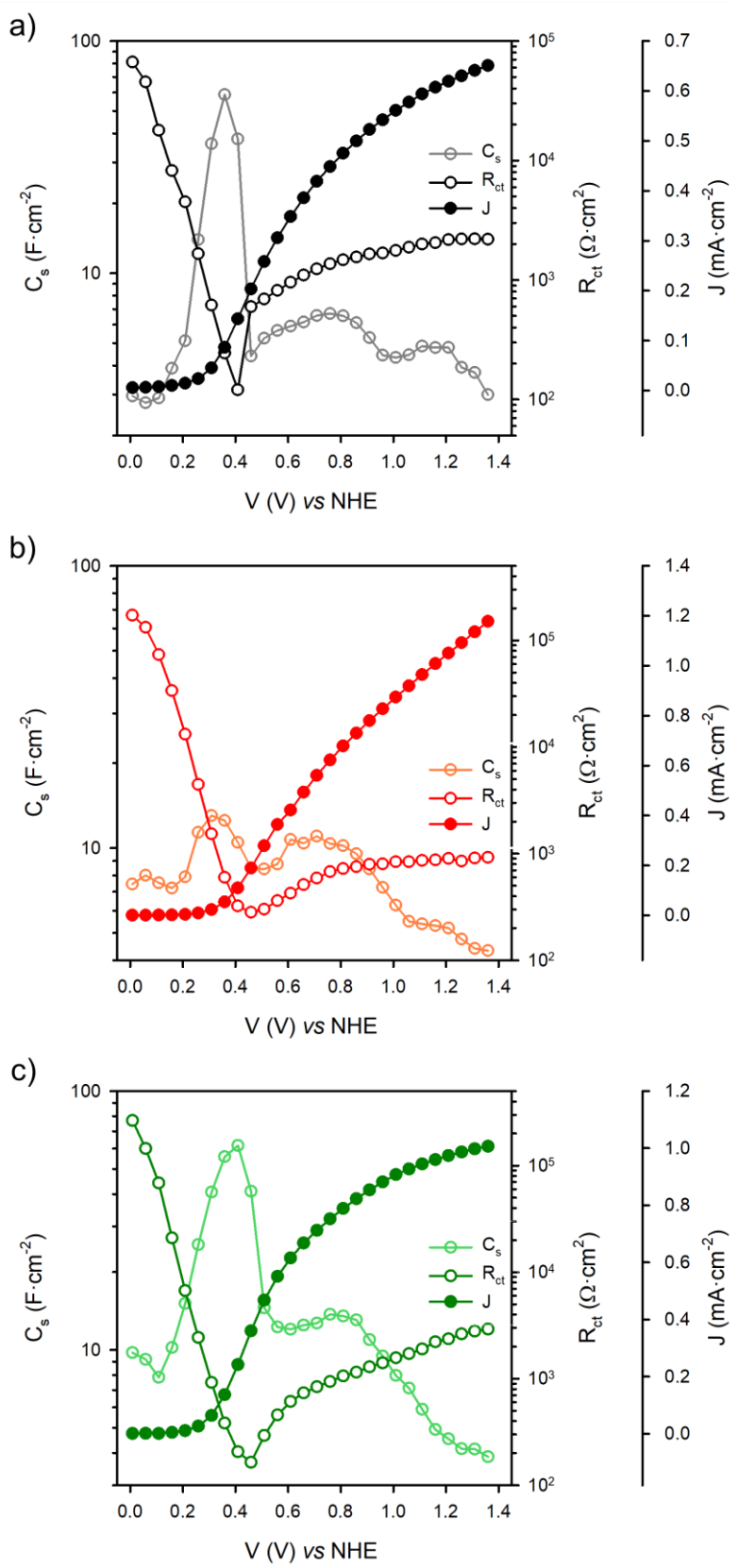

Figure S8. Comparison of C_s, R_{ct} and the J-V as a function of the applied potential for (a) Reference (Black), (b) 1LA-$BiVO_4$ (red) and 3LA-$BiVO_4$ (green). Measurements were performed under illumination at 0.1 M benzyl alcohol oxidation conditions.

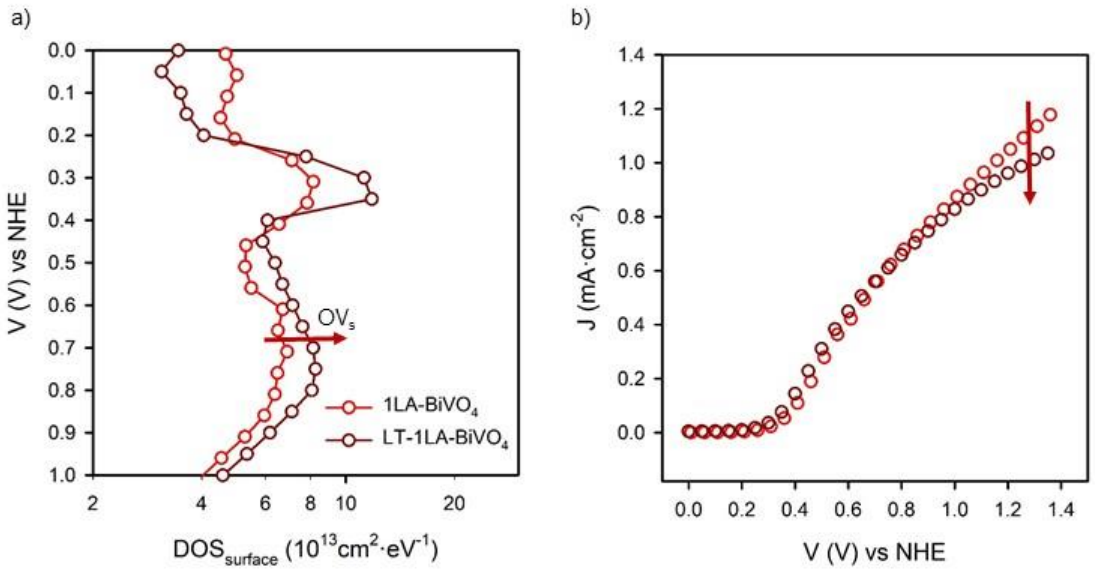

Figure S9. (a) Density of surface states and (b) Steady-state photocurrent as a function of applied potential. 1LA-$BiVO_4$ (Red) and LT-1LA-$BiVO_4$ (Maroon)

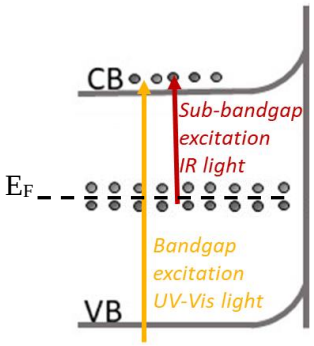

Figure S10. Schematic representation of the light-induced processes in a semiconductor upon bandgap excitation (yellow) using UV-Vis radiation, compared to sub-bandgap excitation (red) upon IR irradiation.

References

(1) Shaddad, M. N.; Ghanem, M. A.; Almayouf, A. M.; Gimenez, S.; Bisquert, J.; Herraiz-Cardona, I. Cooperative Catalytic Effect of ZrO2 and A-Fe2O3 Nanoparticles on BiVO4 Photoanodes for Enhanced Photoelectrochemical Water Splitting. *Chem. Sustain. Energy Mater.* **2016**, *9*, 1–7.

(2) Pavlishchuk, V. V; Addison, A. W. Conversion Constants for Redox Potentials Measured versus Different Reference Electrodes in Acetonitrile Solutions at 25°C. *Inorganica Chim. Acta* **2000**, *298*, 97–102.

(3) Bard, A. J.; Faulkner, L. R. *Electrochemical Methods: Fundamentals and Applications*; 2009.

6. Conclusiones generales y Perspectivas Futuras

En esta tesis doctoral se han abordado sistemas electro- y foto-electroquímicos con el objetivo de conseguir sistemas más eficientes y económicos con respecto a los dispositivos desarrollados hasta el momento. Para ello, se han planteado diferentes estrategias de trabajo: (1) la mejora funcional de los electrodos, fotoelectrodos y sustratos conductores, (2) la comprensión de los mecanismos operacionales de los procesos que ocurren en la celda (foto)-electroquímica y (3) el desarrollo y la evaluación de nuevos procesos electro- y foto-electroquímicos que permitan la síntesis de productos químicos orgánicos con alto valor añadido. Como resultado de estas estrategias, se ha conseguido comprender los mecanismos de reacción que ocurren en diferentes procesos de oxidación como, la oxidación de agua por vía electroquímica y la oxidación de un alcohol primario, como el alcohol bencílico, por vía fotoelectroquímica. Aunque los reactivos sean diferentes, se ha demostrado que en las dos reacciones ocurren a través de estados superficiales. La espectroscopia de impedancia ha resultado una técnica muy eficaz para visualizar y controlar dichos estados de forma fácil y no destructiva. De esta manera, procesos electroquímicos y fotoelectroquímicos pudieron ser diferenciados de otros procesos químicos o foto-químicos, lo que posibilitará el diseño de los sistemas y materiales para mejorar la selectividad y eficiencia de estos procesos. También se identificaron los procesos de degradación fotoquímica que se dan en el vanadato de bismuto y que son críticos para la aplicación de este material en dispositivos funcionales.

De los trabajos de investigación desarrollados resultaron tres artículos de investigación que fueron publicados en revistas de alto impacto, las conclusiones y logros de cada uno de ellos se exponen a continuación:

- Se utilizaron minas de grafito, de las utilizadas en los lápices y portaminas, para la preparación de electrodos decorados con Ni, Fe y NiFe. Más allá del bajo coste y del razonable rendimiento obtenido en la oxidación de agua, en este trabajo se ha proporcionado un análisis detallado de la respuesta electroquímica de estos electrodos a partir de la cual se puede obtener información novedosa que puede ayudar a comprender el comportamiento de los electrodos basados en Ni en general. Nuestros resultados muestran el potencial del uso de la espectroscopia de impedancia para caracterizar estos electrodos en condiciones de funcionamiento. Así, a través del análisis de la capacitancia del electrodo pudimos separar las transiciones redox Ni^{2+}/Ni^{3+} y Ni^{3+}/Ni^{4+}, incluyendo la identificación de las fases hidratada α-$Ni(OH)_2$/γ-NiOOH y no hidratada β-$Ni(OH)_2$/β-NiOOH. A continuación, combinamos los datos obtenidos mediante espectroscopia de impedancia para describir las diferencias en las voltamperometrías cíclicas y las curvas de densidad de corriente-voltaje bajo la

influencia de diferentes relaciones Ni:Fe. Finalmente, con estos datos se pudo hacer visible y resaltar cómo la transición redox Ni^{3+}/Ni^{4+} activa la transferencia de carga y, por tanto, la reacción de evolución de oxígeno, un hecho conocido, pero que hasta ahora ha requerido técnicas más complejas para ser medido.

- Se ha logrado la oxidación fotoelectroquímica del alcohol bencílico utilizando $BiVO_4$ como fotoánodo. Se ha identificado como bajo la influencia de la luz y la atmósfera en la que se realiza la síntesis fotoelectroquímica, esta oxidación también se produce por vías no electroquímicas. En este trabajo demostramos que, bajo luz ultravioleta y en presencia de oxígeno se forma la especie conocida como oxígeno singlete, $^1O_2$. Esta especie altamente reactiva, es capaz de oxidar el alcohol al aldehído correspondiente y llegar hasta el ácido. La supresión de la vía $^1O_2$ conlleva a una mejora de la selectividad y la eficiencia faradaica del proceso siendo ambas del 100 % a altas concentraciones. Además, la formación de $^1O_2$ también explica la producción de H_2O_2 en el medio de reacción. La detección de H_2O_2 como un producto secundario rentable ya se ha reportado en reacciones similares; sin embargo, hasta este trabajo aún no se había descrito una explicación clara para su formación.
- El efecto de los tratamientos de envejecimiento con luz sobre el comportamiento fotoelectroquímico de los fotoánodos de $BiVO_4$ se ha evaluado en el proceso de oxidación de alcohol bencílico. En este trabajo, se ha demostrado que la exposición a la luz tiene un claro efecto sobre las propiedades morfológicas, estructurales, químicas y superficiales de los fotoánodos de $BiVO_4$ y que este proceso es intrínseco del material, no depende de la reacción. Utilizando herramientas de caracterización eléctrica, fotoelectroquímica y HR-TEM se han atribuido las transformaciones químicas que ocurren en el fotoanodo a la segregación de especies de Bi en su superficie. Mediante espectroscopia de impedancia se demuestra que la segregación de Bi conduce a la formación de nuevos estados, intermedios relacionados con la formación de vacantes de oxígeno en el material. Adicionalmente, se reporta por primera vez la generación efectiva de fotocorriente a través de estos estados interbandas con excitación en longitud de onda infrarroja, confirmando la formación de vacantes de oxígeno durante los tratamientos con luz de $BiVO_4$.

Los resultados obtenidos en esta tesis revelan algunas líneas de trabajo con potencial para su explotación en el campo de la investigación básica de procesos electro- y foto-electroquímicos que en estos momentos ya están en marcha:

Las minas de grafito han demostrado tener buenas propiedades para llevar a cabo la reacción de evolución de oxígeno. Por ello, estos electrodos podrían utilizarse para realizar nuevos procesos electroquímicos, como la oxidación de alcoholes primarios o cualquier otro proceso

oxidativo. Además, un análisis similar al realizado mediante espectroscopía de impedancia, revelaría información de interés. Así, medidas de impedancia podrían relacionar estados superficiales del Ni con los diferentes mecanismos por los que ocurren ciertos procesos electroquímicos.

El excelente rendimiento obtenido con $BiVO_4$ para la oxidación fotoelectroquímica de alcohol bencílico puede aplicarse en otros sustratos orgánicos. Por ejemplo, la oxidación de glicerol o de 5-hidroximetilfurfural (HMF) son reacciones muy interesantes para su estudio. La oxidación del glicerol, un subproducto del biodiésel, puede producir dihidroxiacetona, cuyo coste es ~250 veces superior al del propio glicerol, lo que muestra el potencial industrial de esta reacción. Por otro lado, la oxidación de HMF produce el ácido 2,5-furandicarboxílico (FDCA), que es muy interesante para la producción de bioplásticos.

Finalmente, se ha demostrado que las vacantes de oxígeno en óxido semiconductores tienen un papel fundamental en la oxidación fotoelectrocatalítica de alcohol bencílico. Con los resultados aquí presentados, ahora se puede refinar el estudio de la reacción desde un punto de vista catalítico. El estudio de los estados superficiales en el $BiVO_4$, u otros electrodos, mediante el uso de la espectroscopía de impedancia como se ha hecho aquí puedes ser de gran ayuda en estas investigaciones. Adicionalmente, estos análisis, combinados con otras técnicas de caracterización en operación como la espectroelectroquímica o las espectroscopias moduladas en intensidad (IMPS o IMVS) podrán proporcionar detalles mecanísticos adicionales con los que complementar el estudio del funcionamiento de los fotoelectrodos.

Final Conclusions and Future Perspectives

In this doctoral thesis, electrochemical and photoelectrochemical systems have been addressed with the aim of achieving more efficient and economical systems. To this end, different strategies were considered: (1) the improvement of electrodes, photoelectrodes and back contact materials (2) the understanding of operational mechanisms of the different processes occurring in the (photo)-electrochemical cell and (3) the development and evaluation of new photoelectrochemical processes that allow the synthesis of chemical products and provide added value to conventional processes. As a result of these strategies, it has been possible to control and study different oxidation processes such as the oxidation of water by electrochemical means and the oxidation of a primary alcohol, such as benzyl alcohol, by photoelectrochemical means. Although different, both processes have been shown to occur through surface states and impedance spectroscopy has proved to be a very effective technique to visualize and monitor these states easily and non-destructively. In this way, electro- and photo-electrochemical processes can be differentiated from other chemical or photochemical processes, enabling improvements involving the selectivity and efficiency of electro- and photo-electrochemical processes.

From the research work carried out, three research articles were published in high impact journals, the conclusions and achievements of each one of them are presented below:

Pencil Graphite Rods have been performed for the preparation of Ni, Fe and NiFe decorated electrodes. Beyond the low cost and reasonable performance obtained in water oxidation, this work has provided a detailed analysis of the electrochemical response of these electrodes from which novel information can be obtained that can help to understand the behavior of Ni-based electrodes in general. Our results show the potential of using impedance spectroscopy to characterize these electrodes under operating conditions. Thus, through electrode capacitance analysis we were able to separate the Ni^{2+}/Ni^{3+} and Ni^{3+}/Ni^{4+} redox transitions, including the identification of the hydrated α-$Ni(OH)_2$/γ-NiOOH and non-hydrated β-$Ni(OH)_2$/β-NiOOH) phases. Next, we combined the data obtained by impedance spectroscopy to describe the differences in cyclic voltammetries and current-voltage density curves under the influence of different Ni:Fe ratios. Finally, with these data it was possible to make visible and highlight how the Ni^{3+}/Ni^{4+} redox transition activates charge transfer and therefore oxygen evolution reaction, a well known fact that until now has required more complex techniques to be measured.

Photoelectrochemical oxidation of benzyl alcohol has been achieved using $BiVO_4$ as a photoanode. Under the influence of light and the atmosphere in which the photoelectrochemical synthesis takes place, an additional non-electrochemical pathway occurs. In this work we demonstrate that under these reaction conditions, the reactive oxygen species $^1O_2$ is formed. This highly reactive species is able to oxidize the alcohol to the corresponding aldehyde. The

suppression of the $^1O_2$ pathway leads to an improvement of the selectivity and faradaic efficiency of the process being both 100 % at high concentrations. In addition, the formation of $^1O_2$ also accounts for the production of H_2O_2 in the reaction medium. The detection of H_2O_2 as a profitable by-product has already been reported in similar reactions; however, a clear explanation for the formation of this species has not yet been described.

The effect of light aging treatments on the photoelectrochemical behavior of $BiVO_4$ photoanodes is evaluated for benzyl alcohol oxidation. In this work, it has been demonstrated that light exposure has a clear effect on the morphological, structural, chemical and surface properties of $BiVO_4$ photoanodes. Using electrical characterization, photoelectrochemical and HR-TEM techniques, chemical transformations have been attributed to the segregation of Bi species on the surface of the photoanode and by impedance spectroscopy it is shown that Bi segregation leads to the formation of new states, related to the formation of oxygen vacancies in the material. Additionally, it is reported for the first time the effective generation of photocurrent from the interband states by continuous excitation at infrared wavelength, confirming the formation of oxygen vacancies during the treatments with $BiVO_4$ light.

The acquired findings also reveal some lines of exploitation in the field of basic research of electro- and photo-electrochemical processes.

Pencils Graphite Rods have shown to have good properties to carry out the oxygen evolution reaction. Therefore, these electrodes could be used to perform new electrochemical processes, such as the oxidation of primary alcohols or any other oxidative process. In addition, an analysis similar to that performed by impedance spectroscopy would reveal information of interest. Thus, impedance measurements could relate Ni surface states to the different mechanisms by which certain electrochemical processes occur.

The excellent performance obtained with BiVO4 in the photoelectrochemical oxidation of benzyl alcohol can be used for other organic substrate. For example, the oxidation of glycerol or hydromethylfurfural (HMF) are very interesting reactions to study. Interestingly, the degradation of glycerol, a by-product of biodiesel, can produce dihydroxyacetone, whose cost is ~250 times higher than that of glycerol itself. On the other hand, the oxidation of HMF produces FDCA, which is very interesting for the production of bioplastics.

Finally, oxygen vacancies have been shown to play a key role in the photoelectrocatalytic oxidation of benzyl alcohol. With these results presented, the reaction could now be studied from a catalytic point of view. Techniques such as impedance spectroscopy could potentially be used to study the surface states generated by benzyl alcohol on $BiVO_4$. Additionally, other characterization techniques at work such as spectroelectrochemistry (SEC) or IMPS would provide additional mechanistic details to complement this study.

UNIVERSITAT JAUME I

inam Institute of Advanced Materials UJI Castelló

Development and Characterization of Electro- and Photo-Electrochemical Systems for High-Added-Value Products

Ramón Arcas Martínez | 2023